Characterization of Carbon Nanostructures Based on Transmission Line Model.

Zhang, Jiefu

Characterization of Carbon Nanostructures Based on Transmission Line Model

Jiefu Zhang

A Thesis Submitted to the faculty of the University of London

in partial fulfilment of the requirements for the degree of

Doctor of Philosophy

Shool of Electronic Engineering and Computer Science,

Queen Mary, University of London

London E1 4NS, United Kingdom

July 2014

Abstract

In the past two decades carbon nanotubes and graphene have attracted a lot of research attention due to their exceptional electronic properties. The research focus on improving the synthesising techniques will eventually lead to their applications in terahertz wave, millimetre wave and microwave frequencies.

In this thesis, a modelling technique based on the transmission line theory is proposed to calculate the 2-port S-parameters of vertically aligned CNT arrays with finite sizes and arbitrary cross sections. The process takes into account all the coupling in the array and gives the analytical solution of S-parameters. The simulation results from the proposed technique are compared with results obtained by effective single conductor model and shows a good matching for small arrays and an increasing difference with the increase of array sizes.

From the S-parameters, the fundamental properties of CNT arrays such as input impedance and absorption are obtained and compared with measurement results in microwave frequencies. The dependence of these properties on ambient temperature and host medium are also presented to explore the tunability of CNT arrays. From the Fabry-Perot the wave propagating velocity is also calculated for arrays with different sizes and fitted with a power function. The S-parameters allows the extraction of the complex permittivity, permeability and conductivity of the CNT array. The extracted permittivity and absorption are compared with measurement results.

The graphene nanoribbons are simulated in the same manner. The graphene sheet on top of a microstrip gap is simulated using transmission line model at microwave frequencies to show the impact of parasitics and contact resistances.

Finally, a graphene based microwave absorber is proposed and modelled under both electric and magnetic bias. The absorber shows good broadband absorption rate and a potential for turning transparent and opaque to microwaves under both electric and magnetic bias.

Acknowledgements

First of all I would like to express my sincere gratitude to my supervisor, Prof. Yang Hao, whose supervision and advice provided constant support during this research project. His encouragement and guidance is essential for my transition from a student to a researcher. Without his firm support, this thesis would not have been possible. I'm also very grateful for Prof. Clive Parini and Dr. Robert Donnan for their valuable suggestions and comments on my research.

My special thanks to Dr. Anestis Katsounaros and Dr. Hatice Tuncer and Dr. Bian Wu, for their help and advice during this research project, and for the sample fabrication and the help in measurement. They are all very knowledgeable, passionate about research, and humorous. It has been a pleasure to work with them. Also thanks to Mr. Lei Li and Dr. Yuezhou Li for proof reading my thesis and provide valuable suggestions on revision.

Thanks then goes to my other colleagues, Dr. Max Munoz, Dr. Alice Pellegrini, Dr. Hai Lin, Dr. Lian Hong, Dr. Min Zhou, Dr. Yifeng Fan, Dr. Tuba Yilmaz, Mr. Majid, Mr. Darryl, Ms. Khaleda Du, Mr. Ke Yang, Mr. Jin Tian, Mr. Chen Qiao, and all the rest for the inspiring discussions and for creating a great environment for working.

During these years, I was fortunate to meet some valuable friends: Ms. Shan Zhang, Mr. Tian Zhang, Ms. Jie Xia, Mr. Le Yu, Ms. Dodo Chen, and Mr. Xiki Tempura. Thank you for creating many good memories that I will cherish no matter how far we are apart.

Additionally, I would like to thank the CSC for providing financial support during my Ph. D. study.

Above all, special thanks to my family, especially my parents, for all their love, encouragement and spiritual support.

List of Publications

Published

Zhang, J.; Hao, Y., "Characterization of Vertically Aligned Multi-wall Carbon Nanotube Arrays Based on Multi-conductor Transmission Line Model," *Antennas and Wireless Propagation Letters, IEEE* , vol.PP, no.99, pp.1,1

Jiefu Zhang; Yang Hao, "A general technique for THz modeling of vertically aligned CNT arrays," *Antennas & Propagation (ISAP), 2013 Proceedings of the International Symposium on* , vol.01, no., pp.281,283, 23-25 Oct. 2013

Jiefu Zhang; Yang Hao, "Novel technique of signal propagation analysis for arbitrary MWCNT bundles," *Antennas and Propagation Society International Symposium (APSURSI), 2013 IEEE* , vol., no., pp.1596,1597, 7-13 July 2013

Katsounaros, A.; Zhang, J.; Hao, Y., "Microwave characterization of a single multi-wall carbon nanotube," *Electromagnetics in Advanced Applications (ICEAA), 2012 International Conference on* , vol., no., pp.591,594, 2-7 Sept. 2012

Katsounaros, A.; Jiefu Zhang; Yang Hao, "Microwave modeling of single multi-wall carbon nanotubes," *Antennas and Propagation (EUCAP), 2012 6th European Conference on* , vol., no., pp.2673,2676, 26-30 March 2012

Under Review

Bian Wu, Yu-Tong Zhao, Jiefu Zhang, Yang Hao “Modeling and Validation of Optically Transparent Microwave Absorber Based on Graphene”, submitted to MTT

Jiefu Zhang, Yang Hao “Transmission-Line Based Microwave Permittivity Characterization of Vertically Aligned Multi-wall Carbon Nanotubes”, submitted to EL

Jiefu Zhang, Yang Hao “Performance analysis of MWCNT and GNR arrays based on Multi-conductor Transmission Line Model”, invited paper for PIER

Table of Contents

List of Figures

List of Tables

Chapter 1 Introduction

Carbon materials have a long history of application. The isomers of carbon, such as fullerenes, carbon nanotubes (CNTs) and graphene have various atomic or molecular structures [1-3]. In the past two decades carbon nanostructures have attracted a lot of research attention due to their exceptional mechanical [4, 5] and electronic properties. For example, they have been reported to show high electron mobility [6], large current carrying capability [7] and thermal conductivity [8]. CNT and graphene, in particular, has emerged as a new material believed to have many potential applications, such as next-generation integrated circuits [9], gas sensors [10], batteries [11], hydrogen-powered vehicles [12] and high efficiency solar cells [13]. In particular, microwave and terahertz applications of both CNT and graphene, including nano-sized antennas [14], absorbers [15, 16] and interconnects [17] have been proposed and studied.

A graphene is a two dimensional material comprised of a single layer of adjacent honeycomb cells made of carbon atoms. The zero band-gap [18] of graphene is the key to its many unusual properties. This will be elaborated in the following chapters. A CNT can be viewed as a seamless hollow cylinder rolled up from one or several layers of graphene and can be classified as single-wall or multi-wall (SWCNT or MWCNT) accordingly. The diameter of a CNT plays an important role in its conductivity. A SWCNT can be metallic or semiconducting while a MWCNT is usually metallic.

The CNT was first synthesized in 1991 by Iijima [2], who also presented an experimental observation of carbon nanotubes using Transmission Electron Microscopy (TEM). Since then the fabrication techniques has been constantly improved and the lengths of CNTs have been increased from several micrometers to several centimeters [19]. This has further increased the possibility of CNTs for antenna and microwave applications.

The CNTs can be synthesised together to form vertical or horizontal arrays. Unlike the individual CNT, the first CNT array was first reported much earlier in 1966 by Thess [20] and since then, many different techniques have been studied to synthesise CNT arrays with larger aspect ratio, more regular alignment and higher quality [21-25]. The vertically aligned arrays can be synthesised on different substrates such as quartz and silicon using the chemical vaporization deposition (CVD) method, which realizes the growth by placing a nano-particle of catalyst (usually Fe , Ni or Co) on the substrate and pump gases with carbon atoms into a chamber with high temperature [26]. The aligned CNT arrays have similar potential applications as the individual CNT, but due to their large surface area, are also applicable as sensors of detecting DNA, glucose, pH and NO_2 gases [27-30].

The graphene was first experimentally discovered in 2004 [3] by mechanical exfoliation of graphite. In recent years, both synthesizing techniques and terahertz applications have been the focus of research. Current synthesizing techniques includes dry exfoliation [31], wet exfoliation [32], growth on silicon carbide [33] and CVD [34]. The current research focus in the electromagnetic applications for graphene includes plasmonics in terahertz and higher frequencies [35-38], microwaves transistors, absorbers [39, 40], and MEMS switches [40], etc.

Supported by the aforementioned studies, the commercialization of these materials have been steadily going on for more than a decade. For example, CNT composite was used in the winning Tour de France bicycle in 2005 [222] for enhanced strength and reduced weight, the antifouling paint with CNTs were used on ship hull coatings in 2008, and CNT electrostatic discharge shielding (ESD) shield was used in Juno spacecraft in 2011 [222]. For graphene, the first commercialized product is the security smart packaging by Siren Tech in 2012, which uses graphene based ink. In the following two years, graphene was reported to be used in tennis rackets and skis. Also in 2013, graphene based thermal paste was produced to provide better CPU cooling. And finally, in 2014, graphene was also used in composite materials for bicycles and helmets [223].

However, most CNT and graphene production today is used in bulk composite materials and thin films, which rely on unorganized architectures having limited properties [222]. The commercialized electronic devices based on CNT or graphene, is still not available, mainly due to the difficulty in both the modeling and the fabrication of such materials.

To explore the electromagnetic properties and applications for CNTs, it is necessary to characterize the CNTs and extract their material properties, namely permittivity, permeability and conductivity. As the material properties of the CNT depends on the intrinsic structure and dimensions of the CNT itself, it is natural to think of the possibilities of finding the relationship between the CNT dimensions and the material properties and thus we can have a general idea of the electromagnetic capabilities of the material and explore the potential applications even before the actual synthesis process is done, due to the fact that the cost of synthesizing CNTs is still high. Similar situation apply to graphene, except that the graphene is a 2-D surface thus cannot be described by 3-D material properties such as permittivity and permeability. Instead, the graphene is characterized by surface conductivity and resistivity.

However, since the dimensions of both CNTs and the graphene are small compared to the wavelength of microwaves, it is difficult to simulate them directly in the commercial software such as HFSS or CST, especially under microwave frequencies. Therefore, it is urgently needed to develop an efficient modelling tool for the characterization of CNTs and graphene at microwaves. From the 1990s, the pioneering work of characterizing CNTs has been done by P.J Burke by modeling them using effective transmission line (TL) models [41]. In his paper two new components were added to the conventional transmission line theory, namely the quantum capacitance and the kinetic inductance, to simulate the band structure and the movement of electrons in CNTs. Further studies by G. Miano, et, al. [42] and Y. Xu [43] have proven that the TL model can be derived from a 2D fluid model of electrons, making it physically consistent. Using the TL model, it is possible to effectively simulate not only an individual CNT but also CNT arrays.

In this thesis, the fundamental properties of carbon nanotube array and graphene are studied. A multi-conductor transmission line (MTL) based modelling technique to obtain the S-parameter and material properties such as permittivity and permeability is proposed for the vertically aligned multiwall carbon nanotube arrays. The applications of carbon nanotube arrays such as absorbers are discussed. The same transmission line model is also used employed to study the electric properties of graphene strips and patches. Finally, the applications of graphene-based electromagnetic wave absorbers is studied to show the excellent absorption capabilities and a good tunability under both electric and magnetic biases.

The major contributions of this work are as follows:

Based on the MTL theory, a technique to extract the S-parameter of a vertically aligned CNT array with arbitrary cross section is proposed. The advantage of this technique is that it takes into account all the mutual coupling between different CNTs as well as different shells in the same CNT, while previous results neglect at least some of the mutual coupling and consider a multi-conductor transmission line as an effective single-conductor one. Also, this technique gives the analytical form of the 2 port S-parameter from the multi-port network without the need of numerical methods. From the S-parameter, the absorption and input impedance characteristics can be extracted. The influence of temperature and permittivity of the host media on these characteristics are also studied to explore the potential applications of CNT arrays.

The Fabry-Pérot resonance in the CNT array is studied and used to obtain the wave propagating velocity for different array sizes is presented for the first time. The result clearly shows a power law relationship between the propagating velocity and array sizes.

The CVD synthesized vertically aligned CNT samples are measured in X-band and the permittivity and permeability of these samples are extracted from the measured complex S-parameters. Based on the mixing rules of the effective medium [43], the permittivity of an individual CNT is obtained from Maxwell-Garnett formula [43] and matched with the permittivity obtained by optimizing in CST. From the S-parameters obtained from TL model, the permittivity of an individual CNT is also extracted and compared with measurement results.

Various graphene nanoribbon (GNR) arrays are simulated with the same MTL technique and the results is compared with the CNT array. From the TL model for GNRs and the Kubo Formula for graphene sheets, an equation to determine the mean free path (MFP) is derived so that the TL model can be extended to macroscopic graphene patches. A graphene patch placed on top of microstrip lines with gap in middle is simulated using the TL model. The parasitic capacitance and contact resistance between graphene and microstrip is fitted with measurement results.

Finally, a single- and multi-layer graphene based absorber is simulated in microwave frequencies. The tunability of the conductivity of graphene under both electric and magnetic bias are considered.

The wide bandwidth absorbing capabilities and the on-off behavior under magnetic bias are presented.

The organization of this thesis is as follows:

Chapter 2 is an overview of fundamental properties, including the molecular structure, bandgap and conductivity, of both carbon nanotube and graphene. The number of conductive channels, which closely relates to the conductivity of the CNT and the graphene, is also reviewed.

Chapter 3 focus on the modeling techniques of CNT arrays. Starting from the basic transmission line and multi-conductor transmission line theory, both an individual CNT and a CNT array are modeled with an equivalent circuit model based on the Luttinger liquid theory. Then, the circuit components are given in the matrix form and from the 2n-port transfer matrix, the 2-port S-parameter of the vertically aligned CNT (VACNT) array is calculated analytically from microwave to terahertz. The results obtained from both the equivalent single conductor model and the multi-conductor model are compared to show the limitations of the former at high frequencies.

Chapter 4 presents the characterization of VACNT arrays using the techniques developed in chapter 3. From the S-parameters, the absorption and input impedance can be obtained. The influence of array size, shape of cross section, permittivity of host media and temperature is studied and potential applications are discussed. The concept of normalized absorption is presented to cancel out the effect of reflection. The normalized absorption obtained from simulation is compared with measurement data obtained at X-band (8~12GHz) and shows a good matching. Also, the relationship between the absorption and CNT length is presented and the normalization process eliminates the previously unexplained ‘absorption peak’ which occur at certain length of CNT. The Fabry-Pérot resonance of the CNT array is presented and the wave propagation velocity is calculated from the periodicity of the resonance. The relationship between the array size and the wave propagating velocity is studied and a power law function is obtained from the curve fitting which matches very well with all simulation results. The CVD synthesized vertically aligned CNT samples are measured in X-band and the permittivity and permeability of the effective samples are extracted from the measured complex S-parameters based on the Nicolson-Ross-Weir approach. The permittivity of an individual CNT is then extracted from mixing rules of effective medium

and from the TL model directly. The two obtained permittivity are compared, and the relationship between permittivity and the CNT array size is discussed.

Chapter 5 studies the transmission and absorption properties of both GNR and graphene patches. The impact of parasitics and contact resistance in the characterization process is investigated. From the TL model for GNRs and the Kubo Formula for graphene sheets, an equation to determine the mean free path (MFP) is derived so that the TL model can be extended to macroscopic graphene patches. A graphene patch placed on top of a microstrip line with a gap is then simulated with the TL model in microwave frequencies. The parasitic capacitance and contact resistances of the graphene patch is quantified and verified with the measurement data.

Chapter 6 presents a tunable multi-layer graphene absorber under both electric and magnetic bias field. The design demonstrates wide band absorbing capabilities under electric bias and an additional magnetic bias can change the surface conductivity of the graphene layers dramatically, turning the graphene absorber into a reflector.

Finally, a summary of conclusions and discussions for future research topics are presented in chapter 7.

Chapter 2 Fundamental Properties of CNT and Graphene

2.1 Introduction

The forms of existence of carbon element are many and varied. The allotropes of carbon range from graphite, diamond to the less-commonly seen buckyballs, carbon nanotubes and graphene. In these allotropes the structure of carbon atoms and chemical bonds differ greatly, giving them various mechanical, electrical and chemical properties. For example, the graphite is a soft, black solid with good conductivity while diamond is a hard and transparent solid with very little conductivity. Fig 2.1(a) and (b) depicts the atomic structure of carbon nanotube and graphene. Although they have similar atomic bonds, the two still differ in stiffness, conductivity and form of existence.

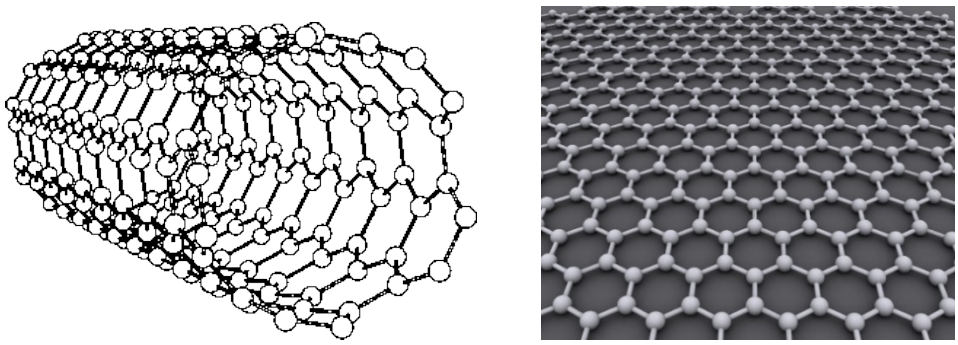

Figure 2.1 Atomic structure of (a) a single-wall carbon nanotube [45] (b) a single-layer graphene [46]

The rapid development in the resolution of microscopes from 1950s made it possible to observe and control structures in nanometers. This led to the discovery of C_{60} buckyball in 1985 [1], of carbon nanotubes in 1991 [2] and of graphene in 2004 [3]. These less-common allotropes of carbon have a lower dimensionality compared to graphite and diamond and embodies a series of unique electric properties. The zero dimensional buckyball is an n-type semiconductor with non-linear optical absorption properties [47], while one dimensional carbon nanotubes can be either semiconducting or metallic [48], and two dimensional graphene is a zero bandgap semi-metal [49].

These newly discovered allotropes soon attracted a lot of research interest and are found of having many extraordinary mechanical, electrical and chemical properties. Thus they are believed to be the materials crucial to build the nano devices of next generation, such as nano-scale antennas [50,51], interconnectors for next generation VLSI circuit [52-54], nano-scale field effect transistors [55, 56], THz filters [57, 58], nano-scale gas detector [59] and high efficiency solar cells [60,61]. To better understand the electric properties of carbon nanotubes and graphene, several models have been proposed to model their conductivity and permittivity from microwave to terahertz frequencies.

2.2 History of Carbon nanotubes and graphene

The history of carbon nanotubes is closely related to the history of carbon fibers, which can be regarded as the macroscopic analogue of carbon nanotubes. Although the first use of carbon fiber can be dated back to the 19th century when Thomas A Edison prepared them to provide a filament for an early model of an electric light bulb, further research on carbon filaments proceed slowly. It was until 1950s when the second stimulus to carbon fiber research came. The boost in space and aircraft industry in the 1950s placed an urgent requirement in material with extraordinary mechanical properties and carbon fibers became the ideal candidate for its strength, stiffness and lightweight. In the following 10 years, this material became very popular and was studied by many laboratories worldwide, such as Union Carbide Corporation, the Aerospace Corporation, etc., resulting in some other important structures such as carbon whiskers. [62, 63]. In 1952, Radushkevich and Lukyanovich published the first paper showing hollow graphitic carbon fibers that are 50nm in diameter [64].

From the early 60s, researchers began to realize that to reduce fiber defects and enhance structures resistive to crack propagation, a new synthesis process must be developed. In the next few decades, the catalytic chemical vapor deposition (CVD) technology intended to gain more control of the synthesis process and improve the strength and modulus of the carbon fiber grew rapidly, and as a result, researchers were able to grow carbon fibers on the micrometer scale. Some very thin filaments with diameters less than 10nm have been occasionally reported [65, 66], and such reports inspired researchers to ask whether there was a minimum dimension for such filaments. The direct stimulus to the study of this question appeared in December 1990, when Smalley gave an update status for his research on fullerenes [67] at a carbon-carbon composite workshop, with two other important papers presented in the same workshop. One was about a new efficient method for fullerene production, presented by Huffman [68] and the other, by M. S. Dresselhaus [69], was a review on carbon fiber research. At this workshop, Smalley started thinking about the existence of carbon nanotubes of dimensions comparable to C-60. In August 1991, at a fullerene workshop in Philadelphia, M. S. Dresselhaus [70] gave an oral presentation on the symmetry proposed for carbon nanotubes capped at either end by fullerene hemispheres. However, the real breakthrough on carbon nanotube research came with Iijima's report [71]. An experimental observation of carbon nanotubes using Transmission Electron Microscopy (TEM) was given at that report. This work from Iijima was the one that verified all the previous theoretical works by others. Only one year later, a new method for producing gram quantities of carbon nanotubes were reported [72]. A new era for the Carbon Nanotube research started.

The history of graphene was even older and closely related to graphite oxide. In 1859, Brodie, using methods described by Schafhaeutl [73], discovered the highly lamellar structure of thermally reduced graphite oxide [74]. It was until a century later in 1962, did Boehm et al. found that the chemical reduction of dispersion of graphite oxide in dilute alkaline media produced thin, lamellar carbon that contained only small amounts of hydrogen and oxygen [75-77]. Several other researchers including Blakely and Bommel proposed various methods of prepare monolayer graphite oxide [78-83] however the free standing monolayer graphene was unable to be found.

Meanwhile, the theoretical study of graphene as a 2-dimensional (2D) graphite has also started from the 1930s [84-86]. With the 2D nature of the graphene, it was considered to be building blocks for graphitic materials of all other dimensions—it can be wrapped up into 0D fullerenes,

rolled into 1D nanotubes and stacked into 3D graphite, thus these early studies laid down the foundations of describing properties of various carbon-based materials. However, graphene was considered to be thermodynamically unstable and could not exist [87, 88], unless grown epitaxially on top of a 3D base [89, 90]. Until 2004, the free-standing graphene was experimentally discovered by mechanical exfoliation [3].

2.3 Structures of graphene and carbon nanotubes

The structure of graphene is a single layer of carbon atoms and are building blocks of other carbon allotropes, such as CNTs, which can be categorized as single-walled (SWNTs) and multi-walled (MWNTs).The atomic structure of SWCNTs are simple to understand, it can be viewed as a single layer of graphene sheet rolled up into a seamless cylinder, as depicted in Figure 2.2, with two hemispherical fullerene ‘caps’ at each end.

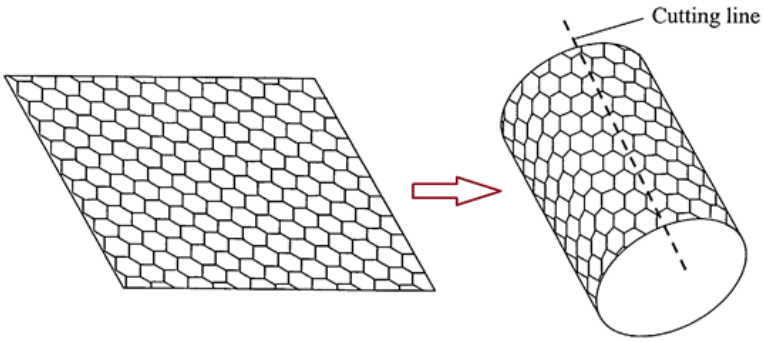

Figure 2.2: Single-Walled Carbon Nanotubes (SWCNTs) can be viewed as a single sheet of graphene rolled up into a seamless cylinder [94].

According to different directions along which the graphene sheet is rolled up, there can be 3 different SWCNT structures. This is called the chirality, which will be discussed in the following sections. The wall of the SWCNT is only one atom thick and the diameter is usually 0.7nm – 10nm [91]. Calculations have shown that collapsing the single wall tube into a flattened two-layer ribbon is energetically more favorable than maintaining morphology beyond a diameter value of about 2.5nm [92].

Compared to the diameter, the length of a CNT is extremely large so that the aspect ratio (length/diameter) of the cylinder is between 10^4 - 10^7 and can reach up to 10^8, as in the observation of the longest carbon nanotubes (18.5cm long) reported in 2009 [93]. These nanotubes were grown on Si substrates using an improved chemical vapor deposition (CVD) method and represent electrically uniform arrays of single-walled carbon nanotubes. Therefore, if we neglect the two ends of a carbon nanotube and focus on the large aspect ratio of the cylinder, a SWCNT can be considered as a one-dimensional nanowire.

The structure of the Multi-Walled Carbon Nanotubes (MWCNTs) is similar to that of SWCNTs, which can be described either with the Russian doll model, in which SWCNTs of different diameters are arranged in concentric cylinders, or the Parchment model, in which a single graphene is rolled in around itself, resembling a scroll of parchment or a rolled newspaper. The diameter of MWCNTs can range from a few nanometers to more than 50 nanometers, with the distance between neighboring graphene layers of 0.34nm—a distance determined by the Van de Waals force and confirmed experimentally [2, 95]. With their big difference in diameter, it is easy to distinguish a MWCNT from a SWCNT using Transmission Electron Microscope (TEM), as shown in Figure 2.3. However, as MWCNTs are comprised of several SWCNTs, it's important to start from SWCNTs to study their structure and properties, as shown in the following sections.

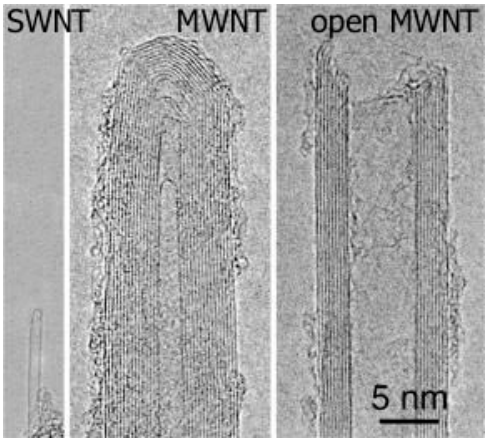

Figure 2.3: Transmission electron microscopy (TEM) image of different nanotubes, left is a SWCNT, middle is a MWCNT with fullerene caps, and right is a MWCNT without cap. Each black line corresponds to one graphene sheet viewed edge-on [96]

It is worth noting that the aforementioned ‘rolled-up graphene’ is only an analogy to help understand the structure of SWCNT. In reality, the SWCNT is not made from graphene sheet, but instead, synthesized using CVD, during which a substrate is prepared with a layer of metal particles. Then gas containing carbon atoms fills into a high temperature chamber in which the substrate is located. CNTs will grow along their vertical axis under such environment. Different number of walls on the CNTs is achieved by controlling the temperature in this process.

2.4 Orbital Hybridization and Chirality

A crystal lattice can be considered as an array of small ‘boxes’ infinitely repeating itself in all three spatial directions. Figure 2.4 shows an unrolled honeycomb lattice of a graphene sheet with a coordinate system. The small dots denote the position of carbon atoms and the line between two carbon atoms represents the carbon-carbon bonds, which are formed through orbital hybridization [97]. Clearly, the solid dots and hollow dots forms two triangular sublattices, thus the unit cell is comprised of adjacent two neighboring atoms from each of the sublattice.

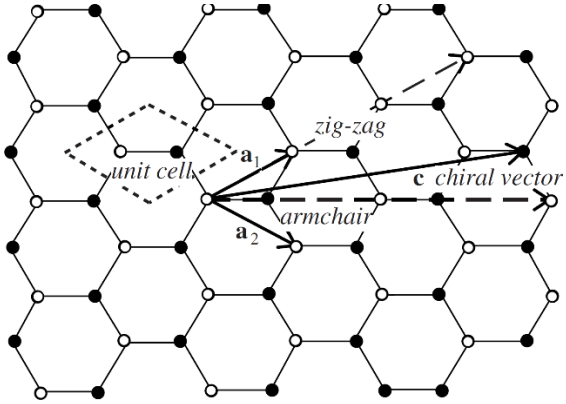

Figure 2.4: A graphene sheet with lattice based vectors and position vectors. Perpendicular to c is the tube axis. The zigzag and armchair chiral vectors, respectively, were highlighted. The dark dots denote carbon atoms [42].

The ground state of a carbon atom is [98]

$$C \qquad \underset{1s}{\uparrow\downarrow}\ \underset{2s}{\uparrow\downarrow}\ \underset{2p_x}{\uparrow}\ \underset{2p_y}{\uparrow}\ \underset{2p_z}{\ }$$

In carbon nanotubes and graphene, the hybridization is sp^2, in which the 2s orbital and two 2p orbitals are hybridized.

$$C^* \qquad \underset{1s}{\uparrow\downarrow}\ \underset{sp^2}{\uparrow}\ \underset{sp^2}{\uparrow}\ \underset{sp^2}{\uparrow}\ \underset{2p}{\uparrow}$$

The result is each carbon atom in graphene has valence bonds with only three neighboring atoms, despite there are four free electrons in a carbon atom. The three sp^2 orbitals that are hybridized make the so called σ bond. As all 3 sp^3 orbitals are identical, the angle between any 2 neighboring carbon-carbon bonds is 120 degrees on a same plane. The fourth electron forms the so called π bond, which is perpendicular to the σ bond plane. The π bond is the one which help several layers of graphene to adhere and finally forming graphite. Note that the π bond is weak compared with σ bond, which means different layers of graphene can easily 'glide' within their own plane. This is the key to the lubricant characteristics of graphite.

The chiral vector $\vec{c}$ in Figure 2.4 defines the direction along which the graphene is 'rolled up', so the vector perpendicular to $\vec{c}$ is the tube axis. The chiral vector can be expressed by the lattice basis vectors (real space unit vectors) $\vec{a_1}$ and $\vec{a_2}$ of the hexagonal lattice defined as [99]:

$$\vec{c} = n\vec{a_1} + m\vec{a_2} \equiv (n, m) \qquad (2.1)$$

where m and n are integers. With different (n, m), a carbon nanotube can have different characters. The property of a SWCNT largely depends on the orientation of the six-membered carbon ring in the honeycomb lattice relative to the axis of the nanotube, i.e. chirality. If the tube axis (perpendicular to the chiral vector) is along the horizontal direction in figure 3, the CNT is called zigzag CNT, for which the chiral vector is (m, 0). If the tube axis is along the vertical direction, the CNT is called armchair, for which the chiral vector is (m, m). CNTs other than zigzag and armchair are called chiral CNTs, for which the chiral vector is (m, n), and $0 < n \neq m$. Figure 2.5 shows an example of 3 CNTs with different chiral vectors.

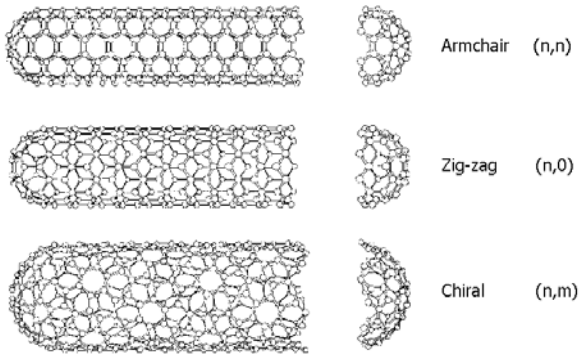

(a)

Figure 2.5: Three CNTs with different Chirality, from top to bottom: armchair, zigzag and chiral [100].

The cross sectional radius r for a CNT is given by [14], [99]:

$$r_c = \frac{a_0}{2\pi}\sqrt{m^2 + mn + n^2} \qquad (2.2)$$

where $a_0 = \left|\vec{a_1}\right| = \left|\vec{a_2}\right| = \sqrt{3}b_0$ is the length of lattice basis vectors, $b_0 = 0.142nm$ is the interatomic distance.

2.5 Electrical Properties

In the previous section, from the orbital hybridization theory we have seen that in a graphene sheet, three of the four electrons in the valence band of a carbon atom form three hybridized σ bond after hybridization. These are tight bonds with the neighboring atoms in the plane and do not play a part in the conduction phenomenon. The fourth electron, the π electron which is perpendicular to the graphene sheet plane is left unconnected and may move freely between the positive ions of the lattice. As a result, this π orbital is responsible for the electronic properties of a CNT because that forms a delocalized π network across the nanotube.

2.5.1 Band structure of graphene

The tight-binding model is an approach to the calculation of electronic band structure using an approximate set of wave functions based upon superposition of wave functions for isolated atoms located at each atomic site. In the tight-binding representation, the interaction between orbitals on different atoms only exists between two nearest neighbors. If we go back to figure 2.4, there are two carbon atoms in the graphene unit cell, which means for each unit cell, the tight-binding model can be applied.

Let's call the two atoms in a unit cell atom A and atom B with position r_s and an unsaturated p orbital described by the wave function $X_{r_s}(r)$. The tight-binding model can be described mathematically as [99]

$$\left\langle \chi_{r_A} \middle| H \middle| \chi_{r_A} \right\rangle = \left\langle \chi_{r_B} \middle| H \middle| \chi_{r_B} \right\rangle = 0 \tag{2.3}$$

$$\left\langle \chi_{r_A} \middle| H \middle| \chi_{r_B} \right\rangle = \left\langle \chi_{r_B} \middle| H \middle| \chi_{r_A} \right\rangle = \gamma \delta_{\vec{a}} \tag{2.4}$$

where $\vec{a}$ is a vector connecting nearest neighbors between A and B sub lattices.

The Bloch wave function for each of the sub lattices can be written as [102]

$$\varphi_{sk}(r) = \sum_{r_s} e^{ik \cdot r_s} \cdot \chi_{r_s}(r) \tag{2.5}$$

where s=A or B refers to each sub lattice and r_s refers to the set of points belonging to sub lattices s. The total wave function is a linear combination of these two functions [99]

$$\psi_k(r) = \frac{1}{\sqrt{2}} \left[\varphi_{Ak}(r) + \lambda_k \cdot \varphi_{Bk}(r) \right] \tag{2.6}$$

The Hamiltonian matrix elements are [99]

$$\begin{aligned}\langle \varphi_{Ak}|H|\varphi_{Ak}\rangle &= \langle \varphi_{Bk}|H|\varphi_{Bk}\rangle = 0 \\ \langle \varphi_{Ak}|H|\varphi_{Bk}\rangle &= \langle \varphi_{Bk}|H|\varphi_{Ak}\rangle^{*} = H_{AB} = \gamma \cdot \sum_{a} e^{ik\cdot a}\end{aligned} \tag{2.7}$$

which leads to the Schrodinger equation in matrix form [99]:

$$\begin{pmatrix} E & -H_{AB} \\ -H_{AB}^{*} & E \end{pmatrix}\begin{pmatrix} 1 \\ \lambda_k \end{pmatrix} \tag{2.8}$$

The solution to (2.8) can be acquired by diagonalization [99]

$$E = \pm|H_{AB}| = \pm\gamma\sqrt{1+4\cos\left(\frac{3}{2}k_y a\right)\cdot\cos\left(\frac{\sqrt{3}}{2}k_x a\right)+4\cdot\cos^2\left(\frac{\sqrt{3}}{2}k_x a\right)} \tag{2.9}$$

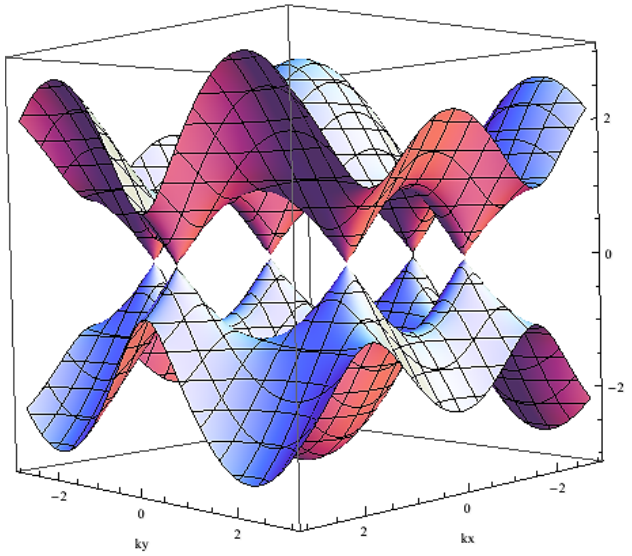

Figure 2.6: Electronic band structure of graphene, calculated within tight-binding model, figure generated by Mathematica.

The graph for the band structure of graphene as a function of k_x and k_y is plotted in Figure 2.6, from which we can see that the valence band and conductance band of graphene only touches each other in six points, as a result, graphene is described as semi-metal. These six points locates at the

corner of Brillouin zone $\left[\left(\pm\frac{4\pi}{3\sqrt{3}a},0\right);\left(\pm\frac{2\pi}{3\sqrt{3}a},\pm\frac{2\pi}{3a}\right)\right]$, and are on a same surface known as the Fermi surface, which is an abstract interface that defines the allowable energies of electrons in a solid.

2.5.2 Band structure of single-walled CNT

From the band structure of graphene we could easily get the band structure of single wall carbon nanotubes. If we quantize the wave vector in the circumferential direction, of the graphene, we can now obtain the band structure of CNTs. This gives [99]

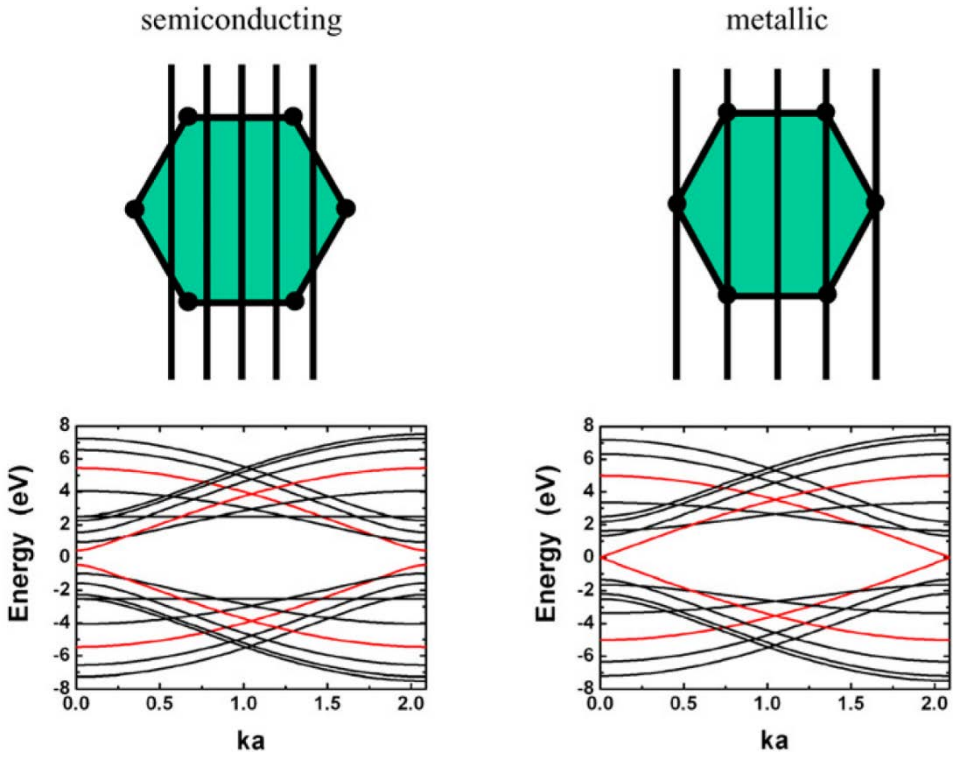

Figure 2.7: Illustration of allowed wave vector lines leading to semiconducting and metallic CNTs and examples of band structures for semiconducting and metallic CNTs [103].

$$k \cdot C = k_x C_x + k_y C_y = 2\pi \cdot p \qquad (2.10)$$

where C is the circumference and p is an integer. This equation defines lines in the (k_x, k_y) plane. Each line gives a one-dimensional energy band by slicing the two-dimensional band structure of graphene shown in Figure 2.7.

The way these lines intersect with the graphene band structure affects the electronic properties of the CNT. Figure 2.7 shows how a CNT can be characterized as semiconducting or metallic. In the left part of the figure, the lines of quantized wave vectors do not intersect with the graphene Fermi points and thus the CNT is semiconducting. In the right one, the lines pass through the Fermi points, leading to crossing bands at the CNT Fermi level and the CNT is metallic. Figure 2.8 summarizes the conditions for CNTs with different chirality to be metallic or semiconducting.

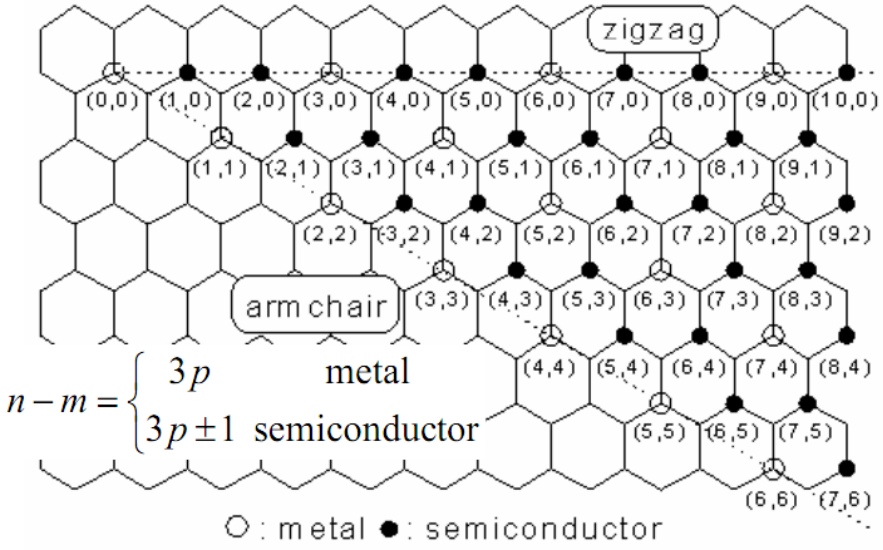

Figure 2.8 Conditions for CNTs with different chirality to be metallic or semiconducting [104].

Tight-binding model is also useful to understand the Density of States (DOS) of CNTs. The DOS can be expressed as:

$$D(E) = \frac{\sqrt{3}a^2}{2\pi R} \sum_i \int dk \cdot \delta(k - k_i) \left| \frac{\partial \varepsilon}{\partial k} \right|^{-1} \qquad (2.11)$$

where $\varepsilon(k_i) = E$. Figure 2.9 shows the DOS for a (11, 0) and (12, 0) nanotube. If we expand the dispersion relation in equation (2.9) around Fermi point, gives:

$$D(E) = \frac{a\sqrt{3}}{\pi^2 R\gamma} \sum_{m=1}^{N} \frac{|E|}{\sqrt{E^2 - \varepsilon_m^2}} \tag{2.12}$$

where $\varepsilon_m = |3m+1|\left(\frac{a \cdot \gamma}{2R}\right)$ for semiconducting tubes and $\varepsilon_m = |3m|\left(\frac{a \cdot \gamma}{2R}\right)$ for metallic tubes.

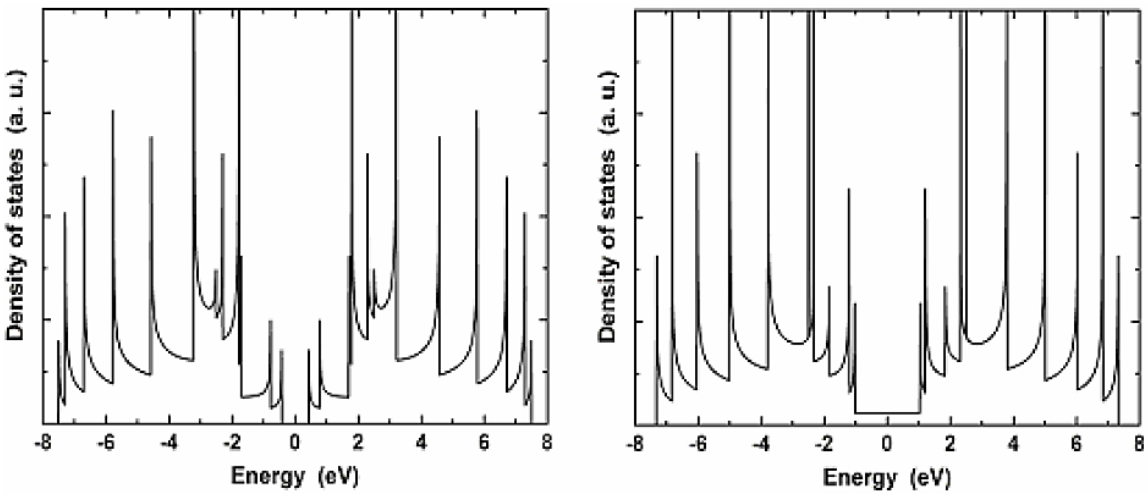

Figure 2.9: Density of states for (11, 0) and (12, 0) CNTs computed from tight binding model, showing van Hove singularities [103].

The expression above shows van Hove singularities when $E = \pm\varepsilon_m$. The existence of these singularities in the DOS makes the DOS of CNTs very unusual and unique and has been verified by scanning-tunneling microscopy of individual nanotubes [104].

Finally, it is important to note, that there are some deviations in the electronic properties of CNTs from the simple π - orbital graphene described so far, due to the curvature. As a result of this curvature, the hybridization between $\sigma - \pi$ orbitals becomes important and thus affects the electronic properties of CNTs. This hybridization in the graphene was negligible. The curvature becomes larger as the diameter of CNT decreases, so large diameter nanotubes are not affected by

the phenomenon above, whereas small diameter nanotubes are significantly affected. Cabria et al. [105] found that small diameter zigzag nanotubes, such as (4, 0) and (5, 0) are semi-metallic instead of semiconducting, which has been predicted by the tight-binding theory. For example, a semiconducting nanotube with a diameter of 1nm has a band gap of 1eV, a semi-metallic nanotube with similar diameter has a band gap of 40 meV. In [106, 107], it is shown that the band gap for semi-metallic CNTs also decreases inversely with an increase in diameter so the large diameter zigzag CNTs become metallic.

2.6 Conductivity of Graphene and Carbon Nanotubes

The conductivity is fundamental in determining the applications of graphene and CNT and thus one of the center of study of these two materials. Due to their similarity in atomic structure and sp^2 hybridized carbon-carbon bond, the conductivity of the two can be analyzed with the same model, only with different boundary conditions.

2.6.1 Conductivity of graphene sheet

The conductivity of a bulk graphene is defined as finite frequency ω as the tensorial ratio between the applied electric field and the resulting electronic current: $\mathbf{J}(\omega) = \boldsymbol{\sigma}(\omega)\mathbf{E}(\omega)$. The Kubo approach is a technique to calculate linear response in materials. It is based on the fluctuation–dissipation theorem that establishes a correspondence between the dissipative out-of-equilibrium response and the fluctuations at the equilibrium [108].

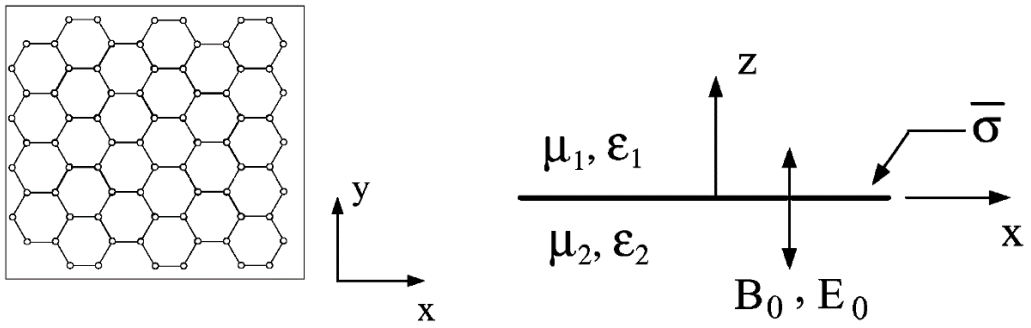

(a) (b)

Figure 2.10 (a) Depiction of graphene (top view) and (b) an anisotropic graphene sheet

characterized by tensor conductivity under bias field. Assume the host medium at two sides of the graphene are the same [109].

An infinitesimally large graphene sheet depicted by Figure 2.10 is located at z=0. It has a tensor conductivity [109]

$$\underline{\underline{\sigma}} = \begin{pmatrix} \sigma_{xx} & \sigma_{xy} \\ \sigma_{yx} & \sigma_{yy} \end{pmatrix} \tag{2.13}$$

From Kubo formalism, 2.13 can be simplified as [109]

$$\begin{aligned} \sigma_{xx} &= \sigma_{yy} = \sigma_d \\ \sigma_{xy} &= -\sigma_{yx} = \sigma_o \end{aligned} \tag{2.14}$$

with

$$\begin{aligned} &\sigma_d\left(E_{bias}, B_{bias}\right) = \frac{e^2 v_F^2 \left|eB_{bias}\right|\left(\omega - j2\Gamma\right)\hbar}{-j\pi} \times \\ &\sum_{n=0}^{\infty}\left\{\frac{f_d\left(M_n\right) - f_d\left(M_{n+1}\right) + f_d\left(-M_{n+1}\right) - f_d\left(-M_n\right)}{\left(M_{n+1} - M_n\right)^2 - \left(\omega - j2\Gamma\right)^2\hbar^2} \times \left(1 - \frac{\Delta^2}{M_n M_{n+1}}\right)\frac{1}{M_{n+1} - M_n}\right. \\ &\left. + \frac{f_d\left(-M_n\right) - f_d\left(M_{n+1}\right) + f_d\left(-M_{n+1}\right) - f_d\left(M_n\right)}{\left(M_{n+1} + M_n\right)^2 - \left(\omega - j2\Gamma\right)^2\hbar^2} \times \left(1 - \frac{\Delta^2}{M_n M_{n+1}}\right)\frac{1}{M_{n+1} + M_n}\right\} \end{aligned} \tag{2.15}$$

and

$$\begin{aligned} &\sigma_o\left(E_{bias}, B_{bias}\right) = -\frac{e^2 v_F^2 eB_{bias}}{-j\pi}\sum_{n=0}^{\infty}\left\{f_d\left(M_n\right) - f_d\left(M_{n+1}\right) + f_d\left(-M_{n+1}\right) - f_d\left(-M_n\right)\right\} \\ &\times\left\{\left(1 - \frac{\Delta^2}{M_n M_{n+1}}\right)\frac{1}{\left(M_{n+1} - M_n\right)^2 - \left(\omega - j2\Gamma\right)^2\hbar^2}\right. \\ &\left. + \left(1 + \frac{\Delta^2}{M_n M_{n+1}}\right)\frac{1}{\left(M_{n+1} + M_n\right)^2 - \left(\omega - j2\Gamma\right)^2\hbar^2}\right\} \end{aligned} \tag{2.16}$$

where

$$M_n = \sqrt{\Delta^2 + 2nv_F^2 \left| eB_{bias} \right| \hbar} \tag{2.17}$$

and where –e is the electron charge, Γ is the electron scattering rate [109], $\hbar = h/2\pi$ is the reduced Planck's constant, $f_d(\varepsilon) = \left(e^{(\varepsilon-\mu_c)/k_BT} + 1\right)^{-1}$ is the Fermi-Dirac distribution, $v_F \approx 10^6$ m/s is the electron's energy-independent Fermi velocity, and Δ is an excitonic energy gap [109]. E_{bias} and B_{bias} are bias electric and magnetic fields that are applied perpendicularly on the graphene sheet. μ_c is the chemical potential, which can be related with E_{bias} by [109]

$$\frac{\varepsilon_r \pi \hbar^2 v_F^2}{q_e} E_{bias} = \int_0^\infty \varepsilon \left[f_d(\varepsilon) - f_d(\varepsilon + 2\mu_c) \right] d\varepsilon \tag{2.18}$$

where ε_r is the permittivity of the host medium. Obviously, 2.16 must be solved numerically, and the relationship between a bias E field and chemical potential is shown in Figure 2.11.

It is worth noting that both 2.14 and 2.15 are consists of two parts, which shows the combined effect of intraband conductivity σ_{intra} and interband conductivity σ_{inter}, respectively. The former is the electron transport within the conduction bands and the latter is the electron transport from valence bands to conduction bands. From (2.16), if $E_{bias} = 0$ or $B_{bias} = 0$, it also results $\sigma_o = 0$ and the graphene is characterized by an isotropic conductivity $\sigma = \sigma_d$.

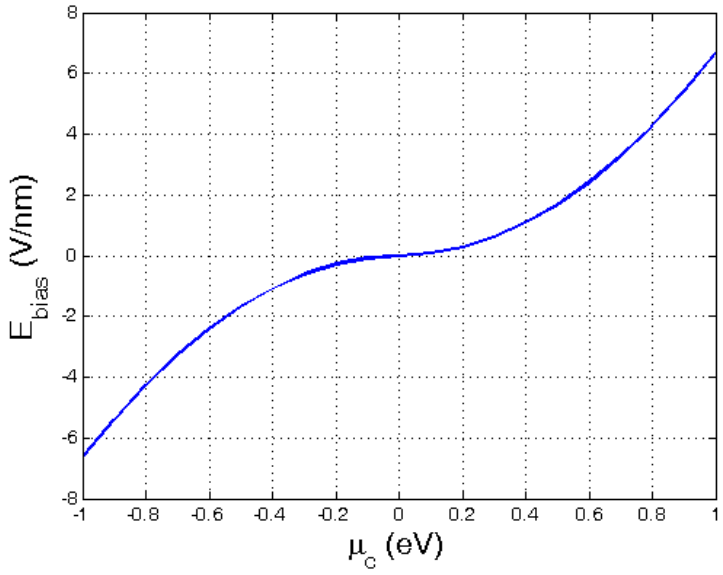

Figure 2.11 Relationship between the chemical potential μ_c and the bias electric field E_{bias}

The energy gap Δ is opened due to the electron interactions under a magnetic field [110], [111]. However, it is diminished at higher temperature (such as room temperature) due to the increased carrier density [110]. Therefore, the conductivity of graphene under room temperature can be approximated by setting $\Delta = 0$. Therefore, under low magnetic bias field conditions, 2.14 and 2.15 can be simplified as [109]

$$\sigma_d = \frac{je^2(\omega - j2\Gamma)}{\pi\hbar}\cdot\left[\frac{1}{(\omega - j2\Gamma)^2}\int_0^\infty \varepsilon\left(\frac{\partial f_d(\varepsilon)}{\partial\varepsilon} - \frac{\partial f_d(-\varepsilon)}{\partial\varepsilon}\right)d\varepsilon - \int_0^\infty \frac{f_d(-\varepsilon) - f_d(\varepsilon)}{(\omega - j2\Gamma)^2 - 4(\varepsilon/\hbar)^2}d\varepsilon\right] \tag{2.19}$$

and

$$\sigma_0 = -\frac{e^2 v_F^2 eB_{bias}}{-j\pi}\cdot\left[\frac{1}{(\omega - j2\Gamma)^2}\int_0^\infty \varepsilon\left(\frac{\partial f_d(\varepsilon)}{\partial\varepsilon} + \frac{\partial f_d(-\varepsilon)}{\partial\varepsilon}\right)d\varepsilon + \int_0^\infty \frac{1}{(\omega - j2\Gamma)^2 - 4(\varepsilon/\hbar)^2}d\varepsilon\right] \tag{2.20}$$

In the absence of electric and magnetic bias, i.e. isotropic case, the frequency dependent intraband

conductivity σ_d of a graphene sheet is shown in Figure 2.12.

The conductivity curve clearly follows the Drude model, which is proposed to explain the transport properties of electron in materials (especially metals). According to the Drude model, the frequency dependent conductivity σ_d can be written as

$$\sigma(\omega) = \frac{\sigma_0}{1 + j\omega\tau} = \frac{\sigma_0}{1 + \omega^2\tau^2} - j\omega\tau\frac{\sigma_0}{1 + \omega^2\tau^2} \tag{2.21}$$

where σ_0 is the DC conductivity, τ is the relaxation time [112]. At frequencies lower than 200GHz, the real part of the conductivity plays a main part in the total conductivity of graphene sheet and at frequencies above 200GHz the imaginary part of the impedance is dominant, until both becomes negligible at optical frequencies.

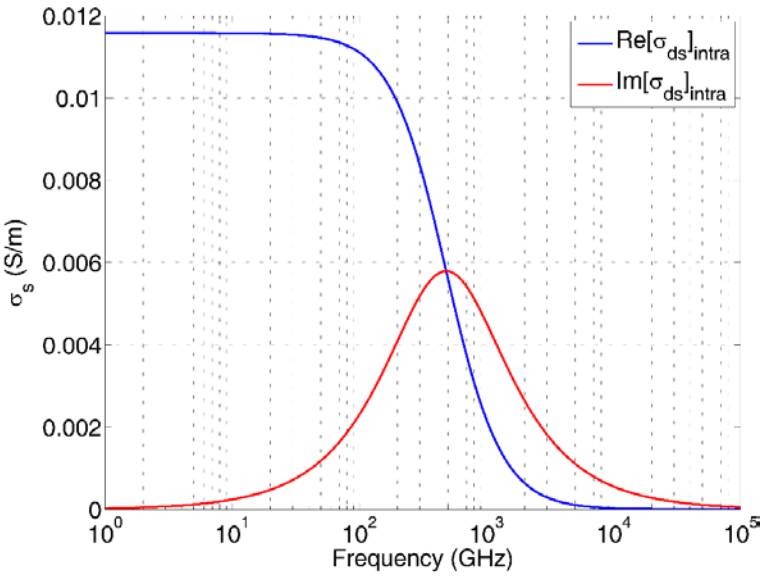

Figure 2.12 Frequency dependent complex intraband conductivity of the graphene sheet.

Alternatively, the Drude model can be applied to Maxwell equations and the permittivity and be related to the permittivity as [195]

$$\varepsilon(\omega) = 1 - \frac{j\sigma}{\omega\varepsilon_0} = 1 - \frac{j}{\omega\varepsilon_0}\left(\frac{\sigma_0}{1 + j\omega\tau}\right) \approx 1 - \frac{\omega_p^2}{\omega^2} \tag{2.22}$$

where ω_p is called the plasma frequency.

It is worth noting that the relaxation time τ of graphene (also CNT) is in the order of 10^{-13} [196] [159], while for normal metals such as copper and silver, τ is in the order of $10^{-14} \sim 10^{-15}$ [197]. As a result, the plasma frequencies in graphene and CNT are in THz range, much lower than that in metals, which almost reaches ultra-violet frequency. So graphene and CNT demonstrate metal-like characteristics, such as plasma excitation and propagation at a much lower frequency compared to metals. This difference in plasma frequency also accounts for the fact that graphene are optically transparent, as the frequency of visible light are much higher than plasma frequency of graphene [198].

Figure 2.13 shows the graphene conductivity under an electric bias and a magnetic bias. As it can be seen, the isotropic conductivity is an even function of E_{bias} and B_{bias}.

It can clearly be seen that the applied electrostatic bias increases the conductivity, while magneto-static bias dramatically decreases the conductivity (because of the Hall effect) and makes transparent the graphene sheet.

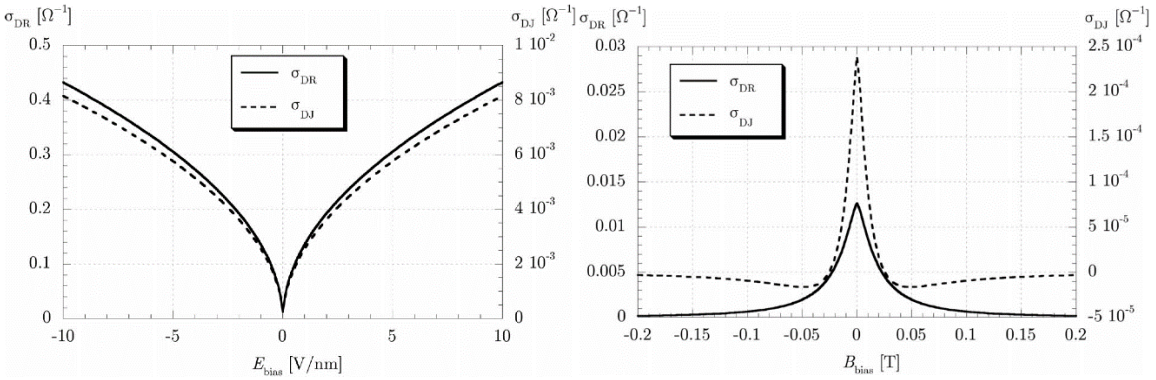

(a) (b)

Figure 2.13 Graphene conductivity under (a) electric bias and (b) magnetic bias. σ_{DR} is the real part and σ_{DJ} is the imaginary part. The minimum conductivity in (a) when $E_{bias} = 0$ is $\sigma_0 = \pi e^2 / 2h = 6.085 \times 10^{-5} (\mathrm{S})$ [113]

2.6.2 Conductivity of graphene nanoribbons (GNRs)

The GNR is a thin nanowire structure comprised of graphene. Usually only several nanometers in width but several micrometers in length, they have a very high aspect ratio and thus are promising in the application of interconnects. The conductivity of GNR is different from the graphene sheet because of the existence of edge scattering [114]. Also the different chirality determines the band structure of GNR, hence must be considered in the calculation of conductivity.

Like CNTs, GNRs can also be calorized into armchair and zigzag. Contrary to CNTs, the zigzag GNRs are always metallic and armchair GNRs have a 1/3 possibility on average to be metallic and a 2/3 possibility to be semi-conducting.

The conductivity of GNRs can be modeled using the tight binding model, in which all particles are assumed to interact with their nearest neighbors.

Under simple tight binding formalism, i.e. the effect of edge scattering and alignment of carbon atoms are neglected, the graphene band structure can be written as [114]:

$$\begin{aligned} E_n &= \left(h v_F / 2W\right)\left|n+\beta\right| && \text{armchair GNR} \\ E_n &= \begin{cases} \left(h v_F / 2W\right)\left(1/2+\left|n\right|\right) & \text{n} \neq 0 \\ 0 & \text{n=0} \end{cases} && \text{zigzag GNR} \end{aligned} \qquad (2.23)$$

where n is an integer, $\beta = 0$ for metallic armchair GNR and $\beta = 1/3$ for semi-conducting armchair GNR.

With the band structure in (2.23), the conductance of the GNR can be calculated by adding the contribution of each subband according to their electron or hole populations as follows [114]

$$G = G_0\left(\sum_{n=-\infty}^{\infty}\frac{1}{e^{\left[(E_n-E_F)/k_BT\right]}+1}+\sum_{n=-\infty}^{\infty}1-\frac{1}{e^{\left[(-E_n-E_F)/k_BT\right]}+1}\right) \qquad (2.24)$$

where $G_0 = 2e^2/h \approx 1/12.9\text{k}\Omega$ is the quantum conductance, E_F is the Fermi energy and the first and second sums represent the contributions of the conduction and valence band. It is worth noting that (2.24) is derived under the simple tight binding models using zone folding approximations,

and the scattering effect of rough edges are also neglected. This approximation is known to be accurate for wide GNRs, but for narrow GNRs, it may not be accurate. However, it has been proven that when the GNR is wider than a few nanometers, the modified tight binding model that takes into account the rough edges does not differ greatly from the simple one.

Figure 2.14 shows the conductance of both armchair and zigzag graphene, normalized to G_0. As G_0 is the quantum conductance of a single conductive channel, this normalized conductance is the number of conductive channels. As shown, the armchair GNR can be either semi-conducting or metallic with a constant number of conductive channels, i.e. 1. This is different from that of CNTs, when the number of conductive channels for small-diameter CNTs are 2. When the width is small and for large width, the semi-conducting armchair GNRs also become metallic and the zigzag GNRs are always metallic.

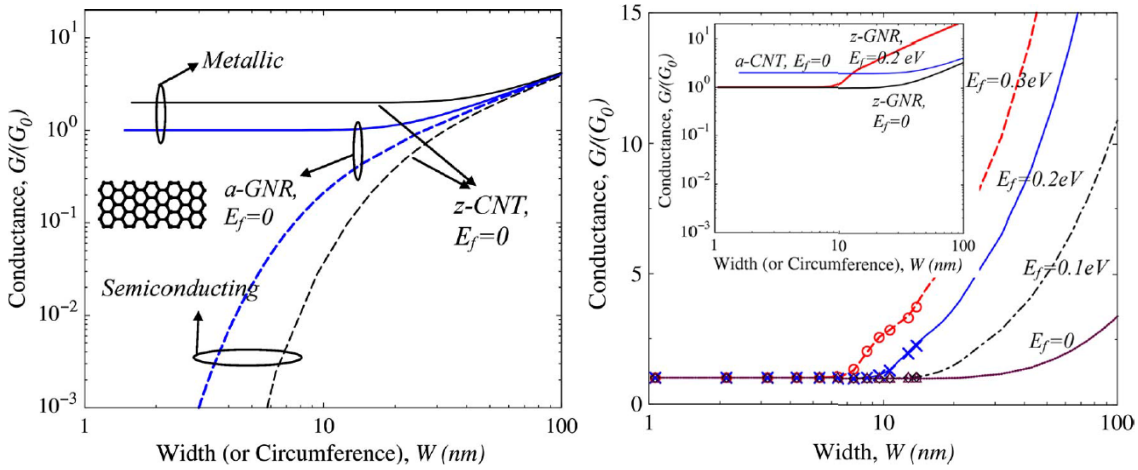

(a) (b)

Figure 2.14 The conductance versus GNR width for (a) armchair GNR and (b) zigzag GNR [114].

Figure 2.14 (a) and the inset of Figure 14(b) shows a comparison of the GNR conductance compared with a CNT with same circumference. It can be seen that in the small width or circumference case, metallic CNTs have double the conductivity than GNRs, while in the case of large width, the conductivity of the two materials are similar.

2.6.3 Conductivity of carbon nanotubes

The conductivity of carbon nanotubes can be derived in the same fashion of the GNR. The equation of (2.24) is still valid for CNTs, only the form of the CNT's band structure E_n needs to be modified.

For a zigzag CNT with chirality (m, 0), E_n can be written as [115]

$$E_n = \pm \frac{3ta_0}{D} \left| n - \frac{2m}{3} \right| \tag{2.25}$$

where a_0 is the length of CNT bonds, t is the Hamiltonian matrix element between neighboring carbon atoms, D is the shell diameter and n is an integer less than m. Although (2.25) is derived for an isolated zigzag CNT, it is also valid for shells of random chirality within a MWCNT or CNT bundles [116], [117].

Substituting (2.25) into (2.24) gives the total number of conductive channel in CNT, as shown in Figure 2.15.

It appears that the number of conductive channels for CNT is a constant number in the case of small CNT diameter, and increases linearly in the case of large CNT diameter. By comparing Figure 2.15 with Figure 2.14, it can be seen that when the number of conductive channels is within the constant region, a CNT has two conductive channels while a GNR has only one. Therefore, in the case of small width or diameter, CNTs have a better conductivity than the corresponding GNRs. Meanwhile, the fact that edge roughness is present in GNRs but absent in CNTs further increases the difference in their conductivities.

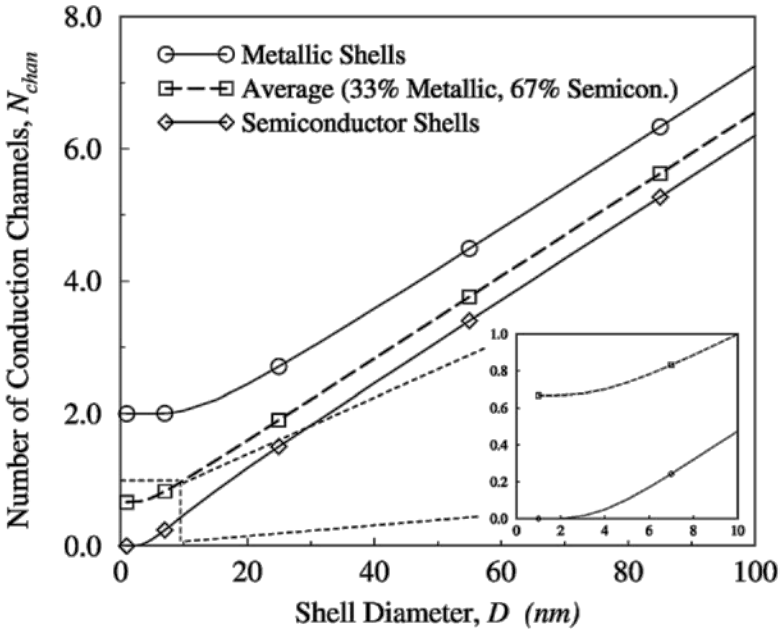

Figure 2.15 Number of conduction channels per graphene shell versus shell diameter for metallic and semiconductor shells. The inset shows the magnified plot for small shell diameters [115].

2.6.4 Comparison of conductivity of CNT, graphene and other metals.

The DC conductivity of metals are usually dependent on temperature. The exact relationship between the two is complex and for a narrow temperature range, a linear approximation is usually used [199]

$$\sigma(T) = \sigma_0 / \left[1 + \alpha\left(T - T_0\right)\right] \tag{2.26}$$

where α is the temperature coefficient, σ_0 is the resistivity at temperature T_0, which is the reference temperature. In practice, T_0 is normally the room temperature.

The graphene and CNT's conductivity is reported to have a better conductivity than copper. Table 2.1 shows the resistivity of graphene, silver and copper at room temperature and their temperature coefficient.

Table 2.1 Conductivity and temperature coefficient of graphene, copper and silver

Material	**DC conductivity σ_0 (S/m)**	**Temperature coefficient α**
Graphene	1.00×10^8	-0.0002 [218]
Carbon nanotube	$10^6 \sim 10^7$	-0.000387 [219]
Silver	6.30×10^7	0.0038 [220]
Copper	5.96×10^7	0.003862 [221]

This shows that first of all, graphene's conductivity is the highest compared to that of silver and copper, while CNT's conductivity is one order smaller, merely comparable to that of copper. Secondly, the negative temperature coefficient shows that the conductivity of graphene and CNT will increase instead of decrease, compared to silver and copper. This means that the resistivity and the heat produced from it will both decrease, which is particularly useful in the application of interconnects and vias that normally operates at a temperature much higher than the room temperature (80~100℃). In these applications, a self-regulating cooling functions are desirable as it can aid in the reliability of their operation.

With the level of integration in VLSI increasing, the dimensions of interconnects are decreasing. However, in recent years, simple scaling of copper wires will encounter problems that degrade the performance. The resistivity of copper wires starts to increase with scaling due to the extra scatterings electrons experience at the wire surfaces once the cross-sectional dimensions become comparable or smaller than the mean-free-path (MFP), which is the mean distance electrons travel between collisions. The comparison of the resistivity of CNT, GNR and copper wires are shown in Fig. 2.16.

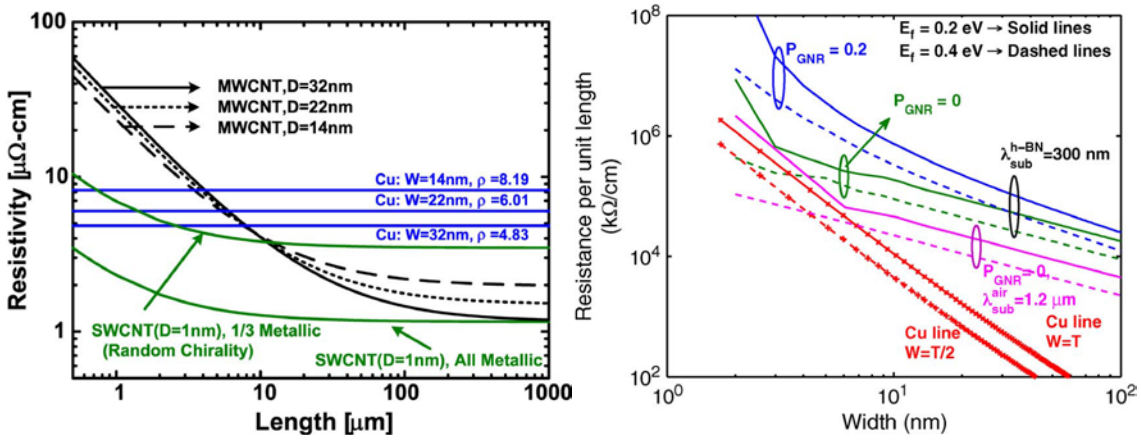

(a) (b)

Figure 2.16 (a) Resistivity of MWCNT with various diameters and bundles of SWCNTs compared to copper wires [133] and (b) per-unit-length resistance of GNR compared to copper wires. W and T are the width and thickness of the Cu wire, respectively [200].

In Figure 2.16(a), one can see that the resistivity of MWCNT and SWCNT bundles are lower than that of copper wires only when the wire reaches certain length. Furthermore, with the scaling of wire cross section, copper wires' effective resistivity will increase even more, due to the extra scattering. In Figure 2.16(b), the per-unit-length resistance of graphene are shown to be smaller than copper wires for small wire dimensions only.

The AC conductivity, as discussed in Figure 2.12, follows the Drude model. However, with the increasing of frequency, the electric current will be distributed within a thin layer close to the surface of the conductor, known as the skin effect. With skin effect, the AC conductivity of metals will be lower than the DC conductivity, as the current is more confined, reducing the effective cross section of the conductor. For example, at 10GHz, the skin depth of copper and silver are only 0.65 μm and 0.64μm, respectively. But for CNT and graphene, the skin depth are always higher than the thickness of one carbon atom, thus the skin effect has no effect on the AC conductivity of them.

2.7 Summary

In this chapter the fundamental physical and electrical properties of both graphene and CNTs are investigated and reviewed. Due to the special band structure of graphene, the graphene is considered as a semi-metal and the carbon nanotube can be either metallic or semi-conducting. The conductivity of the GNT, the 2-D graphene and the carbon nanotube has been discussed and compared based on the tight-binding model and first principal analysis. It has been shown that, the DC conductivity of semi-conducting and metallic GNRs converge when the ribbon width becomes wide, and essentially, it will reach the same value of a graphene sheet. The AC conductivity of the graphene sheet follows the Drude model, and because of graphene's special band structure, the conductivity can also be tuned with a static electric or magnetic bias field. Such properties can be very useful in applications such as tunable absorbers and filters. For carbon nanotube, the conductivity in the case of small radius is 2 times of that of the GNR, and the edge roughness in the GNR made it even less conductive than CNTs with the same circumference.

The conductivity of CNT and GNR are compared with other metals such as copper and silver. The conductivity of CNT and GNR outperform metals in the large length and small width scenario. The negative temperature coefficient provides self-regulating heat control, which is also not found in metals. Furthermore, due to their extremely small thickness of only one-atom, they are not affected by skin effects. All these features makes CNT and GNR promising materials in future VLSI applications.

Chapter 3 Modelling Techniques of Vertically Aligned CNT arrays

3.1 Introduction

The problem of interconnects are considered one of the greatest challenges in VLSI because of the added delay on critical paths, the power dissipation, the noise and jitter induced on one another, and the vulnerability to electron migration. As the integration enters nanoscale, additional factors exacerbate the problems associated with interconnects have to be faced with. For example, the problem of increased resistivity as the interconnect dimensions approach the mean free path of electrons in bulk copper, which is 40nm at room temperature. Under this background, the quantum wires have been proposed as a replacement option since extraordinarily large MFPs have been observed in them already [118]. CNTs are the best example of quantum wires for which electron MFPs on the micrometre scale have been reported, compared to that of 40nm in copper [118].

To accurately model the electrical properties of both SWCNT and MWCNT numerically has been proven difficult. Given their nano-scale dimensions, one has to consider not only the Maxwell equations, but also the Schrödinger equations, which describes the quantum state of electrons. However, given the very high aspect ratio of CNTs, the electron transportation is mainly restricted in the axial direction. Therefore, a CNT can be effectively approximated as a one-dimensional system of interaction electrons.

To understand the interaction of electrons (or other fermions), the most successful theory by far is Landau's theory of Fermi liquids, which pointed out that the low-lying excitations of a Fermi liquid are not electrons, but in fact quasi-particles which, like Fermi gas, are non-interacting [118].

However, Landau's Fermi liquid theory breaks down in one-dimensional systems [119], such as nanowires and carbon nanotubes [121]. To deal with this problem, Tomonaga [122] and Luttinger [123] described a simplified model for interacting electrons in one dimension, which later became known as the Tomonaga-Luttinger liquid model, or simply the Luttinger liquid model.

The Luttinger liquid model and the Fermi liquid model have several differences. One is that spin density waves, together with particle waves, are the elementary excitations of the Luttinger liquid. Another difference is the particles' momentum distribution function does not 'jump', in contrast to the Fermi liquid where this jump indicates the Fermi surface. Thirdly, there is no quasi-particle peak in the momentum-dependent spectral function in the Luttinger liquid. The Luttinger liquid model is thought to describe the universal low-frequency/long-wavelength behaviour of any one-dimensional system of interacting fermions, its applications include artificial quantum wires, electrons in carbon nanotubes, and fermion atoms in quasi-1D atomic traps, etc. In 2002, P. J. Burke applied Luttinger liquid theory to model a single wall SWCNT [124]. Since then, the transmission line model has been widely used in the modelling of CNTs. In rom one dimensional electron fluid model, a similar TL model was derived [125]. To reduce the high DC resistance of an isolated CNT, bundles of parallel CNTs have also been studied and an effective single conductor (ESC) TL model of both a stand-alone multi-wall CNT (MWCNT) and a single-wall CNT (SWCNT) array was derived in [126] and [127]. Finally, a diameter dependent circuit model was proposed in [128].

In the aforementioned ESC models however the magnetic inductance between CNTs are usually neglected, resulting in a simplification of the mutual coupling in the array. There have been studies that suggests when the CNT bundle becomes large, such simplification may not be valid and drew the conclusion that inductances should not be neglected [129].

In this chapter, the transfer (ABCD) matrix of the CNT array are calculated by the full MTL approach and a novel technique is proposed to analytically solve the 2-port input impedance, S-parameters and absorption with all the mutual coupling taken into calculation.

3.2 Transmission line theory

The transmission line model was first developed by Oliver Heaviside in the 1880s. In the model, the telegrapher's equations, which are a pair of coupled, linear differential equations to describe the voltage and current on an electrical transmission line with distance and time, were proposed. Later, the original transmission line theory was expanded to the multi-conductor case and the matrix-formed telegrapher's equations were proposed.

3.2.1 Single-conductor transmission line (STL)

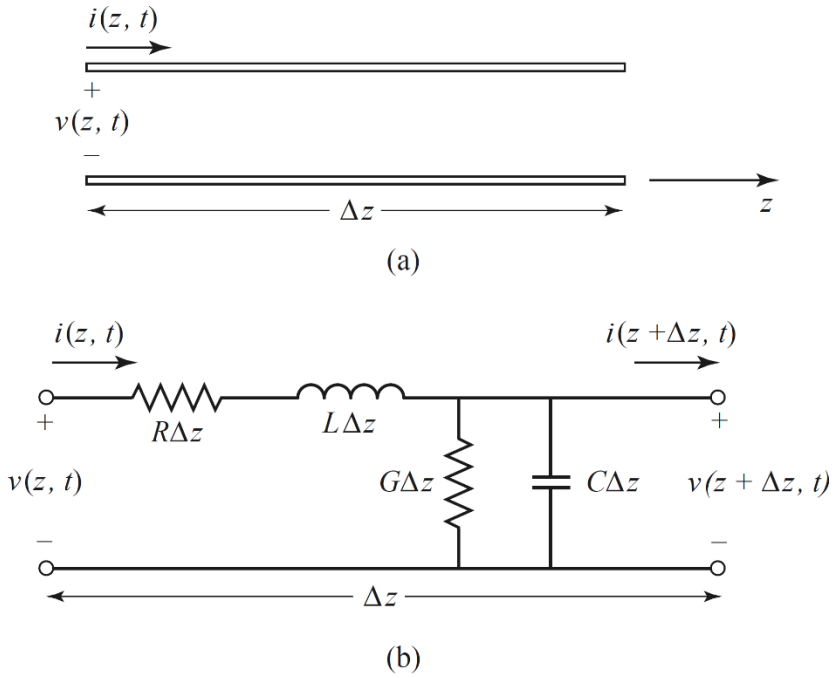

Figure 3.1 A unit cell in (a) an infinitely long transmission line and (b) its effective circuit model [130].

The general depiction of a homogeneous single-conductor transmission line (STL) is shown in Figure 3.1(a). The STL is comprised of two lines, one carries the current and the other that serves as the reference conductor, i.e. ground. The effective circuit model of such a STL is shown in Figure 3.1(b), in which R represents the per-unit-length series resistance, L represents the per-unit-

length series inductance, C represents the per-unit-length parallel capacitance and G represents the per-unit-length parallel conductance.

By applying Kirchhoff's voltage and current law in Figure 3.1(b), one have [130]

$$\begin{cases} v(z,t) - R\Delta z i(z,t) - L\Delta z \dfrac{\partial i(z,t)}{\partial t} - v(z+\Delta z,t) = 0 \\ i(z,t) - G\Delta z v(z+\Delta z,t) - C\Delta z \dfrac{\partial i(z+\Delta z,t)}{\partial t} - i(z+\Delta z,t) = 0 \end{cases} \tag{3.1}$$

Dividing (3.1) by Δz and taking the limit as $\Delta z \to 0$ gives the set of differential equations:

$$\begin{cases} \dfrac{\partial v(z,t)}{\partial z} = -Ri(z,t) - L\dfrac{\partial i(z,t)}{\partial t} \\ \dfrac{\partial i(z,t)}{\partial z} = -Gv(z,t) - C\dfrac{\partial v(z,t)}{\partial t} \end{cases} \tag{3.2}$$

These equations are the time-domain form of the transmission line, or telegrapher equations.

For the sinusoidal steady-state condition, with cosine-based phasors, (3.2) simplify to

$$\begin{cases} \dfrac{dV(z)}{dz} = -(R + j\omega L) I(z) \\ \dfrac{dI(z)}{dz} = -(G + j\omega C) V(z) \end{cases} \tag{3.3}$$

Equation 3.3 can be solved simultaneously to give wave equations for V(z) and I(z):

$$\begin{cases} \dfrac{d^2V(z)}{dz^2} - \gamma^2 V(z) = 0 \\ \dfrac{d^2I(z)}{dz^2} - \gamma^2 I(z) = 0 \end{cases} \tag{3.4}$$

where $$\gamma = \alpha + j\beta = \sqrt{(R + j\omega L)(G + j\omega C)} \tag{3.5}$$

is the complex propagation constant, which is a function of frequency. Traveling wave solutions to 3.4 can be found as

$$\begin{cases} V(z) = V_0^+ e^{-\gamma z} + V_0^- e^{\gamma z} \\ I(z) = I_0^+ e^{-\gamma z} + I_0^- e^{\gamma z} \end{cases} \tag{3.6}$$

where $\gamma = \alpha + j\beta = \sqrt{(R + j\omega L)(G + j\omega C)}$ is the complex propagation constant, which is a function of frequency. Traveling wave solution of (3.6) can be found as

$$\begin{aligned} V(z) &= V_0^+ e^{-\gamma z} + V_0^- e^{\gamma z} \\ I(z) &= I_0^+ e^{-\gamma z} + I_0^- e^{\gamma z} \end{aligned} \tag{3.7}$$

where $e^{-\gamma z}$ term represents wave propagation in the +z direction and the $e^{\gamma z}$ term represents wave propagation in the –z direction. Applying (3.3) to (3.6) gives the current as

$$I(z) = \frac{\gamma}{R + j\omega L}\left[V_0^+ e^{-\gamma z} + V_0^- e^{\gamma z}\right] \tag{3.8}$$

Comparing with (3.7) a characteristic impedance, Z_0 can be defined as

$$Z_0 = \sqrt{\frac{R + j\omega L}{G + j\omega C}} \tag{3.9}$$

Converting back to the time domain, the wavelength and the phase velocity on the line can be obtained as

$$\begin{aligned} \lambda &= \frac{2\pi}{\beta} \\ v_p &= \frac{\omega}{\beta} = \lambda f \end{aligned} \tag{3.10}$$

3.2.2 Multi-conductor transmission line (MTL)

The geometric configuration of a general n+1 multi-conductor transmission line is depicted in Figure 3.2(a) and its effective circuit model is depicted in Figure 3.2(b). It consists of n conductor and a reference conductor. By expanding the TEM transmission line theory from single-conductor

to multi-conductor [131], the MTL equations can be written in a similar form with STL equations as

$$\begin{aligned}\frac{\partial}{\partial z}\mathbf{V}(z,t) &= -\mathbf{R}\mathbf{I}(z,t) - \mathbf{L}\frac{\partial}{\partial t}\mathbf{I}(z,t)\\ \frac{\partial}{\partial z}\mathbf{I}(z,t) &= -\mathbf{G}\mathbf{V}(z,t) - \mathbf{C}\frac{\partial}{\partial t}\mathbf{V}(z,t)\end{aligned} \tag{3.11}$$

where **L**, **G**, **C**, and **R** are symmetric matrixes, **V**(*z*,*t*) and **I**(*z*,*t*) are column vectors.

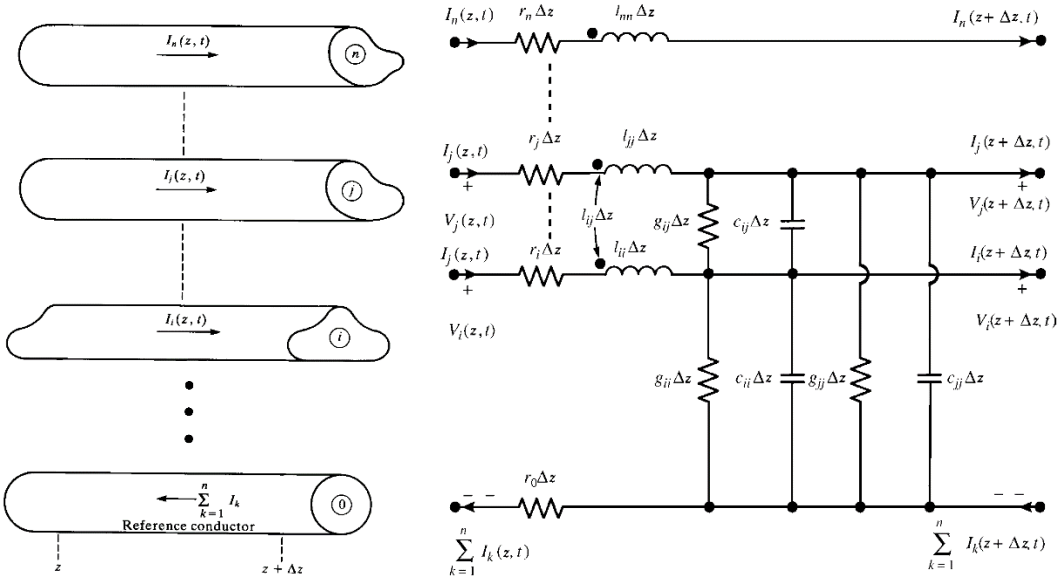

(a) (b)

Figure 3.2 (a) The geometric configuration of a general n+1 multi-conductor transmission line and (b) its effective circuit model [131].

Using the similar process as (3.4), the uncoupled, second-order ordinary differential equations can be obtained from (3.11) as [131]

$$\begin{cases}\dfrac{d^2\mathbf{V}(z)}{dz^2} - \mathbf{Z}\mathbf{Y}\cdot\mathbf{V}(z) = 0\\ \dfrac{d^2\mathbf{I}(z)}{dz^2} - \mathbf{Y}\mathbf{Z}\cdot\mathbf{I}(z) = 0\end{cases} \tag{3.12}$$

Notice that (3.12) are coupled together because **ZY** and **YZ** are full matrices. To get the frequency domain solution of (3.11), the modal analysis technique is employed, which transform the original voltage and current quantities to mode quantities, in order to decouple (3.12) by similarity transformations. The mode quantities can be written as [131]

$$\begin{aligned} \mathbf{V}(z) &= \mathbf{M}\mathbf{V}_m(z) \\ \mathbf{I}(z) &= \mathbf{N}\mathbf{I}_m(z) \end{aligned} \tag{3.13}$$

Substituting (3.13) to (3.12), we get [131]

$$\begin{cases} \dfrac{d}{dz^2}\mathbf{V}_m(z) = \mathbf{M}^{-1}\mathbf{Z}\mathbf{Y}\mathbf{M}\mathbf{V}_m(z) = \gamma^2\mathbf{V}_m(z) \\ \dfrac{d}{dz^2}\mathbf{I}_m(z) = \mathbf{N}^{-1}\mathbf{Y}\mathbf{Z}\mathbf{N}\mathbf{I}_m(z) = \gamma^2\mathbf{I}_m(z) \end{cases} \tag{3.14}$$

where γ^2 is the diagonal matrix of the eigenvalue of the matrix **ZY**. And (3.14) are decoupled because γ^2 is diagonal.

The vertically aligned CNT array can be modelled by either STL or MTL model described above, depending on the number of shells in a single CNT and the number of CNTs in the array.

3.3 The Circuit model for a SWCNT

This section presents an equivalent-circuit model for a rolled graphene cylinder that can be either a SWCNT or a shell in a MWCNT. The model, which is based on the Luttinger liquid theory, considers a SWCNT as a 1-D nanowire. An SWCNT, because of its band structure, has two propagating channels [121], and the electrons can spin up and down. Hence, an SWCNT can be considered as 4 ‘spinless’ channels connected in parallel [124].

The geometry of a spinless one-channel is shown in Figure 3.3. The CNT is placed above a ground plane, with the distance from the centre of the CNT to the ground plane *h* and the CNT diameter *d*.

3.3.1 Impedance components

The impedance of a SWCNT is comprised of 5 parts [124]: distributive resistance, kinetic inductance, quantum capacitance, magnetic inductance and electrostatic capacitance. On the contact of metal electrodes and SWCNT there will also be contact resistances.

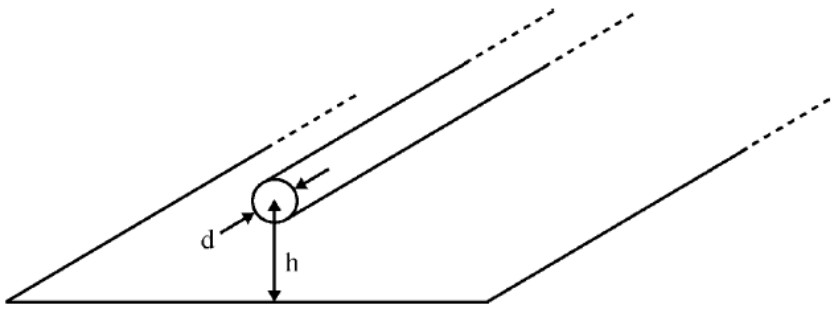

Figure 3.3 Geometry of CNT above a ground plane [124]

Like conventional transmission line, the equation describing the energy stored in the magnetic inductance can be written as [124]

$$\frac{1}{2}L_M I^2 = \frac{1}{2\mu}\int B(x)^2 d^3x \tag{3.15}$$

Using the relationship between I and B in the geometry of interest, the L_M can be solved as [124]

$$L_M = \frac{\mu}{2\pi}\cosh^{-1}\left(\frac{2h}{d}\right) \tag{3.16}$$

The equation describing energy stored in the electrostatic capacitance can be written as [124]

$$\frac{Q^2}{2C} = \frac{\varepsilon}{2}\int E(x)^2 d^3x \tag{3.17}$$

and the electrostatic capacitance can thus be solved as [124]

$$C_E = \frac{2\pi\varepsilon}{\cosh^{-1}\left(2h/d\right)} \tag{3.18}$$

The difference of a quantum wire is that apart from the magnetic inductance and electrostatic capacitance, it also has kinetic inductance and quantum capacitance.

The physical origin of the kinetic inductance is the charge-carrier inertia: electrons do not instantaneously respond to an applied electric field and there is some delay. For periodic electric fields, the electron velocity lags the electric field in phase, i.e., the current lags the voltage in phase. This can be modelled with an inductance.

In order to calculate the kinetic inductance per unit length, method in [124] is used. First we calculated the kinetic energy per unit length, which, for a 1-D wire, is described as the sum of the kinetic energy of the left moving electrons and right moving ones. If the Fermi level of the left moving electrons is raised by $e\Delta\mu/2$ and the Fermi level of the right moving ones is decreased by the same amount, the net current flowing through the wire is $I = e^2/h\Delta\mu$ [124]. The net increase in energy of the system $N = e\Delta\mu/2\delta$ is the excess number of electrons in one side against the other, multiplied by the energy added per electron, which equals $e\Delta\mu/2$. The single particle energy level spacing δ is related to the Fermi velocity $\delta = \hbar v_F 2\pi / L_{CNT}$ [124] where L_{CNT} is the CNT's length. By equating the total excess kinetic energy $\frac{hI^2}{4v_F e^2}$ to the energy of the kinetic inductance $LI^2/2$, the kinetic inductance can be expressed as

$$L_k = \frac{h}{2e^2 v_F} \tag{3.19}$$

where v_F is the Fermi velocity which is $8\cdot10^5 m/s$ [124].

The quantum capacitance comes from the finite density of states at the Fermi energy. In a quantum particle in a box, the spacing between allowed energy levels is finite. Because of this, to add an extra electron to the system takes a finite amount of energy above the Fermi energy. In 1-D systems, this can be equated with energy per unit length.

The distance between quantum states is described as $\delta E = 2\pi\hbar v_F / L$ and by equating this to an effective quantum capacitance [124], [132] with energy given by $e^2 / C_q = \delta E$, the per unit length capacitance can be expressed as [124]

$$C_q = \frac{2e^2}{hv_F} \tag{3.20}$$

Now consider the spin of electrons and band structure of a real metallic carbon nanotube described in Chapter 2. Each metallic SWCNT has two propagating channels and at the same time each electron can be spin up or spin down. Hence there are four conductive channels in a metallic CNT. For the final interactive circuit diagram for a metallic SWCNT, the effective values of the inductance and capacitance equal the value of four quantum wires in parallel [124]:

$$\begin{aligned} L_k^{'} &= L_k / 4 \\ C_q^{'} &= 4C_q \end{aligned} \tag{3.21}$$

where $L_k^{'}$ and $C_q^{'}$ are the total kinetic inductance and quantum capacitance of a metallic SWCNT, respectively. Note that for typical nanowires, $L_M / L_k \sim 10^{-4}$ and $C_{ES} / C_q \sim 1$, thus the magnetic inductance can be neglected while the electrostatic capacitance cannot. So the wave velocity on the nanowire can be calculated as

$$v_p = \sqrt{\frac{1}{L_{total} C_{total}}} \approx \sqrt{\frac{1}{L_k^{'} C_q^{'}}} = v_F \tag{3.22}$$

Note that the wave velocity in (3.22) and in all following chapters of this thesis are phase velocity. The Fermi velocity for a SWCNT is approximately $8\times10^5 m/s$, while the wave velocity for conventional transmission line is $v_{free} = \sqrt{\frac{1}{L_M C_{ES}}} = \sqrt{\frac{1}{\mu\varepsilon}} = \frac{c}{\sqrt{\mu_r \varepsilon_r}}$. It can be seen that the wave velocity on the nanowire is about 0.01c only.

The resistance of a SWCNT is more complex. The general equation for the resistance of the SWCNT is [133]

$$R = R_Q + R_s = R_0 / 2 + R_0 / 2l_{eff} \cdot L_{CNT} \tag{3.23}$$

where $R_0 = h / 2e^2 = 12.9\ \text{k}\Omega/\mu\text{m}$ is the intrinsic quantum resistance, l_{eff} is the effective MFP and L is the length of the SWCNT. From (3.23) one can see that the resistance is comprised of 2 parts, the lumped quantum contact resistance R_Q and the distributed scattering-induced resistance R_S . As R_0 and L_{CNT} are constants, clearly the l_{eff} is the factor that most influences the resistance of a SWCNT and is discussed in the next section. The effective SWCNT circuit model per channel can thus be demonstrated as Figure 3.4.

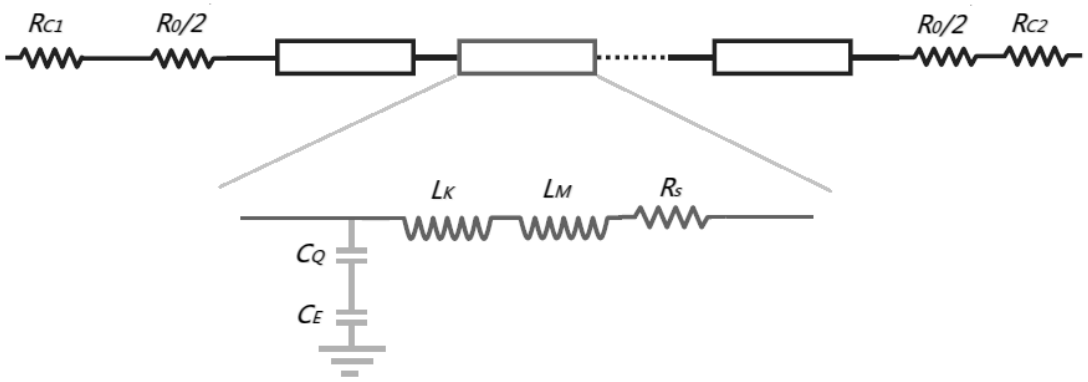

Figure 3.4 Effective Circuit model of a SWCNT channel, with distributed components and terminal resistances

3.3.2 The effective mean free paths of a SWCNT

There are several scattering mechanisms for electrons in nanotubes, including acoustic and optical phonon scattering as well as impurity and defect scattering. The effective MFP is the effects of these scattering lengths combined and is dependent on diameter, bias voltage and temperature.

In [134] the electrical-thermal transport in SWCNT was studied and a resistivity model that comprised of both elastic scattering of acoustic phonons and absorption/emission of optical phonons was proposed.

The general effective MFP as a function of temperature, SWCNT length and bias voltage is represented as [134]

$$l_{eff}^{'} = \left(l_{AC}^{-1} + l_{OP,ems}^{-1} + l_{OP,abs}^{-1} \right)^{-1}. \tag{3.24}$$

The l_{AC} , $l_{OP,ems}$ and the $l_{OP,abs}$ is the temperature dependent acoustic phonon scattering length , the OP emission length and the temperature dependent optical phonon absorption length, respectively. However, here the physical meanings of the three parts are not of focus point of this chapter, which only focus on the mathematical terms and the temperature-length-dependence of the MFP itself.

In (3.24), l_{AC} is the is written as [134], [139]

$$l_{AC} = l_{AC,300} \cdot \frac{300}{T}, \tag{3.25}$$

where $l_{AC,300} \approx 1600 \mu m$ [134] and T is the temperature.

The second part of (3.24) $l_{OP,ems}$ is comprised of 2 parts [134]

$$l_{OP,ems} = \left[\left(\frac{\hbar \omega_{OP}}{eV} L + \frac{N_{OP}(300)+1}{N_{OP}(T)+1} l_{OP,300} \right)^{-1} + \left(l_{OP,abs} + \frac{N_{OP}(300)+1}{N_{OP}(T)+1} l_{OP,300} \right)^{-1} \right]^{-1} \tag{3.26}$$

where $l_{OP,300} \approx 15nm$ is the spontaneous optical phonon emission length at 300K and $N_{OP}(T) = 1/\left[\exp\left(\hbar \omega_{OP} / k_B T \right) - 1 \right]$ is the optical phonon occupation. $\hbar \omega_{OP} \approx 0.18$ eV is the optical phonon emission threshold energy. Note that (3.26) takes into account not only the temperature, but also the bias voltage and the length of the SWCNT.

The last part of (3.24), $l_{OP,abs}$ can be written as [134]

$$l_{OP,abs} = l_{OP,300} \cdot \frac{N_{OP}(300)+1}{N_{OP}(T)}. \tag{3.27}$$

By substituting (3.25)-(3.27) into (3.24), the temperature and bias voltage dependent effective MFP can be calculated and thus the per unit length resistance is $R_0 / 2l_{eff}$, where $R_0 = h / 2e^2 = 12.9\text{k}\Omega$ is the quantum resistance per conductive channel.

In ideal ballistic transport there's no scattering at the contacts or along the SWCNT length, and only quantum conductance is present. In the presence of contact scattering there'll be contact resistance ranging from several mega-ohms to only a few hundred ohms [135-137]. Additional resistance also occurs in the presence of defects or when the path length becomes comparable to or larger than the MFP.

In [138], an approximation of the above MFP result was proposed under the low bias (<0.45V) and normal temperature (<600K) conditions, neglecting the voltage dependent factors and the spontaneous scattering. And the resistance induced by the elastic scattering of acoustic phonons is defined as the quantum resistance per conductive channel divided by the MFP and then multiply the temperature amendment factor, shown as (3.23)

$$R_e = R_0 T / (1000 D \cdot T_1), \tag{3.28}$$

where $T_1 = 400K$ [140] and D is the diameter of the CNT.

The resistance due to absorption of optical phonon is represented as

$$R_{abs} = R_0 \exp\left(-\hbar\omega_{op} / k_B T\right) / l_{op}, \tag{3.29}$$

where $\hbar\omega_{op} \approx 0.18$ eV and $l_{op} \sim 20D$ [134, 140].

The overall per unit length resistance is $R = 2R_{abs} + R_e$. A linear approximation is also proposed in [141] that for 270K<T<420K, the error is less than 10%

$$R \approx \frac{R_0}{1000D}\left(\frac{T}{T_0} - 2\right), \qquad T_0 = 100K \tag{3.30}$$

So the effective MFP is

$$l_{eff} = \frac{1000D}{T/T_0 - 2} \tag{3.31}$$

In [142] and many that followed, the resistance was expressed using the extracted data from experimental results under room temperature and it simplifies the resistance as only a function of the CNT diameter.

$$R = R_0 / l_{eff} \approx R_0 / 1000D, \tag{3.32}$$

The l_{eff} is proportional to the diameter reported in [142] and the average MFP in both theoretical predictions [143-145] and measurement [146] is in the order of 1 μm for a SWCNT with the diameter of about 1nm so l_{eff} is approximated as 1000D.

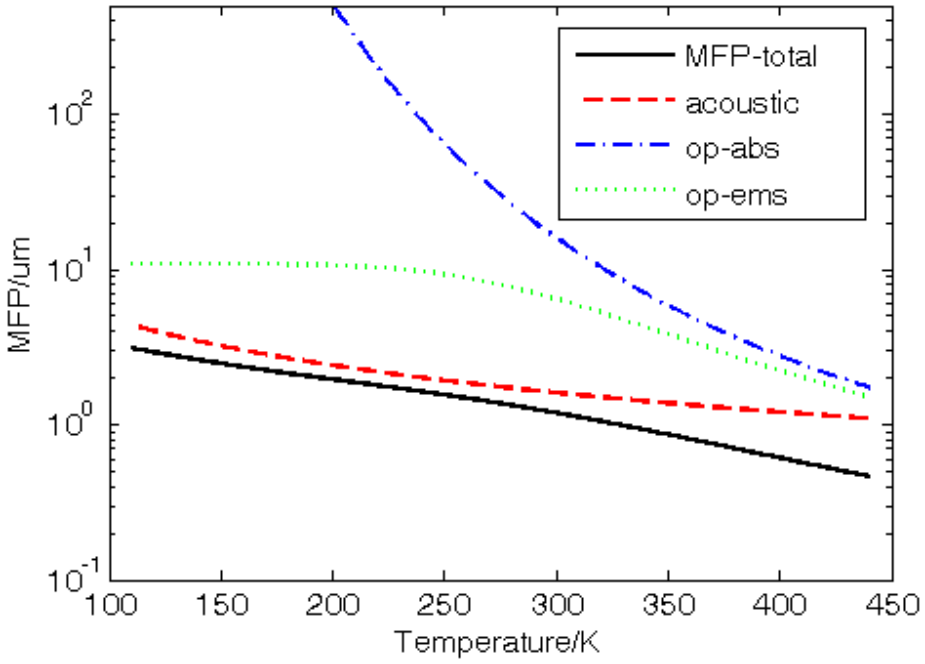

Figure 3.5 Simulated temperature dependent MFPs at low-bias conditions.

To validate the aforementioned two approximations in (3.31) and (3.32), The MFP of a SWCNT with different diameters, lengths and bias voltage is calculated. First of all, the temperature dependent MFPs of a 3 μm SWCNT with the diameter of 2.4nm under low bias excitation (50mV)

is shown in Figure 3.5. This result is identical with that in [134]. It is also shown in Figure 3.5 that the total MFP is dominated by acoustic scattering at lower temperatures but when the temperature grows higher the two optical phonon induced parts become more and more non-negligible, as shown in (3.24).

Now the total MFP under the temperature range of 270K<T<420K can be simulated using the aforementioned different approximation equations, respectively. The simulated temperature dependence of the total MFP is shown in Figure 3.6.

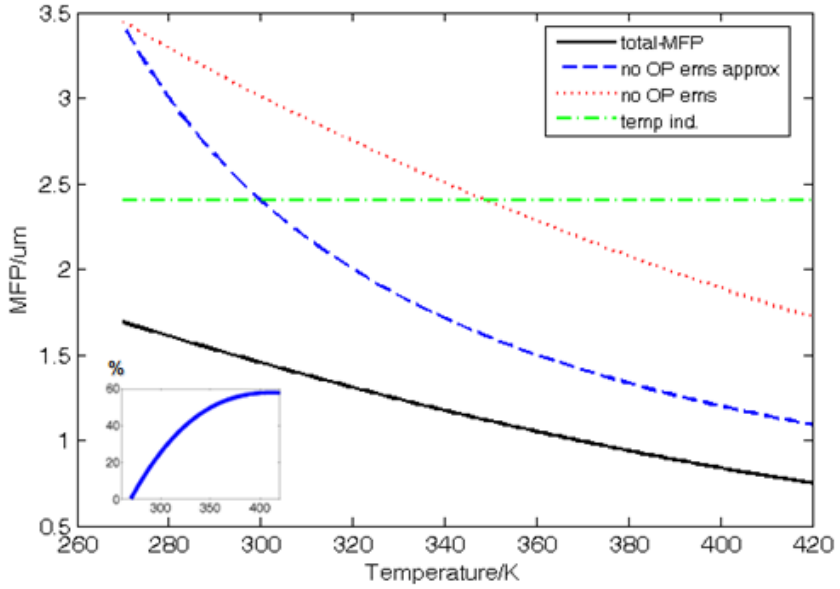

Figure 3.6 Comparison of the approximation equations with the original full MFP equation, insert graph shows the error between MFP without OP emission and its approximation.

Figure 3.6 shows that the full MFP in [134] is about half the value compared to that of [138], the reason for this is the equation used for calculating l_{AC} i.e. the dominate factor that affects MFP is different. The equation used in [134] was $1600 \cdot 300 / T$ and that used in [138] was a diameter dependent value of $1000D \cdot 400 / T = 4 \times 10^5 D$. Although [134] didn't give a diameter dependent equation, one can still assume it increases linearly with diameter. So for the SWCNT of the same quality with a different diameter, l_{AC} would be $1600 / 2.4 \cdot 300 \cdot D / T = 2 \times 10^5 D.$ Comparing these two equations, one can easily find that the l_{AC} in [134] is exactly half of that in [138]. This explains

well why the black line is only about a half of the red line yet the two keeps almost parallel across the entire simulated temperature. The cause for this difference may well be the different quality SWCNTs used in the measurement from which the MFP equations were extracted.

Although different l_{AC} values were reported for different SWCNTs, it's important to notice that [134] was published in 2005 and [138] in 2008, so considering the improvement of synthesis methods over time, equation in [138] that gives larger MFP values will be used in all the following simulations of this thesis.

Finally, the most simplified MFP value is represented by the green line in Figure 3.6. The equation (3.32) was extracted from measurement results, so it already takes into account the material defects and the imperfect contacts' effects. This equation derived from small radius SWCNTs, however as it's energetically more efficient to collapse a SWCNT into a graphene sheet when the radius is larger than 2.5nm, in practice one can consider the conditions for this equation to be accurate will always hold.

The other thing worth pointing out is that the blue line is the approximated value of red line and is reported to be less than 10% error [138]. However in the simulation it's quite inaccurate as the insert graph shows as high as 60% error. The reason for this should be the vague value of l_{op} used (~20D) in (3.29). However, taking the relationship of l_{op} and D in [134] and replace the ~20D term, a modified version of (3.29) can be acquired as $R_{abs} = R_0 \exp\left(-\hbar\omega_{op} / k_B T\right) / 6.25\mathrm{D}$. Figure 3.7 shows the modified curve and its approximation.

Using the modified l_{op} value, the approximation error can be reduced to less than 20%. Thus, the $l_{op,300}$ in (3.26) and (3.27) can be replaced by 6.25D to make it diameter dependent.

$$l'_{OP,ems} = \left[\left(\frac{\hbar\omega_{OP}}{eV} L + \frac{N_{OP}(300)+1}{N_{OP}(T)+1} \cdot 6.25D \right)^{-1} + \left(l_{OP,abs} + \frac{N_{OP}(300)+1}{N_{OP}(T)+1} \cdot 6.25D \right)^{-1} \right]^{-1} \qquad (3.33)$$

$$l'_{OP,abs} = 6.25D \cdot \frac{N_{OP}(300)+1}{N_{OP}(T)}. \qquad (3.34)$$

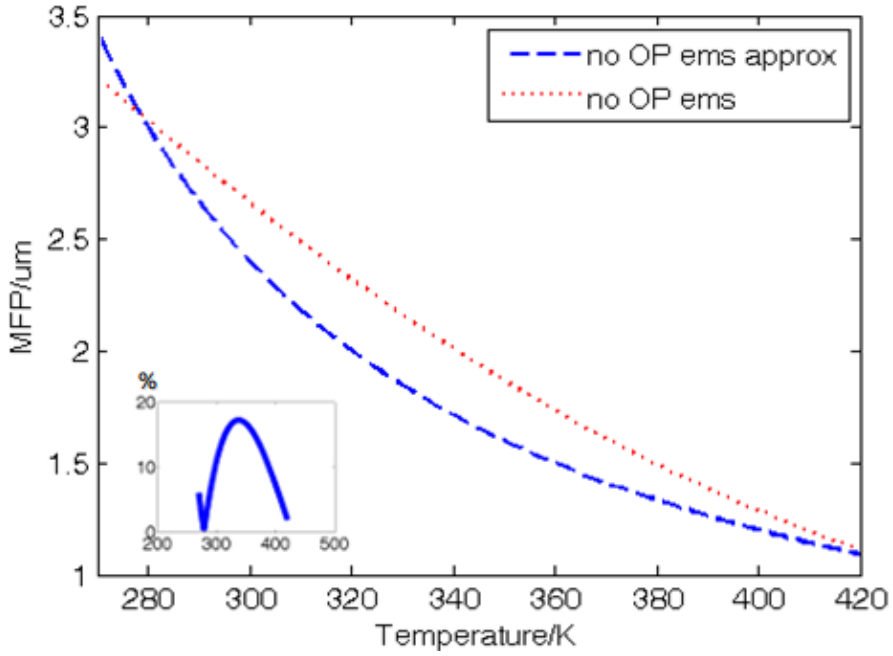

Figure 3.7 MFP without OP ems, original and approximation, after modification.

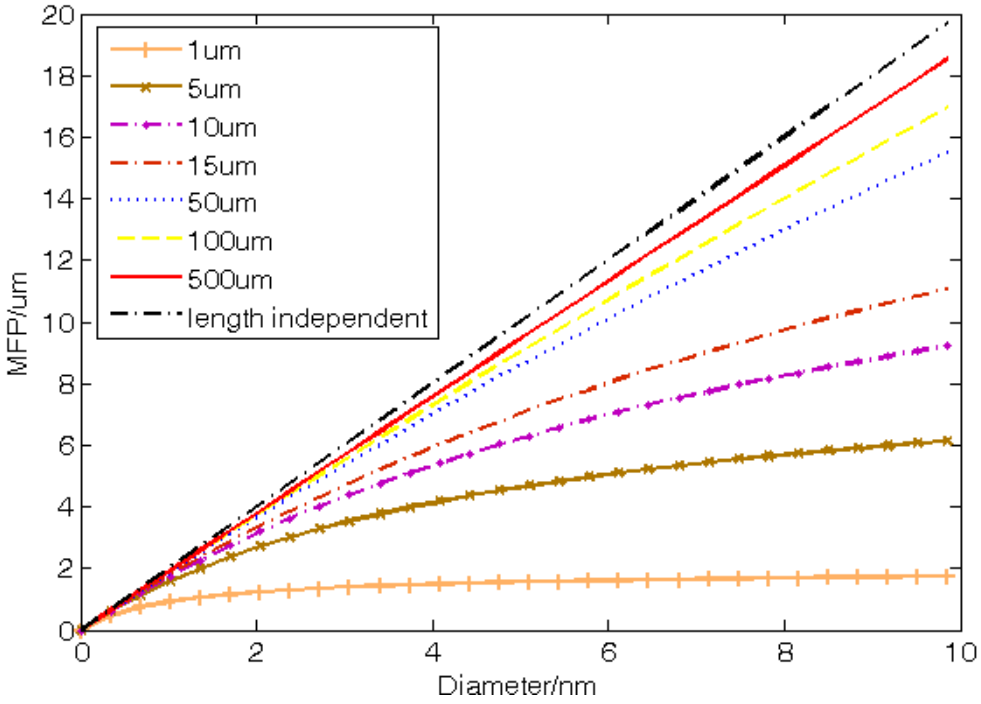

Figure 3.8 MFP as a function of diameter, with different SWCNT length grouped and the comparison with the length independent approximation.

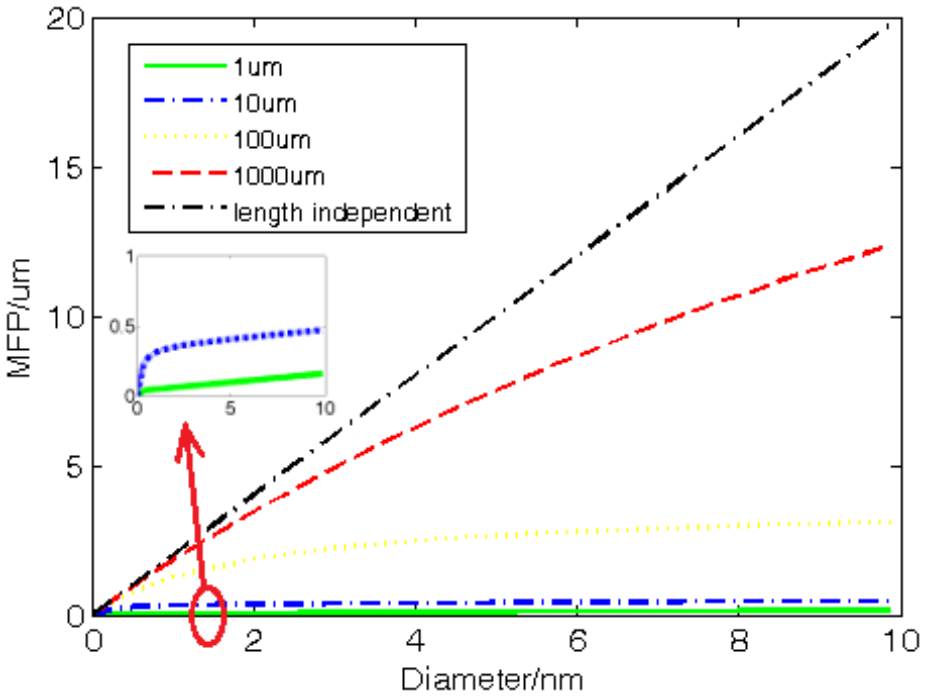

Figure 3.9 High bias MFP as a function of diameter, with different SWCNT length and the comparison with the length independent approximation

Using the modified equation (3.33) and (3.34) the MFP at 300K with different SWCNT diameters is simulated. The MFP for different SWCNT length was grouped and compared with the length-independent model ($l_{eff} \approx 1000D$). Figure 3.8 shows simulated results. One can clearly see that at room temperature, the MFP increases with the increase of the diameter, but for small length SWCNTs, the increase becomes non-linear at larger diameters. In other words, the longer the SWCNT is, the more it can hold the linear increment of the MFP. Also it's shown that the longer the SWCNT is, the length-dependent MFP grows closer to the length-independent result, this is important because it shows that for short interconnects the approximation (3.32) will introduce large errors and for long interconnects the approximation error is less than 10%. Figure 3.8 also shows that the increase speed of the MFP cannot 'catch up' with that of the SWCNT length, so only SWCNTs with very small length (L<5um) can have ballistic electron transmission. The electron transmission in longer SWCNTs will be diffusive.

And finally, the reliability of (3.32) is tested under high-bias conditions. The bias voltage is increased from 50mV to 5V and the result is shown in Figure 3.8. It shows that under high-bias, the MFP curve loses linearity much faster than low-bias case, so (3.32) is totally invalid even for very long length SWCNTs with very small radius. This conclusion is consistent with [142], which mentions that (3.32) works for low-bias conditions and the high-bias case was not supported. Figure 3.9 also shows that for high-bias, the MFP curves for SWCNTs with different length are 'condensed'. From the inserted graph in Figure 3.9 it can be seen that even for small radius SWCNTs the electron transmission will still be diffusive. In other words, the self-heating caused by high-bias breaks the ballistic transport in SWCNTs.

3.3.3 Summary of SWCNT MFP

In this section, the fundamental modeling techniques for a graphene shell i.e. a SWCNT are reviewed. Besides the electrostatic inductance and capacitance, the kinetic inductance and quantum capacitance resulting from the band-structure of graphene and the quantum interaction of electrons at nano scale is introduced and their value analytically expressed. The focus is on the MFP calculation which is the key factor that influences the resistance and with the above discussion, the conclusion can be drawn that

1. The acoustic phonon induced resistance is dominant in the overall resistance. However, when the temperature is high the optical phonon induced resistance is non-negligible.
2. By comparing the three different MFP equations, the constant value of $l_{ac,300}$ and $l_{op,300}$ in [134] is replaced with the function of diameter. This modified model is compared with its approximated model and has reduced the error from precious results by 40%.
3. With this modified equation, the MFP with the now generally used approximation is calculated and compared and it is found that when the SWCNT is short (<10um), the error from this approximation would be too large to be accurate.
4. The (3.32) approximation will hold only for low-bias, long length SWCNTs. For low-bias, the electron transport is ballistic with SWCNT length L<5um, and diffusive for L>5um. For high-bias, serious self-heating will destroy the ballistic transport and all electrons will be transported diffusively.

Thus, in the following section and chapters of this thesis the modified full MFP expression (3.33) will be used instead of the simplified expressions.

3.4 Simulation of a single SWCNT

Assume the SWCNT over ground geometry with 2 terminals added to each end of the SWCNT, as depicted in Figure 3.10.

The two terminal contacts are symmetric, so the metallic contact resistance Rc at each terminal is the same. The total contact resistance is Rc+R0/2. The voltage excitation is set at port 1 as V_{01} and the reference impedance at each port is Z_0. This becomes the classical transmission line (TL) problem and by using the techniques in [130]. The total S-parameter can be solved as

$$S_{11} = 2 \cdot \frac{V_1}{V_{01}} - 1 = \frac{Z_{in} - Z_0}{Z_{in} + Z_0}, \tag{3.35}$$

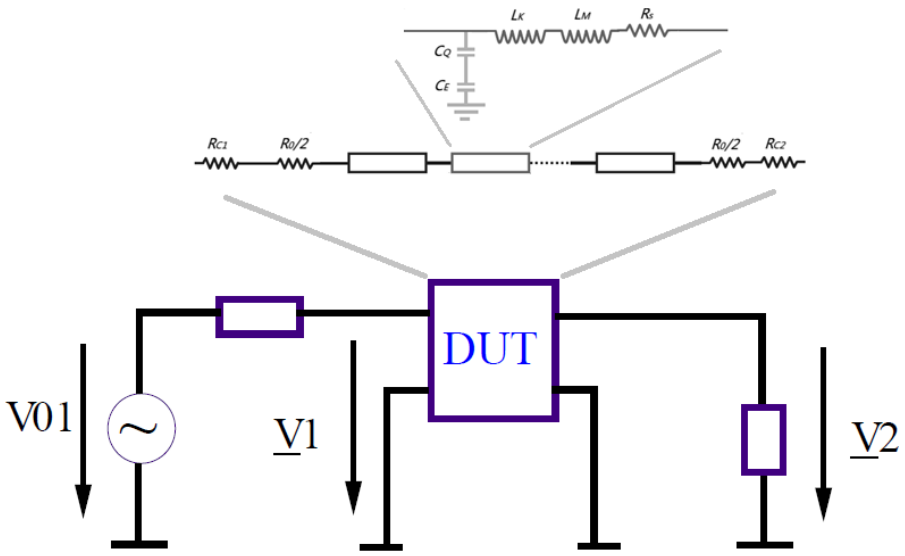

Figure 3.10 Terminal configuration for a SWCNT

where Z_{in} is the input impedance seen from port 1

$$S_{21} = \frac{2V_2}{V_{01}}. \tag{3.36}$$

The characteristic impedance of the CNT is given by

$$Z_c = \sqrt{\frac{R + j\omega L_{tot}}{j\omega C_{tot}}}, \tag{3.37}$$

where R is the resistance per unit length, $L_{tot} = L_k^{'} + L_M$ and $C_{tot}^{-1} = C_q^{'-1} + C_E^{-1}$.

The S-parameter of a single SWCNT with radius of 2nm, length of 10um and the distance between itself and the ground set to be 1um is simulated using both ADS and MATLAB. First of all the MFP needs to be checked to ensure the transport is diffusive otherwise the distributed circuit model degenerates into a lumped one. According to chapter 2, for such a SWCNT, $l_{eff} = 3.72\ \mu\text{m}$. This is smaller than the length of SWCNT, so the condition holds.

The ADS simulation configuration is shown in Figure 3.11 and the result is shown in Figure 3.12. In Figure 3.11, each box is one per unit length and its detailed circuit is shown at the upper right corner. The green circle at the left side shows the reference impedance used in the simulation is 50Ohms.

From Figure 3.12 we can see that up to 750GHz, the two simulations have identical results. From 800GHz upwards, the S11 shows some error but is within 0.5%. This should be caused by the additional parameters in ADS's build-in library that affects the high frequency behaviour. But the frequency of interest of this thesis is in microwave, at which the two results are identical.

Note that the simulated S11 is very high and S21 very low, which means almost all the energy is reflected. This is because the reference impedance is still set to be 50 Ohms, while the intrinsic impedance of the SWCNT is ~12.9KOhm, creating a serious mismatch at the interface. If the SWCNT can be loaded to high reference impedance, a better transmission will be achieved.

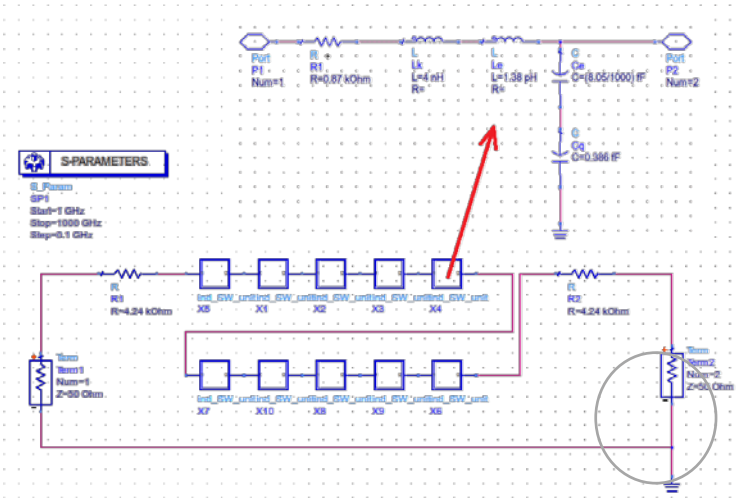

Figure 3.11 ADS configuration of a single SWCNT S-parameter simulation, each box represents one unit length and upper right shows its circuit.

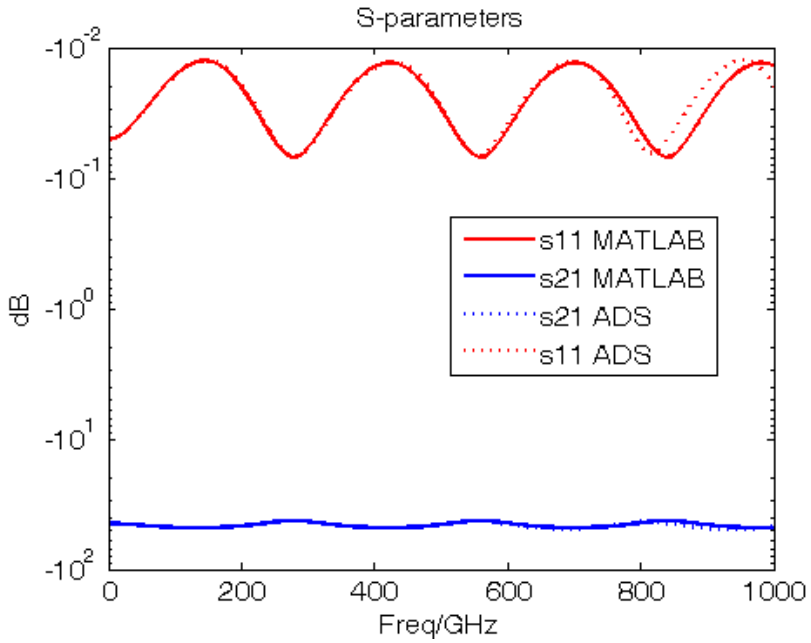

Figure 3.12 S-parameter simulation result from ADS (dashed line) and MATLAB (solid line), across the frequency simulated the error is within 5%.

3.5 Simulation of a SWCNT bundle under common-mode excitation

For a SWCNT bundle, Burke has proved that there're three spin modes (neutral) and one charged mode i.e. common mode. In this thesis we only consider the common mode, in which all channels in the SWCNT bundle are excited with same voltage.

The signal propagation in a SWCNT bundle have been studied in many papers [147-149], and an effective single conductor model was proposed in [126]. These studies were all based on the assumption that in inter-CNT electrostatic coupling is weak [150, 151]. However, these papers are mainly for interconnection purposes and the S-parameter which is important to microwave applications and characterizations is not the major concern. Furthermore, it is suggested in [152] that when the CNT bundle becomes large, the electrostatic coupling will eventually increase to the same order of kinetic inductance or even higher and cannot be neglected. So it's important to do a comparison of the S-parameter of a SWCNT bundle with electrostatic coupling taking into account and that of an effective single-conductor that neglects the coupling.

The difficulty to do so is that the calculations is essentially solving a multi-conductor transmission line (MTL) equation with 2n-port i.e. 2n unknowns, while the 2-port configuration gives only 2 terminal conditions. Thus it forms an under-determined set of equations from which S-parameter is impossible to be calculated using conventional techniques. Thus, it is very necessary to develop a new technique to calculate the 2-port S-parameter of a 2n-port bundle with all electrostatic coupling taking into account.

3.5.1 Configuration and MTL equation

Figure 3.13 shows the cross section of a SWCNT bundle over ground. The distance from the bottom line of SWCNT to the ground is H and the distance between neighbouring SWCNTs is d. There're n layers of SWCNT and each layer has m SWCNTs, so the total number of SWCNT in the bundle is m*n. To locate an arbitrary SWCNT in the bundle, simply multiply the layer number with the number in the layer, for example, the SWCNT in the red circle is number (n-2)*2, and the SWCNT in the blue circle is number (n-1)*m. Thus, any SWCNT in the bundle can be uniquely identified.

The MTL propagation equation for the MWCNT can be written as [131]

$$\frac{d}{dx}\vec{V}(x) = -\mathbf{Z}\vec{I}(x)$$
$$\frac{d}{dx}\vec{I}(x) = \mathbf{Y}\vec{V}(x), \tag{3.38}$$

where

$$\mathbf{Z} = \mathbf{R}_s + j\omega\{\mathbf{L}_e + \mathbf{L}_k\}$$
$$\mathbf{Y} = j\omega\{\mathbf{C}_e^{-1} + \mathbf{C}_q^{-1}\}^{-1}. \tag{3.39}$$

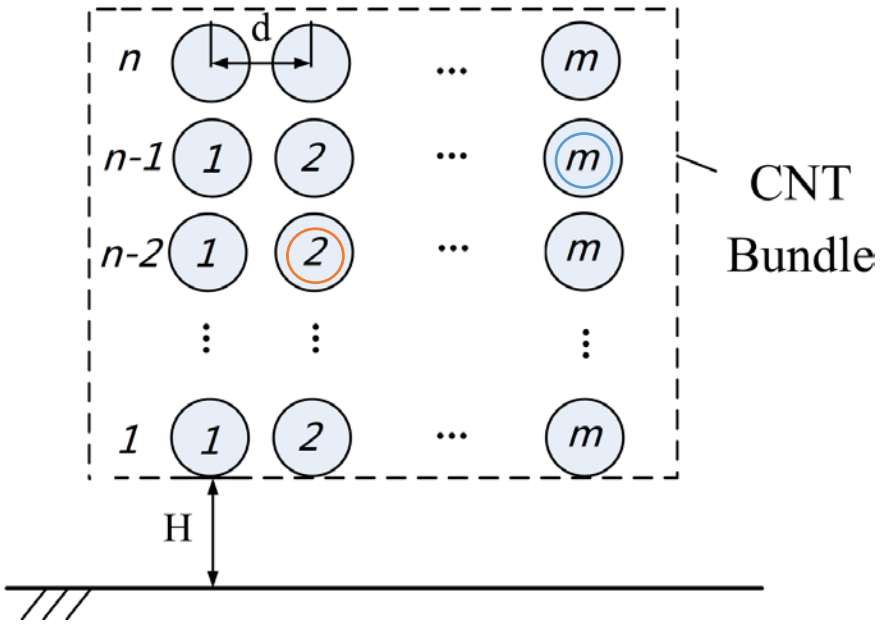

Figure 3.13 Cross sectional view of a SWCNT bundle above ground.

The distributed circuit elements are calculated using equations in chapter 2, although the average number of metallic SWCNTs in the bundle is 1/3 of the total SWCNTs so an effective number of conductive channels of 2/3 is generally used, considering the distribution of the metallic SWCNT is random, the effect is only that the effective distance between neighboring SWCNTs increases. So it's considered that all SWCNTs in the simulation is metallic and the number of conductive channels is still 2. The bold term in (3.38) and (3.39) means matrix, so $\mathbf{R}_s$ is a diagonal matrix of

per unit length diffusion resistance, $\mathbf{L}_{\mathrm{k}}$ is the diagonal matrix of per unit length kinetic inductance, $\mathbf{C}_{\mathrm{q}}$ is the diagonal matrix of the per unit length quantum capacitance, $\mathbf{L}_{\mathrm{e}}$ is the full symmetric matrix of the per unit length electrostatic inductances, and finally, $\mathbf{C}_e$ is the full symmetric matrix of the per unit length electrostatic capacitances.

The diagonal elements of $\mathbf{L}_{\mathrm{e}}$ can be expressed analytically as [124]

$$L_e^{i,i} = \frac{\mu}{2\pi} \mathrm{a\cosh}\left(\frac{h_i}{r_i}\right), \tag{3.40}$$

where r_i is the diameter of the i-th SWCNT and h_i is the distance from the center of i-th SWCNT to the ground.

The off diagonal elements of $\mathbf{L}_{\mathrm{e}}$ is [131]

$$L_e^{i,j} = \frac{\mu}{2\pi} \ln\left(\frac{\sqrt{s_{i,j}^2 + 4h_i h_j}}{s_{i.j}}\right) \tag{3.41}$$

where $s_{i,j}$ is the distance between i-th SWCNT and j-th SWCNT.

Considering the identification rule shown in Figure 3.13, (3.40) and (3.41) can be further developed into

$$L_e^{i,i} = \frac{\mu}{2\pi} a\cosh\left(\frac{H + d\lfloor i/n \rfloor}{r_i}\right) \tag{3.42}$$

$$L_e^{i,j} = \frac{h}{2\pi} \ln\left(\sqrt{\frac{4\left(\lfloor j/n \rfloor + H\right)\left(\lfloor i/n \rfloor + H\right) + d^2\left[\left(\lceil j/n \rceil - \lceil i/n \rceil\right)^2 + \left(j \bmod m - i \bmod m\right)^2\right]}{d^2\left[\left(\lceil j/n \rceil - \lceil i/n \rceil\right)^2 + \left(j \bmod m - i \bmod m\right)^2\right]}}\right) \tag{3.43}$$

The matrix $\mathbf{C}_e$ can be calculated using the equation

$$\mathbf{C}_e = \mu\varepsilon \cdot \mathbf{L}_e^{-1} \tag{3.44}$$

where μ and ε is the permeability and the permittivity of the host medium that fills the space between SWCNTs.

3.5.2 Modal analysis and ABCD matrix

The transmission line model (3.38) can be solved applying the modal analysis method in [131], which gives an ABCD matrix expression as

$$\begin{bmatrix} \vec{V}(l) \\ \vec{I}(l) \end{bmatrix} = \begin{bmatrix} \mathbf{\Phi_{11}}(l) & \mathbf{\Phi_{12}}(l) \\ \mathbf{\Phi_{21}}(l) & \mathbf{\Phi_{22}}(l) \end{bmatrix} \begin{bmatrix} \vec{V}(0) \\ \vec{I}(0) \end{bmatrix}, \tag{3.45}$$

where

$$\begin{aligned} \mathbf{\Phi_{11}}(l) &= \mathbf{M} \cdot \cosh(\boldsymbol{\lambda} \cdot l) \mathbf{M}^{-1} \\ \mathbf{\Phi_{12}}(l) &= -\mathbf{M} \cdot \cosh(\boldsymbol{\lambda} \cdot l) \mathbf{M}^{-1} \cdot \mathbf{Z}_c \\ \mathbf{\Phi_{21}}(l) &= -\mathbf{N} \cdot \cosh(\boldsymbol{\lambda} \cdot l) \mathbf{N}^{-1} \cdot \mathbf{Y}_c \\ \mathbf{\Phi_{22}}(l) &= -\mathbf{N} \cdot \cosh(\boldsymbol{\lambda} \cdot l) \mathbf{N}^{-1} \end{aligned} \tag{3.46}$$

Matrix $\mathbf{M}$, $\mathbf{N}$ is the eigenvector matrix of $\mathbf{Z} \cdot \mathbf{Y}$ and $\mathbf{Y} \cdot \mathbf{Z}$, respectively and $\boldsymbol{\lambda} \cdot \boldsymbol{\lambda}$ is the diagonal eigenvalue matrix of $\mathbf{Z} \cdot \mathbf{Y}$. As $\mathbf{Z}$ and $\mathbf{Y}$ are symmetric, it can be proven that $\mathbf{Z} \cdot \mathbf{Y} = (\mathbf{Y} \cdot \mathbf{Z})^T$ and $\mathbf{M}^{-1} = \mathbf{N}^T$. $\mathbf{Z}_c$ is the characteristic impedance of the MTL network [131]:

$$\mathbf{Z}_c = \mathbf{Y}^{-1} \cdot \mathbf{M} \cdot \boldsymbol{\lambda} \cdot \mathbf{M}^{-1}, \tag{3.47}$$

and the characteristic admittance $\mathbf{Y_c} = \mathbf{Z_c}^{-1}$.

If we take the lumped contact resistance into consideration, the ABCD matrix Γ of the entire MTL becomes

$$\mathbf{\Gamma}_{2m \times 2m} = \begin{bmatrix} \mathbf{E}_{m \times m} & \mathbf{R_c} + \mathbf{R_q}/2 \\ \mathbf{0}_{m \times m} & \mathbf{E}_{m \times m} \end{bmatrix} \cdot \mathbf{\Phi}_{2m \times 2m} \cdot \begin{bmatrix} \mathbf{E}_{m \times m} & \mathbf{R_c} + \mathbf{R_q}/2 \\ \mathbf{0}_{m \times m} & \mathbf{E}_{m \times m} \end{bmatrix}, \tag{3.48}$$

where $\mathbf{E}$ is the diagonal unity matrix and $\mathbf{R}_c$ is the diagonal matrix of the contact resistance at each terminal.

3.5.3 A Novel technique of solving 2-port S-parameters of an arbitrary 2n-port network

First, incorporate the transfer matrix with common mode port excitations and calculate the S-parameters from the overall current at the two terminals without solving the currents on each of the CNT.

Figure 3.14 shows the configuration of the terminal excitations. Assume the array is excited by a common mode terminal voltage $\vec{V_s} = \begin{bmatrix} V_s & V_s & ... & V_s \end{bmatrix}^T$, and there's no mutual coupling between each two terminals. The port impedances are set to z_0 at both ends. To calculate the S-parameter of the array, the following equations need to be solved:

$$\mathbf{V_s} - z_0 \cdot \overrightarrow{\sum \mathbf{I}(\mathbf{0})}_{m\times 1} = z_0 \cdot \mathbf{\Gamma_{11}} \cdot \overrightarrow{\sum \mathbf{I}(\mathbf{l})}_{m\times 1} + \mathbf{\Gamma_{12}} \cdot \mathbf{I}(\mathbf{l}) \tag{3.49}$$

$$\mathbf{I}(\mathbf{0}) = z_0 \cdot \mathbf{\Gamma_{21}} \cdot \overrightarrow{\sum \mathbf{I}(\mathbf{l})}_{m\times 1} + \mathbf{\Gamma_{22}} \cdot \mathbf{I}(\mathbf{l}) \tag{3.50}$$

where

$$\overrightarrow{\sum \vec{I}(0)} = \left[\underbrace{\sum \vec{I}(0), \sum \vec{I}(0), ..., \sum \vec{I}(0)}_{mn} \right]^T \text{ and } \overrightarrow{\sum \vec{I}(l)} = \left[\underbrace{\sum \vec{I}(l), \sum \vec{I}(l), ..., \sum \vec{I}(l)}_{mn} \right]^T .$$

From (3.50) one can get

$$\vec{I}(l) = \mathbf{\Gamma}_{12}{}^{-1} \cdot \vec{V_s} - z_0 \cdot \mathbf{\Gamma}_{12}{}^{-1} \cdot \overrightarrow{\sum \vec{I}(0)} - z_0 \cdot \mathbf{\Gamma}_{12}{}^{-1} \cdot \mathbf{\Gamma}_{11} \cdot \overrightarrow{\sum \vec{I}(l)}. \tag{3.51}$$

Note that $\vec{V_s}$, $\overrightarrow{\sum \vec{I}(0)}$ and $\overrightarrow{\sum \vec{I}(l)}$ are three vectors whose every element is identical, so by summing up the elements at both sides of (3.51) and get

$$\sum \vec{I}(l) + z0 \cdot \sum\sum \left(\mathbf{\Gamma}_{12}{}^{-1} \cdot \mathbf{\Gamma}_{11} \right) \cdot \sum \vec{I}(l) = \sum\sum \mathbf{\Gamma}_{12}{}^{-1} \cdot \vec{V_s} - z_0 \cdot \sum\sum \mathbf{\Gamma}_{12}{}^{-1} \cdot \sum \vec{I}(0). \tag{3.52}$$

In this way, the original matrix equation (3.50) of $2 \cdot mn$ unknowns becomes a scalar equation (3.52) of only 2 unknowns, namely $\sum \vec{I}(l)$ and $\sum \vec{I}(0)$.

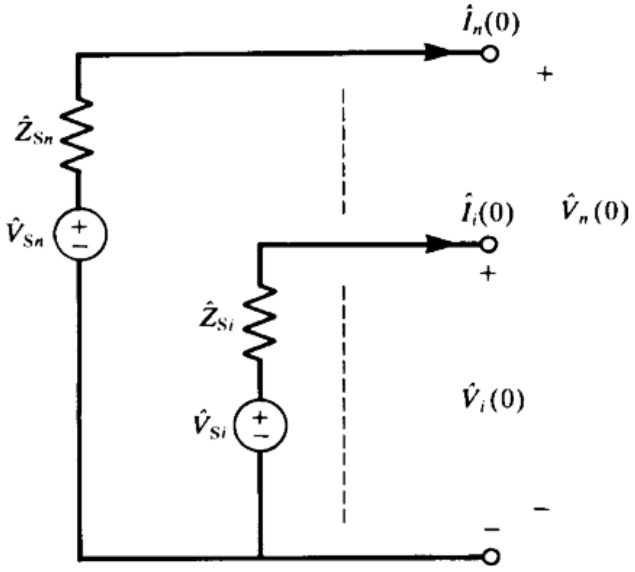

Figure 3.14 Configuration of terminal excitations [131]

Similarly, from (3.49) one can get

$$\begin{aligned}\sum \vec{I}(0) = z_0 \cdot \sum\sum \boldsymbol{\Gamma}_{21} \cdot \sum \vec{I}(l) + \sum\sum \left(\boldsymbol{\Gamma}_{22} \cdot \boldsymbol{\Gamma}_{12}^{-1}\right) \cdot \left[\vec{V_s} - z_0 \cdot \sum \vec{I}(0)\right] \\ - z_0 \cdot \sum\sum \left(\boldsymbol{\Gamma}_{22} \cdot \boldsymbol{\Gamma}_{12}^{-1} \cdot \boldsymbol{\Gamma}_{11}\right) \cdot \sum \vec{I}(l).\end{aligned} \tag{3.53}$$

Finally, (3.52) and (3.53) forms a set of 2 equations with 2 unknowns. And the total current at 2 ports (x=0 and x=l) can be solved as

$$\sum \vec{I}(0) = \frac{\sum\sum \left(\boldsymbol{\Gamma}_{22} \cdot \boldsymbol{\Gamma}_{12}^{-1}\right) + P}{1 + z_0 \sum\sum \left(\boldsymbol{\Gamma}_{22} \cdot \boldsymbol{\Gamma}_{12}^{-1}\right) + z_0 \cdot P} \cdot V_s, \tag{3.54}$$

where $P = \dfrac{z_0 \left[\sum\sum \boldsymbol{\Gamma}_{21} - \sum\sum \left(\boldsymbol{\Gamma}_{22} \cdot \boldsymbol{\Gamma}_{12}^{-1} \boldsymbol{\Gamma}_{11}\right)\right] \cdot \sum\sum \boldsymbol{\Gamma}_{12}^{-1}}{1 + z_0 \sum\sum \left(\boldsymbol{\Gamma}_{12}^{-1} \cdot \boldsymbol{\Gamma}_{11}\right)}$,

and

$$\sum I(l) = \frac{\sum\sum \boldsymbol{\Gamma}_{12}^{-1} \cdot \left[V_s - z_0 \sum \vec{I}(0) \right]}{1 + z_0 \sum\sum \left(\boldsymbol{\Gamma}_{12}^{-1} \cdot \boldsymbol{\Gamma}_{11} \right)}, \tag{3.55}$$

Once the 2 total port currents are solved, the input impedance can be easily solved as

$$Z_{in} = \left[V_s - z_0 \sum I(0) \right] / \sum I(0), \tag{3.56}$$

and finally, the 2-port S-parameters can be solved using (3.35) and (3.36).

3.6 Comparison of effective single conductor model and full model

In this section, a detailed comparison of ESC and MTL models for different CNTs is presented. As the ESC model is significantly time efficient compared to the MTL model, it is beneficial to show the validity range of the ESC model where accuracy is not affected.

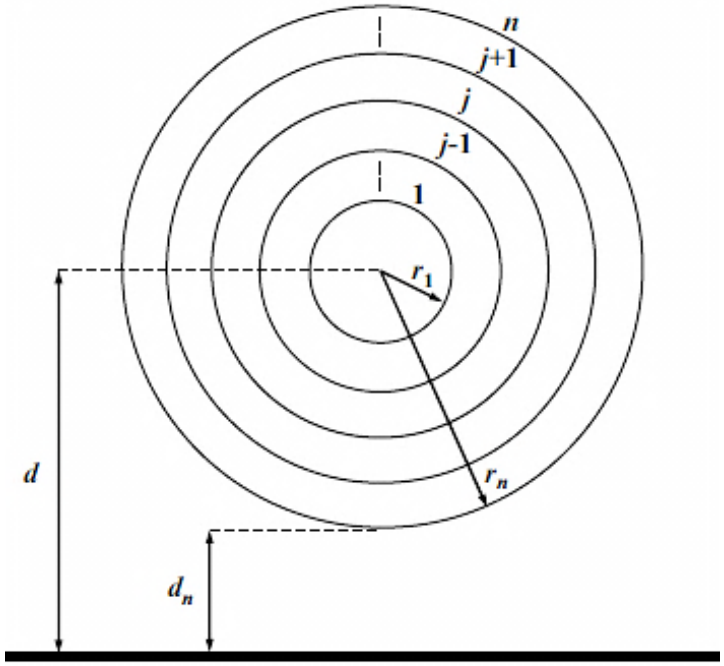

Figure 3.15 Schematic configuration of a MWCNT above ground plane [153].

The configuration of a single MWCNT above an infinitely large ground plane is shown in Figure 3.15.

First of all, the distance between each 2 neighboring shells in a MWCNT is $\delta = 0.34nm$ so given the outer radius and inner radius, the structure of a MWCNT is fixed and the total number of shells can be calculated as

$$N = \left\lfloor \frac{(r_{out} - r_{in})}{\delta} \right\rfloor + 1 \tag{3.57}$$

the number of conducting channels is no larger than 2 for each shell of the MWCNT. Instead, they can be expressed by the following equation [133].

$$\begin{cases} N_c = 7.74e-4 \cdot T \cdot r + 0.2 & \text{r>650/T} \\ N_c = 2/3 & \text{other} \end{cases} \tag{3.58}$$

3.6.1 A single MWCNT

For small radius shells, (3.58) calculate the number of conductive channels using the average number of conductive channels of a SWCNT, and for larger radius shells, (3.58) is radius dependent (assume same temperature), which means that even the chirality of the CNT does not satisfy the metallic conditions, as long as the diameter is large enough, the MWCNT is always conductive. Like the SWCNT bundle, the per unit length parameters of the MWCNT are matrices. The electrostatic couplings are different from the SWCNT bundle cases. The mutual capacitance C_e is a band diagonal matrix because the capacitive interactions between non-neighboring shells. The non-zero elements of C_e is [153]

$$
\begin{aligned}
C_e(i,i+1) &= -\frac{2\pi\varepsilon}{\ln(r_{i+1}/r_i)} \\
C_e(i-1,i) &= -\frac{2\pi\varepsilon}{\ln(r_i/r_{i-1})} \\
C_e(i,i) &= -C_e(i-1,i) - C_e(i,i+1) \\
C_e(n,n) &= -C_e(n-1,n) + \frac{2\pi\varepsilon}{\cosh^{-1}(d/r_n)}.
\end{aligned}
\tag{3.59}
$$

As mutual capacitance array is largely comprised of zero elements, it is expected that the results from ESC and MTL models does not vary too much.

To compare the ESC model of a single MWCNT with full MTL model, four individual MWCNTs with different outer radii are simulated with both ESC and full MTL models. The inner and outer radii are 2:4, 5:10, 10:20 and 8:24 respectively. Generally the ratio of inner and outer radius ranges from 0.3~0.7, and the average value 0.5 is often used.The 8:24 MWCNT is used to make the simulation more general. The result is shown in Figure 3.16. Note that in order to make S11 more visible, reference impedance z_0 is set to be 12.9KOhm, i.e. good matching between the port and the MWCNT.

So the conclusion is that for a single MWCNT, the accuracy of the ESC model is well within the acceptance range, so in order to simplify the simulation process, a single MWCNT can be simulated as an effective SWCNT.

3.6.2 An array of CNTs

A CNT array depicted in Figure 3.13 can be reduced into the effective single conductor model, as shown in Figure 3.17.

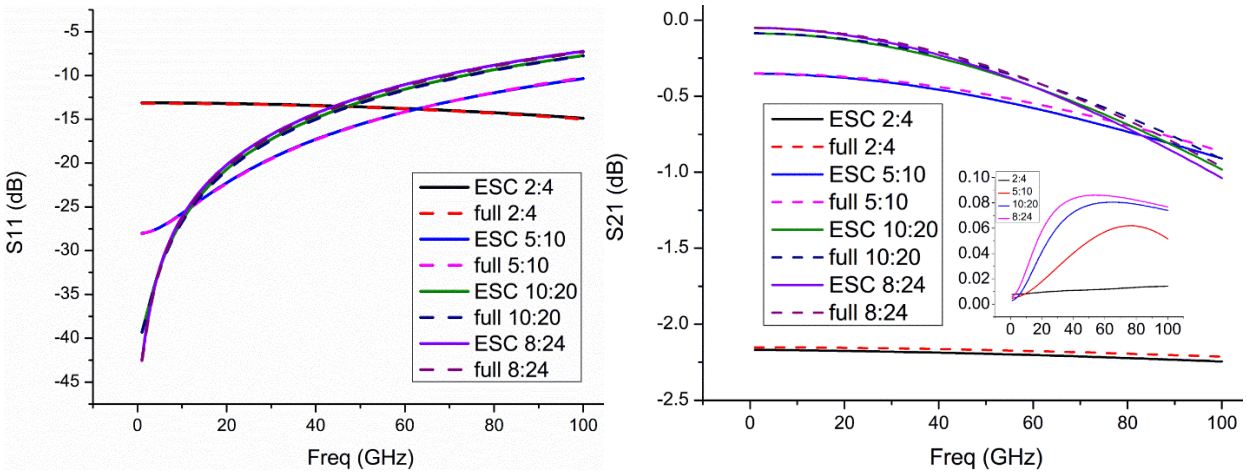

(a) (b)

Figure 3.16 Comparison of S-parameters of a single MWCNT with 4 sets of inner: outer radius. (a) is the S11 and (b) is the S21. The inset in (b) is the error between two models.

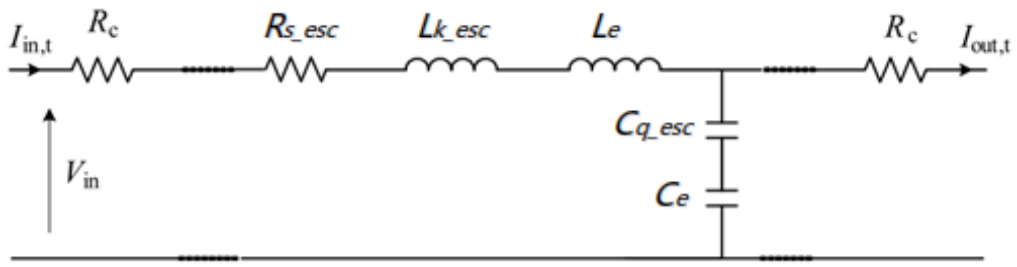

Figure 3.17 Circuit representation of Effective single conductor model of a SWCNT bundle.

By neglecting the mutual coupling, only the electrostatic inductance and capacitance between the SWCNT and ground is taken into account, which gives:

$$R_s^{esc} = R_s / 2\sum N_c \tag{3.60}$$

$$L_k^{esc} = L_k^{'} / 2\sum N_c \tag{3.61}$$

$$C_q^{ecs} = C_q^{'} \cdot 2\sum N_c \tag{3.62}$$

The case when m=n is simulated. In this case, effective conductor radius is half the length of the bundle and the height above ground is from the center of the bundle to the ground.

We compare the S-parameters of three 100um long MWCNT arrays calculated by the MTL technique depicted above and the ESC model [5], which uses a single effective conductor to represent the multi-conductor array of MWCNTs. The first array has a total number of 20×20 MWCNTs with innermost radius $r_1=3nm$ and 9 shells, the second array has a same number of MWCNTs with innermost radius $r_1=10nm$ and 30 shells, while the third array has a total number of 2×2 MWCNTs with the same innermost radius and number of shells as the first array. The distance above ground is 1um for all three cases. The simulation frequency is from 1GHz to 2 THz. The spacing between every neighboring MWCNTs (edge to edge) are set as 100nm. Such a spacing makes the MWCNT array sparse enough so that the mutual coupling in (3.41) is valid. At the same time, the wavelength at 2THz, which is 150μm, is much larger than the spacing of neighboring MWCNTs so that a TEM transmission is guaranteed. Thus the transmission line model is valid across the entire frequency of interest. Like in 3.6.1, to make the resonant peak of S_{11} deep enough for comparison, the reference impedance z_0 is set as the characteristic impedance of a metallic SWCNT instead of 50Ω.

The simulated S-parameter are shown in Figure 3.18. Clearly the results from two models are identical up to around 200GHz, while at higher frequencies, a small shift in periodicity appears in MTL, as it considers the coupling between every two CNTs. This difference is due to the fact that with the increase of frequency, the impedance introduced by the magnetic inductance becomes dominant. This inductance part is taken into account in the MTL model but completely neglected in the ESC model. Due to the same additional impedance, the MTL results shows multiple spikes between two resonant peaks and it seems the maximum difference between the results of the two models appears at these spikes. This difference between the results given by MTL and ESC models in the third array is smaller than that in the first array, and the difference between the two models are largest in the second array. So the conclusion is that for arrays with the same geometry, the difference between MTL and ESC model increases with the increase of an array's total size, i.e. the number of CNTs in the array, as well as the diameter of each CNT.

From the above comparison, the conclusion can be drawn that for a large CNT array and frequencies above 100GHz, the ESC model is no longer valid and the MTL model should be used instead.

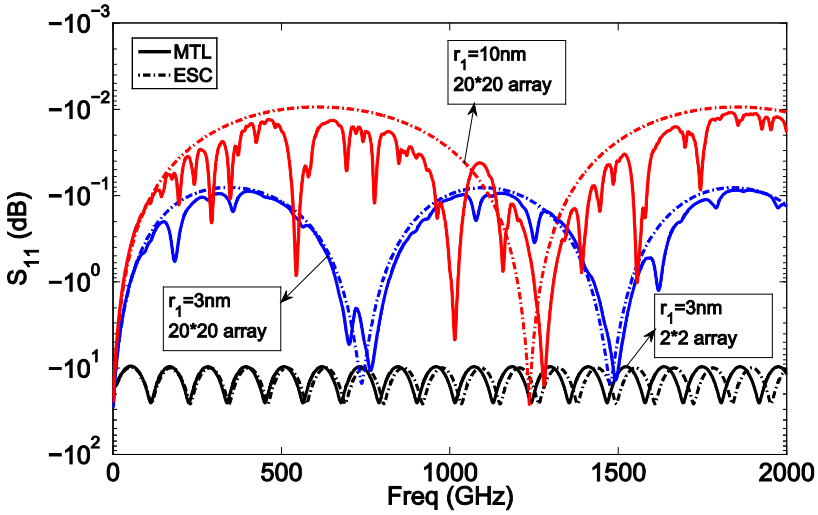

(a)

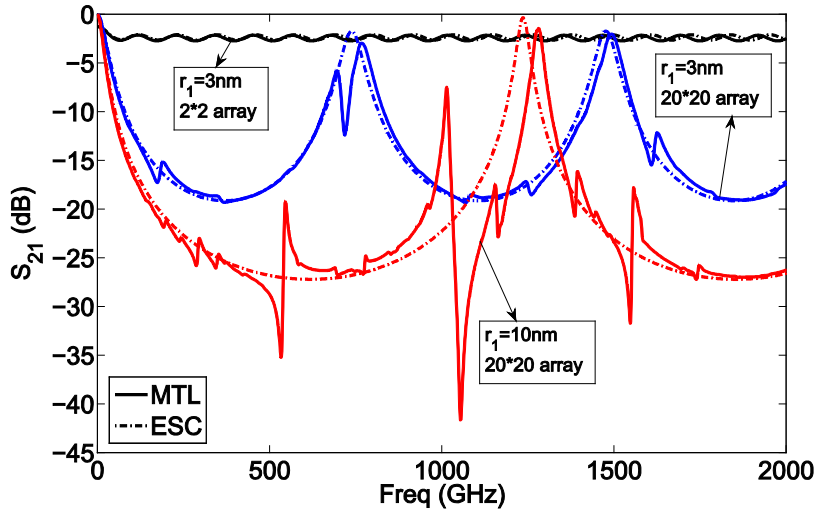

(b)

Figure 3.18 Simulated S11 (a) and S21 (b) of three MWCNT arrays with different CNT radii and array sizes using MTL (solid) and ESC (dashed) models.

3.7 Summary

In this chapter, the transmission line model in both single- and multi-conductor configurations are investigated and the equivalent circuit model for a SWCNT is studied. From the equivalent circuit model, a general technique to analyze an arbitrary CNT arrays is proposed to calculate the S-matrix from the multi-conductor transmission line (MTL) model. The proposed technique takes into account all the effect of mutual coupling and presents the analytical solution of the 2-port S-matrix of complex CNT arrays directly from the 2n-port network equations. The simulated S-parameters from low GHz to THz are compared with previous ESC models and the results that due to the neglecting of mutual coupling components , the ESC model is no longer accurate for large arrays or small arrays from sub-THz. can be used as guidelines for future analysis of CNT based interconnects, antennas and absorbers.

Chapter 4 Characterization of the Vertically Aligned Multi-Wall CNT arrays

In chapter 3, an analytical technique to extract the 2 port S-parameters from an arbitrary VACNT array is proposed. This chapter focuses on the characterization of both SWCNT and MWCNT arrays under different temperature, host medium, and cross section.

4.1 Input impedance

The input impedance is one of the important characteristics of CNT arrays. Although it has been studied using the ESC modelling [126], we focus on the comparison of input impedance with MTL modelling. Furthermore, the published results assume air as host medium and room temperature, here we also compare the results under different host medium and temperature.

With the conclusion in chapter 3, it is straight forward to model an MWCNT array. First replace the MWCNT's MTL model to the effective SWCNT model, and the MWCNT array is the same as a SWCNT array, the S-parameters of which can be calculated using the same techniques described in chapter 3.

First of all, the proposed model is applied to the simulation of the propagation characteristics of a horizontal MWCNT. The external shell of the nanotube is located at the distance d=100nm from the perfect conducting ground plane, with radius of the inner-most shell r_1=0.5nm and that of the outer-most radius depending on the number of shells n. The calculation is performed assuming

that the MWCNT is excited in common mode by an ideal sinusoidal voltage source with an RMS value 0.01V from 100MHz to 100GHz. The CNT transmission line is terminated with the load impedance Z_L in common mode configuration.

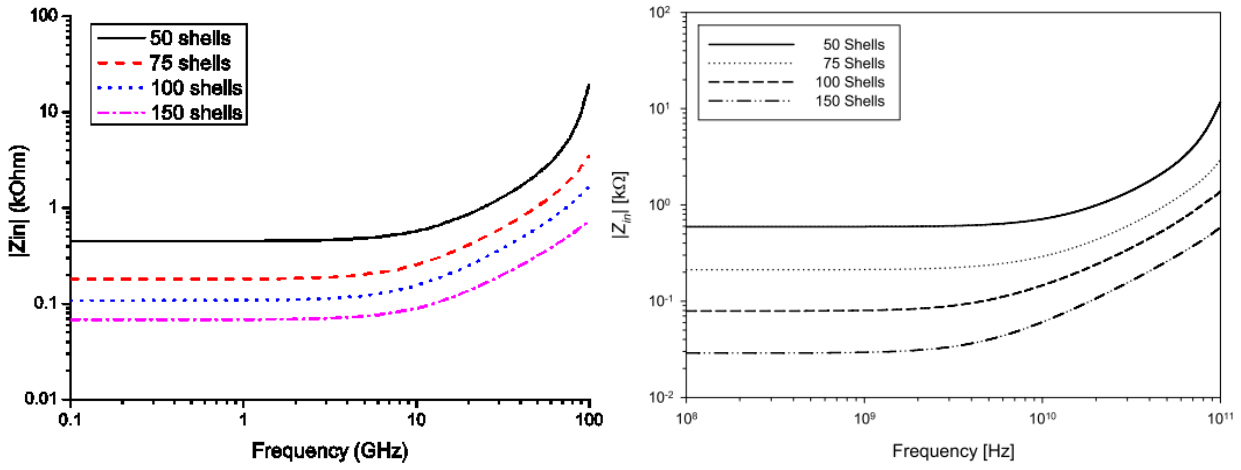

(a) (b)

Figure 4.1 amplitude of input impedance of a single MWCNT of 50, 75, 100 and 150 shells above ground plane, (a) is our simulation and (b) is from published paper [153].

Figure 4.1(a) and (b) show the frequency spectra of the input impedance Z_{in} of the MWCNT, computed in short-circuit terminal configurations ($Z_L = 0$) with permittivity of host medium set as 1. The length of the line is 50μm, and the number of shells are 50, 75, 100 and 150, respectively. From the result one can see that firstly, the magnitude of the input impedance increases with frequency and decreases as the number of shells n increases. The result matches very well with previously published results [153].

With the validation of the extraction technique in Figure 4.1, one can simulate an array of MWCNTs at a wider frequency range. Figure 4.2 shows the real and imaginary part of the input impedance of a 20μm long 2×2 MWCNT array under different temperature and host permittivity. The array is comprised of MWCNTs with $r_1 = 3nm$ and 9 shells. The reference impedance z_0 is set as 50Ω.

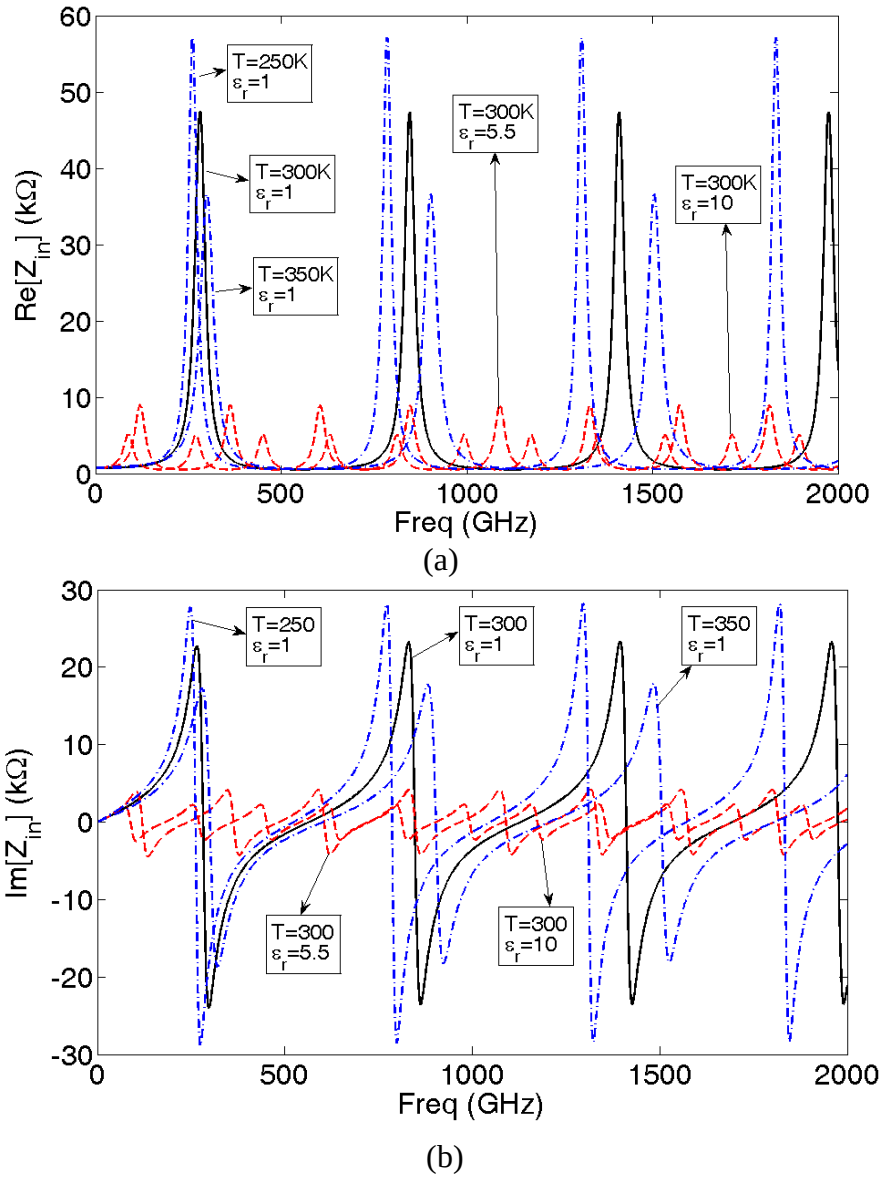

Figure 4.2. Real (a) and imaginary (b) part of the input impedance of MWCNT arrays in host medium with different permittivity and temperature.

Clearly, both the real and imaginary part of the input impedance changes periodically with frequency. Within each period, the Im[Z_{in}] has two zero points, where the real part reaches the minimum and maximum values , respectively. This result suggests multiple applications. At the frequency points where Re[Z_{in}] is the minimum, the CNT array can be used for antenna applications for low loss and easy of matching, while at frequency points where Re[Z_{in}] is

maximum, the CNT array is suitable for the application of nano-cables connecting devices such as THz photomixers, which typically have a high output impedance.

The change of permittivity changes the periodicity of the array, and the peak magnitude as well. The number of resonant peaks increases with the increase of the permittivity. This can be used to pull down the working frequency of CNT devices. From the case of $\varepsilon_r = 1,\ 5$ and 10 it is evident that increasing the host medium's permittivity reduces the peak magnitude of the input impedance of the MWCNT array significantly. In comparison, the temperature change has the similar effects. From 250K to 350K, the temperature increase causes the peak magnitude of the input impedance to decrease. But the scale is much smaller, especially the change in periodicity. This shows that by embedding the CNT in appropriate host medium, the input impedance can have large tunable ranges and the heat generated will further reduce the impedance, increasing the overall efficiency.

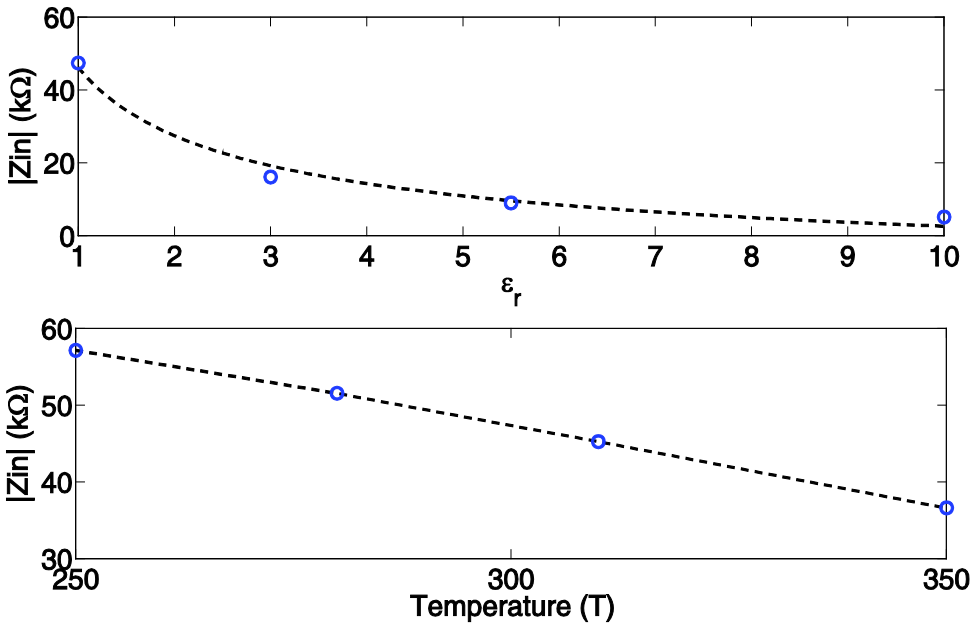

Figure 4.3. Different tenability curve of input impedance. The upper shows its relationship with permittivity and the lower shows that with temperature.

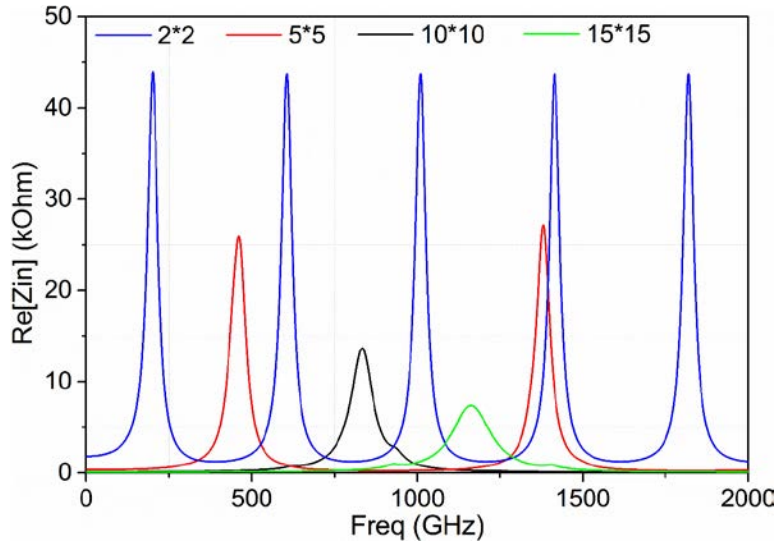

(a)

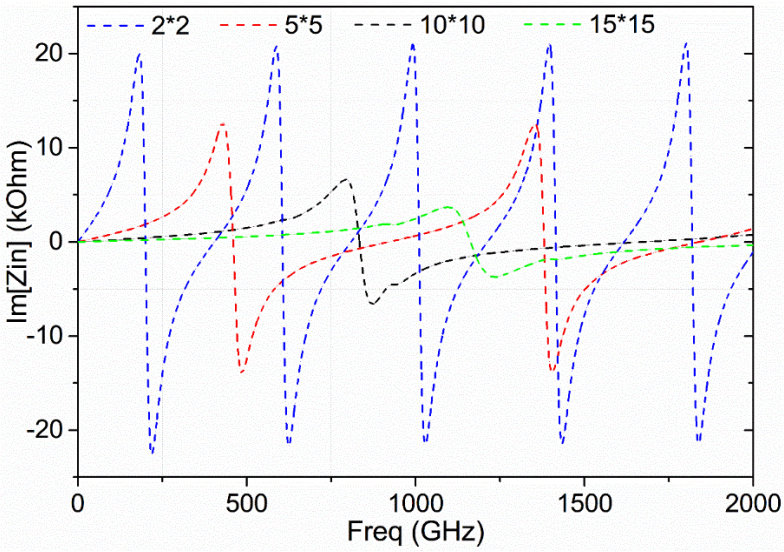

(b)

Figure 4.4. Real (solid) and imaginary (dashed) part of an MWCNT array's input impedance with array size.

Furthermore, Figure 4.3 shows the relationship between $|Z_{in}|$ and different permittivity and temperature. One can see that the $|Z_{in}|$-ε_r relationship can be well fitted by a square root function, as the wave impedance $\eta \propto \frac{1}{\sqrt{\varepsilon_r}}$. This indicates that the area with largest tunability is the one

closest to $\varepsilon_r = 1$ and with the increase of permittivity the tunable range will decrease rapidly. On the other hand, the $|Z_{in}|$ ~T relationship is linear, which suggests that the tuning through temperature is more controllable. However, the working temperature for electronic devices are mostly above 250K and below 400K, the tunable range through temperature is limited.

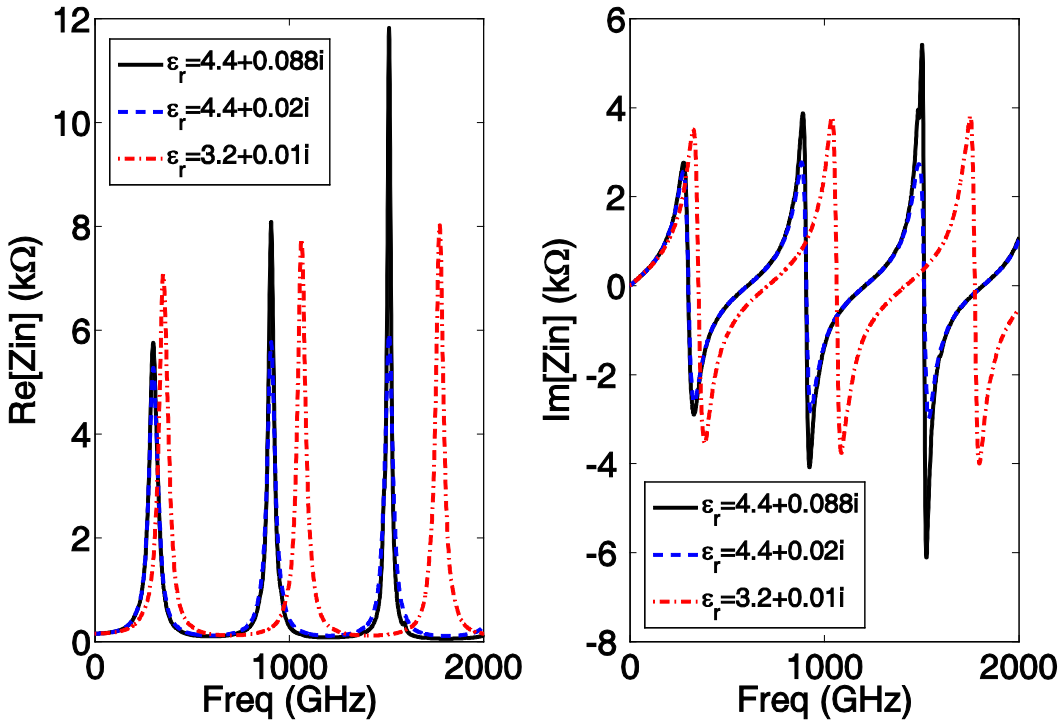

Figure 4.5 Input impedance for a 5x5 MWCNT array in 3 different lossy medium, (a) is the real part and (b) is the imaginary part.

In the above analysis the input impedance for a fixed MWCNT array in different host medium and temperature is present. Similarly, the input impedance of different MWCNT arrays with various sizes are also compared. We simulated four MWCNT arrays comprising 2x2 5x5, 10x10 and 15x15 CNTs, respectively. The CNT radius and array lengths are the same with the previous case. The real and imaginary part of the input impedance in Figure 4.4 shows that increasing the number of CNTs has a similar effect on the input impedance with increasing permittivity and temperature. This is understandable as increasing the number of CNTs connected in parallel leads to the increasing of total number of conductive channels, thus decreasing the total input impedance.

In previous analysis the host medium are set as lossless, which is not so in reality. So a general case where MWCNT arrays are fixed in lossy medium is also discussed. We simulate an array with 5x5 CNTs and host them in the medium with permittivity $\varepsilon_r = 4.4 + 0.088i$ (FR4 epoxy), $\varepsilon_r = 4.4 + 0.02i$ and $\varepsilon_r = 3.2 + 0.01i$ (polyester), respectively.

First of all, for the medium with the same real part, the resonant periodicities are exactly the same, which means the resonant frequency is independent on the imaginary part of the permittivity. Second, with the presence of the imaginary part, the peak magnitude of both the real and the imaginary part of the input impedance increase over the frequency. The larger the loss tangent, the larger this increase of the impedance is.

4.2 Network parameters and absorption

4.2.1 ABCD and impedance matrix

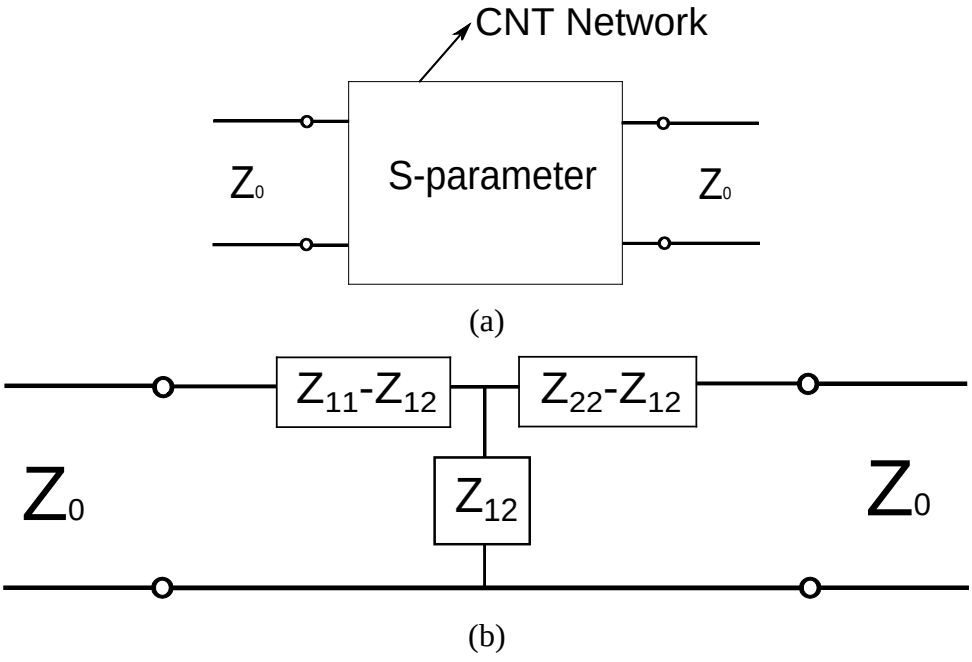

Figure 4.6 (a) The CNT network as a black box, only 2-port characteristics need to be considered, (b) the effective T-shaped effective network

In Chapter 3, the technique to extract the 2-port S-parameters from the MWCNT array is presented. This technique enables us to regard the entire MWCNT network as a black box and only consider its 2-port characteristics, as shown in Figure 4.6(a). In this section, we are going to further explore all other network parameters, which are convertible from each other, and finally, discuss the absorption properties of the array.

The ABCD matrix can be obtained from the S-parameter as

$$\begin{bmatrix} A & B \\ C & D \end{bmatrix} = \frac{1}{2S_{21}} \begin{bmatrix} (1+S_{11})(1-S_{22})+S_{12}S_{21} & Z_0(1+S_{11})(1+S_{22})-S_{12}S_{21} \\ \frac{1}{Z_0}\left((1-S_{11})(1-S_{22})-S_{12}S_{21}\right) & (1-S_{11})(1+S_{22})+S_{12}S_{21} \end{bmatrix} \quad (4.1)$$

and the impedance matrix **Z** can be obtained from ABCD matrix as

$$\mathbf{Z} = \begin{bmatrix} Z_{11} & Z_{12} \\ Z_{21} & Z_{22} \end{bmatrix} = \frac{1}{C} \begin{bmatrix} A & AD-BC \\ 1 & D \end{bmatrix}. \quad (4.2)$$

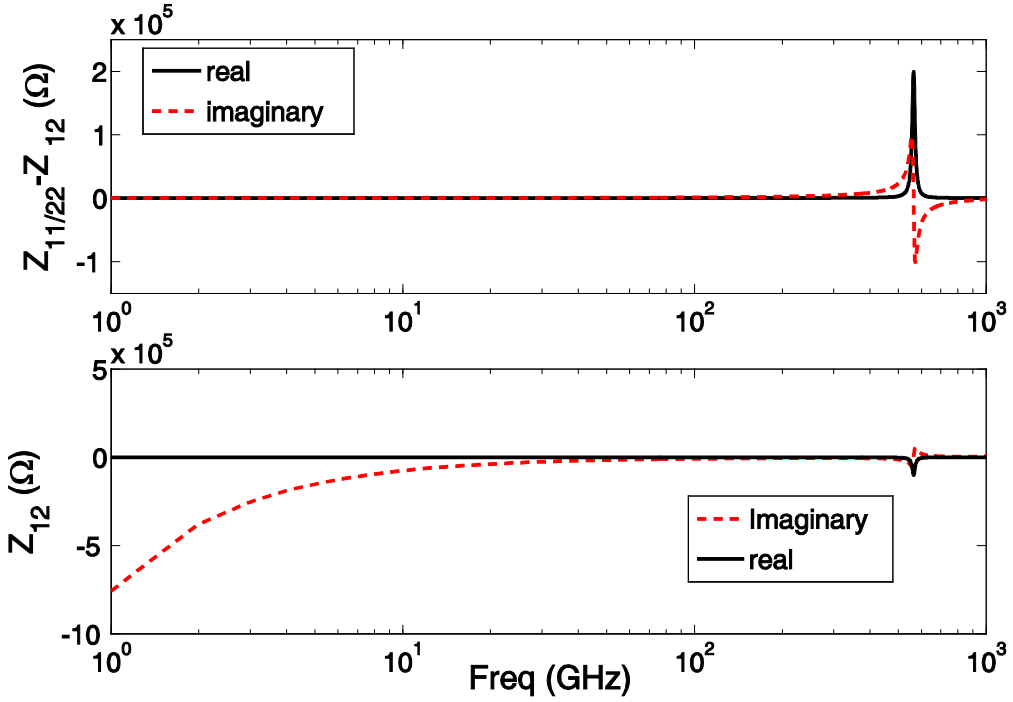

Figure 4.7 Impedance components of the effective T-shaped network.

Since the network is reciprocal, (4.1) and (4.2) can be further simplified by substitute S_{12} with S_{21} and S_{22} with S_{11}.

Figure 4.6(b) shows the effective T-shaped network of the CNT network with the same geometry as before and the host medium of air. The corresponding impedance components are plotted in Figure 4.7.

It appears that all the real part of the impedance are very low up to 500GHz. The imaginary part for the impedance components of $Z_{11} - Z_{12}$ changes simultaneously with the real part and follows a similar trend with the total input impedance, while the imaginary part for Z_{12} shows very strong capacitive behaviour at low frequencies.

4.2.2 Absorption

It has been widely reported that CNTs are lossy, and due to the 'slow wave' effect one of their most promising applications is probably the wide band ultra-thin absorbers. So it's good to use the MTL model to do an estimation of their absorbing capabilities.

With the S-parameters calculated, the absorption of the CNT can be calculated using

$$absoption = 1 - |S_{11}|^2 - |S21|^2 \qquad (4.3)$$

As the absorption in (4.3) is a function of both S11 and S21, it will change according to different reference impedances z_0. Different CNT arrays will also have different reflections so it is difficult to compare directly the absorption of different CNT arrays. In order to get the relationship between total power that flows into the CNT and the proportion of the power absorbed during this process, the absorption is normalized to the total transmission and the reflection, i.e. S11 is calibrated out.

$$normalized\ \ absorption = \frac{absorption}{1 - |S_{11}|^2}. \qquad (4.4)$$

In this way, the Next sections will discuss the influence on different parameters of the CNT array, e.g. number of shells, size of the array, length, etc.

a) The influence of number of shells on absorption

Two groups of a single MWCNT is simulated in this case. The first group has a fixed outer radius of 6nm and the inner radius changes from 1nm to 3nm. The second group has a fixed outer radius of 20nm and the inner radius changes from 2nm to 10nm.

The absorption and normalized absorption are shown in Figure 4.8, from which one can find that due to the resonances of S-parameters as shown in Chapter 3, the absorption itself also resonates periodically across the wide frequency range and there is no comparable relationship between any of the two CNTs. However, the normalized absorption clearly shows that first of all, the CNTs with a larger outer radius have much lower absorption than the ones with a smaller outer radius, also, for CNTs with a same outer radius, the one with a smaller inner radius has lower absorption.

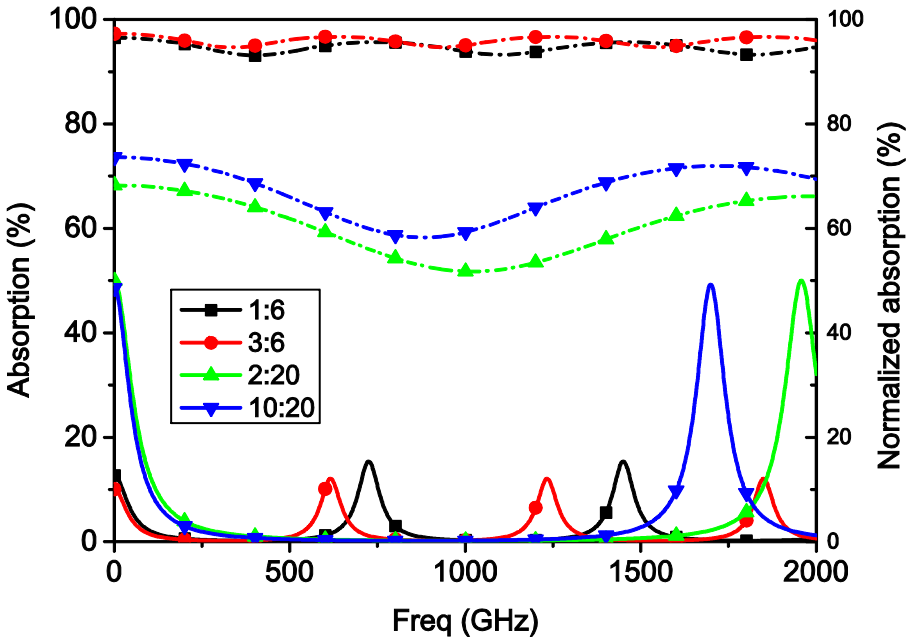

Figure 4.8. Absorption and normalized absorption for two different groups of CNTs. One group has a fixed outer radius of 6nm and the other has a fixed outer radius of 20nm, while the inner radii change.

This result is understandable. The absorption, i.e. loss is achieved by the per unit length resistance in a CNT. The shells in the MWCNT are connect in parallel in the common mode excitation and the more shells there are, the less the total per unit length resistance, thus less absorption.

b) The influence of number of CNTs on absorption

Four SWCNT arrays with the number of CNTs inside them being 2x2, 4x4, 8x8, and 16x16 are simulated. The radius of the SWCNT is 5nm and the length of the array is 10μm. Other parameters remain the same as before.

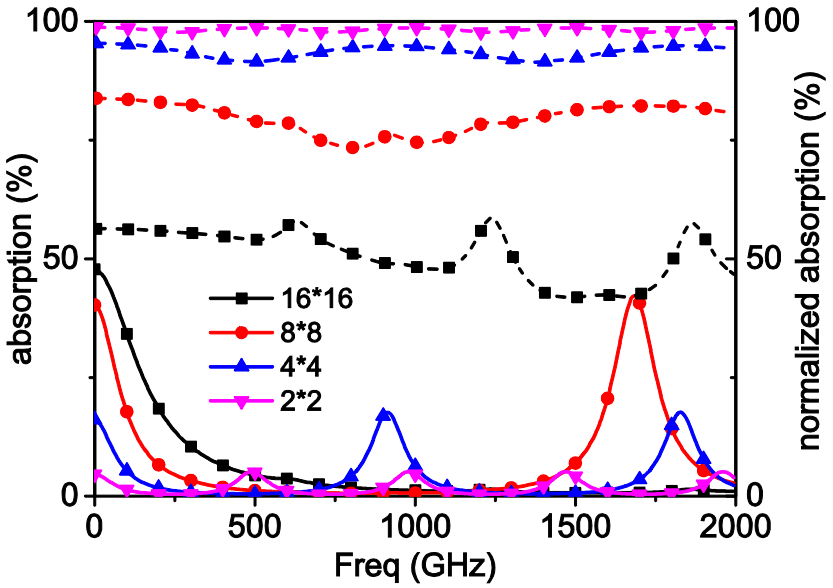

Figure 4.9 . Absorption and normalized absorption for two different groups of CNTs. One group has a fixed outer radius of 6nm and the other has a fixed outer radius of 20nm, while the inner radii change.

The result in Figure 4.9 shows that the larger the array is, the smaller the absorption, for the same reason as explained in section a). This also means that the efficiency of CNT devices such as interconnect or antenna can be improved by replacing stand-alone CNT with arrays. As the number of CNTs in the array can be increased much easier than increasing the number of shells in the CNT since the process of CVD synthesis is largely uncontrollable. In this case, it is much more

applicable to use CNT bundles to increase the efficiency and decrease absorption than to synthesize large-diameter CNTs.

c) Influence of length on absorption

Three arrays comprised of 8x8 CNTs and lengths of 10µm, 20µm and 30µm, respectively are simulated. The result is shown in Figure 4.10.

It appears that the peak magnitude of the absorption increases with the increase of the lengths and the 30µm array has the highest peak absorption. However, due to the difference in resonant frequencies, the normalized absorption of a 30µm array is not always higher than that of a 10µm array. Nevertheless, in lower frequencies (up to 300GHz), the normalized absorption of a longer array is always higher than a shorter array.

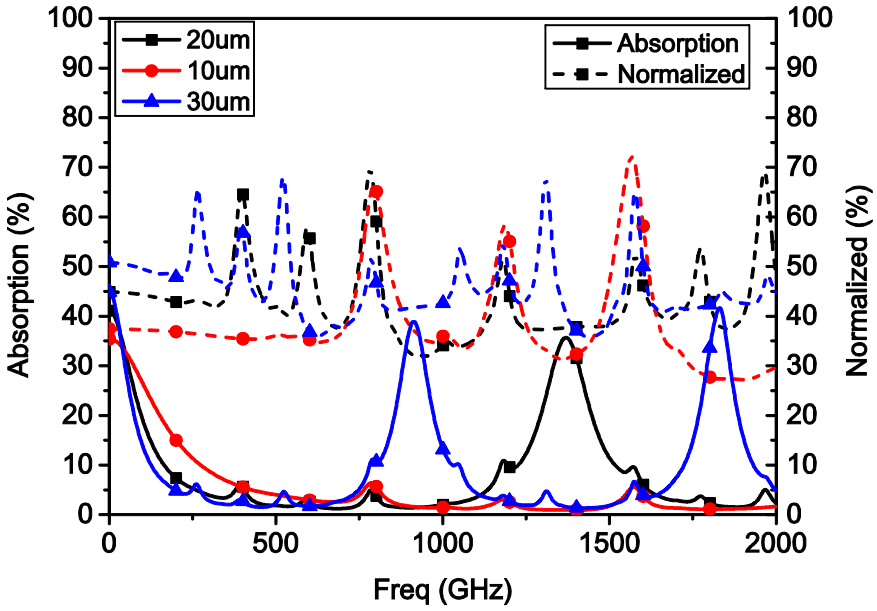

Figure 4.10. Absorption and normalized absorption of three 8x8 MWCNT arrays with different length.

d) Influence of CNT concentration on absorption

Finally, three arrays comprised of 8x8 CNTs length of 20µm with different concentration, i.e. distance between neighbouring CNTs are simulated. In Chapter3, it has been mentioned that a

typical distance between neighbouring CNTs are 100nm and in this part, the distance are 50nm, 100nm, 200nm, respectively. From the result in Figure 4.11, one can find that in microwave frequencies, the absorption for different concentration are almost identical. At higher frequencies such as THz, the peak magnitude of the absorption remains the same, but shifts in frequency. The normalized absorption for a densely packed CNT array is lower than a loosely packed CNT array.

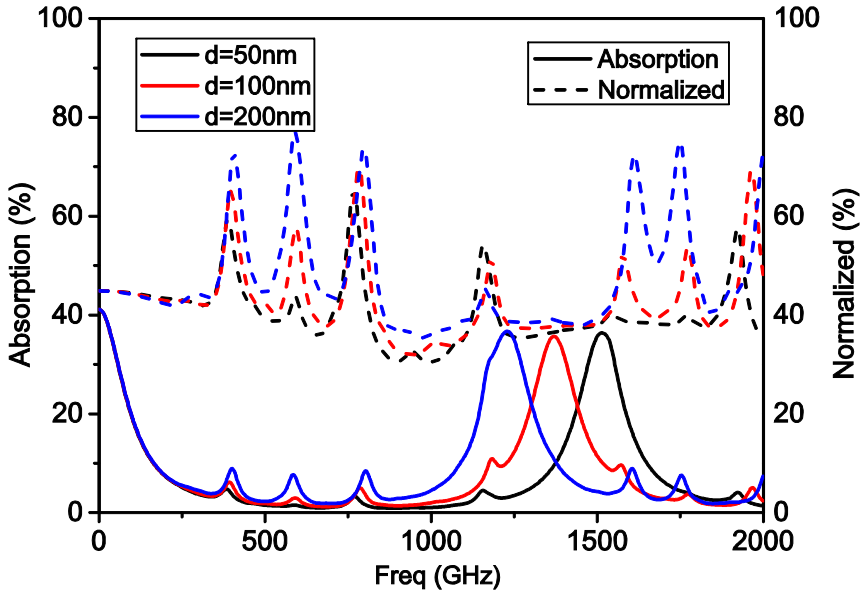

Figure 4.11. Absorption and normalized absorption of three 8x8 MWCNT arrays with different concentration

With the influence of all parameters of a CNT array on its absorption discussed, the general case where the CNT array is fixed in a lossy medium with different temperature is studied. The CNT array being simulated is comprised of 2x2 CNTs. The inner radius is 3nm and number of shells is 9. The host medium is FR4 epoxy with $\varepsilon_r = 4.4 + 0.088i$ and the length of the array is 10μm.

The simulation results in Figure 4.12 shows that compared to the S-parameters in Chapter 3, one can see that lossy materials will increase the magnitude of each resonant peak of the S21 and decrease that of S11. As a result, the absorption also increases in magnitude as the frequency goes higher. However, the normalized absorption shows that the absorption capability of the array actually decreases with the increase of frequency. This suggests that for arrays in lossy medium,

the better working frequency band for the CNT array is in higher frequencies.

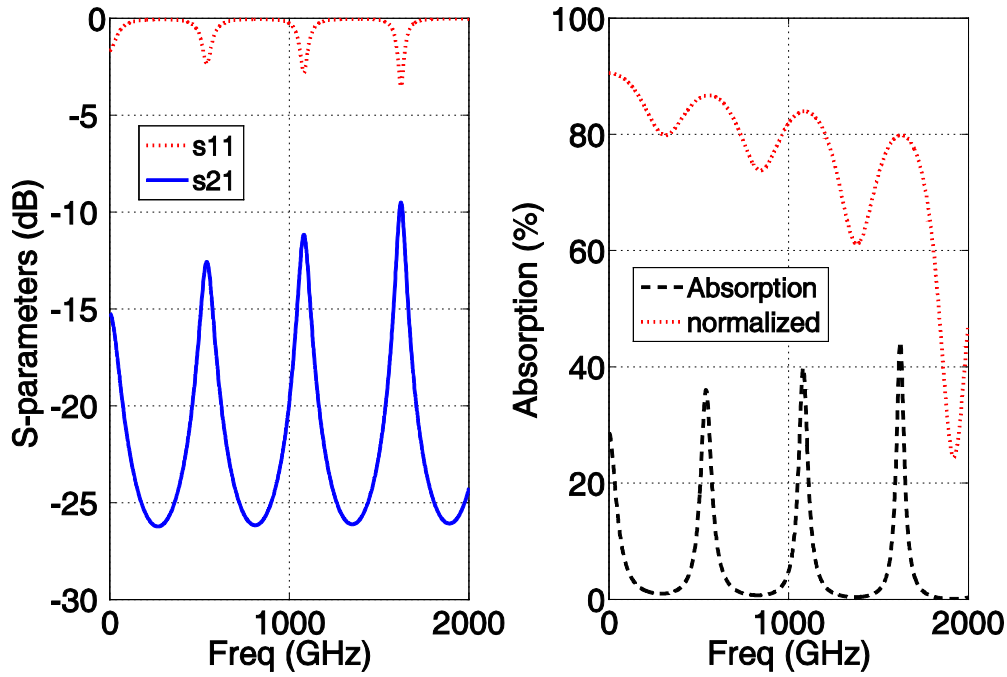

Figure 4.12 S-parameters and absorption for a MWCNT array in lossy medium

4.3 MWCNT arrays with arbitrary cross section

In previously analysis, a square cross section of the MWCNT array is always assumed, which is not the case in reality. Especially, different applications usually require MWCNT arrays with a different aspect ratio. In order to influence of different cross sections on the network parameters and absorption, a total of 1225 MWCNTs with aspect ratio of 1 (square cross section), 25 (rectangular cross section with 7 layers and 175 CNTs each layer), 49 (rectangular cross section with 5 layers and 245 CNTs each layer) and 12250 (rectangular cross section with 1 layer and 1225 CNTs each layer) are simulated, respectively. For comparison, a CNT array with a triangular cross section and a same number of CNTs (49 layers in total) are also simulated.

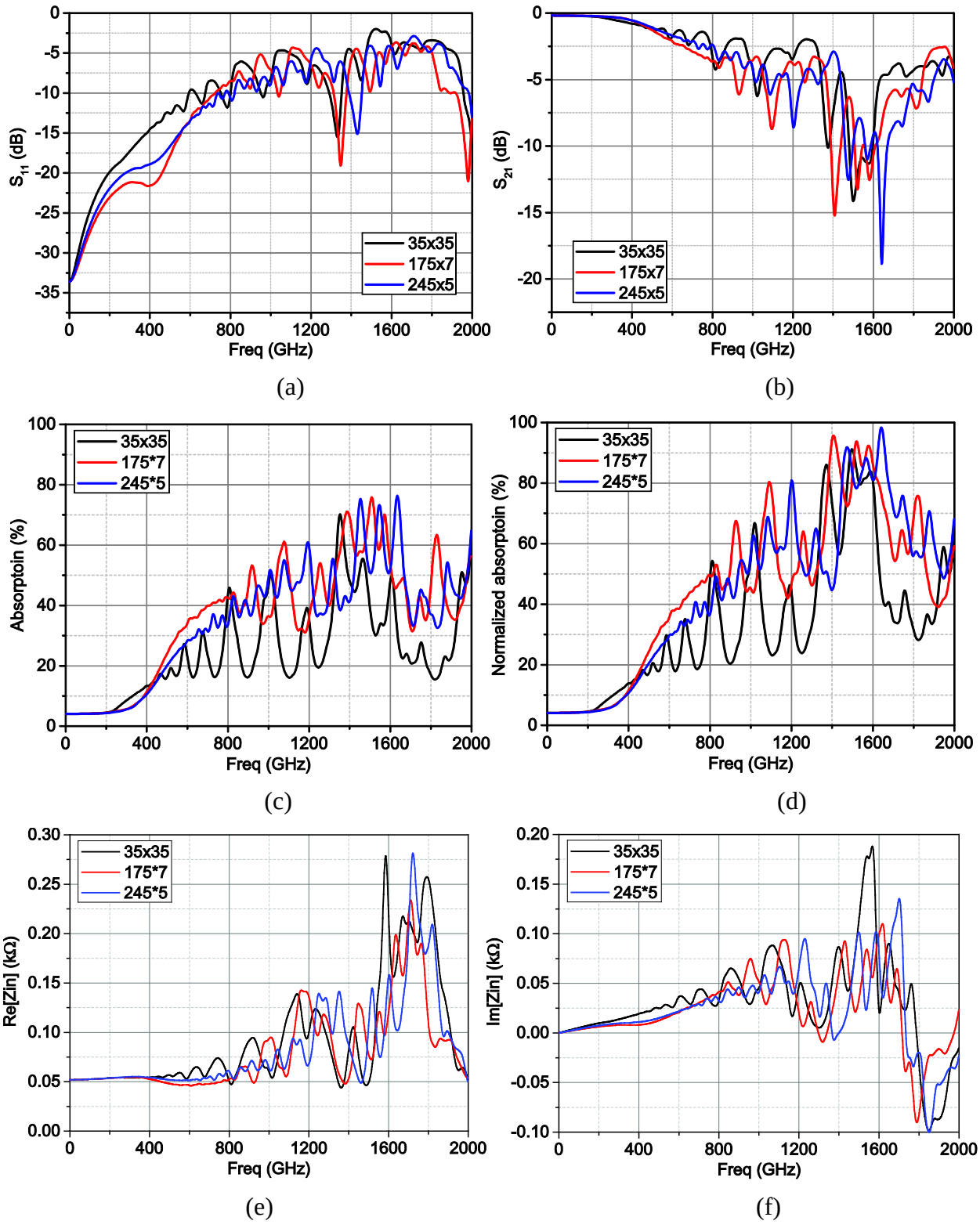

Figure 4.13. Simulated (a) S11, (b) S21, (c) absorption, (d) normalized absorption, (e) real part of the input impedance and (f) imaginary part of the input impedance of a total number of 1225 CNTs with a rectangular cross section of different aspect ratio.

4.3.1 Rectangular cross section

The S-parameter, input impedance, absorption and normalized absorption of the CNT arrays with the aspect ratio of 1, 25, and 49 are shown in Figure 4.13. For a large array like this, the S-parameters are no longer periodic in the simulated frequency, instead, it shows a series of small resonances at high frequencies with no clear periodicity, due to the increasingly large total coupling in the array.

However, the absorption and normalized absorption are almost identical for all three arrays up to 200GHz, which means at microwave and millimetre wave frequencies, changing the aspect ratio of very large arrays does not have a significant impact on the absorption.

The real part of the input impedance shows that by employing large arrays, the high intrinsic impedance of CNT of $h/2e^2$=12.9kΩ can be reduced to several hundred Ohms and at low frequencies very close to 50Ω, which is the characteristic impedance of the coaxial transmission line. However, the imaginary part of the input impedance does not have any zeroes at microwave and millimetre wave frequencies, which limits its application as antennas in such frequencies. On the other hand, the first zero point in Im[Z_{in}] appears at 1.3THz, with the corresponding aspect ratio being 25, where the corresponding Re[Z_{in}] is still very close to 50 Ω. Note that the first zero point appears at 1.8THz for the square cross section and 1.4THz for the aspect ratio of 49, suggesting that first, a large array can be very promising in THz antenna applications and second, the smaller aspect ratio is, the lower frequency the first zero point in the imaginary part of the input impedance is.

4.3.2 Triangular cross section

The S-parameter, input impedance, absorption and normalized absorption of the CNT arrays with a triangular cross section are shown in Figure 4.14, in comparison of the array with rectangular cross section. The result are similar to the case of cross section, especially the aspect ratio of 25. Similar to the rectangular cross section case, the absorption and normalized absorption are almost identical up to 200GHz, but from 200GHz to 700GHz the absorption of the triangular cross section are always higher than that of the square cross section.

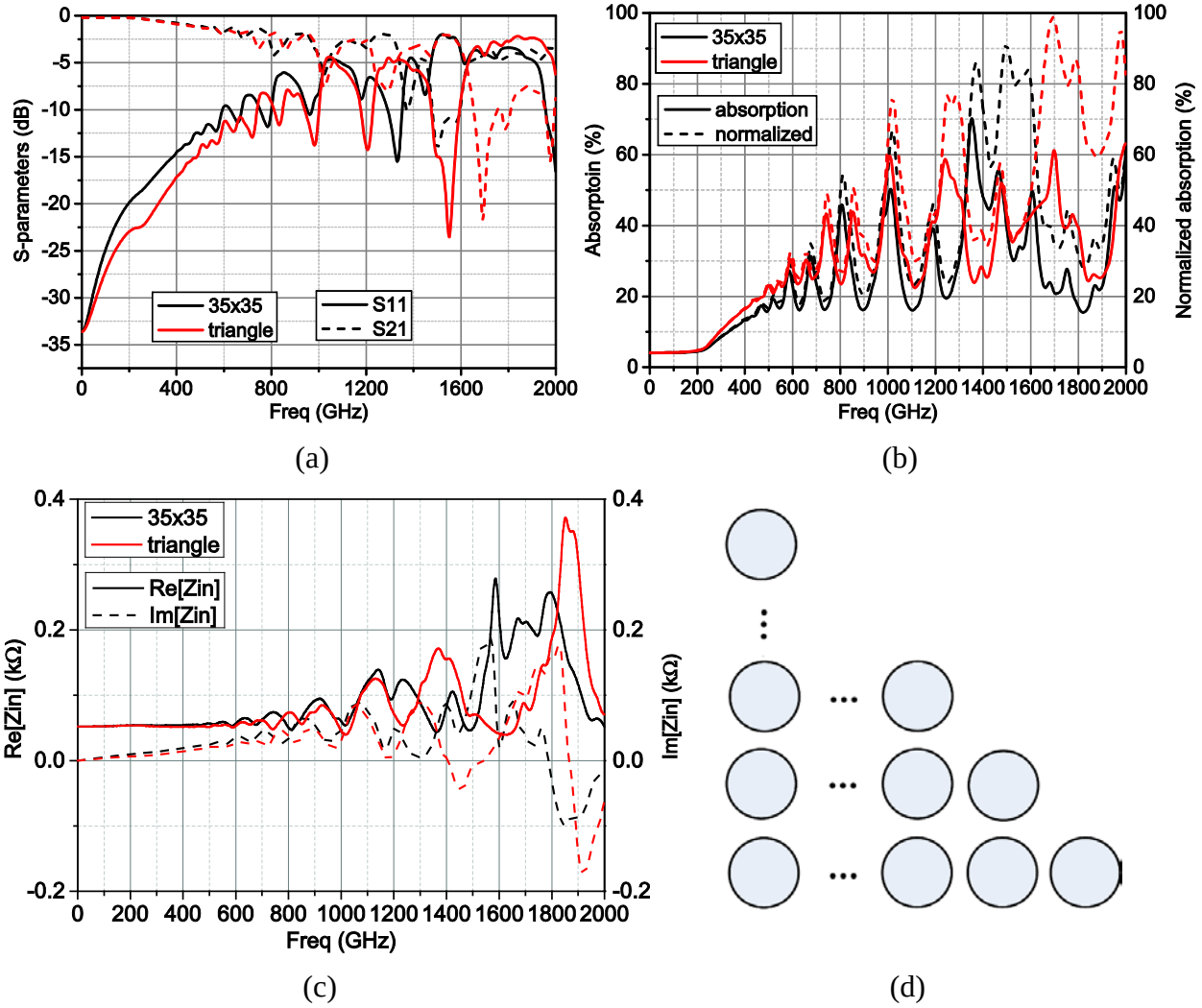

(a) (b)

(c) (d)

Figure 4.14. Simulated (a) S-parameters, (b) absorption and normalized absorption, (c) input impedance and (d) geometry of the cross section of a total number of 1225 CNTs with a triangular cross section in comparison to the square cross section array.

4.3.3 Rectangular cross section with aspect ratio of 1225:1

Finally, the special case where there is only 1 layer of 1225 CNTs is simulated and compared to the square cross section case in Figure 4.15. Previously results in Figure 4.13 shows that the larger the aspect ratio, the lower the S11, however the single layer case shows the largest S11 in all cross sections simulated. As a result, the normalized absorption start to deviant from the absorption at 400GHz, which is the lowest of all cases. The normalized absorption increases linearly with

frequency from 400GHz to 1200GHz and does not have multiple absorption peaks in this frequency, which is different from all other cases. Similarly, the S-parameter and input impedance also shows the smoothest curves from 1GHz to 1200GHz, without any resonant peaks.

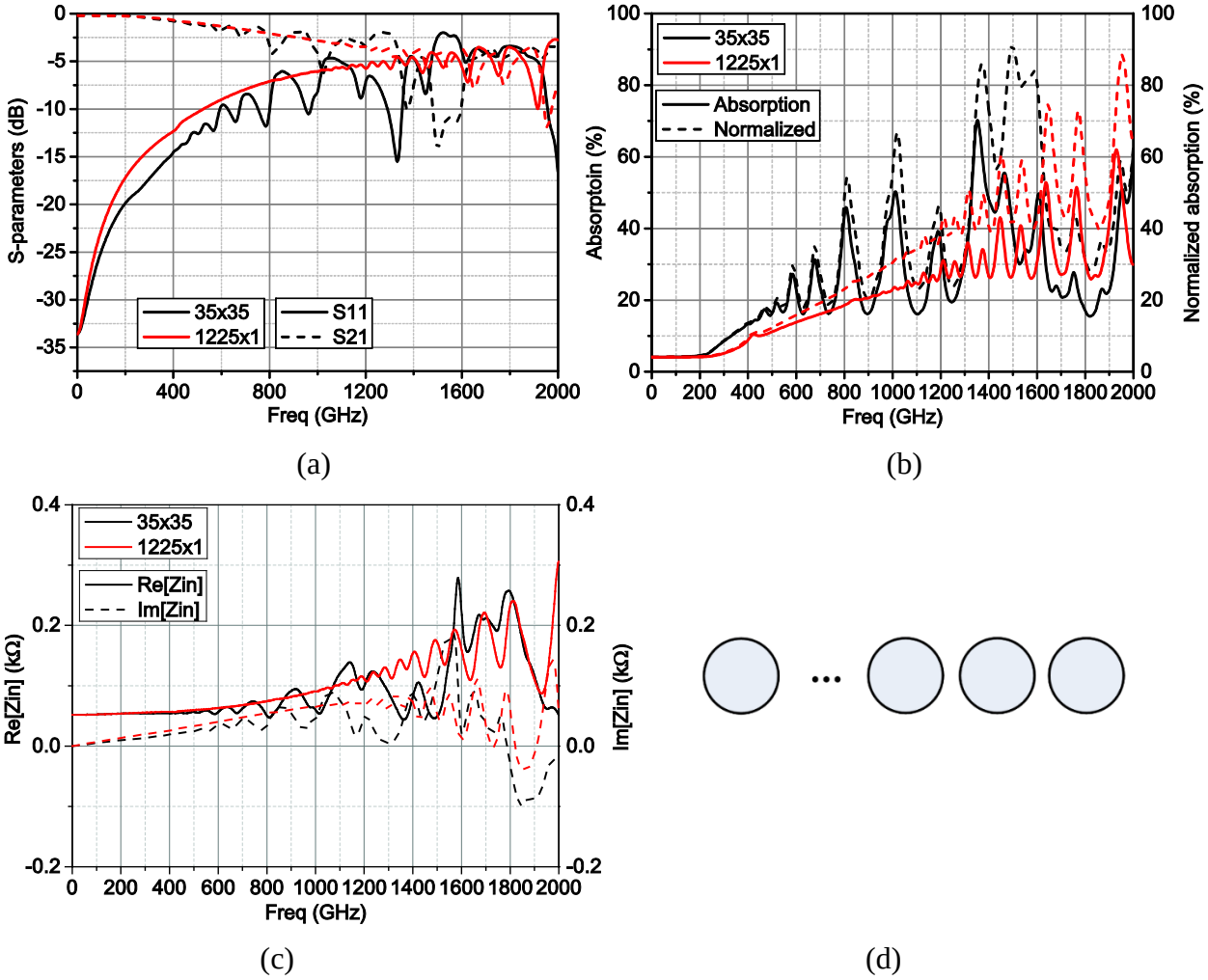

Figure 4.15. Simulated (a) S-parameters, (b) absorption and normalized absorption, (c) input impedance and (d) geometry of the cross section of a single layer of 1225 CNTs with the aspect ratio of 1225, in comparison to the square cross section array.

4.4 Wave propagating velocity inside the CNT array.

It has been reported that due to the large kinetic inductance, the wave propagating velocity in a CNT is $v = \sqrt{L_k C_q} \approx 8.0 \times 10^5$ m/s , as mentioned in Chapter 3. To further study this conclusion, the wave velocities is calculated from the Fabry-Perot resonance (F-P resonance) for a series of CNT arrays with different sizes.

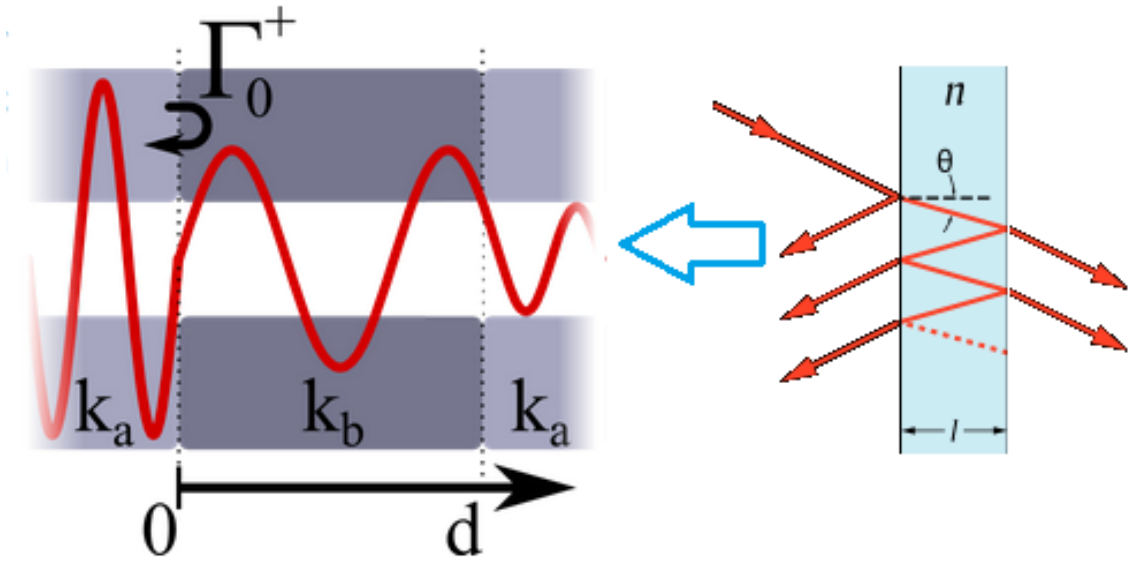

Figure 4.16. Illustration of the Fabry-Perot resonance caused by inserting a different media into another, creating a cavity in which wave can reflect multiple times.

The periodical change of both input impedance and absorption is the result of typical Fabry-Perot resonance. The Fabry-Perot resonance is caused by the insertion of a media into another with a different wave number, as shown in Figure 4.16. The transmission line theory has stated that the wave propagates inside such a structure will have multiple reflections at the boundary of the two different medium, forming standing waves, as observed in the simulation results in Figure 4.3 and Figure 4.

The Fabry-Perot resonance is controlled by the length of the MWCNT array and for a fixed length array, the wave propagation velocity can be obtained from the Fabry-Perot resonance condition.

$$\lambda = 2 \cdot L / n, \qquad n = 1, 2, \ldots \tag{4.5}$$

where l is the length of CNTs and λ is the wavelength. As λ =v/f the wave velocity can be calculated as

$$v = \Delta f \cdot 2L \tag{4.6}$$

where Δf is the frequency gap between each 2 neighboring peaks in Zin.

Four different MWCNTs with r_1 of 2.5nm, 3nm, 4nm and 5nm and 8, 27, 48 and 16 shells are simulated respectively with different array sizes and the result is shown in Table 1, in which the last column is the total number of conducting channels in a single MWCNT.

Table 4.1 Wave propagating velocity for MWCNT arrays

Inner radius	**v/c for different array sizes**				$\sum N$
	1x1	**2x2**	**5x5**	**10x10**	
2.5	0.036	0.066	0.152	0.274	8.455
5	0.062	0.115	0.247	0.425	31.250
3	0.082	0.151	0.322	0.527	51.919
4	0.128	0.233	0.477	0.702	143.236

From Table 1, one can see that the wave velocity for a single MWCNT is in the same order of that in a metallic SWCNT, which is Fermi velocity. For the same MWCNT, the larger the array size, the larger the wave velocity. Clearly, increasing the total number of conducting channels causes an increase in wave velocities. Figure 4.17 shows the wave velocities for 6 MWCNT arrays with a square cross section and different number of CNTs, respectively. Clearly, the wave velocity does not increase linearly with the increase of the array size. Instead, it follows a power function and slowly converges to 1, when the array size becomes infinite. In this way, the data can be fitted with a power function $y(m)=a+b\cdot(m+c)^d$ where $y(m)$ is the ratio of the wave velocity and the speed of

light in free space, m is the number of CNTs in the array and a, b, c and d are constants. Consider the boundary conditions $\lim_{m\to 0} v(m) = 0$ and $\lim_{m\to \infty} v(m) = c$ the constants can be simplified as

$$y(\mathrm{m}) = 1 - \mathrm{a}^{-b} \cdot (m + a)^{b} \qquad (4.7)$$

For example, for arrays with r_1 of 2.5nm, a=5.65 and b=-0.10.The fitted curves (solid line) fit very well with simulated velocities, which are represented by discrete dots.

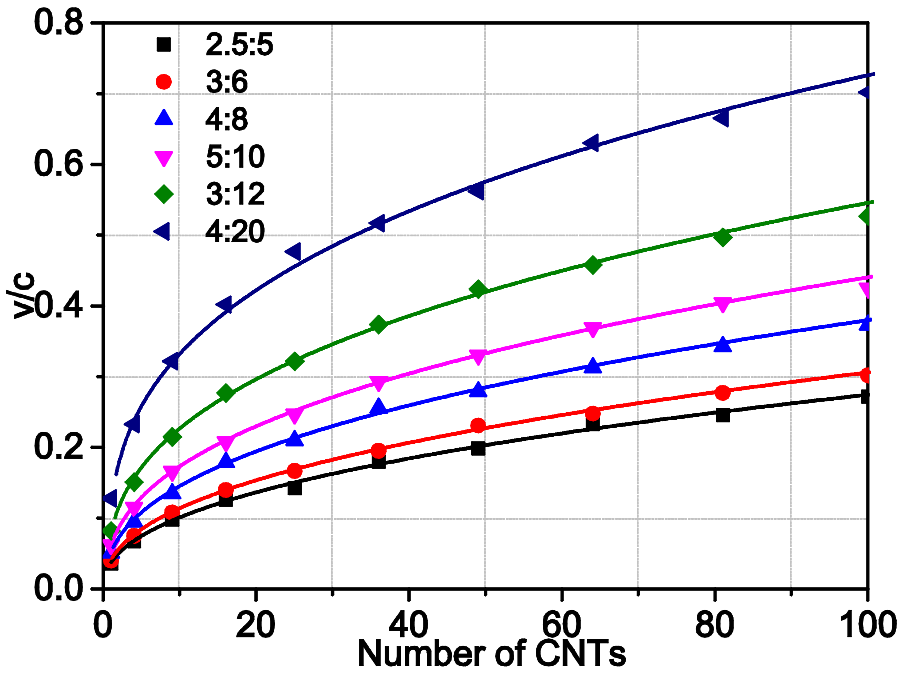

Figure 4.17. Wave propagation velocity versus the number of CNTs for six CNT arrays comprised of MWCNT with different radius and number of shells. Discrete dots are the simulated data and solid lines are fitted curve from a power function.

4.5 Measurement of CVD synthesized VACNT samples

4.5.1 Fabrication process

Plasma Enhanced Chemical Vapor Deposition (PECVD) is an excellent alternative for depositing a variety of thin films at lower temperatures compared to those of CVD reactors. For example,

high quality silicon dioxide films can be deposited at 300ºC to 350ºC compared to CVD which requires temperatures in the range of 650 to 850 degrees centigrade to produce similar quality films.

All the samples of the vertically aligned multi-walled carbon nanotube films were fabricated at the Center for Advance Photonics and Electronics at Cambridge University (CAPE). They are based on an n-type doped single crystal silicon wafer, with dimensions of 42mm x 50mm. Fe catalyst and Al diffusion barrier thin films were deposited onto silicon substrates by sputter coating, to prevent the formation of $FeSi_x$. The thickness of the silicon wafer is 510μm and the resistivity is expected to be 0.015-0.025 $\Omega \cdot cm$. Upon annealing with H2 for 3mins, the Fe thin film breaks up into nanoparticles which seed the further growth of the nanotubes.

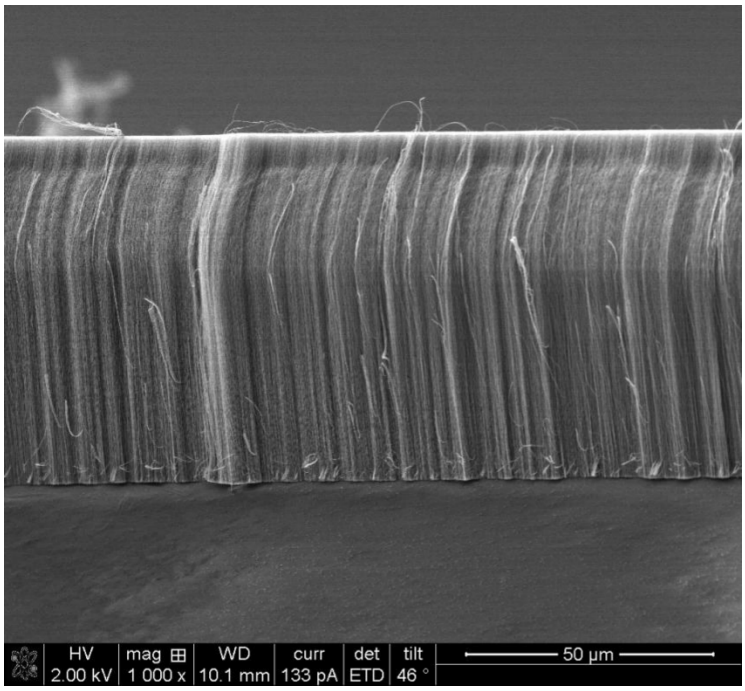

Figure 4.18. SEM image of the vertically aligned vertically aligned MWCNT film [154]

PECVD uses electrical energy to generate plasma to which the energy is transferred into a gas mixture. This transforms the gas mixture into reactive radicals, ions, neutral atoms and molecules, and other highly excited species. These atomic and molecular fragments interact with the silicon substrate and depending on the nature of these interactions, two processes, either etching or

deposition processes, occur at the substrate. Since the formation of the reactive and energetic species in the gas phase occurs by collision, the substrate can be maintained at a low temperature. Hence, film formation can occur on substrates at a lower temperature than that possible in the conventional CVD process. This is a major advantage of PECVD.

The nanotubes were grown in a bell jar vacuµm chamber with a residual pressure of 10 mbar. Growth was initiated immediately by introducing C2H2 into the chamber and applying direct current (DC) glow discharge. By applying different growth times 20s, 40s, 60s, 90s, 2mins and 5mins, six different nanotube samples with lengths of 21µm, 30µm, 35µm, 70µm, 121µm and 252µm respectively, were obtained. Figure 4.18 shows the scanning electron microscope image of the vertically aligned MWCNT film.

4.5.2 X-band measurement

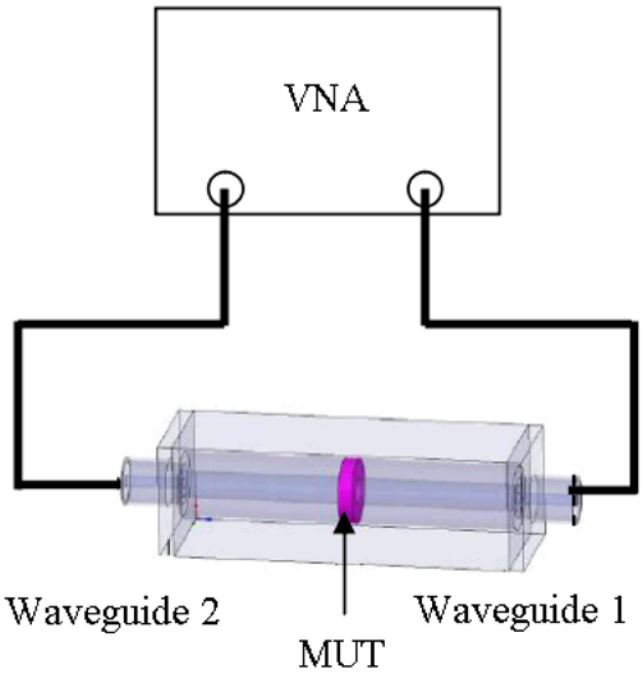

Figure 4.19. Measurement setup using transmission/reflection method with a waveguide [155].

To characterize the aforementioned vertically aligned MWCNT samples, the transmission/reflection line technique employed, which will be further elaborated later. The

sample was placed inside a rectangular waveguide and measured at X-band (8~12GHz). This method enables the accurate extraction of the effective material parameters from the measured S-parameters. As the measurement was done using a vector network analyser (VNA), both the magnitude and the phase information were obtained, thus both the permittivity and permeability can be extracted from a single measurement.

The measurement setup was shown in Figure 4.19. The MWCNT films were viewed as an effective medium with a known thickness and placed between two sections of rectangular waveguides of the same aperture. The VNA was connected to each end of the waveguide and used to measure both magnitude and phase of the S-parameters.

Three samples with the length of 30μm, 95μm, and 252μm, respectively, were measured for several times to achieve good consistency, as shown in Figure 4.20(a). From the measured S-parameters, the absorption information can be obtained using (4.3) and (4.4), as shown in Figure 4.20(b).

For the absorption obtained from (4.3), it appears that the absorption does not increase as the thickness increases and has a maximum absorption at 95μm. However, by normalizing the absorption to the total power that transmits through the CNT, it is clear that the absorption actually increases with the thickness of the sample. This complies with the conclusion in 4.4.2 (c) that in microwave frequencies, the absorption increases with the increase of the length.

The absorption is one of the CNT's intrinsic properties and is only dependent on the geometric properties, i.e. radius, length and concentration, etc. and after calibration, the normalized absorption should be independent from the input impedance and S-parameters of the array. In this way, the normalized absorption from the transmission line simulation can be compared with that obtained from measurement. An array of 16x16 CNTs are simulated with different inner and out radius and distance between neighboring CNTs, and the normalized absorption from measurement are used as target. Figure 4.21 shows that the fitting of the normalized absorption matches well for both the 95μm and 252μm case, for the 30μm case, the simulated result shows less absorption due to the fact the CNT growth cannot yet be accurately controlled in the CND process, and thus the fabricated CNTs may have a different radius scale than the assumed values in simulation.

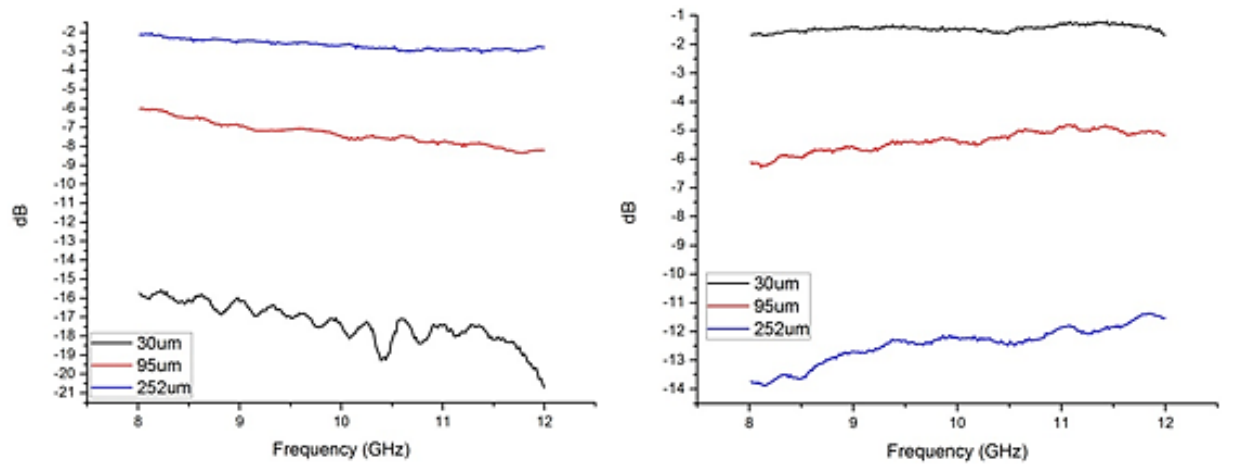

(a)

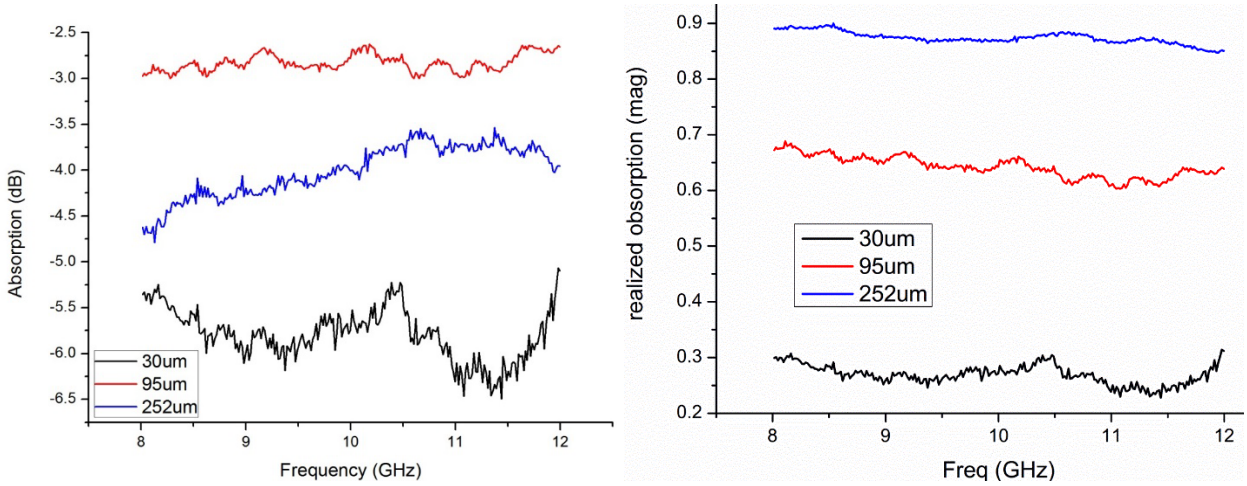

(b)

Figure 4.20 (a) measured S11 (left) and S21 (right) results, (b) absorption (left) and normalized absorption (right) of the three samples.

Several other measurement on MWCNT based absorbers with various thickness and construction have also been reported, including a Co- and Fe-filled MWCNT forest, which shows a changing absorption of 50% to 90% in X-band [201], [202], a CNT-fused silica composite which shows an absorption of 90% at 2.5% volume and almost 100% absorption at 10% volume in X-band [203], and a vertically-aligned CNT array which shows near perfect absorption in visible range [204]. The measured and simulated data shows that the vertically aligned CNT sample in this thesis has an absorption slightly lower than the horizontal aligned arrays with metal filling or CNT

composites, but by increasing length, the absorption quickly becomes comparable with previously reported one. Furthermore, the vertically-aligned CNT arrays have a flatter absorption curve in X-band.

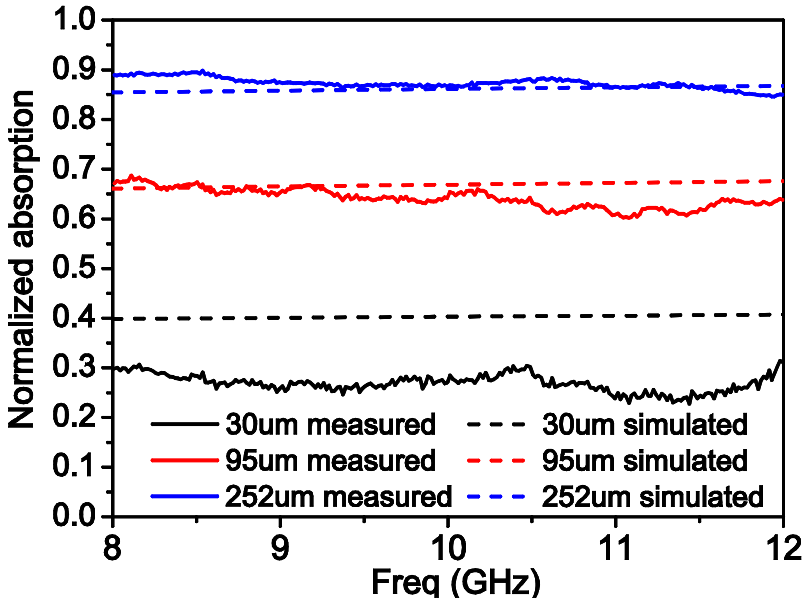

Figure 4.21 Comparison of normalized absorptions between measurement (solid) and simulation (dashed). The CNT's size parameters are optimized to fit the measurement result. The optimized inner radius and number of shells are 2nm and 6, respectively. The array size is 16x16.

4.5.3 Parameter extraction

With the complex S-parameters obtained, the Nicolson-Ross-Weir (NRW) approach was employed to extract the permittivity and permeability of the CNT sample. The detail procedure are described below.

When the wave propagates through the CNT array, it will attenuate and shift in phase according to the complex propagation constant $\gamma = \alpha + j\beta$. The propagation factor τ of the CNT array with a physical length *l* is

$$\tau = e^{-\gamma l}. \qquad (4.8)$$

The two-port scattering parameters can be determined by using the signal flow graph [156]

$$S_{11} = \frac{b_1}{a_1} = \frac{\Gamma\left(1-\tau^2\right)}{1-\Gamma^2\tau^2} \tag{4.9}$$

$$S_{21} = \frac{b_2}{a_2} = \frac{\tau\left(1-\Gamma^2\right)}{1-\Gamma^2\tau^2} \tag{4.10}$$

Solving (4.8) and (4.9) by the NRW approach [157], [158], Γ can be obtained as

$$\Gamma = k \pm \sqrt{k^2-1} \tag{4.11}$$

where the sign of $\pm$ is determined by $\left|\Gamma\right| < 1$and

$$k = \frac{S_{11}^2 - S_{21}^2 + 1}{2S_{11}} \tag{4.12}$$

With Γ obtained, we can relate the permeability μ with it as

$$\Gamma = \frac{\mu\gamma_0 - \gamma}{\mu\gamma_0 + \gamma} \tag{4.13}$$

where $\gamma_0 = \sqrt{k_c^2 - k_0^2}$ and $\gamma = \sqrt{k_c^2 - \mu\varepsilon k_0^2}$ are the propagation constants in the air filled waveguides and the CNT sample, respectively, $k_0 = \omega/\mathrm{c}$ is the wave number in free space, $k_c = \pi/a$ is the cutoff wave number with a=22.86mm being the width of the rectangular waveguide in X-band.

To solve (4.13), there is an ambiguity that needs to be clarified once the propagation constant is solved in terms of the transmission coefficient, caused by the function $\ln\left(1/\tau\right)$ which as in finite number of solutions when τ is complex. The propagation constant can be written as

$$\gamma = \frac{\ln\left(1/\tau\right) + j\left[\arg\left(1/\tau\right) + 2m\pi\right]}{l} \tag{4.14}$$

where m is any integer. Equation (4.14) is a continuous function, this a different value of the branch index m may be required. Once γ is determined, (4.13) gives the permeability of the CNT sample as

$$\mu = \frac{\gamma(1+\Gamma)}{\gamma_0(1-\Gamma)} \tag{4.15}$$

Substituting (4.15) into the propagation constant, the permittivity of the sample is calculated as

$$\varepsilon = \frac{k_c^2 - \gamma^2}{\mu k_0^2} \tag{4.16}$$

The extracted permittivity and permeability for the three samples are shown in Figure 4.22 [159]. Although it is expected that the permittivity and permeability does not change with the thickness, the extracted values are different. The reason is that the three samples were grown by the same procedure but the condition in which the CNTs in each sample were grown was impossible to accurately control. The unpredictable effects such as entanglement and air gaps with neighbouring CNTs, different concentrations of CNTs, etc. caused the permittivity and permeability to exhibit large differences with each other.

The permeability of the carbon nanotube is expected to be $\mu = 1 + j0$ as carbon nanotube under the aforementioned experimental setup should not have magnetic properties. However the extracted permeability has the real part close to 1 but the imaginary part as high as 38. This is due to the fact that in the synthesize process, metal catalyst such Ni was used for the continuous growth of nanotubes. In the entire process, there was not an effective cleaning to the CNT array and the catalyst, which was ferromagnetic, remained in the CNT array as impurities. As a result, the S-parameters were influenced by these impurities and hence the extracted permeability.

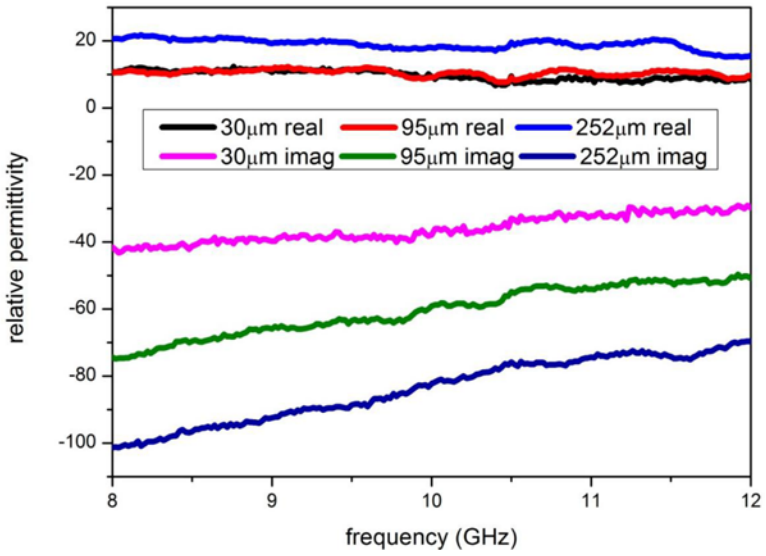

(a)

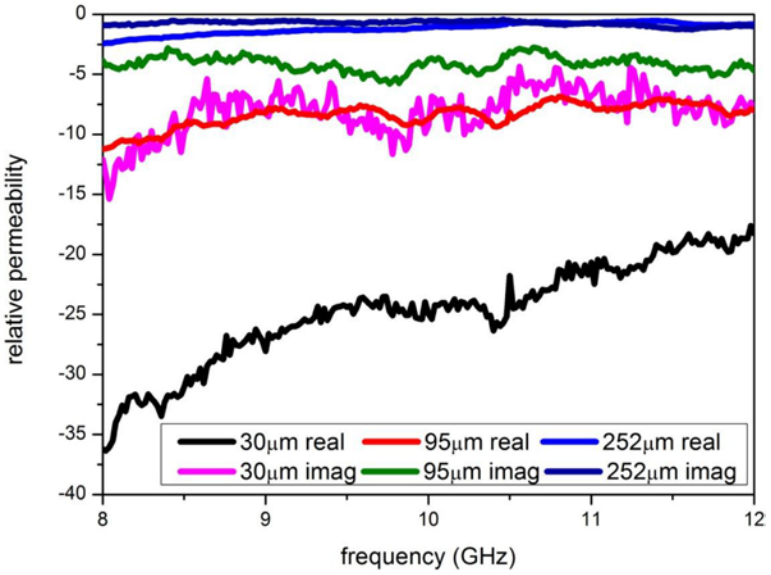

(b)

Figure 4.22. Effective medium extracted relative (a) permittivity and (b) permeability of the three VACNT samples [159].

Moreover, the real part of the permeability is smaller than zero in all three samples. This is due to the very small thickness of the samples that were measured. As a result, the phase measurement of the scattering parameters becomes very sensitive and only the amplitude is considered to be accurate. That appears to affect the real part of the permeability to take negative values.

To remove the permittivity brought in by impurity while maintaining the propagation constant in the CNT array, we can set $\mu = 1 + j0$ and calculate the effective permittivity in this assμmption. The modified effective permittivity of the 95μm sample is shown in Figure 4.23.

It can be seen that after setting permeability to be 1+0i, the both the real and imaginary part of the effective permittivity changed signs, but they clearly follows the Drude model [159] and can be fitted with the model

$$\varepsilon_m(\omega) = \varepsilon_{CNT}^{\infty} - \frac{\omega_p^2}{\omega^2 + i\Gamma\omega} + \frac{i\sigma}{\omega\varepsilon_0} \tag{4.17}$$

where $\varepsilon_{CNT}^{\infty}$ is the permittivity at infinite frequency, ω_p is the plasma frequency, σ is the conductivity and Γ is the electron relaxation rate.

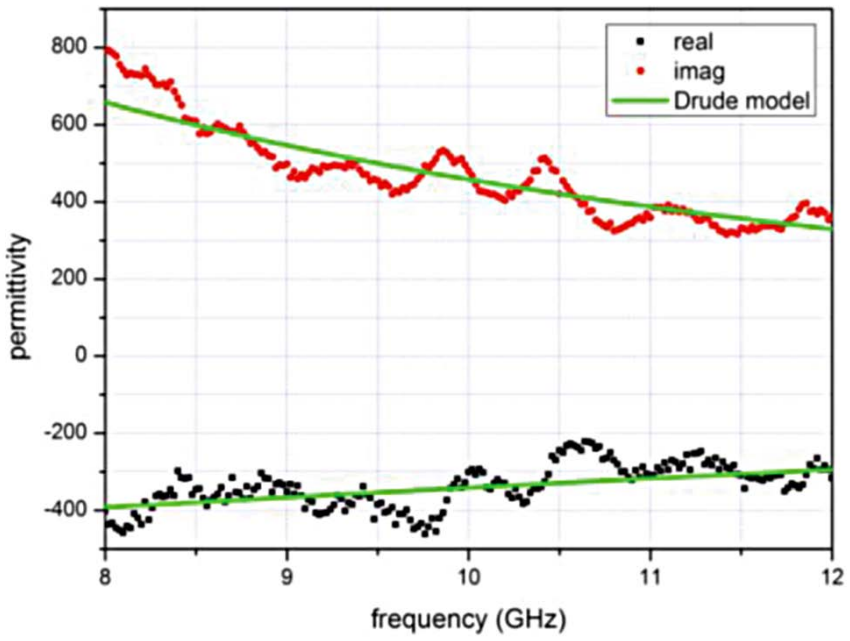

Figure 4.23. Effective medium permittivity extracted from the VACNT film [160].

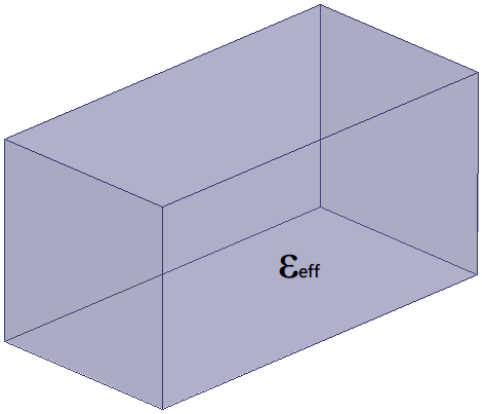

Figure 4.24. The CNT sample is represented by a homogeneous effective medium slab and simulated in CST with plane wave incidence and periodic boundaries

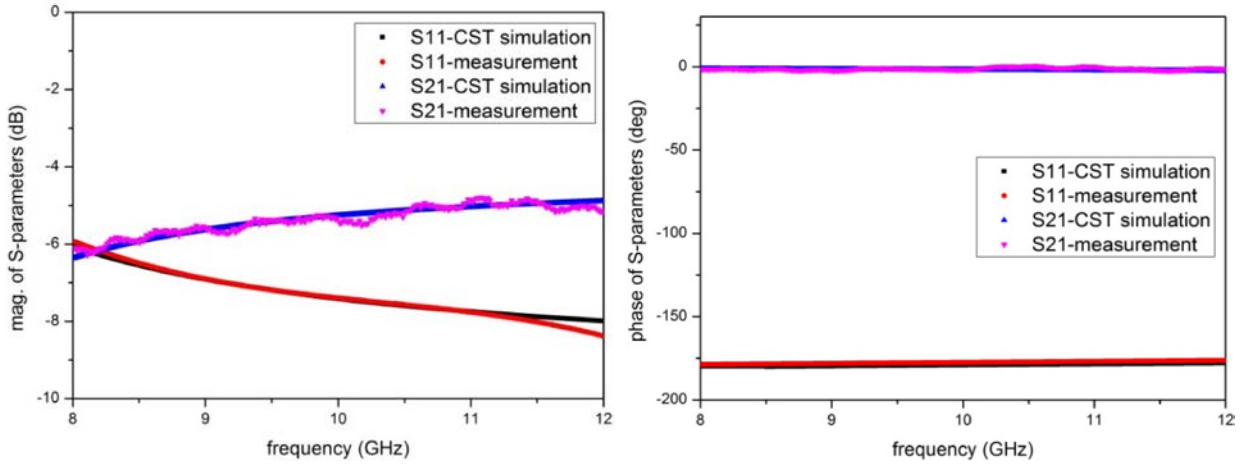

(a) (b)

Figure 4.25. Simulated and measured reflection and transmission coefficients of the 95µm VACNT sample, (a) magnitude and (b) phase

To validate the effective permittivity, the extracted values as shown in Figure 4.21 are imported to CST microwave studio as a homogeneous material. A slab of this material with the same thickness of 95nm and surrounded by a periodic boundary is then simulated assuming plane wave incidence, as shown in Figure 4.24. The S-parameter result of the measurement and simulation are shown in

Figure 4.25. It appear that in the entire X-band, the S-parameter obtained from the effective medium with modified permittivity matches very well with the measurement results.

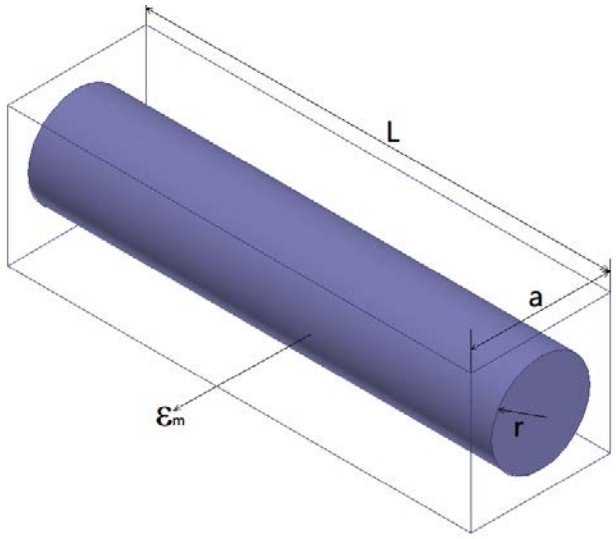

Figure 4.26. A single CNT is represented as a dielectric rod and simulated in CST with periodic boundary conditions. The radius of the CNT is r, the spacing between neighbouring CNTs are a-2r, and the length of the CNT L=95μm.

From the effective medium of the slab, the permittivity of a single CNT can be further extracted, from the Maxwell-Garnett formula for effective medium. The simulation setup in CST is shown in Figure 4.26, the radius of the CNT rod is r=40nm, L=95μm and a=90nm. Then, an optimization is done every 0.5GHz in CST with the measured S-parameter as the target.

The permittivity obtained by optimization is shown as dots in Figure 4.27. The relative permittivity of an individual array has much larger absolute value than the effective one, due to the fact that the effective medium is a mixture of air and CNT itself. The loose dots of the optimized value can be fitted very well by the Maxwell –Garnett formula

$$\varepsilon_m(\omega) = \frac{\varepsilon_{eff}(\omega) - 1 + \eta}{\eta} \tag{4.18}$$

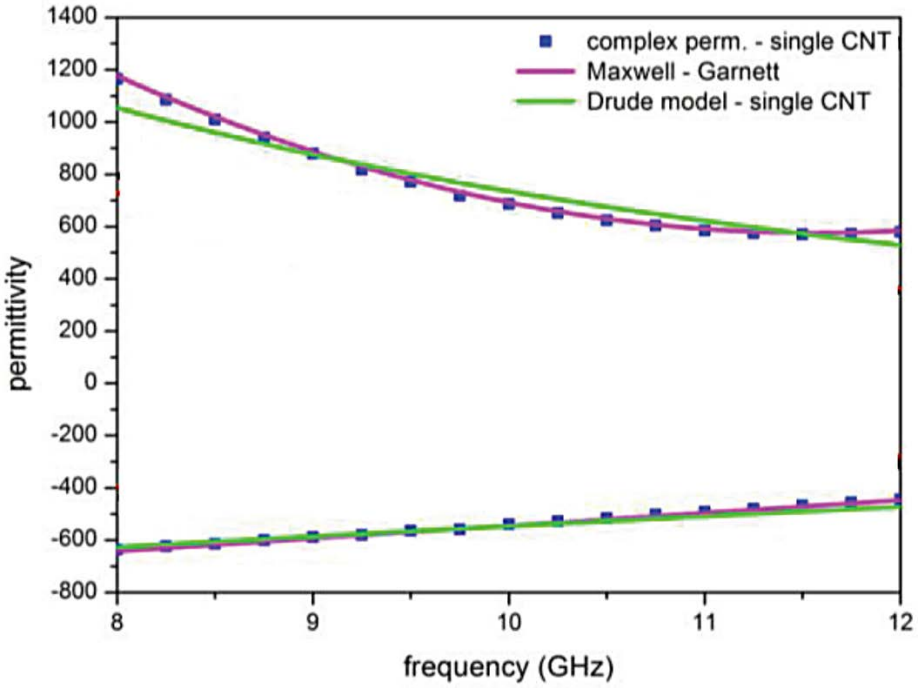

Figure 4.27. Optimized permittivity of a single CNT (loose dots), which can be fitted very well with the Maxwell-Garnett formula and the Drude model.

where ε_m is the permittivity of a single CNT, ε_{eff} is the permittivity of the effective medium and η is the volume fraction. Moreover, the optimized permittivity can also be fitted with Drude model, which appears to dominate the electric behaviour of a single CNT.

4.6 Material extraction from the transmission line model

In the last section, the technique to extract the permittivity and permeability (mainly permittivity, due to the influence of sensitive phase and ferromagnetic impurities on the permeability) of both the CNT array and an individual CNT is presented. However, in the transmission line model discussed in Chapter 3, the wave are assumed to propagate in quasi-TEM mode in the CNT array, thus is equivalent to the plane wave incident on an dielectric material. Moreover, the distribution of the CNTs are assumed to be uniform, so the permittivity of the CNT array is homogeneous. In

this case, from the S-parameters obtained from the transmission line model, it is also possible to extract the permittivity and permeability of the CNT array.

4.6.1 Extraction of permittivity and permeability from transmission line

The extraction procedure is no different from the NRW approach in (4.8)-(4.12), but in the plane wave incidence (TEM mode), the reflection coefficient Γ for a wave passing from a reference line into the effective medium is

$$\Gamma = \frac{Z_c - Z_{ref}}{Z_c + Z_{ref}} \tag{4.19}$$

where Z_c and Z_{ref} are the characteristic impedance of the effective medium and the reference line, respectively.

On the other hand, the relationship between Z_c and the reference impedance Z_0 of a standard air filled transmission line is

$$Z_c = Z_0 \sqrt{\mu_{eff} / \varepsilon_{eff}} \tag{4.20}$$

Hence, $z_{eff} = \sqrt{\mu_{eff} / \varepsilon_{eff}}$ can be obtained by combining (4.19) and (4.20) as

$$z_{eff} = \sqrt{\frac{\mu_{eff}}{\varepsilon_{eff}}} = \left(\frac{1+\Gamma}{1-\Gamma}\right)\frac{Z_{ref}}{Z_0} \tag{4.21}$$

where Γ is expressed by scattering parameters in (4.9) and (4.10). Furthermore, the propagation constant can be determined by

$$\gamma = \pm\frac{1}{L}\cos^{-1}\left(\frac{1-S_{11}^2+S_{21}^2}{2S_{21}}\right) = \pm j\frac{\omega}{c}\sqrt{\mu_{eff}\varepsilon_{eff}} \tag{4.22}$$

The effective refractive index is then

$$n = \pm\frac{1}{jl}\frac{c}{\omega}\cos^{-1}\left(\frac{1-S_{11}^2+S_{21}^2}{2S_{21}}\right) \tag{4.23}$$

For passive material, the imaginary part of n must be smaller than zero. This fixes the sign in (4.22). And from (4.23) and (4.21), the effective permittivity and permeability can finally be obtained as

$$\mu_{eff} = n \cdot z_{eff} \tag{4.24}$$

$$\varepsilon_{eff} = n / z_{eff} \tag{4.25}$$

4.6.2 Extraction examples

In this section several MWCNT arrays with different geometric parameters are extracted. Like in section 4.5, the permeability is fixed as $\mu = 1 + 0i$ and only the permittivity are studied.

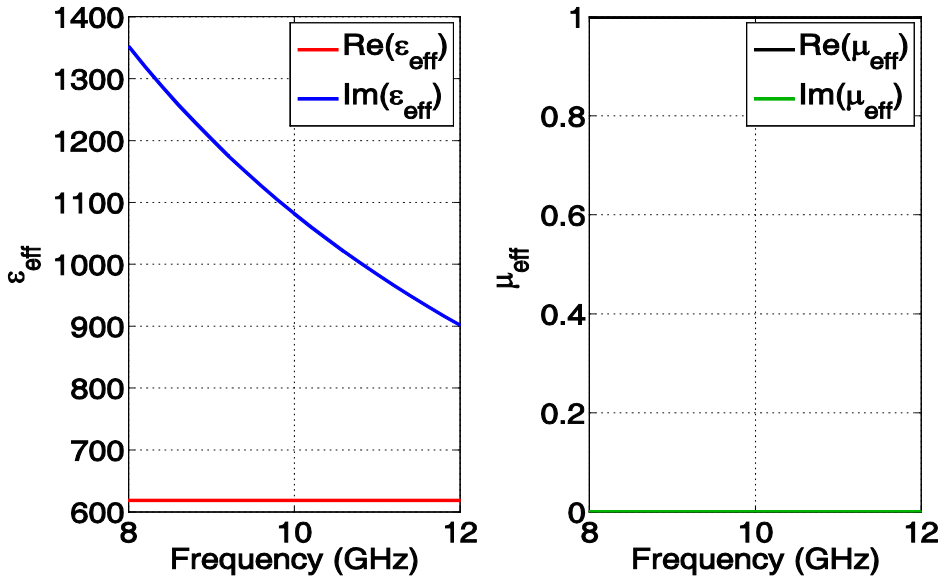

Figure 4.28 The extracted relative permittivity of a single CNT with inner radius=3nm and 9 shells (outer radius≈6nm)

Figure 4.28 shows the extracted permittivity of a single CNT with inner radius of 3nm and 9 shells. It appears that the extraction result matches very closely with the optimization done in CST for the measurement result, only that the real part of the permittivity is positive. However, the imaginary part has the same sign and the absolute value of the loss tangent are similar in both cases.

Figure 4.29(a) shows the extracted permittivity for 3 different CNTs with the inner radius of 3nm, 5nm and 10nm, respectively and all outer radius is the closest value to make the $r_{out} : r_{in} \approx 2$. From the result we can see that for a single CNT with larger outer radius, i.e. more conductive channels, the smaller the permittivity. The loss tangent in Figure 4.29(b) shows that the CNT with more conductive channels also are less lossy, which matches well with the absorption simulation shown in Figure 4.8.

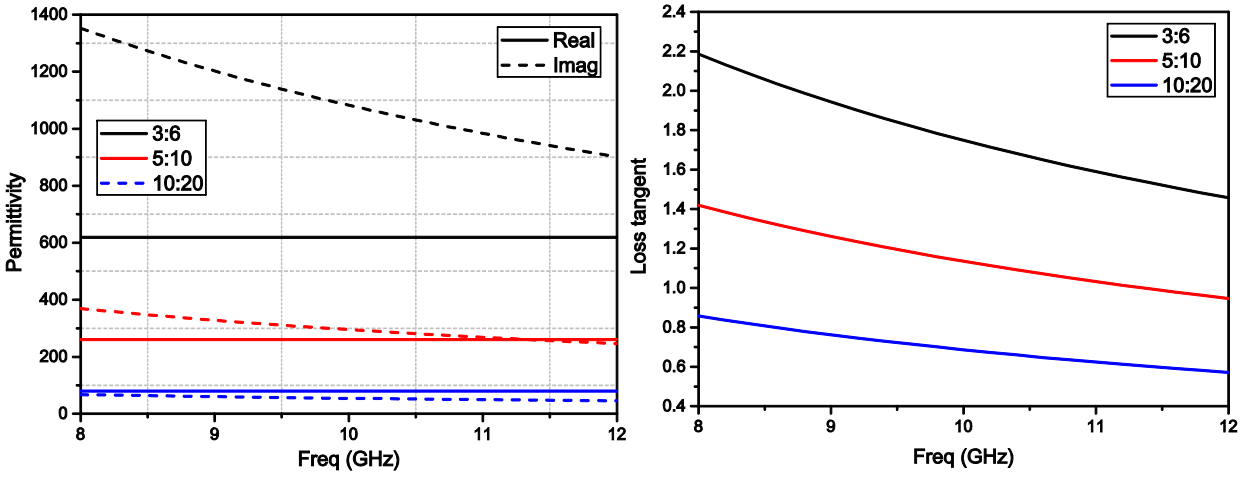

(a) (b)

Figure 4.29 (a) Extracted permittivity for 3 MWCNTs with different radius and (b) loss tangent.

Similarly, the permittivity for a CNT array can also be extracted for different array sizes, as shown in Figure 4.30. Again the permittivity, as well as the loss tangent, decreases with the increase of the number of CNTs inside the array. This result matches the absorption simulation shown in Figure 4.9.

Furthermore, the conductivity can be calculated from the imaginary part of the permittivity as $\sigma(\omega) = \varepsilon_0 \varepsilon'' \cdot \omega$ and the result for both CNT array and a single CNT is shown in Figure 4.31. It appears that in X-band, for a CNT array comprised of a fixed tube radius, the larger array shows a lower conductivity and for a single CNT, the one with larger radius shows smaller conductivity. This result matches with previously theoretical analysis [133].

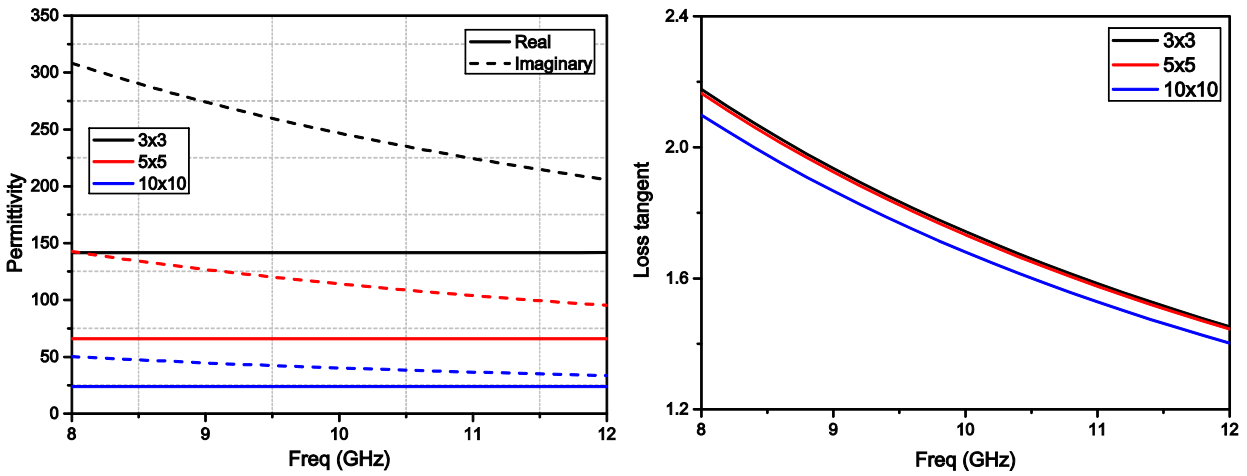

(a) (b)

Figure 4.30 (a) Extracted permittivity for 3 CNT arrays with different size and (b) loss tangent.

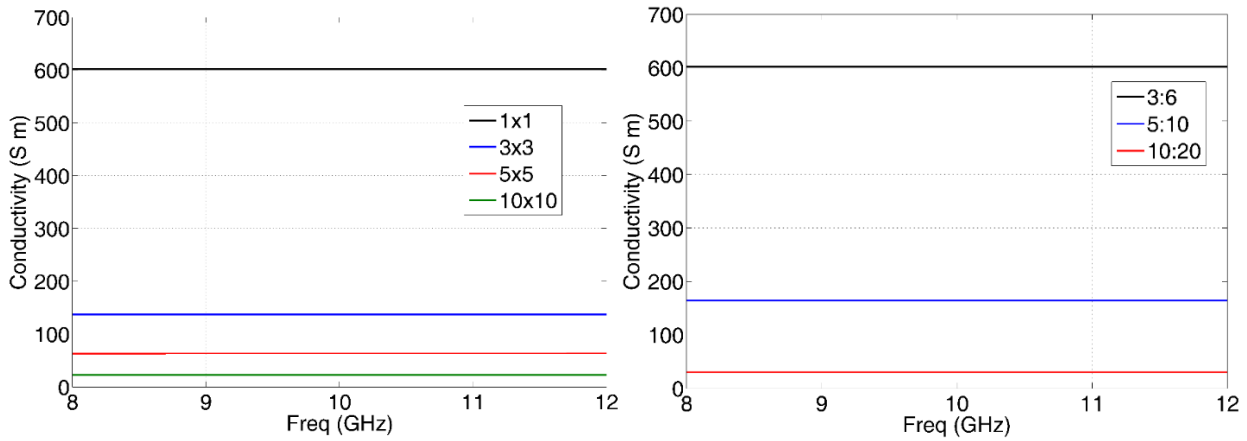

(a) (b)

Figure 4.31 Conductivity of (a) CNT arrays with different number of CNTs and (b) a single CNT with different radius.

We calculate the permittivity and loss tangent versus the number of shells at a fixed frequency, and the result is concluded in Table 2.

The permittivity and loss tangent in Table 2 is plotted versus the number of CNTs in the array, as shown in Figure 4.32. It appears that the permittivity change can be fitted with a power function similar to the one in Figure 4.17. The fitting equation can be summarized as

$$\varepsilon_r(m) = \varepsilon_r(8\text{GHz}) \cdot m^{-0.68} \qquad (4.26)$$

For imaginary part, (4.25) can be written as $\varepsilon_r = \frac{\sigma}{8\times10^9}\cdot m^{-0.68}$.

Table 4.2 Change of permittivity and loss tangent with different size of the CNT array.

Freq	Permittivity				Loss Tangent			
	1x1	3x3	5x5	10x10	1x1	3x3	5x5	10x10
8	618.6+j1352.6	141.6+j308.4	65.9+j142.7	24.0+j50.3	2.19	2.18	2.16	2.10
9	618.6+j1202.3	141.7+j274.2	65.9+j126.9	24.0+j44.7	1.94	1.94	1.73	1.68
10	618.6+1082.0	141.7+j246.8	65.9+j114.3	24.0+j40.3	1.75	1.74	1.73	1.68
11	618.6+j983.7	141.7+j224.4	66.0+j105.8	24.0+j36.6	1.59	1.58	1.57	1.53
12	618.6+901.7	141.7+j205.8	66.0+j95.3	24.0+j33.6	1.46	1.45	1.44	1.40

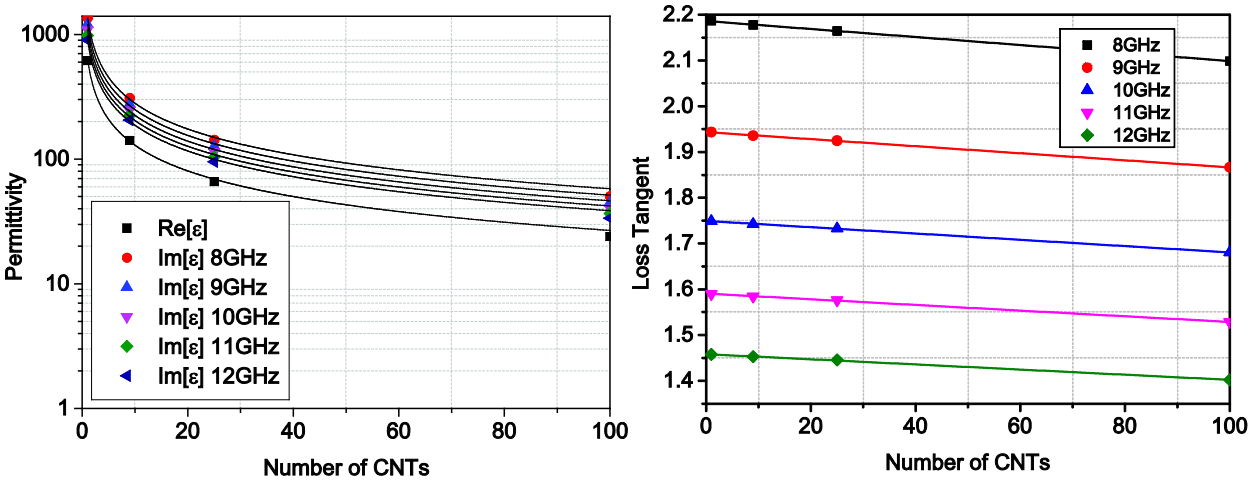

(a) (b)

Figure 4.32 Permittivity and loss tangent for different number of CNTs in the array.

On the other hand, the loss tangent can be fitted with a linear function by dividing the imaginary part in (4.25) with the real part. Equation (4.25) and (4.7) provides useful insight on the wave propagating velocity, permittivity and loss tangent with respect to the size of the CNT array, which can be helpful in designing the proper dimensions of the CNT array in the future when accurate control of the CNT growth is achieved.

4.7 Summary

In this chapter, both the single MWCNT and MWCNT arrays are characterized. From the extracted S-parameters, the electric properties of the CNT, such as input impedance, absorption, wave propagation velocity have been simulated and discussed. It has been shown that due to Fabry-Perot resonance, the VACNT array has two frequency point where the imaginary part of the input impedance is zero, where the real part of the input impedance are minimum and maximum, respectively. This could lead to applications in antenna design as wells as interconnection with devices with high output impedance, such as THz photomixers. Although CNT bundles or a single CNT with larger radius have lower input impedance and lower input impedance, the higher resonant frequency prevents them from being applicable as antennas in microwave frequencies and in this frequency, a better application would be absorbers, since the CNT arrays have shown a very good absorbing capabilities across a very wide band in both simulation and measurement.

The Nicolson-Ross-Weir method have been implemented to extract the material properties, such as permittivity and conductivity. The absorption and extracted permittivity are then compared with the X-band measurement results of three VACNT samples with different lengths grown by charged enhanced CVD. The simulation and measurement have shown a good matching. Furthermore, the absorption and permittivity as a function of the size of the CNT array have been studied and a power function has been proposed to accurately fit the simulated data. The fitting provides useful insight on the wave propagating velocity, permittivity and loss tangent with respect to the size of the CNT array, which can be helpful in designing the proper dimensions of the CNT array in the future when accurate control of the CNT growth is achieved.

Chapter 5 RF Characterization of Graphene transmission lines

5.1 Transmission line model of GNR

The GNR, like CNT, can be regarded as a 1 dimensional nano-wire. Recent studies have suggested that they are promising candidates in applications such as interconnects in future VLSI circuits [161], wide band optical amplifiers [162], and the creation of quantum dots to achieve quantum confinement [163].

The simulation of GNR as 1-D nano-wire is similar to that of CNTs, and the same multi-conductor transmission line model can be used, only with modifications to per unit length circuit parameters and the expression of mutual coupling, due to GNR's flat nature.

The per unit length *R*, L_k, C_q can be expressed as

$$R = \frac{R_q}{l_{mfp}} = \frac{h}{2e^2 \cdot N_c \cdot l_{mfp}} \tag{5.1}$$

$$L_k = \frac{h}{4e^2 v_F} \cdot \frac{1}{N_c} \tag{5.2}$$

$$C_q = \frac{4e^2}{h v_F} \cdot N_c \tag{5.3}$$

where *e* is the charge of electron, *h* is the Plank constant, v_F is the Fermi velocity, the number of conductive channels N_c is the conductivity normalized to the quantum conductance $G_0 = 2e^2/h \approx 1/12.9\text{k}\Omega$ and l_{mfp} is the mean free path (MFP). For a GNR with either zigzag or armchair edge, the expression for N_c has been presented as (2.23) in Chapter 2.

The MFP for a narrow GNR in graphene is large yet finite [164], and similar to the case of CNTs, electrons in a GNR can get scattered by phonons, defects, and rough edges and thus the MFP is comprised of three parts. According to Matthiessen's rule, the total MFP can be expressed as

$$l_{mfp}^{-1} = l_s^{-1} + l_D^{-1} + l_E^{-1} \tag{5.4}$$

where l_D is the MFP of the carriers in the presence of impurities and can be expressed as

$$l_D \approx \frac{4W}{\sqrt{3}} \cdot \frac{\gamma^2}{2\sigma_\varepsilon^2 + 8\sigma_\gamma^2} \tag{5.5}$$

where σ_ε and σ_γ are variances [165], [166], W is the width of the GNR and $\gamma = 3eV$ is the overlap integral between nearest neighbor π orbits [167].

Like in the case of CNT, l_D of graphene can be approximated as a function of width

$$l_D \approx 450W \tag{5.6}$$

Note that (5.6) is for a single layer GNR. For multilayer GNR, l_D will decrease due to the existence of interlayer electron hopping [168].

The l_s is the electron-phonon scattering and it has been reported that for a 10nm wide GNR in room temperature, $l_s \approx 70\ \mu\text{m}$ [169]. This results shows that the acoustic phonon scattering is negligible as compared to the long-range defect scattering.

One significant difference of the GNR compared to CNT is the presence of edge scattering, which is the result of the roughness of the GNR's edges, especially for narrow GNRs. The impact of edge roughness on the scattering of carriers can be significant [170]. The corresponding MFP l_E is given by

$$l_E = W\sqrt{\left(\frac{2WE_F / h\nu_F}{n+\beta}\right)^2 - 1} \tag{5.7}$$

where E_F is the Fermi energy, n is the mode number, and β is 0 for metallic GNR and 1/3 for semiconductor GNR. According to [171], (5.7) can be approximated as

$$l_E = 1.5W^{2.5}\left(\frac{2E_F}{h\nu_F}\right)^{1.5} \tag{5.8}$$

For the case of very narrow GNR (1-D system), the dominant mode is the first propagating mode, which travels along the edges. Therefore, the impact of the edge scattering is negligible [171].

The self and mutual capacitance and inductance of the GNR is different from that of CNTs. Due to the existence of fringing effect, the capacitance of the GNR can be quite complex and need to be discussed separately. Once the capacitance is obtained, the inductance can be calculated either by $L = \mu\varepsilon_e / C$, where ε_e is the effective permittivity, or by the analytical equations described below.

5.1.1 Capacitance of stacked GNR

The geometry of a stacked GNR is shown in Figure 5.1, where the total height of the stacked graphene is H, the width of each GNR is w, the distance between each two neighboring layers is δ, the material permittivity is ε_r and the thickness of the dielectric is d. In reality, the stacked GNR are usually synthesized on copper substrate by thermal CVD [205], or by exfoliating multilayer graphene flakes [206]. In both cases, similar to CNTs, δ is 0.34nm, known as the Van de Waals gap. For δ>0.34nm, the Van de Waals force is too weak to hold layers of graphene

together and it is unrealistic to make one layer 'hover' above layers below it, so the gap between every two neighboring layers must be filled with dielectrics, normally PMMA or quartz, and thus the stacked graphene becomes sandwiched graphene.

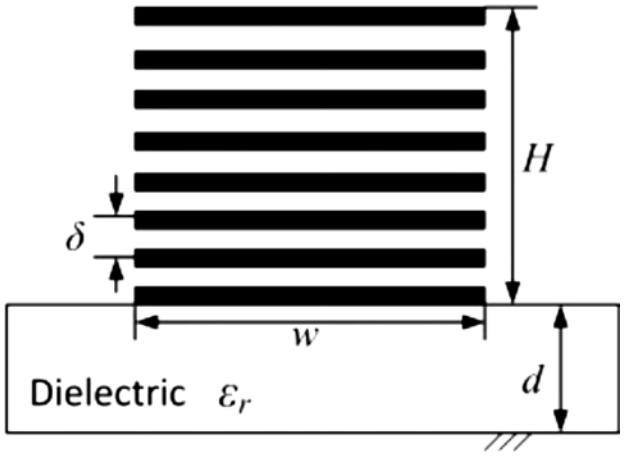

Figure 5.1 Geometry of a stacked GNR above ground, the dielectric medium with permittivity ε_r fills the space between the bottom layer and ground.

The per-unit-length capacitance of the bottom layer GNR was given by Palmer [172]

$$C_e = \varepsilon_0 \varepsilon_r \frac{w}{d}\left[1+\frac{h}{\pi w}+\frac{h}{\pi w}\ln\left(\frac{2\pi w}{d}\right)\right] \tag{5.9}$$

Recently, Ashkan, et al. has derived a new model for the GNR fabricated on the silicon substrate with a layer of silicon dioxide between the substrate and GNR [173].

$$C_e = \varepsilon_0 \varepsilon_r \left\{\frac{\pi}{\ln\left[6\left(d/w+1\right)\right]}+\frac{w}{d}\right\} \tag{5.10}$$

Figure 5.2 shows the comparison of (5.8) and (5.9) for a GNR above ground with air filling the gap. The distance d from ground is 50nm and 10nm, respectively, and the width of GNR w changes from 1nm to 100nm.

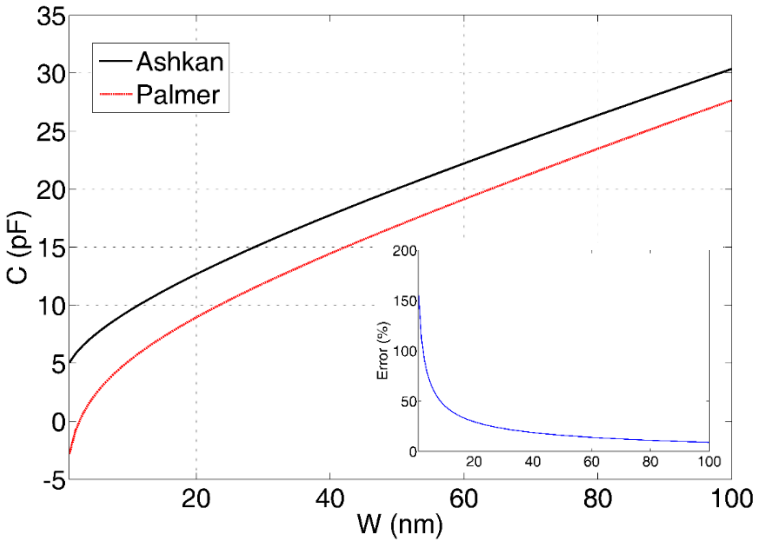

(a)

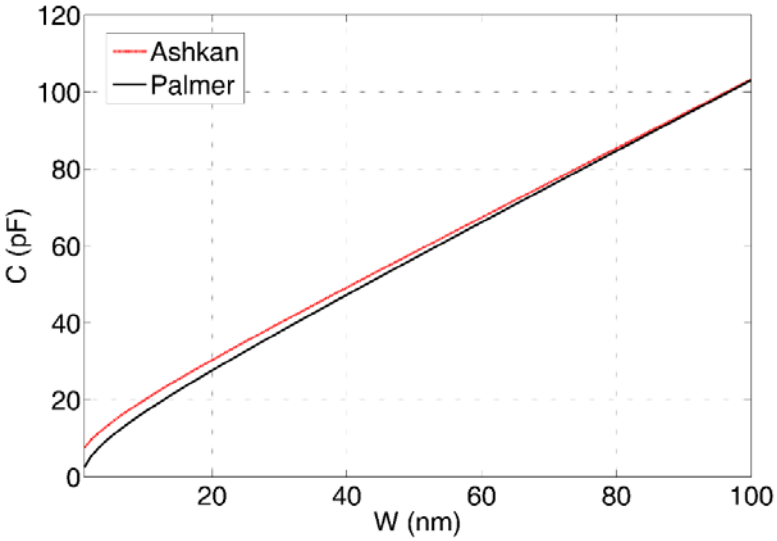

(b)

Figure 5.2 Comparison of Palmer's model and Ashkan's model for the capacitance of GNR for (a) d=50nm, (b) d=10nm. The inset is the relative error.

It appears in Figure 5.2(a) that for a large d, both function follows the same curve, only differs in the value of C_e. The inset shows the relative difference between the two. For small width, the difference are very large and it decreases exponentially with the increase of the width. Figure 5.2(b) shows that for a small d, the two methods gives almost identical results. It can also be found that the capacitance in (5.9) is small than zero for $w << d$, which cannot be valid, which indicates that

(5.9) is derived on the premise that w is comparable with d. Considering that GNR's are usually several nanometers wide and several hundred nanometers above ground, (5.10) is preferred and used in the rest part of this thesis.

Apparently, for the mutual capacitance between vertically neighboring GNRs, (5.10) is also applicable. Note that the self-capacitance between GNR and ground only exists for the bottom layer, all upper layers were shielded and only have a mutual capacitance.

5.1.2 Capacitance for parallel GNRs on a same layer

The geometry setting of two parallel GNRs on a same layer is shown in Figure 5.3. The width of each GNR is w, the edge to edge and center to center distance between two neighboring GNRs is s and a, respectively. The substrate thickness d is the same with 5.1.1. The per unit length mutual inductance L_m between the two GNRs is given as [174].

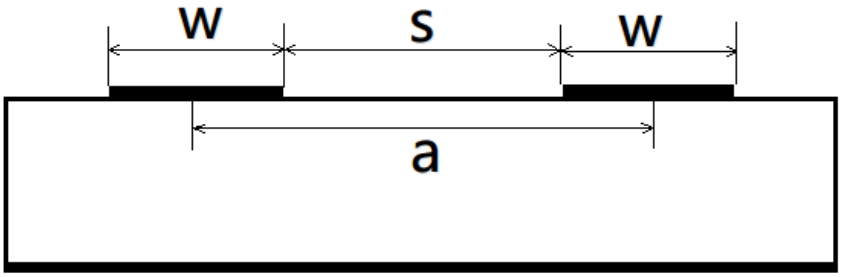

Figure 5.3 Geometry setting of two parallel GNRs on a same layer

$$L_m = \begin{cases} \dfrac{\mu}{2\pi}\left[\ln\left(\dfrac{l}{a}+\sqrt{\left(\dfrac{l}{a}\right)^2+1}\right)+\dfrac{a}{l}-\sqrt{\left(\dfrac{a}{l}\right)^2+1}\right] & \text{a>3w} \\ \dfrac{\mu}{2\pi}\left[\ln\left(\dfrac{2l}{a}-1\right)\right] & \text{l>>a, a>3w} \end{cases} \quad (5.11)$$

While the per unit length mutual capacitance C_m is calculated by [174]

$$\frac{C_m}{\varepsilon_0\varepsilon_r}=\frac{0.5}{1+\left(s/\left(d+H\right)\right)^2}C_{[BCP]}\left(\frac{H}{s/2},\frac{2d}{s/2}\right)+\left[\frac{0.87}{1+\left(s/2/\left(d+H\right)\right)^2}\right]C_{[CP]}\left(w/s\right) \quad (5.12)$$

where $C_{[BCP]}$ and $C_{[CP]}$ are given in [175] as

$$C_{[BCP]}\left(z,y\right)=\frac{\varepsilon}{2}M\left(k_{[BCP]}\left(z,y\right)\right) \quad (5.13)$$

where

$$k_{[BCP]}\left(z,y\right)=\frac{\sqrt{\sinh\left[\frac{\pi}{2}\left(z+y\right)\right]\sinh\left(\frac{\pi}{2}z\right)}}{\cosh\left[\frac{\pi}{2}\left(z+\frac{y}{2}\right)\right]} \quad (5.14)$$

$$C_{[CP]}\left(z\right)=\frac{\varepsilon}{4}M\left(k_{[CP]}\left(z\right)\right) \quad (5.15)$$

where

$$k_{[CP]}\left(z\right)=\sqrt{1-\frac{1}{\left(1+2z\right)^2}} \quad (5.16)$$

and

$$M\left(k\right)=\begin{cases}\dfrac{2\pi}{\ln\left[2\dfrac{1+\left(1-k^2\right)^{1/4}}{1-\left(1-k^2\right)^{1/4}}\right]} & 0\le k\le\dfrac{1}{\sqrt{2}}\\ \dfrac{2}{\pi}\ln\left[2\dfrac{1+\sqrt{k}}{1-\sqrt{k}}\right] & \dfrac{1}{\sqrt{2}}\le k\le 1\end{cases} \quad (5.17)$$

The capacitance and inductance formulae of (5.11) ~ (5.17) are exact analytical results and can be used for GNRs with arbitrary width and number of stacking.

The per unit length self-inductance is given by simplified Ruehli's formula with the assumption of zero thickness [176].

$$L_s = \frac{\mu}{6\pi}\left\{3\ln\left[u+\sqrt{u^2+1}\right]+u^2+\frac{1}{u}+3u\ln\left[\frac{1}{u}+\sqrt{\frac{1}{u^2}+1}\right]-\left[u^{4/3}+\left(\frac{1}{u}\right)^{2/3}\right]^{3/2}\right\} \quad (5.18)$$

where $u = \frac{l}{w}$. The per unit length self-capacitance can be calculated by $L_s \cdot C_s = \mu\varepsilon_e$.

The mutual coupling between three or more GNRs are more complex, and in the case of very small *s*, because the shielding effect by the GNR in the middle, the coupling between the two GNRs at the edge are weak and thus neglected. In this way, only the coupling between neighboring GNRs are considered. In the case of wide separation (*s*>>*w*), all the coupling were considered.

5.2 Comparison of GNR and CNT arrays

From the transmission line model described in 5.1, the performance of GNR and CNT in terms of input impedance, absorption and S-parameters can be compared. Unlike CNT which has a height equal to its diameter, graphene is considered as a 2-D surface. Even with stacking, the gap between each layer is in the order of several nanometers. Moreover, the stacking of graphene will cause each layer to interact with each other and eventually become graphite. So the stacked graphene can still be considered as a 2-D sheet with zero thickness. In this way, when comparing the CNT and GNR arrays, the low-profile setup of the CNT array discussed in chapter 4 is always considered.

5.2.1 A single GNR

First of all, the S-parameters of a single GNR is simulated in terms of different width, length, substrate permittivity and thickness. It is expected that GNR also has a high intrinsic characteristic impedance thus the reflection will be high for a common 50Ω environment. As a result, like in Chapter 3, to make the changes in S11 the more significant, the reference impedance are set as the

quantum resistance $R_q = \frac{h}{2q^2 N_c} \cdot \frac{1}{n}$, where n is the number of stacked GNRs and 1 in this case. The substrate is assumed to be air and the

The solid lines in Figure 5.4 shows both the S11 and S21 of four different GNRs with the length of 5nm 10nm, 15nm and 50nm, respectively. For comparison, the S-parameters of 4 CNTs with the same circumferences are also shown as the dash-dot lines.

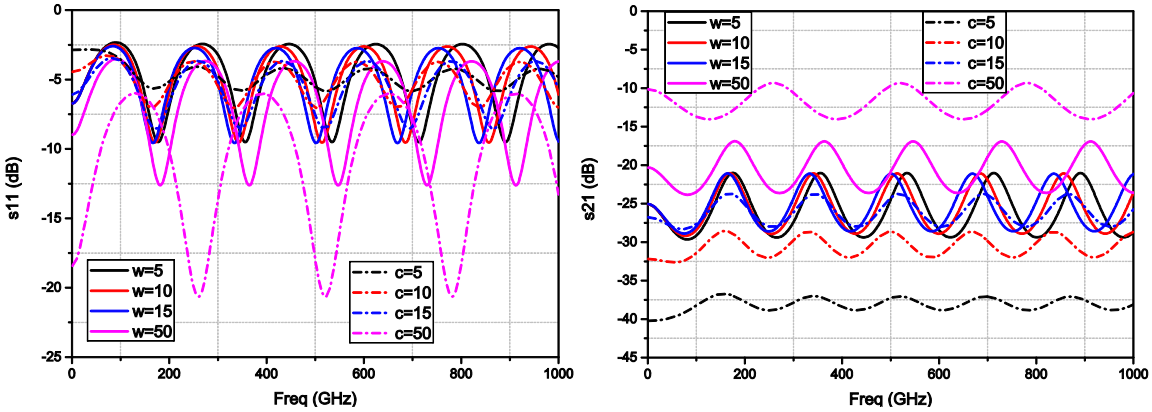

(a) (b)

Figure 5.4 S-parameter of three GNRs with different width and that of the corresponding CNTs with a same diameter, (a) is S11 and (b) is S21.

It appears that similar to the CNT, the increase in the width of the GNR results in less reflection and more transmission, due to the decrease of the characteristic impedance. Overall, the GNR's S-parameters are less sensitive to the change of width. The periodic occurring peaks shows the same Fabry-Perot resonance as in CNTs but the smaller change in Δf between two neighboring peaks suggests that the wave velocity in GNRs does not increase as fast as in the CNTs.

Figure 5.5 shows the real and imaginary part of the input impedance of a single GNR and a single CNT with the same circumference. Note that from this part, all reference impedances are set as 50Ω. First of all, the peak magnitude of the input impedance of a GNR is in the same order of that of a CNT and again all simulated results shows a periodic resonanting behavior. Interestingly, it appears that the peak impedance for a single GNR decreases with the width while that of a single CNT increases. The reason is that the radius of the CNT simulated here are very small and the

number of conduction channels has not reached the area where it grows with radius, except for the c=50nm case (which corresponds to r=7.95nm). And the fact that the radius changes with a constant number of conduction channels results in the increase in the input impedance. With further increase in the radius, the input impedance will decrease again, as shown before in Chapter 4. Furthermore, the GNRs show a much closer resonant points for different width, which again proves that GNR's transmission properties are less sensitive to the change of width.

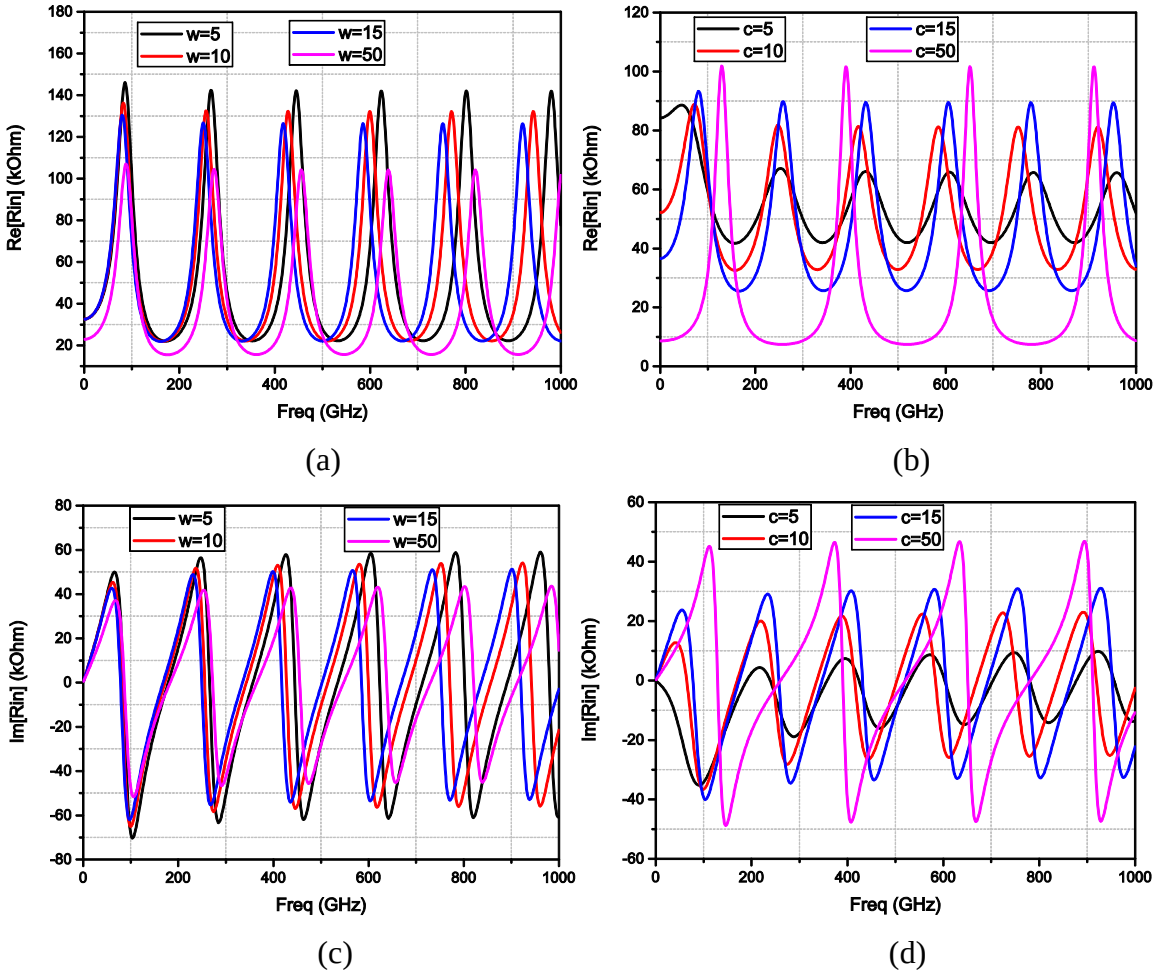

Figure 5.5 Input impedance of a single GNR and CNT. (a) Re[Zin] of a single GNR, (b) Re[Zin] of a single CNT with the same circumference, (c) Im[Zin] of a single GNR and (d) Im[Zin] of a single CNT with the same circumference.

The absorption and normalized absorption are shown in Figure 5.6. It can be seen that while the absorption of GNRs are within the range of only 0%~2%, the absorption of CNTs are within the

range of 20%~40%, both the GNR's and CNT's peak absorption increases with the increase of width or circumference. On the other hand, the normalized absorption shows the true absorption capability and both the GNR and CNT shows increased absorption with the decrease of width or circumference. It can be seen that for the same width (circumference), the normalized absorption of the GNR is higher than that of the CNT. This is even more significant for large width GNRs.

Finally, a single 100nm wide GNR's input impedance and absorption under different substrate permittivity and temperature is shown in Figure 5.7. From Figure 5.7(a) and (b), it can be found that higher substrate permittivity dramatically decreases both the real and imaginary part of the input impedance and at the same time increases the resonant peaks across the simulated frequency. The higher the real part of the permittivity, the more resonant peaks appear. Also, at the presence of dielectric losses, the impedance increases with frequency and higher loss tangent results in a faster increase.

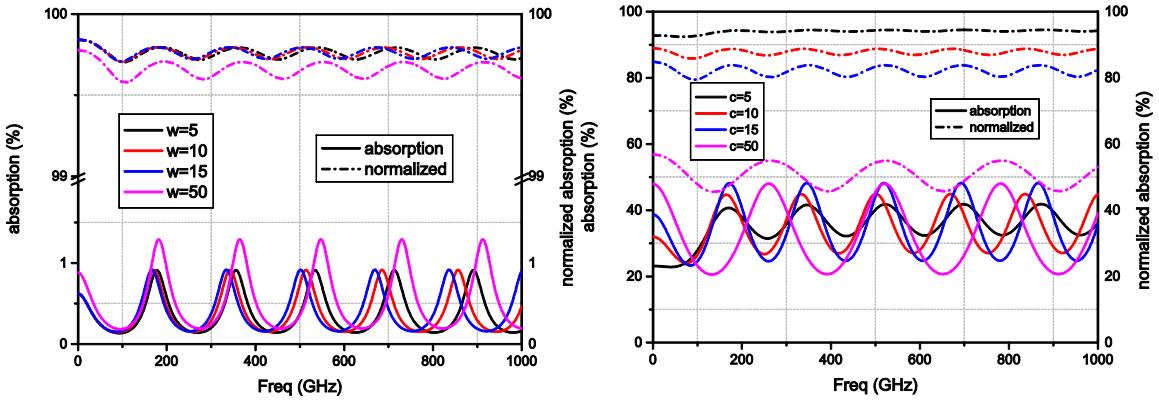

(a) (b)

Figure 5.6 Absorption and normalized absorption of (a) three GNRs with different width and (b) that of the corresponding CNTs with a same diameter.

Figure 5.7(c) and (d) shows that changing the temperature does not change the magnitude of the input impedance much, but the number of resonant peaks increase with the decrease of temperature. This phenomenon becomes more significant in higher frequencies which means that the heat generated by the working environment may have a big impact on the impedance matching and efficiency of the GNR based interconnects and devices.

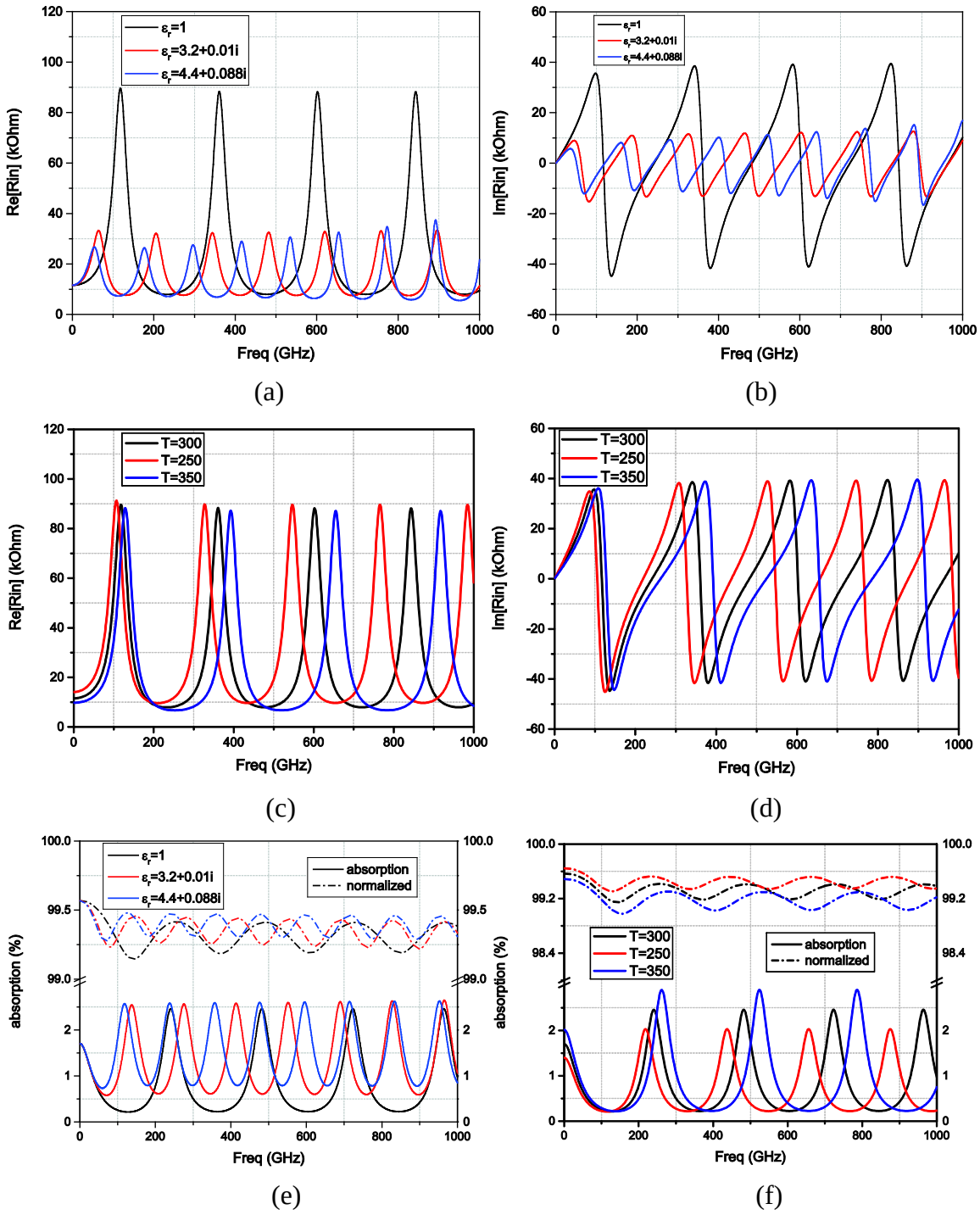

Figure 5.7 The influence of substrate permittivity and temperature on the input impedance and absorption of a single GNR with width w=50nm.

The absorption and normalized absorption in Figure 5.7 (e) and (f) shows that changing the real part of the substrate permittivity does not change the peak magnitude of the absorption, but only the number of resonant peaks. At the presence of a loss tangent, the absorption also increases with

the increase of the frequency. However, changing the temperature changes the peak magnitude of the absorption and normalized absorption. This is different from the absorption of a single CNT, whose peak magnitude decreases at the presence of a lossy substrate, as shown in Figure 4.12.

5.2.2 Stacked GNR arrays

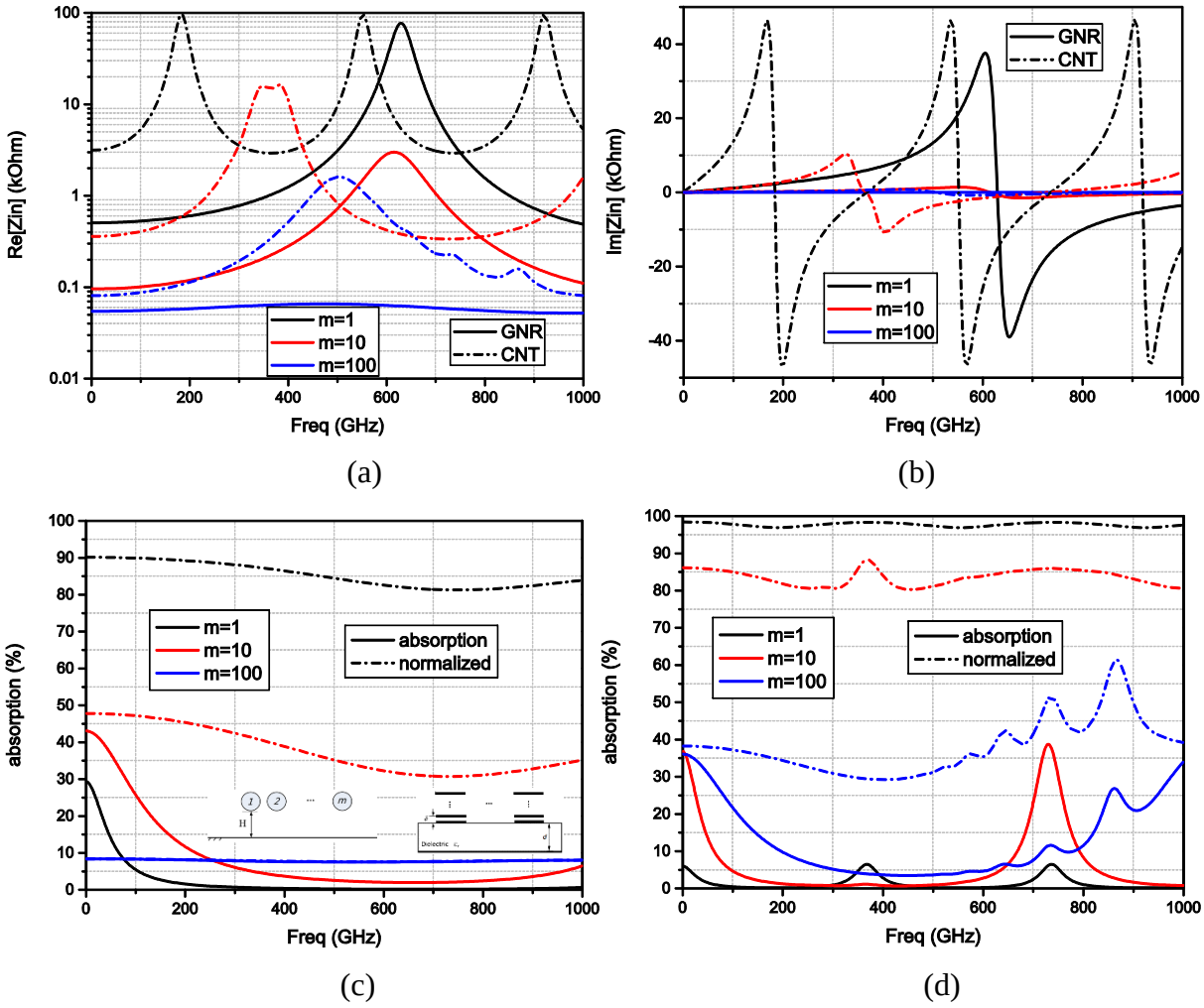

Figure 5.8 Input impedance and absorption of GNR and CNT arrays with a total number of m stacks of GNRs or m CNTs. Each stacks of GNR is comprised of 10 layers and each layer has a width of 50nm. The CNT array for comparison is comprised of a CNTs with the same circumference. The real and imaginary part of the input impedance is shown in (a) and (b), respectively, the absorption of the GNR array is shown in (c) and that of a CNT array is shown in (d). The inset in (c) shows the difference in the geometry of CNT and GNR arrays.

With the basic transmission and absorption properties of a single GNR discussed, such properties of a stacked GNR array can be further discussed. As mentioned before, due to the 2-D nature of graphene, the stacked GNR array can still be considered as a 2-D array and the comparison is made between such GNR arrays and a 1 layer CNT array.

Figure 5.8 shows the input impedance and absorption of three stacked GNR arrays with a total number of m stack in parallel, as shown in Figure 5.3. The substrate permittivity is 1, the width of each stacking is 50nm and the length of each stack is 10um. For comparison, three CNT arrays comprised of CNTs with the same length, circumference and number of CNTs are also simulated.

First of all, Figure 5.8(a) and (b) shows that the GNR and CNT arrays have a similar input impedance when the array size is small, but the input impedance of the GNR decreases dramatically with the increase of the array size. By comparing the resonant frequencies it can be found that changing the size of the GNR array has far less impact on the resonant frequencies than changing the size of the CNT array, this is very similar to a single GNR with different width case.

The absorption simulation in Figure 5.8(c) and (d) shows that both the CNT and GNR arrays show a good absorption capabilities in microwave frequencies. It is worth noticing that the normalized absorption of the GNR array decreases much faster than the CNT array. For example, when m=100, the normalized absorption of a GNR quickly decreases from 80% to less than 10%, while that of CNT remains at 40%. What's more, the absorption of the GNR array appear to have a much lower periodicity than that of the CNT array.

Combing the simulation results in Figure 5.8 the conclusion can be draw that the GNR array's input impedance and absorption changes much faster with the change of the array size, thus it can be more suitable in the nanoscale applications that requires a small input impedance and low loss, such as antennas.

Finally, the input impedance and absorption of stacked GNR arrays on top of a lossy substrate with permittivity of $\varepsilon_r = 4.4 + 0.088i$ is shown in Figure 5.9. It appears that with the presence of a dielectric constant larger than 1, the impedance of the GNR array is lower than the case when the dielectric constant is 1. At the same time the absorption slightly increases. Another apparent

different to the case of $\varepsilon_r = 1$ is that the real part of the permittivity decreases the periodicity and thus there are more resonant peaks in the simulated frequency band. The presence of the loss tangent causes the peak magnitude of the input impedance to increase with frequency while the absorption decreases with frequency.

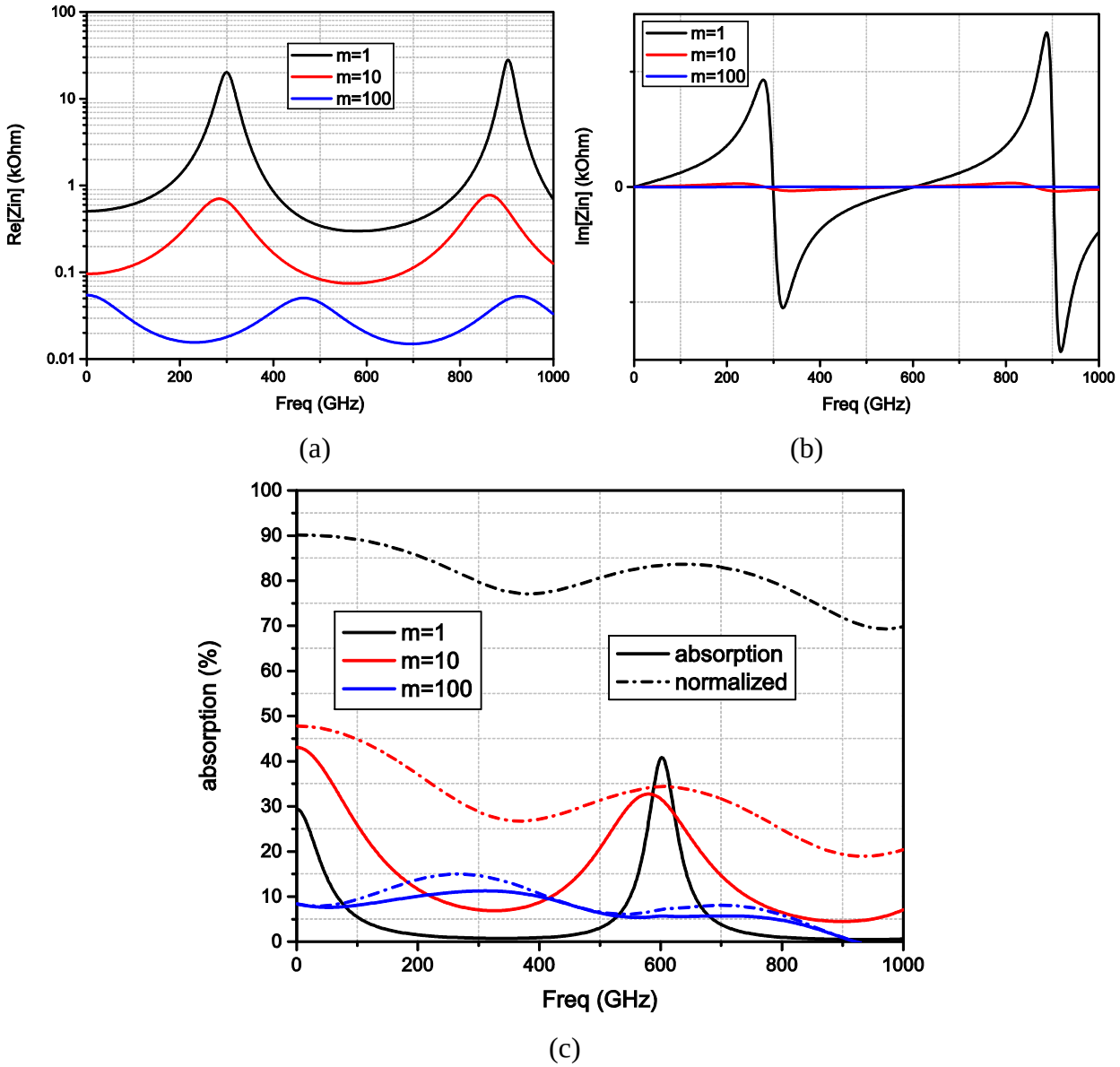

Figure 5.9 Real (a) and imaginary (b) part of the input impedance and absorption (c) of GNR arrays with $\varepsilon_r = 4.4 + 0.088i$.

5.2.3 Summary of GNR impedance/absorption simulation.

We have compared the performance of both a single GNR and GNR arrays to the corresponding CNT arrays with the same circumference. Several conclusions can be summarized as follows:

1. The GNR array and CNT arrays have a similar transmission and absorption properties. The intrinsic impedance are both high and a single GNR or CNT connected directly to a 50Ω testing environment will result in almost total reflection and zero transmission. Using arrays can effectively reduce the input impedance and lower absorption.

2. Unlike the case of CNTs, increasing only the width of a GNR does not change the input impedance or absorption much, the reason is that due to the curvature structure of the CNT, its number of conductive channels goes out of the constant area and increase linearly when the radius is larger than only 2nm (room temperature), while for GNT, the number of conductive channels remains constant for all the width smaller than ~50 nm. Thus, increasing the width of the GNR cannot effectively increase the number of conductive channels. However, the magnitude of the GNR's input impedance and absorption decreases significantly with stacking and arrays, the speed of decrease is much faster than that of CNTs.

3. For a single GNT, increasing the substrate permittivity can effectively reduce the input impedance but the absorption almost the same. It is still much more effective to reduce the absorption by stacking and using arrays. So GNR arrays are better candidates than CNT arrays for nanoscale applications that requires low loss, especially in microwave frequencies.

4. The heating of the working environment may change the input impedance for both GNR and CNT arrays, this is a potential problem that needs to be solved to really make use of these carbon based materials in VLSI circuits. Unlike the case of CNT, increasing the temperature slightly reduces the normalized absorption of GNR arrays, which makes the GNR to perform better than CNT in low frequencies, where the changing of temperature does not significantly shift the input impedance.

5.3 Impact of port impedance and parasitics on GNR and CNT measurement.

In Chapter 4 and the first half of this chapter, various simulations of CNTs and GNRs have been presented. However, for microwave applications, the size of the GNR is set to be several centimeters and even higher. On the other hand, due to the high sheet resistance of graphene and typical 50 Ω microwave testing systems, in real measurements, the high reflection poses a significant impact on the microwave characterization of graphene and CNT based devices, because the influence of parasitics are overshadowed. Furthermore, the existence of high contact resistances have made it even harder to properly match the graphene patch to the testing facilities.

As mentioned in Chapter 3 when comparing the S-parameters, the reference impedance was set to the intrinsic properties of the CNT, instead of 50 Ω, to make the differences in S-parameters visible enough. Here a simple S-parameter example is presented, to demonstrate the influence of the impedance mismatching and the parasitics, an example is shown below.

Figure 5.10 (a) shows the schematic of a graphene strip of 1 unit length and a parasitics of 50fF between the input and output ports. The reflection and transmission coefficients are plotted in Figure 5.10(b) and (c) for the graphene per unit length $R_s = 1.2\text{k}\Omega$ and $R_s = 4\text{k}\Omega$, respectively. It can be seen from Figure 5.11(b) that if the port impedance in Term1 and Term is set as 50Ω, due to significant mismatch, transmission is very low at lower frequencies. As frequency increases, the coupling of parasitic capacitance becomes stronger and the transmission slowly increases while reflection decreases at the same time.

However, the small parasitics is overshadowed by the high impedance of GNR and the results for $R_s = 1.2\text{k}\Omega$ and $R_s = 4\text{k}\Omega$ are indistinguishable from each other. Furthermore, the S11 results are very small, thus are very sensitive to ambient noises, adding large uncertainties to the measurement, especially at low GHz. On the other hand, suppose a matching network is added to the input and output sections of the circuit and make the port impedance increase to 6.5kΩ, and the parasitic capacitance is reduced to 0.05fF, the simulated S-parameters in Figure 5.10(c) shows that the reflection is greatly reduced for low GHz by about 4dB, and the transmission is increased for about 20dB, making a distinguishable from the noise floor. Furthermore, the change in the per unit length

resistance R_s now have an obvious impact on the S-parameters for the entire frequency band simulated. This example shows that proper impedance matching and parasitic reduction is essential in the experimental characterization of an individual GNR or CNT.

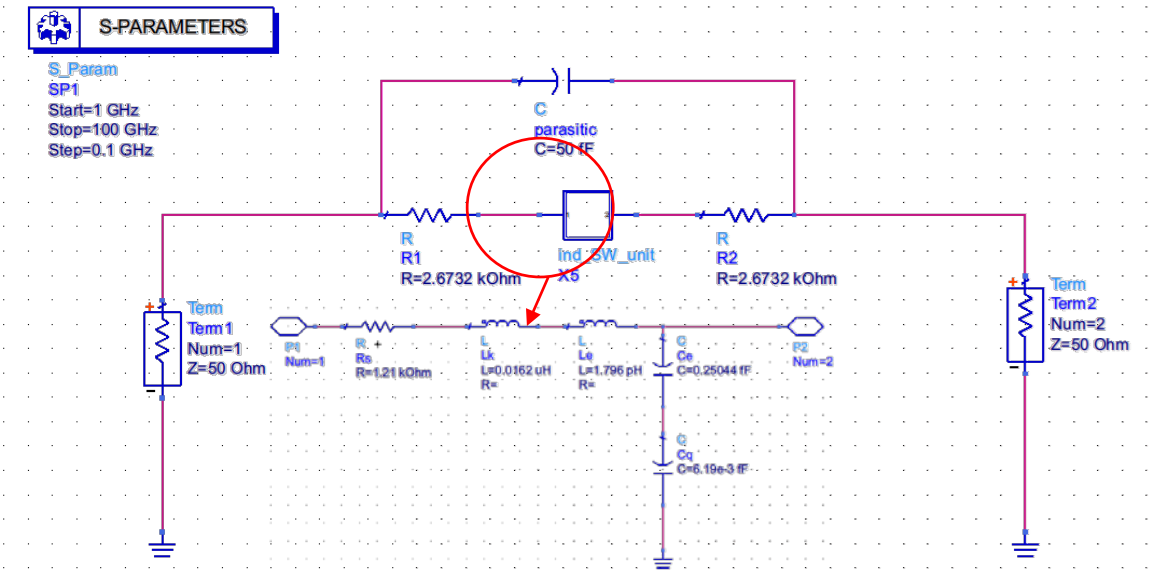

(a)

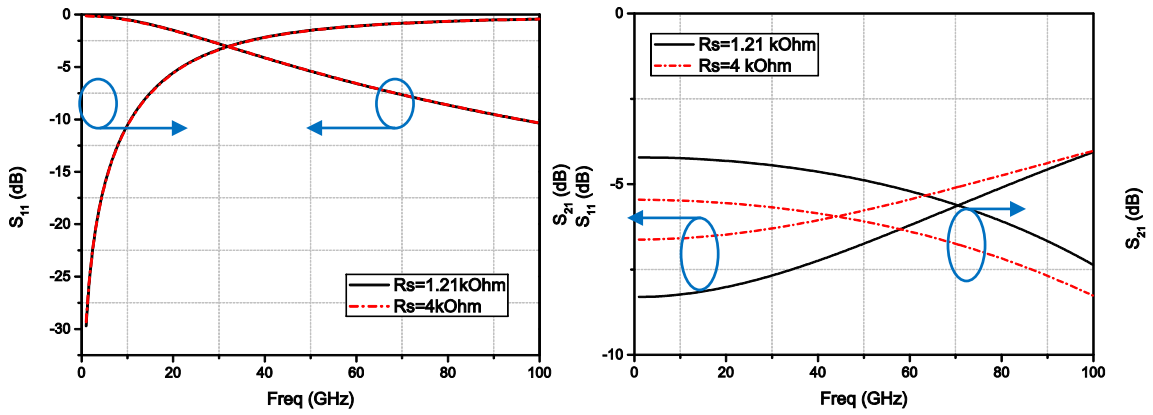

(b) (c)

Figure 5.10 Demonstration of the impedance mismatch and parasitic effect on high-impedance device characterization. (a) Without matching network, $C_{parasitic}$=50fF, (b) Reference impedance in Term1 and Term2 set as 6.5kΩ instead of 50Ω, $C_{parasitic}$=0.05fF.

In 5.3 and 5.4, the conductivity of a GNR patch and the impact of impedance mismatching and To further study the impact from the port impedance, parasitics and contact resistance, the parasitics from a typical microstrip gap are first determined. First of all, the configuration of a 50 Ω microstrip line with gap in the middle and its equivalent circuit model is shown in Figure 5.12(a)

and (b), respectively. The dimensions can be realized by the parameters shown in Table 5.1, where w is the width of the microstrip line, s is the length of the gap, h is the height of the substrate ε_r is the permittivity of the substrate, and a is the width of the GNR.

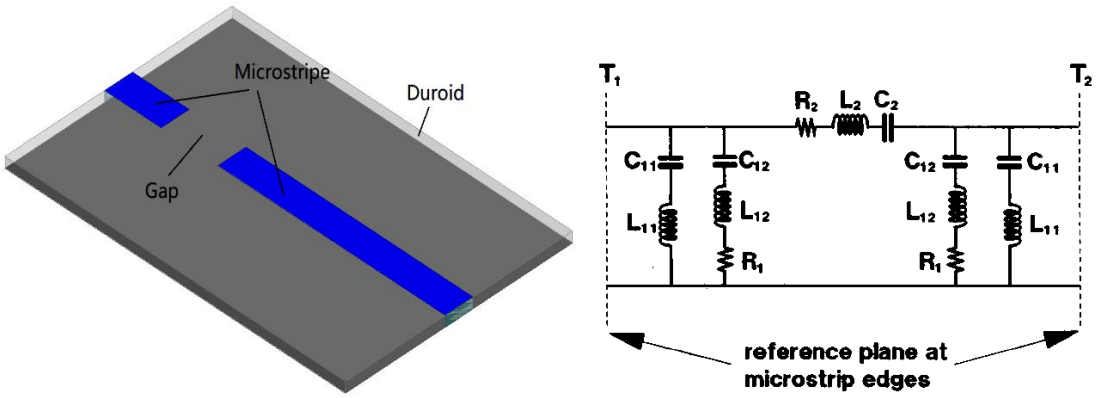

(a) (b)

Figure 5.11 Configuration of a microstrip line with a gap in the middle (a) and its effective circuit model (b).

Table 5.1 Design parameters for a 50Ω microstrip line with a gap in the middle.

ε_r	**h (mm)**	**w (mm)**	**gap (mm)**	**a (nm)**
2.2	0.157	0.478	0.05	30

The equivalent circuit model in Figure 5.11 is frequency independent, and the accuracy has been validated in [177] by comparing the simulation results using the circuit to the result of the full wave analysis.

The values of each parameter in Figure 5.12(b) is also given in [177] as follows:

$$C_{11} = \frac{h}{25Z_0}\left[1.125\tanh\left(1.358\frac{w}{h}\right) - 0.315\right]\cdot\tanh\left[\left(0.0262 + 0.184\frac{h}{w}\right) + \left(0.217 + 0.0619\ln\frac{w}{h}\right)\frac{s}{h}\right] \tag{5.19}$$

$$C_{12} = \frac{h}{25Z_0}\left[6.832\tanh\left(0.0109\frac{w}{h}\right) + 0.910\right]\cdot\tanh\left[\left(1.411 + 0.314\frac{h}{w}\right) + \left(\frac{s}{h}\right)^{1.248+0.36\tan^{-1}\frac{w}{h}}\right] \tag{5.20}$$

$$L_{11} = \frac{hZ_0}{25}\left[0.134 + 0.0436\ln\frac{h}{w}\right]\cdot\exp\left[-\left(3.656 + 0.246\frac{h}{w}\right)\cdot\left(\frac{s}{h}\right)^{1.739+0.39\ln\frac{w}{h}}\right] \tag{5.21}$$

$$L_{12} = \frac{hZ_0}{25}\left[0.008285\tanh\left(0.5665\frac{w}{h}\right) + 0.0103\right] + \left[0.1827 + 0.00715\ln\frac{w}{h}\right]\cdot\exp\left[-\left(5.207 + 1.283\tanh\left(1.656\frac{h}{w}\right)\right)\cdot\left(\frac{s}{h}\right)^{0.542+0.873\tan^{-1}\frac{w}{h}}\right] \tag{5.22}$$

$$R_1 = Z_0\cdot 1.024\tanh\left(2.025\frac{w}{h}\right)\cdot\tanh\left[\left(0.01584 + 0.0187\frac{h}{w}\right)\frac{s}{h} + \left(0.1246 + 0.0394\sinh\left(\frac{w}{h}\right)\right)\right] \tag{5.23}$$

$$C_2 = \frac{h}{25Z_0}\left[0.1776 + 0.05104\ln\left(\frac{w}{h}\right)\right]\frac{h}{s} + \left[0.507 + 0.3615\frac{h}{w} + 1.156\ln\left(\frac{w}{h}\right)\right]\cdot\operatorname{sech}\left(2.3345\frac{s}{h}\right) \tag{5.24}$$

$$L_2 = \frac{hZ_0}{25}\left[0.00228 + \frac{0.0873}{7.52w/h + \cosh\left(w/\mathrm{h}\right)}\right]\cdot\sinh\left(2.3345\frac{s}{h}\right) \tag{5.25}$$

$$R_2 = Z_0 \cdot \left[-1.78 + 0.749\frac{w}{h} \right] \frac{s}{h} + \left[1.196 - 0.971 \ln\left(\frac{w}{h} \right) \right] \cdot \sinh\left(2.3345\frac{s}{h} \right) \tag{5.26}$$

where Z_0 is the characteristic impedance of the microstrip line. The values of these parameters are summarized in Table 5.2.

Table 5.2 Calculated parasitics for a microstrip line with gap in the middle

C_{11}	C_{12}	L_{11}	L_{12}	R_1	C_2	L_2	R_2
1.26fF	5.23fF	0.77nH	1.06nH	25.41Ω	11.23fF	49.22pH	12.64Ω

With the parasitics value obtained, the S11 and S21 coefficients with and without a GNR or CNT array can be simulated. The simulated S-parameters of the GNR or CNT are imported into Agilent Advanced Design Systems (ADS) as an effective component, and added to the circuit model of the microstrip gap, as shown in Figure 5.12.

First, the case in which the structure under test is connected directly to the ports with reference impedance of 50 Ω without any impedance matching network is considered. The GNR array is comprised of 5 stacked GNRs and each stack contains 5 layers of graphene. Each GNR has a width of 30nm, a length equal to the gap length s, a distance of 1um above ground, and a distance of 1um between neighboring GNR stacks. The simulated S11 and S21 with and without the GNR array is shown in Figure 5.13.

It can be seen that the simulated magnitude of S11 is close to 0dB for both a bare gap, which means that most of the energy is reflected. The presence of a GNR array does not affect the S11 much, because the array is small and has a high intrinsic impedance, thus the impact of parasitics dominates. At the same time the magnitude of S21 is very low, especially at low frequencies. This shows that connecting a GNR array directly to a microstrip gap will cause high uncertainties in the measured data obtained from the Vector Network Analyzer (VNA). The phase of the S11 of the gap only and the gap with GNR array are also almost identical and the only simulated data that

shows a good separation is the S21 phase. From the above discussion, it is clear that for a GNR array directly connected to a microstrip gap, most of the S-parameters will not be measureable.

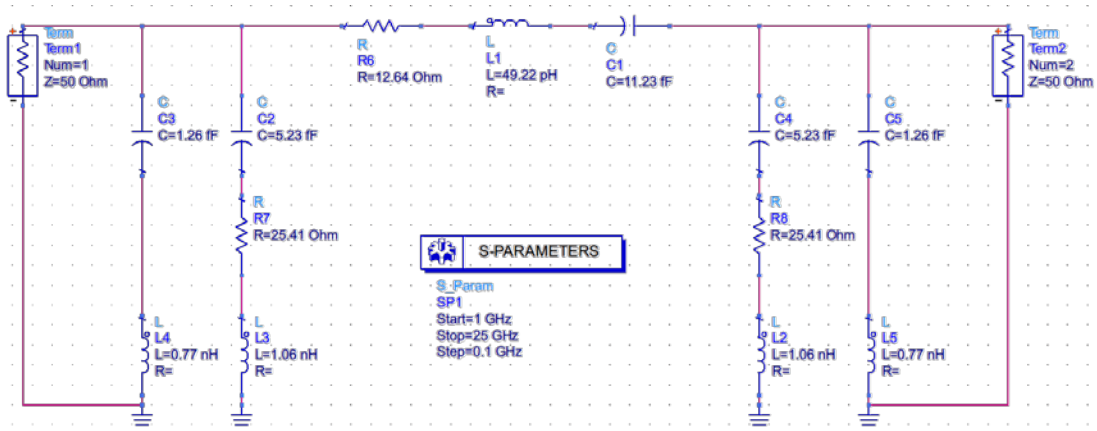

(a)

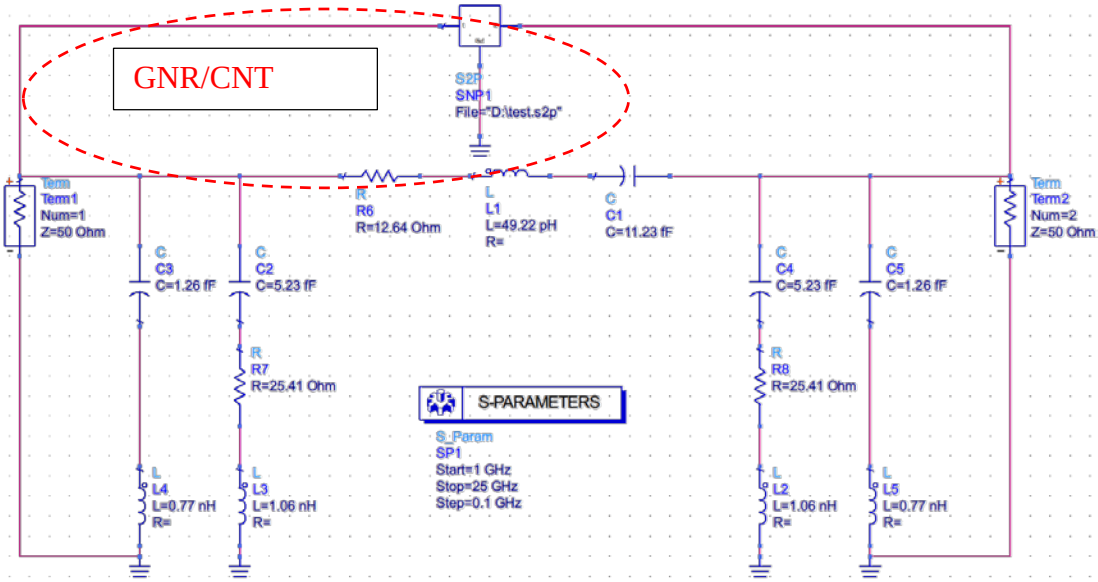

(b)

Figure 5.12 Circuit schematic for S-parameter simulation (a) without and (b) with a GNR or CNT array across the gap.

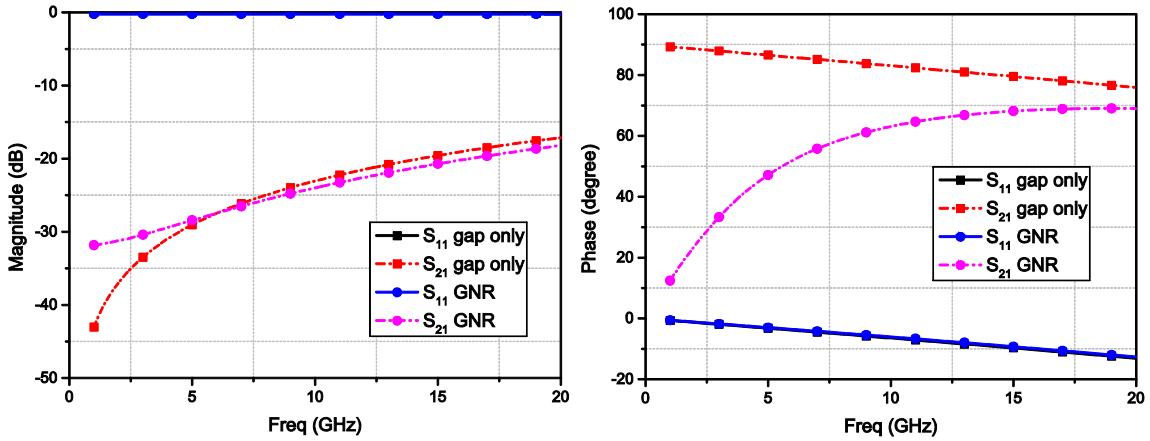

(a) (b)

Figure 5.13 Simulated S11 and S21 in (a) magnitude and (b) phase of only the microstrip gap and the microstrip gap connected by a GNR array. No matching network is present and the reference impedance is 50Ω.

Next, the same structure is simulated with the reference impedance changed from 50Ω to 6.5kΩ. As shown in Figure 5.14, for low frequencies less than 8GHz the S11 is greatly reduced, from 0dB to -10 dB in low frequencies and the S21 is increased from -40dB to -5dB. At this signal level the uncertainties from the VNA can be greatly reduced. At the same time a good separation is also achieved for both magnitude and phase. The worst case is the phase of S11, which provides only ~5º but this can be improved by changing the reference impedance to other values, which can be easily done in simulations.

However, the impedance matching does not completely solve the problem. It can be seen that from 8GHz up, the magnitude of S11 increased to close to 0dB and at the separation is again very poor, as the two curved are almost identical. At the same time, the magnitude of S21 decreases to -20dB, and the separation between the phase of both S11 and S21 becomes very close. Under this circumstances, reducing the parasitics is necessary to the characterization of GNR or CNT arrays.

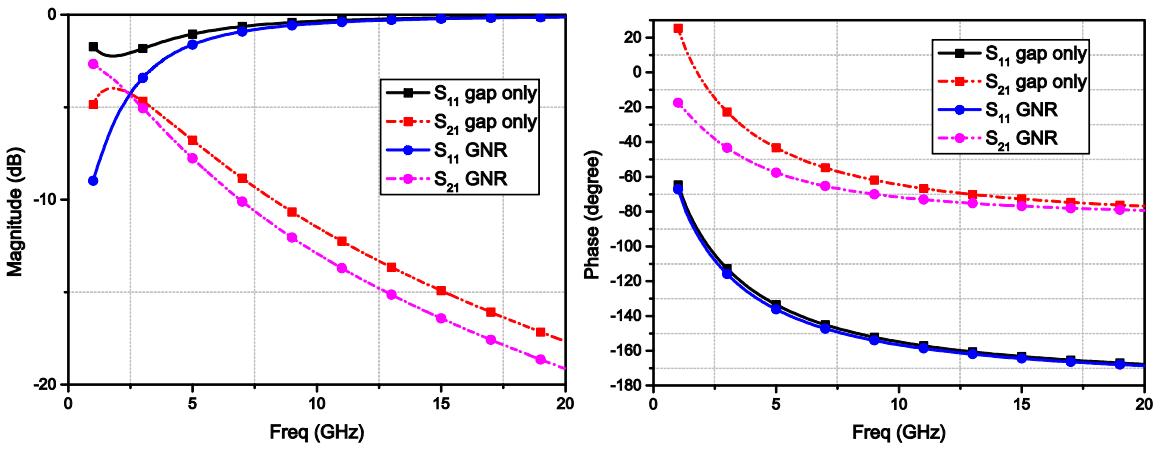

(a) (b)

Figure 5.14 Simulated S11 and S21 in (a) magnitude and (b) phase of only the microstrip gap and the microstrip gap connected by a GNR array. A matching network is present and the reference impedance is 6.5kΩ.

5.4 Equivalent circuit model of very wide GNR

In chapter 2, the conductivity of GNR is calculated from the tight-binding model. It has been shown that when the width of a GNR is as small as several nano-meters, the number of conductive channel, i.e. conductivity normalized to quantum conductance, is equal to 1 if the GNR is metallic and close to 0 if the GNR is semi-conducting. When the width of a GNR is large, the number of conductive channels increases with the width of the GNR, no matter it is metallic or semi-conducting. However, these analysis only shows the number of conductive channels of a GNR up to 100nm and in reality, the RF applications of graphene require macroscopic graphene stripes and patches. In these applications, it is desirable that the number of conductive channels be calculated efficiently without going through the complex equations of the tight binding model. Figure 2.14 shows that when the width of a GNR is sufficiently large, the number of conductive channels starts to converge into a uniform curve, no matter metallic or semi-conducting GNRs. To show more clearly this uniform curve, the relationship between width and conductivity from 100nm to 1um is calculated by the same equation of (2.22) and (2.23), as shown in Figure 5.15. It can be seen that specifically, when the width of a GNR is larger than 100nm, the number of conductive channels increases linearly for both types of GNR.

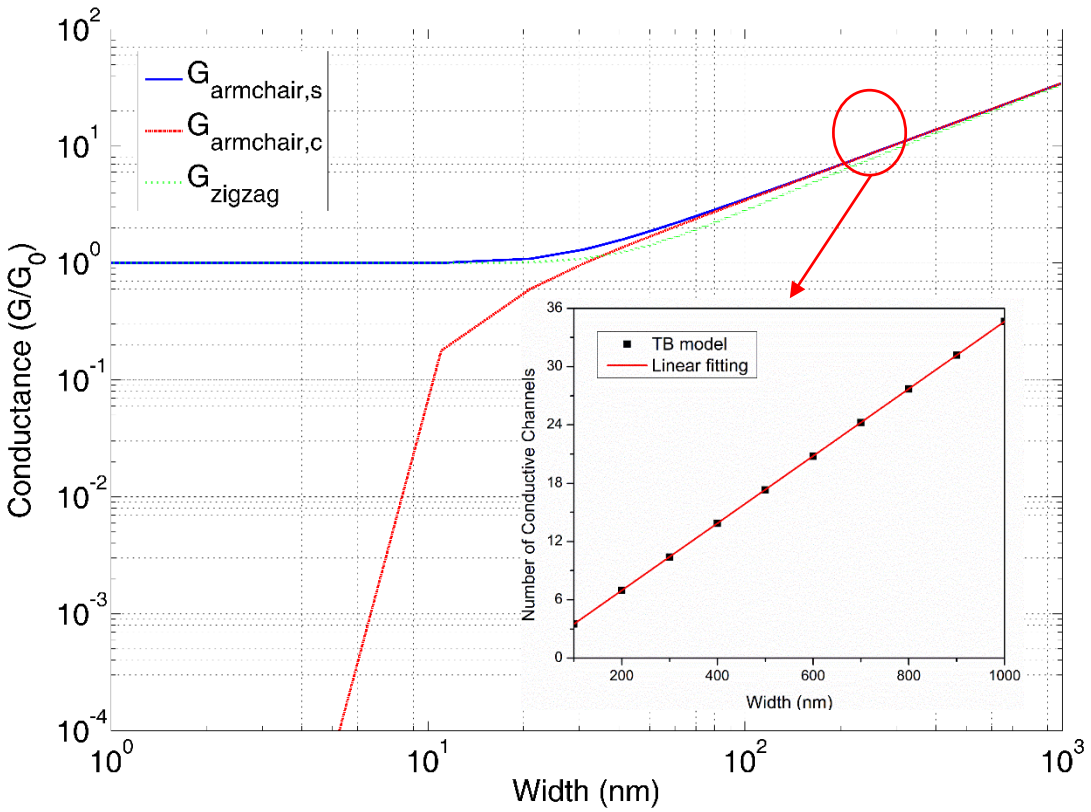

Figure 5.15 Number of conductivity vs width for GNRs. Dots are results of discrete widths obtained by tight binding model, the curve is the linear fitting.

Clearly, the conductivity of both armchair and zigzag GNRs with width larger than 100nm converges to a uniform linear function. Using linear fitting a simple equation can be obtained to calculate the number of conductive channels as

$$N_c = 0.040 + 0.0346 \cdot W \tag{5.27}$$

As discussed in 5.1, the MFP in GNRs are normally several hundred micrometers and can be expressed as a function of width, as shown in (5.6) and (5.8). However, for very large GNR, or a graphene patch, the l_{mfp} cannot grow infinitely and therefore must be derived in another way.

The conductivity of a 2-D graphene patch is given by the well-known Kubo Formula [177]

$$\sigma_D = -j\frac{q^2 k_B T}{\pi\hbar^2(\omega - j2\Gamma)}\left[\frac{\mu_c}{k_B T} + 2\ln\left(1+\exp\left(-\frac{\mu_c}{k_B T}\right)\right)\right] \tag{5.28}$$

where $\hbar$ is the reduced Plank constant, k_B is the Boltzmann constant, ω is the angular frequency, T is the temperature and Γ is the electron scattering rate.

In the absence of a bias field, the chemical potential $\mu_c = 0$ and (5.21) becomes

$$\sigma_D = -j\frac{q^2 k_B T}{\pi\hbar^2(\omega - j2\Gamma)}\cdot 2\ln 2 \tag{5.29}$$

On the other hand, for the limit of $W \to \infty$ the conductivity of a GNR is expressed as [167]

$$\sigma_D = \frac{2q^2}{h}\cdot\frac{\pi l_{mfp}}{h v_F}\cdot 2k_B T\ln 2 \tag{5.30}$$

By combining (5.29) and (5.30), the MFP can be derived as

$$l_{mfp} = \frac{-j2v_F}{\omega - j2\Gamma} \tag{5.31}$$

Equation (5.31) gives the MFP of a 2-D graphene patch in the absence of bias field. So the total per unit length sheet resistance of the macroscopic graphene strip or patch can be determined by (5.1).

5.5 The impact of contact resistance

In the previous sections, the contact resistance are all neglected and perfect metallic contact are assumed. However, in reality, the contact resistance between GNR or CNT arrays with metal can range from several hundred ohms to several hundred kilo-ohms [178], [179] and thus can greatly affect the design and measurement of graphene or CNT based nano devices. To demonstrate the impact of the contact resistance, a macroscopic graphene patch is simulated using the number of

conductive channels N_c and the MFP l_{mfp} described in (5.19) and (5.24). The dimensions of the graphene patch and the corresponding microstrip line is summarized in Table 5.3.

Table 5.3 Calculated parasitics for a microstrip line with gap in the middle

ε_r	**h (mm)**	**w (mm)**	**gap (mm)**	**a (mm)**
2.2	1.58	4.89	10	10

From 5.2, it is clear that the increase of a GNR's width will reduce its resistivity. So it is expected that for such a wide graphene patch, the resistivity will be greatly reduced and even a direct connection to the 50Ω reference impedance without any matching network will not give nearly 0dB reflection. So first of all, we check the influence of parasitics for the 10mm x 10mm graphene patch.

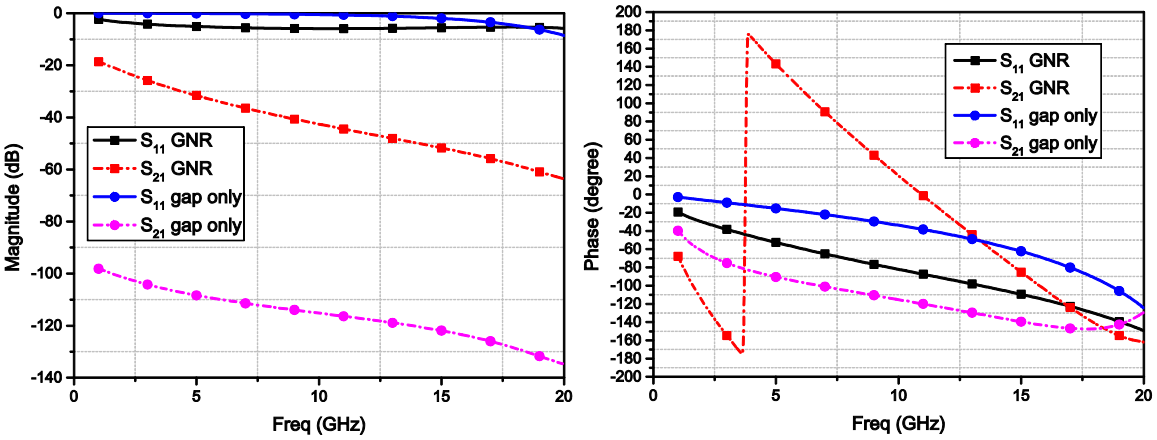

(a) (b)

Figure 5.16 Simulated S11 and S21 in (a) magnitude and (b) phase of only the microstrip gap and the microstrip gap connected by a 10mm x 10mm graphene patch. No matching network is present and the reference impedance is 50Ω.

Figure 5.16 shows the Simulated S11 and S21 in (a) magnitude and (b) phase of only the microstrip gap and the microstrip gap connected by a 10mm x 10mm graphene patch. No matching network is present and the reference impedance is 50Ω. Clearly, as the gap is very wide, the parasitics that connects across the gap is very weak and thus the S21 is very low and can be considered as non-existent. When the GNR patch is connected, the S-21 increases greatly from -100dB to -20dB, and gradually decreases to noise floor.

Nevertheless, both the magnitude and phase of the S-parameters show a good separation between the gap with and without graphene. It means that for a graphene patch, the impact of parasitics are no longer significant and it is much easier to characterize graphene patch as a 2-D surface.

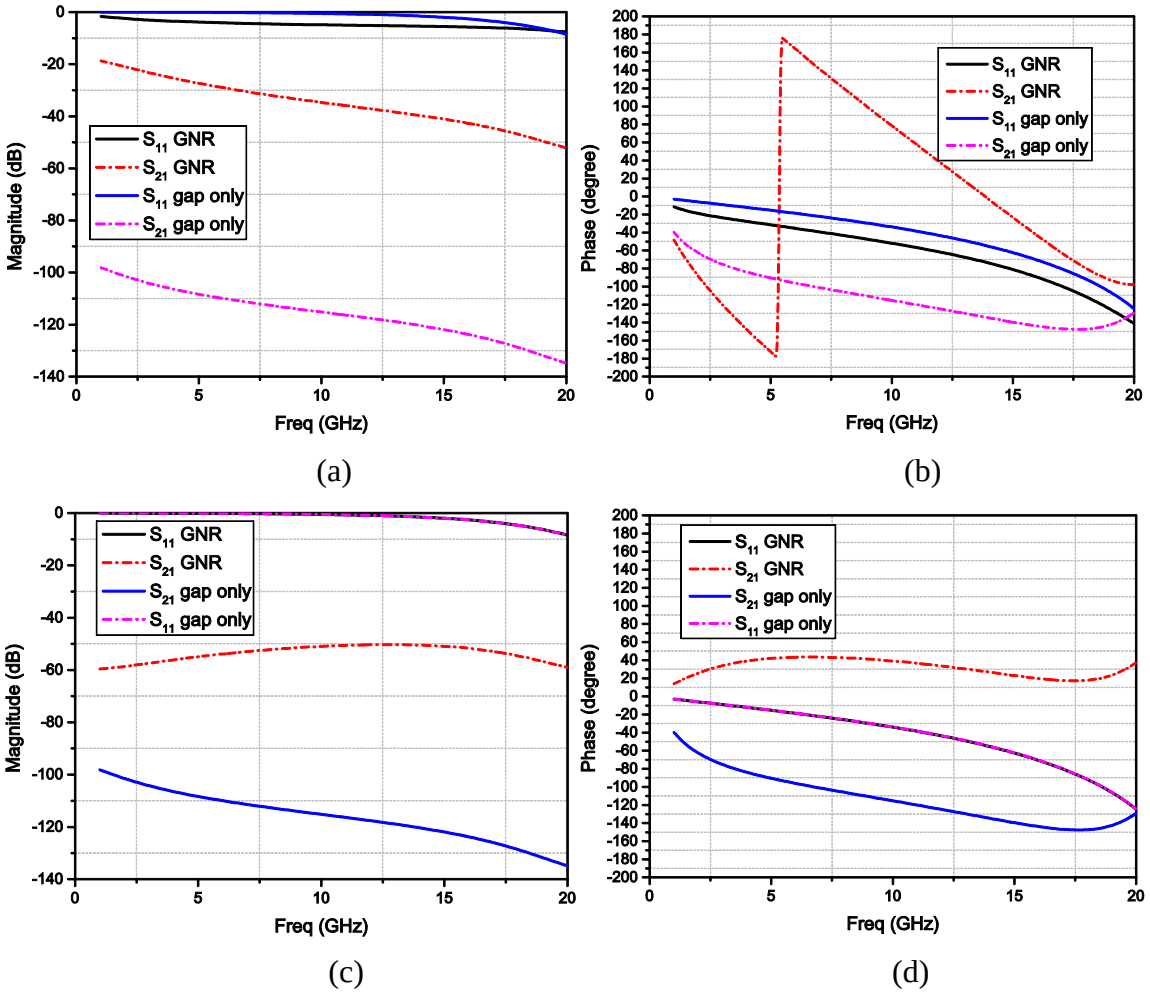

Figure 5.17 Simulated S11 and S21 in magnitude and phase of only the microstrip gap and the microstrip gap connected by a 10mm x 10mm graphene patch. No matching network is present and the reference impedance is 50Ω. The contact resistance is 50 Ω in (a) and (b), and 50kΩ in (c) and (d), respectively.

The impact of contact resistance is shown in Figure 5.17. The parasitics is set as 0.1fF. In Figure 5.17(a) and (b) the magnitude and phase with and without the patch with contact resistance of 50Ω is shown. It can be seen that with a small contact resistance, the results with and without the patch have a clear separation. The signal level is close to 0dB for S11 and is low but still measurable in low frequencies for S21. However, for the contact resistance of 50kΩ, Figure 5.17 (c) and (d) shows that the magnitude of S11 becomes identical without any separation, and the magnitude of S21 are too low to be measurable. The same applies to the phase result.

In this way, the conclusion can be drawn that compared to the GNR, it is possible to characterize the graphene patch without the need to build the matching network, as long as the contact resistance can be kept low. This requires high quality metal contact in the interface of graphene and the testing fixture. Otherwise, a matching network is still needed.

Finally, a fitting result of the parasitics and the contact resistance is presented. A 10mm x 10mm graphene patch as described above are measured with the microstrip gap, and by optimization of the contact resistance and parasitic capacitance, the simulation and measurement result can be matched.

The graphene sample was synthesized by thermal CVD in a cold–walled, commercially available reactor (Aixtron Ltd., Black Magic). 500 nm–thick copper was magnetron sputtered onto 200 nm thermally oxidized Si h100i subsequently annealed at 850 8C for 30 min in a 20:1500 standard cubic centimeters per minute H2:Ar atmosphere at 4 mbar.20 Graphene growth was initiated by introducing 7 sccm CH4 (99.9%) under maintained H2 (99.98%) and Ar (99.998%) dilution. All samples were cooled to room temperature under ultra–high purity N2 (99.999%). Temperatures were monitored using two type K bimetallic thermocouples and a surface infrared interferometer. Pressures and temperatures were accurate to within $\pm$ 1 mbar and $\pm$ 1°C, respectively. Standard FeCl wet–etching and poly (methyl methacrylate)–mediated graphene transfer were used [207]. The sample is then immersed in an aqueous ammonium persulfate $((NH_4)_2S_2O_8)$ for 12 hours to etch the Cu catalyst. The floating PMMA-graphene films were transferred to water baths using a microscope glass slide and rinsed several times to remove the etchant and residual contaminants [208]. The sample is then transferred on to optically fused quartz substrate and placed upside down

to cover the gap of the microstrip, so that the graphene and copper has contact. The detailed setup is shown in Figure 5.18.

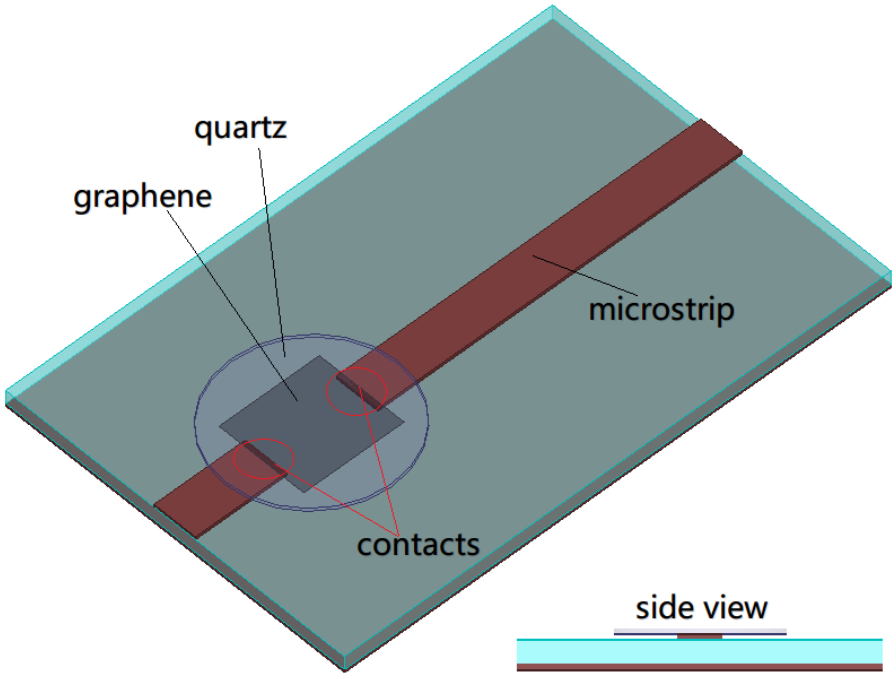

Figure 5.18 Experimental setup of the contact resistance characterization of the graphene-copper contact.

First of all, considering the parasitics introduced by the graphene sheet, as shown in Figure 5.19. The parasitics are first optimized in ADS to match the result in full-wave simulation software HFSS, as shown in Figure 5.20.

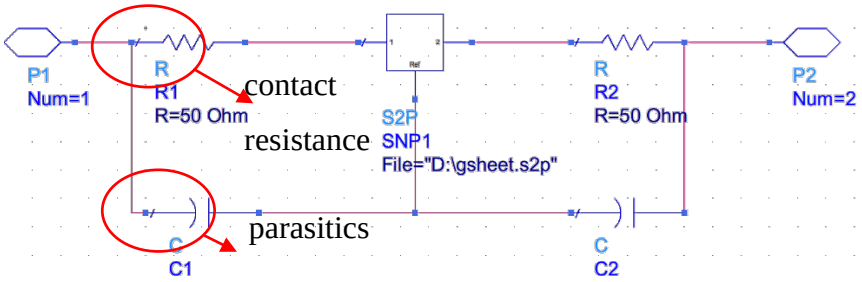

Figure 5.19 Schematic view of a graphene sheet with contact resistance and parasitic capacitance.

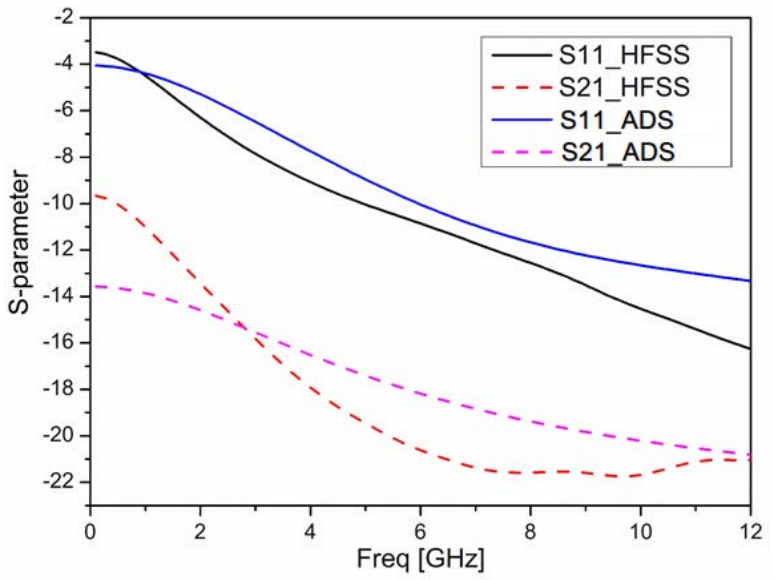

Figure 5.20 Matching of the parasitics between ADS and HFSS.

From Figure 5.20, it can be seen that with the optimization of parasitics, the simulation S-parameter simulation from ADS result matches with the full wave simulation in HFSS. Next, the contact resistance is optimized to match the result of the measurement, as shown in Figure 5.21.

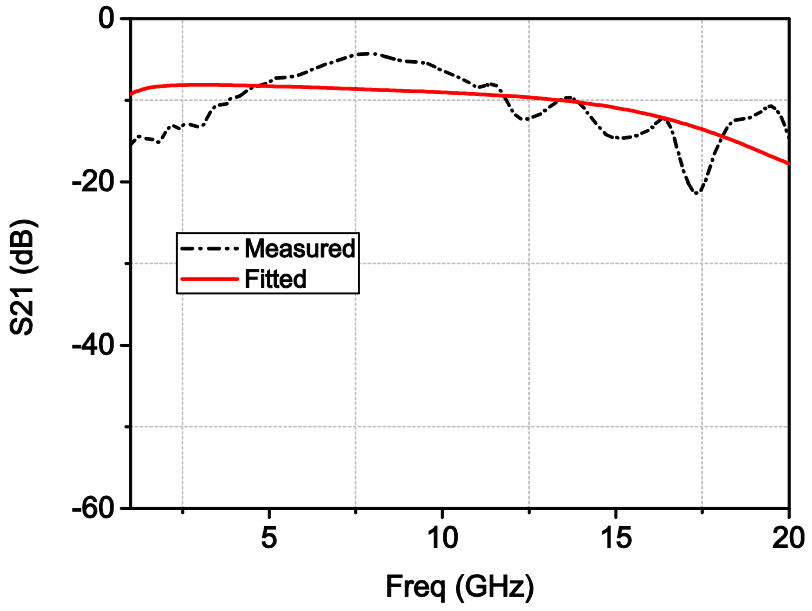

Figure 5.21 Simulated and measured S21 by the optimization of contact resistance.

By the optimization of parasitics and the contact resistance, the simulated and measured transmission are matched. The two curves does not match each other perfectly because the sample being measured was a 5 layer graphene patch with a quartz substrate. The difference between the fitted and measured data can be explained by the existence of the quartz substrate, as well as liquid residuals in between layers of graphene. The final value of parasitic capacitance and contact resistance are 2.39pF and 3.23kΩ, respectively. The width of the microstrip line is 5mm and the contact lengths at each side is about 2mm. Assuming the thickness of a single layer graphene is 0.34nm, this gives the contact resistivity of $\rho_c = 5.5\times10^{-9}\ \Omega\cdot\mathrm{m}^2$, which is well within the previously reported values [209]-[212]. In addition, it appears that the parasitic capacitance are very large (in the pF scale) compared to the parasitics of the microstrip gap.

5.6 Summary

In this chapter, the transmission line model is applied to GNR. The mutual couplings between vertically and horizontally neighboring GNRs are first briefly reviewed, and the simulated S-parameters, input impedance and absorption are compared to the CNTs with a same circumference.

The GNR array and CNT arrays have a similar transmission and absorption properties with high intrinsic impedances. Unlike CNTs, increasing only the width of a GNR does not change the input impedance or absorption much, due to the GNRs' flat nature. Thus, increasing the width of the GNR cannot effectively increase the number of conductive channels. However, the magnitude of the GNR's input impedance and absorption decreases significantly faster with stacking and arrays than that of CNTs. So GNR arrays are better candidates than CNT arrays for nanoscale applications that requires low loss, especially in microwave frequencies. Unlike the case of CNT, increasing the temperature slightly reduces the normalized absorption of GNR arrays, which makes the GNR to perform better than CNT in low frequencies, where the changing of temperature does not significantly shift the input impedance.

The impact of parasitics and contact resistance for the characterization of a small GNR or CNT arrays are discussed. It has been shown that due to the high intrinsic impedance, the parasitics will dominate if the array is connected directly to the normal 50Ω testing environment. An example of a GNR array placed in between a mircostrip line with gap clearly demonstrates that as a result, the

S11 will be close to 0 dB and S21 close to the noise floor, furthermore, the measured results with and without the array under test will be indistinguishable from each other. However, a matching network from 50Ω to several kΩ can effectively solve such problems. A quarter wavelength stepped impedance transformer can be used to build the matching network, as it is natural to connect the different width between microstrip line and the GNR array without further introducing discontinuities.

Finally, a gapped microstrip line covered with a thermal CVD synthesized graphene sheet is analyzed using TL model for very wide GNRs. The contact resistance between copper and graphene is characterized and compared with published records. It shows that the contact conductivity is well within the range of previous measurements.

Chapter 6 Applications of Tunable Graphene Devices in Microwave Frequencies

6.1 Introduction

Currently research has shown that graphene's applications are mainly in THz and optics. The low real part of the impedance and high imaginary part of the impedance at these frequencies have been shown to be very promising in applications of surface plasmons. Several work has been presented ranging from THz waveguides [180], filters [57, 58] to mixers [181]. Also an effective circuit model for THz plasmon transmission has been proposed [182, 183]

On the other hand, the application of graphene in microwaves have not been attracting too many attention, due to the high loss and difficulty of matching, the application related to transmission is limited to a few areas such as graphene based RF transistors [39], [184], FET mixers [185-187] and tunable resistive devices such as metasurfaces [188] and absorbers [15], [16]. Moreover, current tunable designs mainly focuses on the tuning of chemical potential by applying an electric bias to the graphene, and overlooks the tenability of the magnetic field.

In this chapter, the tensor conductivity of the graphene are first studied to show the influence of both the electric and magnetic field on the conductivity of graphene. Second, a tunable stacked graphene absorber is proposed and its absorbing performances for TE and TM wave under both biases are presented.

6.2 Resonant absorbers

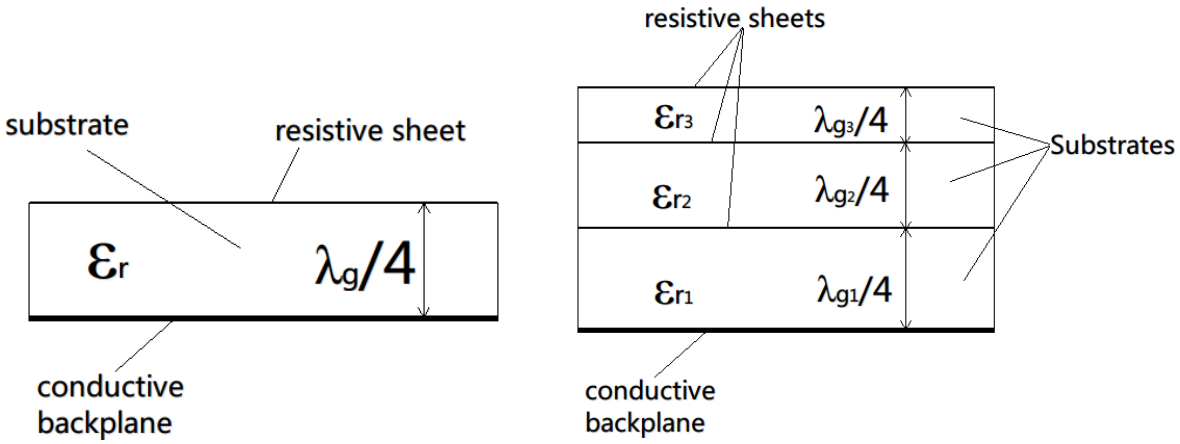

(a) (b)

Figure 6.1 Basic structure of a (a) Salisbury screen and (b) Jaumann screen.

Electromagnetic absorbers are specifically chosen or designed materials that can inhibit the reflection or transmission of electromagnetic radiation. In microwave frequencies, absorbers are useful for many applications such as electromagnetic shielding of electronic circuits and computers [189], cavity resonation reduction [190] and the walls of anechoic chambers. Many absorbing materials and structures [191] have already been used in these fields and graphene for its good absorbing performance in microwave frequencies and very small thickness, has become a new candidate for microwave absorbers. The three main advantages of graphene over other materials are that it is optical transparent and can be seamlessly integrated on other transparent substrates such as glass, that it is flexible, thus can be placed on conformal surfaces, and that it is tunable with both electrostatic and magnetostatic bias field.

The simplest type of resonant absorber is the Salisbury screen [192], which is comprised of a thin conductive sheet placed in front of a conductive backplane. The distance between the two layers is $\lambda_g / 4$, where λ_g is the wavelength in the material between two sheets. As can be expected, a Salisbury screen is narrow band, and can only cope with the normal incidence case. To increase the bandwidth, the Jaumann screen [193] extends the Salisbury screen to multiple layers. It is comprised of the several parallel layers of resistive sheet placed in front of the backplane, with the

distance between each layer being a quarter wavelength in the material that fills the space between them. A demonstration of the structure of these two absorbers are shown in Figure 6.1.

6.3 2-D sheet conductivity of graphene

The 2-D graphene sheet can be characterized by a conductive layer without thickness. The surface conductivity of the graphene is described by the Kubo-Formula. Here, we consider the tensor conductivity of the graphene to include the magnetic bias into consideration, as discussed in Chapter 2.

Under room temperature and low magnetic bias conditions, the original equation of (2.13)-(2.17) can be simplified as [109]

$$\sigma_{d,\text{intra}} \approx -j\frac{q^2 k_B T}{\pi\hbar^2(\omega - j2\Gamma)}\left(\frac{\mu_c}{k_B T} + 2\ln(e^{-\frac{u_c}{k_B T}} + 1)\right) \tag{6.1}$$

$$\sigma_{d,\text{inter}} \approx \frac{-jq^2}{4\pi\hbar}\ln\left(\frac{2|\mu_c| - (\omega - j2\Gamma)\hbar}{2|\mu_c| + (\omega - j2\Gamma)\hbar}\right) \tag{6.2}$$

$$\sigma_{o,\text{intra}} = \frac{-q^3 v_F{}^2 B_{bias}}{\pi\hbar(\omega - j2\Gamma)^2}\left(1 - 2\left(e^{-\frac{\mu}{k_B T}} + 1\right)^{-1}\right) \tag{6.3}$$

where ω is radian frequency, μ_c is chemical potential, Γ is a phenomenological scattering rate, T is temperature, q is the charge of an electron, $\hbar$ is the reduced Plank's constant and k_B is the Boltzmann's constant. Clearly, (6.1) and (6.2) are independent of B_{bias} and (6.3) is a linear function of B_{bias}.

In room temperature and for frequencies below the THz regime, the intraband contribution of the tensor conductivity $\sigma_{o,\text{inter}}$ is very small compared to the intraband term and thus can be neglected [109].

It is worth pointing out that (6.1) and (6.3) are only valid for small magnetic limit. To demonstrate the impact of increasing the of magnetic bias on the accuracy of the simplified equation, the conductivity of a 2-D graphene is calculated using (2.13)~(2.17) and (6.1)~(6.3) from 1GHz to 50GHz, respectively. The chemical potential is set to $\mu_c = 0.1eV$, the scattering rate is $\Gamma = 0.11\text{meV}$ and different values of B_{bias} were simulated to show the applicable range of the simplified equations.

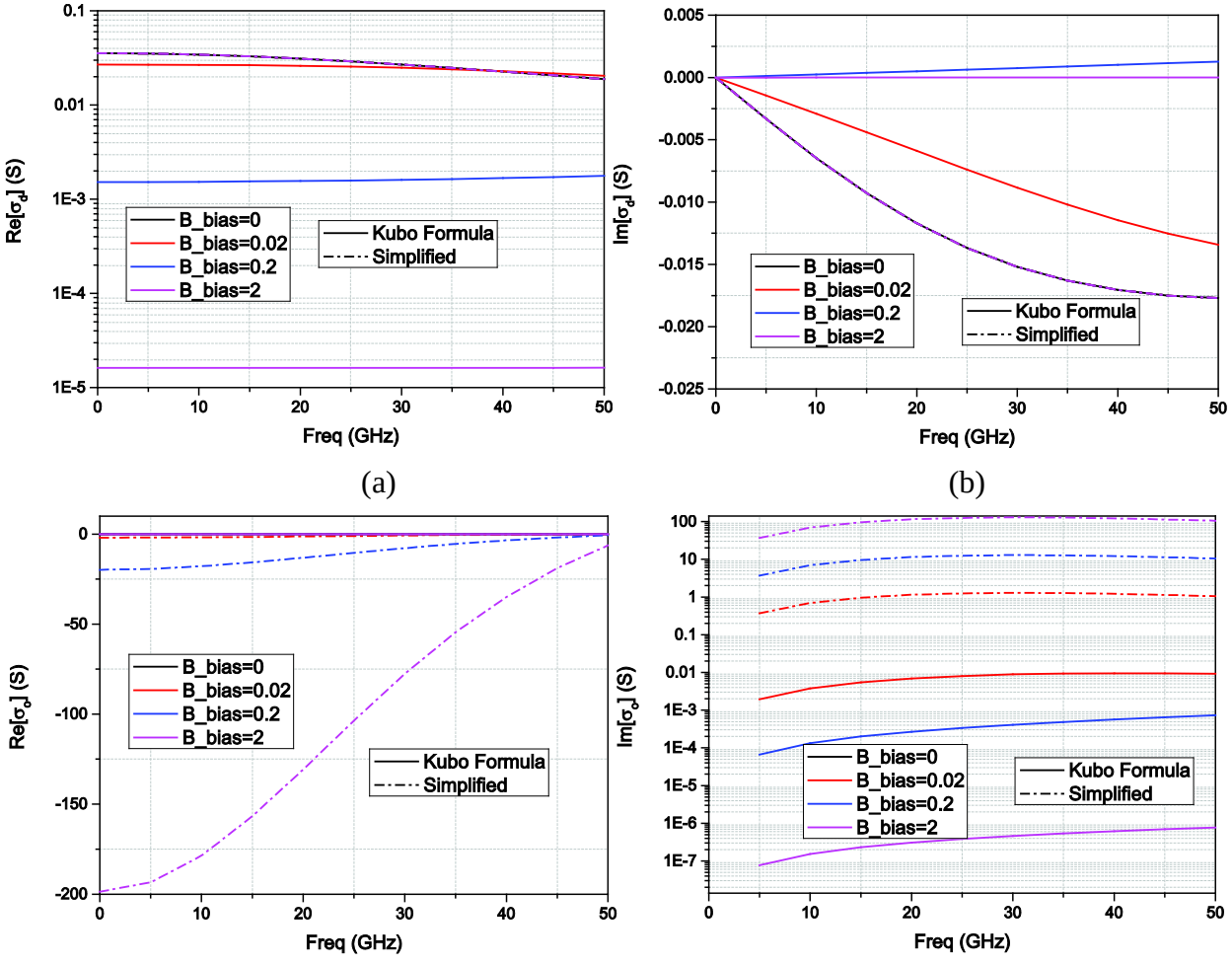

Figure 6.2 Simulated anisotropic conductivity of a 2D graphene sheet under both electric and magnetic bias. (a) and (b) are the real and imaginary part of σ_D, (c) and (d) are the real and imaginary part of σ_O.

Figure 6.2 shows that in the absence of the magnetic bias, the simplified equation gives exactly the same results with the original formula, but with the increase of the magnetic bias, the conductivity obtained from the simplified equations are no long accurate, especially for the Hall conductivity σ_0. Figure 6.2 (c) and (d) shows that the simplified equation gives the conductivity 3 orders higher than the Kubo Formula, even for $B_{bias} = 0.02T$, which is the smallest bias field simulated. It is now clear that the simplified model is only valid for very small B_{bias}, specifically, in the case of B_{bias} 0.01. Figure 6.3 also shows that the anisotropic conductivity component σ_d and σ_0 does not change linearly with the change of the magnetic bias. For example, the imaginary part of σ_d is higher when $B_{bias} = 0.2\,\mathrm{T}$ than $B_{bias} = 2\,\mathrm{T}$, and the imaginary part of σ_0 takes minimum when $B_{bias} = 0$ and maximum when $B_{bias} = 0.02\,\mathrm{T}$. These facts suggests that for each μ_c and Γ there is a specific B_{bias} where the σ_d or σ_0 takes maximum or minimum values, which is useful in the tuning of graphene resonant absorbers.

6.4 Modeling of the stacked graphene absorber

The graphene has a rich potential as absorbers. An almost total absorption at near infrared frequencies has been proposed in [213] and experimentally verified in [214]. The absorber was realized by coupling the graphene absorption to a guided resonance of a photonic crystal slab. The utilization of photonic crystal guided resonances provide a particularly effective mechanism for critical coupling into graphene, as the graphene has a high transmittance and a low single-pass absorption relatively independent of the frequency at infrared frequency, minimizing perturb to the photonic crystal below. So the design and tuning of the absorber can be focused on the design of photonic crystals itself. Another different design of total absorber at optical frequencies was proposed in [215] by utilizing periodic arrays of graphene disks. Apart from the normal incidence case, the design also discussed the absorption of incident angle ranging from 0 to 90 ℃. A multi-layer wide band absorber from microwave to THz has been proposed in [216].

The aforementioned designs, however, either focuses on optical frequencies, and required patterning of graphene or complex preparation of photonic crystals, or lacking the discussion of

the tunability of the graphene absorber under external bias. In this section, a single and multi-layered graphene absorber with simple structure is proposed and their tunability under electric and magnetic bias is discussed. Furthermore, the influence of different incident angle on absorption of both single and multi-layered graphene is also discussed.

6.4.1 Single layer, single stack of graphene

The geometry configuration and effective circuit model of a single-layered graphene absorber is shown in Figure 6.2. In this structure, the resistive sheet is comprised of only 1 stack of graphene.

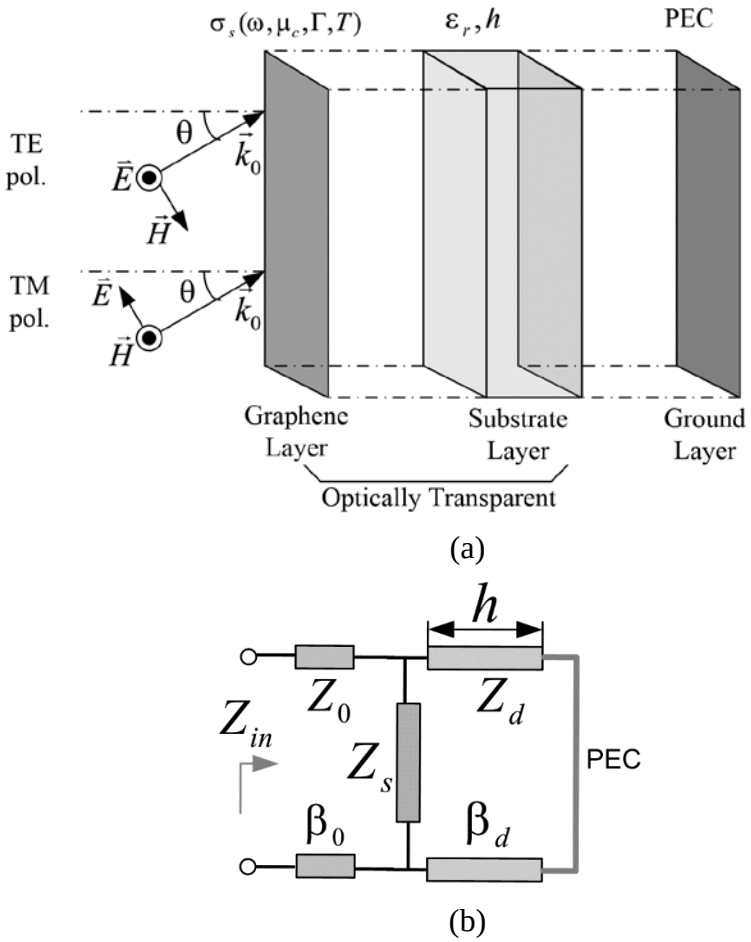

Figure 6.3 A single layer of graphene on top of a dielectric substrate (a) geometric configuration and (b) equivalent circuit model.

The graphene layer is placed on top of a dielectric substrate, which has a perfect conducting plane as ground at the bottom. The dielectric substrate has the relative permittivity of ε_r, the height of h.

The effective circuit model in Figure 6.2(b) shows that the graphene sheet suspended on top of the ground layer can be represented by a resistive sheet with a characteristic impedance $Z_s = 1/\sigma_s = R_s + jX_s$, where R_s is the sheet resistance and X_s is the sheet reactance. The substrate can be represented by a transmission line segment with propagation constant of β_d and characteristic impedance of Z_d. Finally the characteristic impedance and propagation of free space is Z_0 and β_0.

The analytical expression for TE and TM polarized wave with incident angle θ can be expressed as [194]

$$k_0 = \frac{\omega}{c}, \beta_0 = k_0 \cos\beta, \beta_d = k_0\sqrt{\varepsilon_r - \sin^2\theta} \tag{6.4}$$

$$Z_0 = \begin{cases} \dfrac{\eta_0}{\cos\theta} & \text{(TE)} \\ \eta_0 \cos\theta & \text{(TM)} \end{cases} \tag{6.5}$$

$$Z_d = \begin{cases} \dfrac{\eta_0}{\sqrt{\varepsilon_r - \sin^2\theta}} & \text{(TE)} \\ \dfrac{\eta_0\sqrt{\varepsilon_r - \sin^2\theta}}{\varepsilon_r} & \text{(TM)} \end{cases} \tag{6.6}$$

where c is the speed of light in vacuum, ω is the angular frequency, and $\eta_0 = \sqrt{\mu_0/\varepsilon_0} = 377\Omega$ is the intrinsic wave space of the free space.

With the presence of a magnetic bias, Z_s is given as [113]

$$Z_s = \begin{cases} \left(\sigma_D + \dfrac{\sigma_o^2}{2Y_0^{TM} + \sigma_D} \right)^{-1} & \text{(TE)} \\ \left(\sigma_D + \dfrac{\sigma_o^2}{2Y_0^{TE} + \sigma_D} \right)^{-1} & \text{(TM)} \end{cases} \tag{6.7}$$

With the value of Z_s, Z_0 and Z_d known, the total input impedance of the effective circuit in Figure 6.3(b) is given by

$$Z_{in} = \frac{Z_s Z_d}{Z_d - jZ_s \cot\left(\beta_d h\right)} \tag{6.8}$$

The wave will be totally reflected by the ground plane, so the transmission (S_{21}) is 0. The absorption and reflection of the graphene absorber is

$$S_{11} = \frac{Z_{in} - Z_0}{Z_{in} + Z_0} \tag{6.9}$$

$$A = 1 - \left|S_{11}\right|^2 \tag{6.10}$$

From (6.8) and (6.9) it is clear that the highest absorption is achieved when $Z_{in} = Z_0$, aka, the case of impedance matching.

As an example, we consider a graphene sheet with a chemical potential μ_c of 0eV, 0.1eV, 0.2eV and 1eV respectively. The scattering rate Γ is 5meV and the $B_{bias} = 0$, i.e. only the electric bias is present. The substrate is quartz with a relative permittivity of $\varepsilon_r = 3.8$ and a thickness h of =3 mm. The absorber is simulated from 1GHz to 100GHz. Figure 6.4 shows the simulated S11 and absorption.

Across the entire simulated frequency range, several absorption peaks occur, and while the magnitude of the maximum absorption changes with the chemical potential, the frequencies where the absorption reaches maximum remains the same. From (6.10) it is obvious that each absorption

peak appears at the frequency where S11 is minimum. For $\mu_c = 0$, the maximum absorption is only 30%, but for $\mu_c = 0.2\,\mathrm{eV}$, the maximum absorption is more than 90%. However, continue to increase the chemical potential will lead to the decrease in the maximum absorption, because the characteristic impedance of the graphene sheet no longer matches that of the free space. However, the bandwidth of the absorber appears to increase with the increase of the chemical potential.

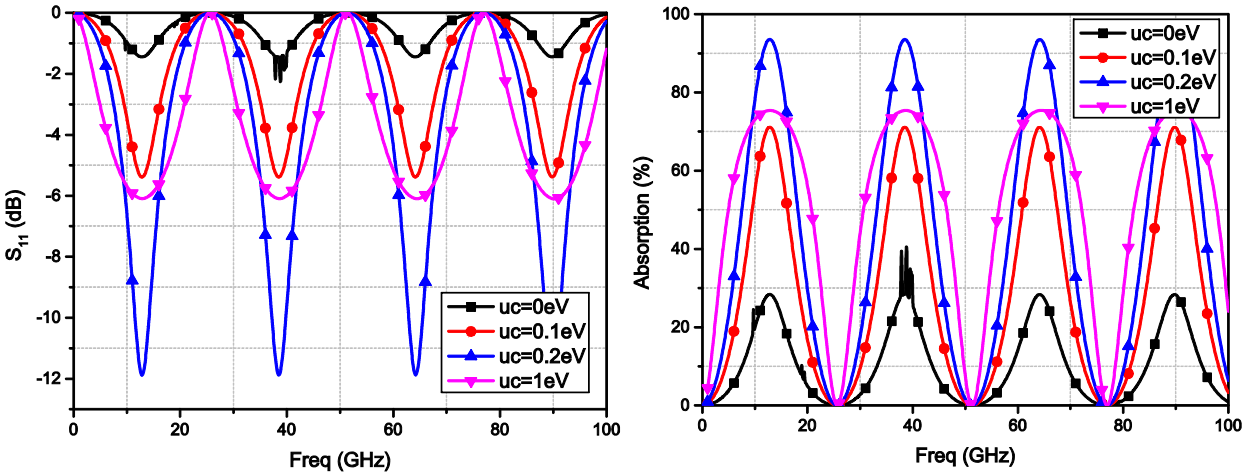

(a) (b)

Figure 6.4 Simulated (a) S11 and (b) absorption for a graphene microwave absorber with different chemical potential, i.e. electric bias.

The absorption for different substrate thickness is also simulated, as shown in Figure 6.5. It appear the the first absorption peak appears at the fundamental resonant frequency $f_0 = c / 4h\sqrt{\varepsilon_r}$ and the periodic absorption peak appear at $f_i = (2i-1) f_0$ (where i=1, 2,…). As the thickness h increases, both the resonant frequency and the bandwidth for each absorption peak is decreased accordingly.

For the wave incidence not normal to the graphene sheet, the case with a thickness of quartz h =1.3mm is simulated with all other parameters the same with previous cases. The absorption spectra of the proposed absorber with different incident angles are shown in Figure 6.6. First of all, the result indicates that the proposed graphene-based absorber keeps good absorption ability for most incident wave cases, for the worst case scenario, the absorption decreases from 95% to

70%, which is still good for such a large incident angle. As the incident angle increases from 0° to 60°, the absorption peaks and the resonant frequencies slowly increases for the TE polarization, while for the TM polarization, the absorption peaks decreases relatively quickly, compared to the speed of the increase of the TE polarization.

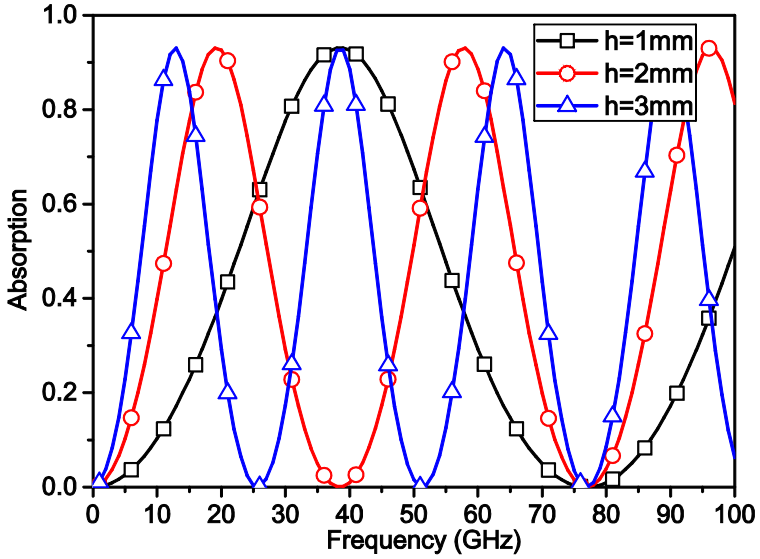

Figure 6.5 Absorption spectra of the graphene-based microwave absorber with different thickness of transparent quartz slab. The chemical potential is fixed, $\mu_c = 0.2\text{eV}$

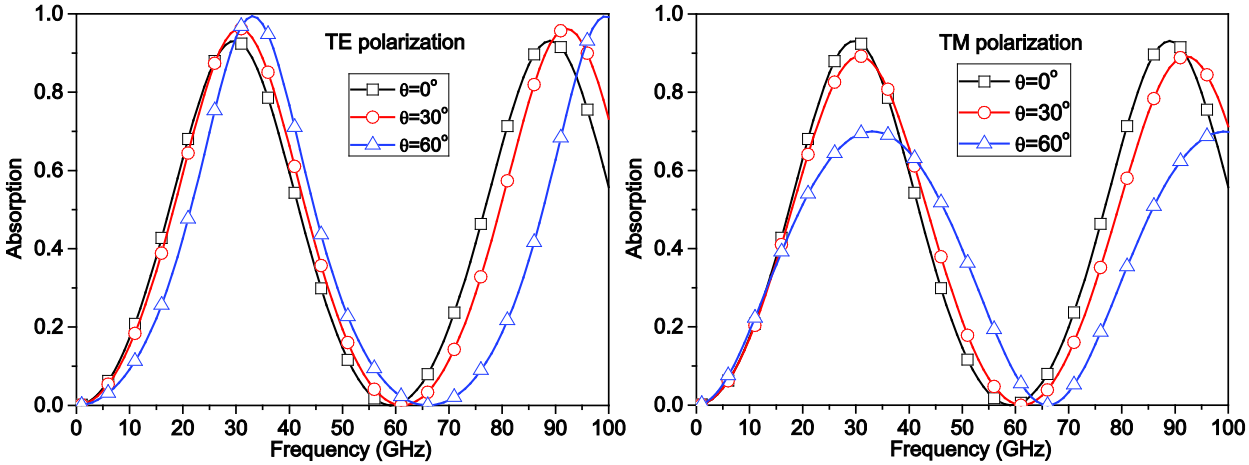

(a) (b)

Figure 6.6 Absorption spectra of the graphene-based microwave absorber with different incident angles. (a) TE polarization. (b) TM polarization.

Next, the magnetic bias is added to the graphene absorber with a chemical potential of $\mu_c = 0.1\text{eV}$. The bias B_{bias} is 0.02T, 0.2T, and 2T respectively. It needs to be point out that the infinite series of the Kubo formula converges very slowly, especially for small magnetic bias. Therefore the simulation frequency is reduced to up to 50GHz, and meanwhile the substrate thickness h is set as 3mm. From Figure 6.5 it is clear that the first absorption peak appears at 12GHz, so 50GHz is enough to observe at least 1 absorption peak. The simulated absorption spectra is shown in Figure 6.7.

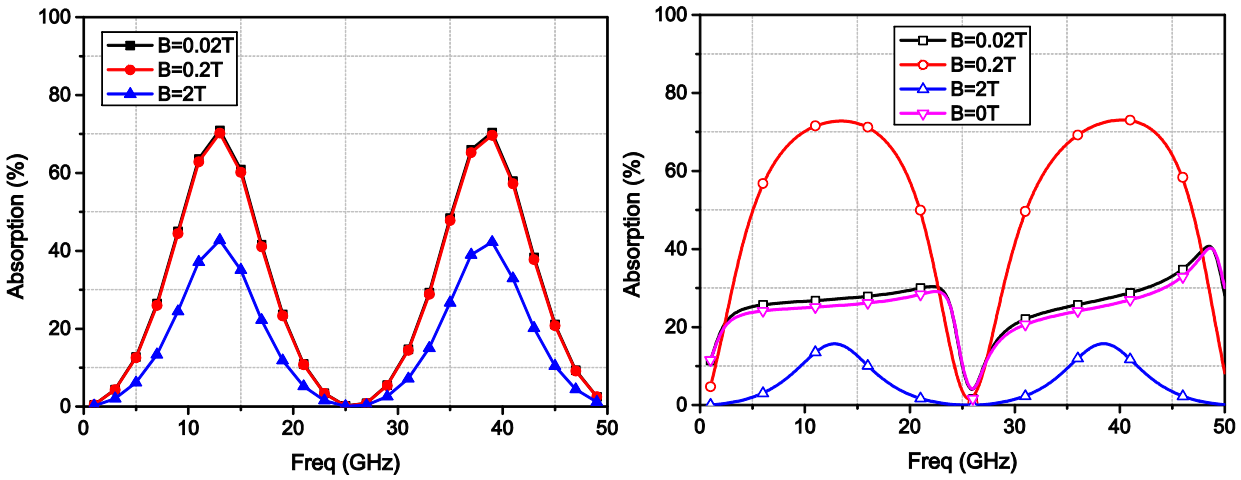

Figure 6.7 Absorption spectra of the graphene-based microwave absorber with $\mu_c = 0.1\text{eV}$ and different magnetic bias. The electron scattering rate Γ is 5 meV in (a) and 0.11 meV in (b).

It appears that for the case of $\Gamma = 5\text{meV}$, the absorption of $B_{bias} = 0.02T$ and $B_{bias} = 0.2T$ are very close to the case with only electric bias, which is shown in Figure 6.4 (b). On the other hand, the absorption of $B_{bias} = 2T$ is reduced by almost 50%. The same happens to the case of $\Gamma = 0.11\text{meV}$ and $B_{bias} = 0.02T$.

This shows that a weak magnetic field does not tune the absorption of a single layer graphene absorber. Interestingly, the absorption for $\Gamma = 0.11\text{meV}$ shows a flatter curve and has more bandwidth in the case of small magnetic bias. For $B_{bias} = 0.2T$, the absorption is not reduced, but

enhanced from 30% to 70% and $B_{bias} = 2T$, the absorption is again reduced by about 50%, compared to no magnetic bias case.

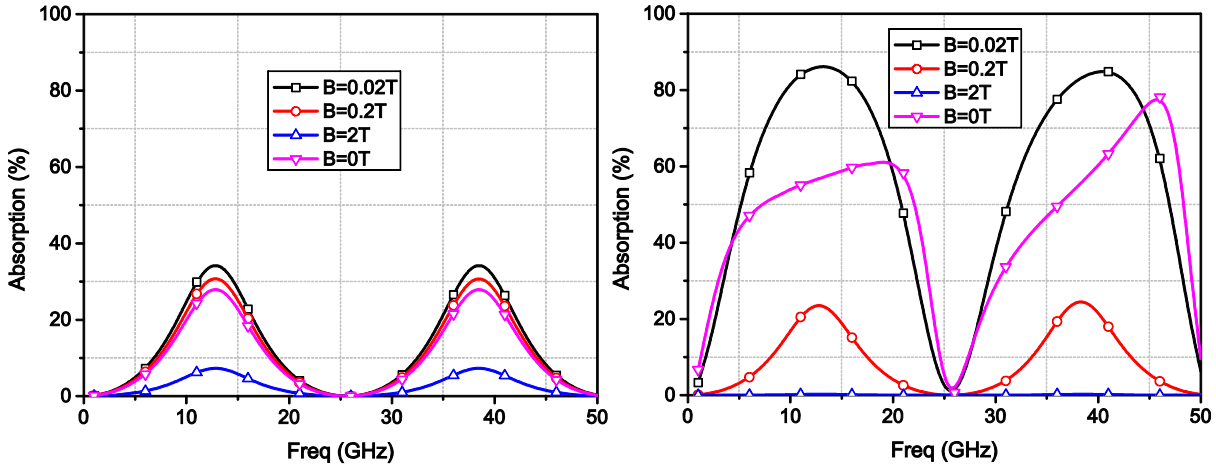

Figure 6.8 Absorption spectra of the graphene-based microwave absorber with $\mu_c = 0$ and different magnetic bias. The electron scattering rate Γ is 5 meV in (a) and 0.11 meV in (b).

Figure 6.8 shows the absorption spectrum of the graphene absorber with magnetic bias but without electric bias, i.e. $\mu_c = 0\text{eV}$. The added B_{bias} are the same as the case of Figure 6.7. Compared to Figure 6.7, the absorption is much less for the case of B=0 in both Γ, but the tuning effect is more significant. For Γ=5 meV, the absorption is slightly increased for B=0.02T and B=0.2T, and significantly decreased from 34% to 13% for B=0.02T. This is similar to the case shown in Figure 6.7 (a). However, the Γ=0.11 meV in Figure 5.8 (b) shows a much stronger tuning effect. For B=0.02T, the absorption is significantly increased and further increasing the magnetic bias field decreases the absorption. For B=2T, the absorption is 0, and the graphene absorber turns transparent to microwaves.

Finally, the absorption for differnet incident angles and different magnetic bias are simulated. Figure 6.9 shows the result for the case of $\Gamma = 5\text{meV}$. It appears that for the incident wave not normal to the graphene plane, the absorption can still be tuned by magnetic bias, and the peak absorption decreses with the increase of the magnetic bias. By comparing to the normal incidence case shown in Figure 6.7, it can be seen that the applied magnetic bias does not affect the

conclusion that the absorption for TE wave increases with the increase of the incident angle, while the corresponding absorption for TM wave decreases.

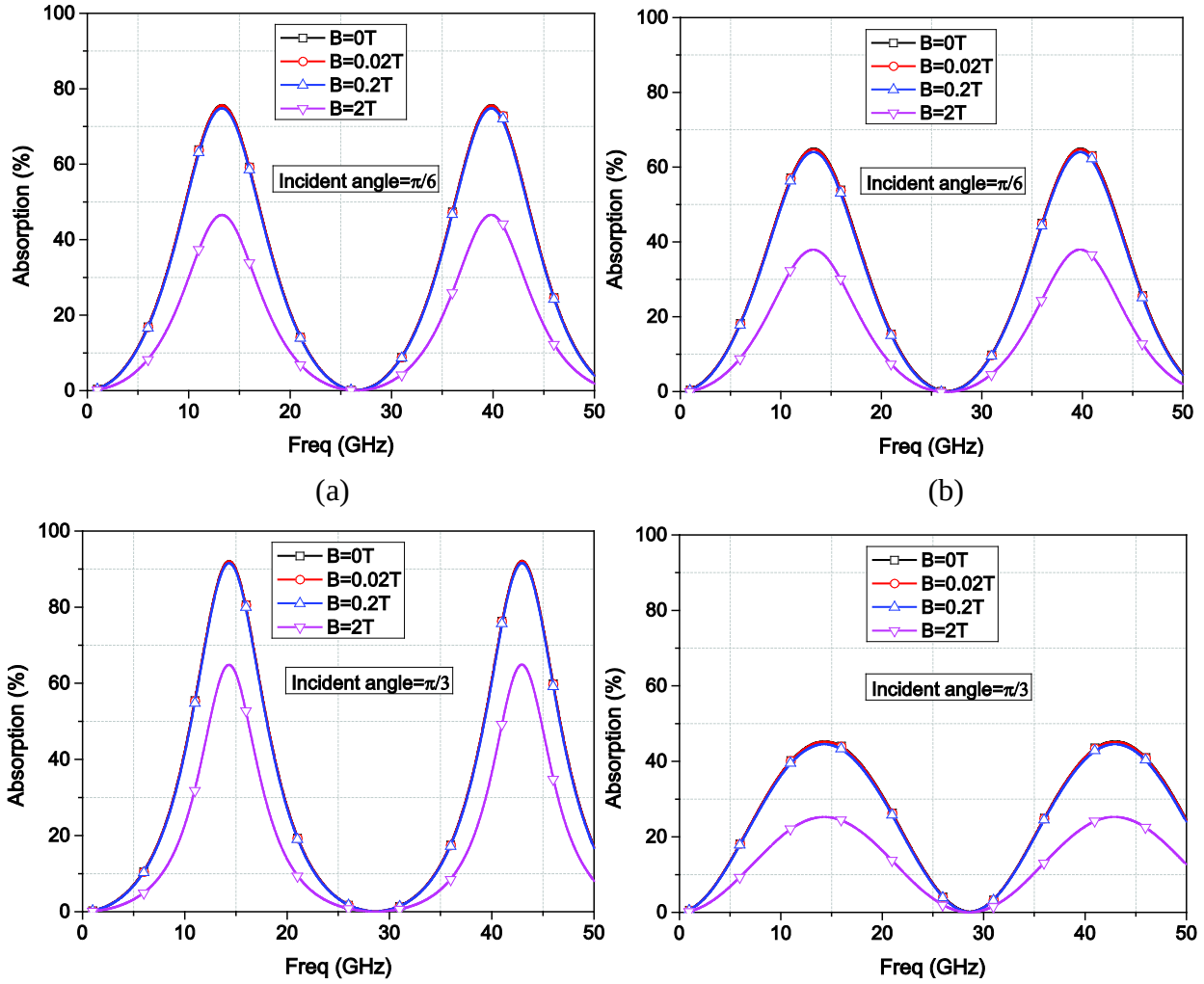

Figure 6.9 Absorption spectra for of the graphene absorber with different incident angles and magnetic bias. $\Gamma = 5\text{meV}$. (a) and (c) are TE polarization. (b) and (d) are TM polarization.

Figure 6.10 shows the same simulation for the case of $\Gamma = 0.11\text{meV}$. Similar to the normal insidance case, the magnetic field keeps a good tunability on the maximum absorption. Contrary to the results in Figure 6.8, in the case of $\Gamma = 0.11\text{meV}$, the peak TE absorption decreses with the increase of the incident angle while the corresponding peak TM absorption increases. It can also

be observed that the bandwidth of the absorption spectra for both TE and TM polarization increases slightly.

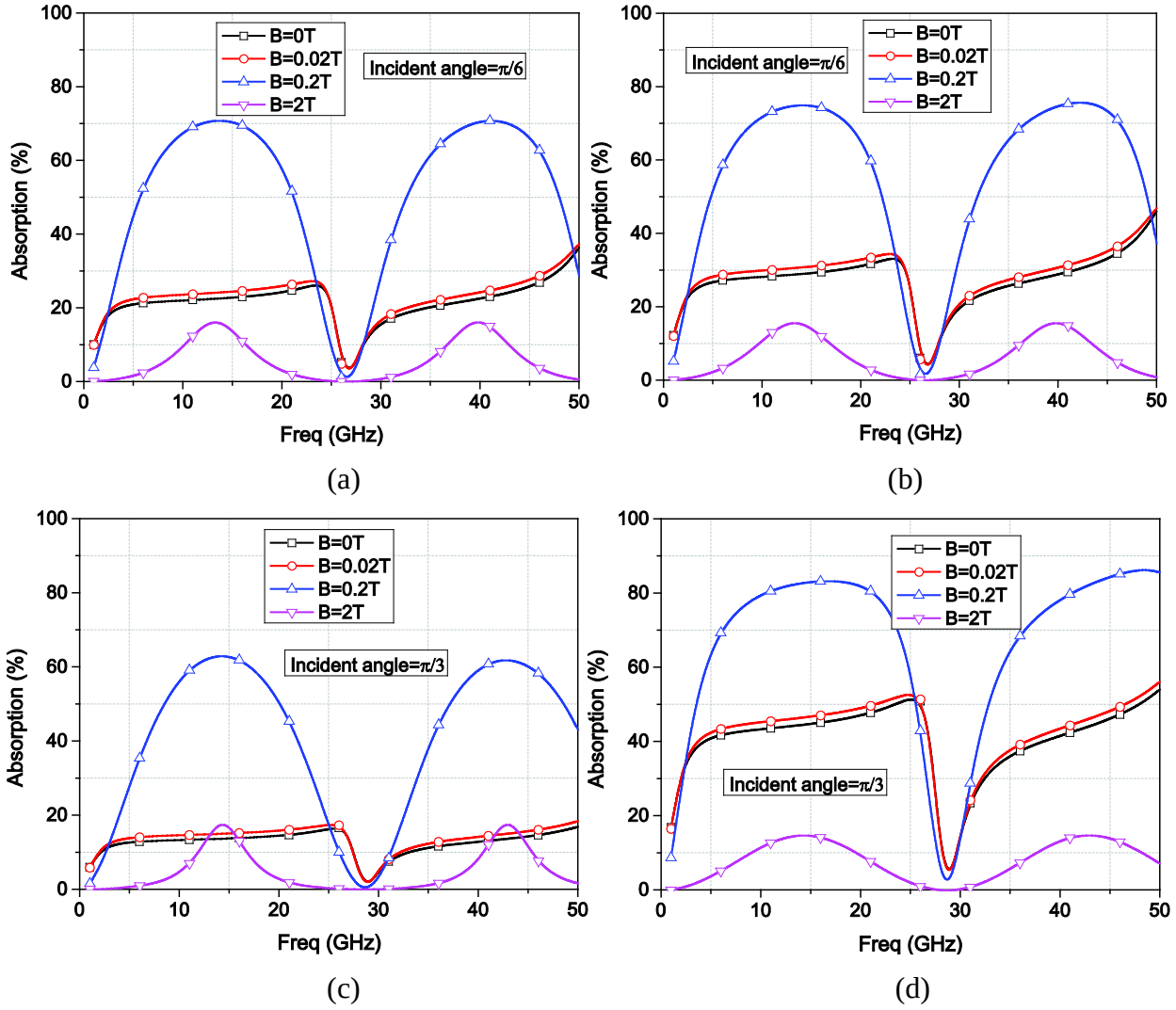

Figure 6.10 Absorption spectra for of the graphene absorber with different incident angles and magnetic bias. $\Gamma = 0.11\text{meV}$. (a) and (c) are TE polarization. (b) and (d) are TM polarization.

6.4.2 Single layer, multiple stacks of graphene

If the inter-graphene electron hopping is neglected, for a resistive sheet comprised of several graphene sheet stacked together, the total surface conductivity σ_s can be calculated as $\sigma_s = \sum_{i=1}^{p} \sigma_i$

where p is the total number of stacks. For simplification, assume all graphene in the stack has a same surface conductivity $\sigma_s^{'}$, so the total conductivity is $\sigma_s = p \cdot \sigma_s^{'}$.

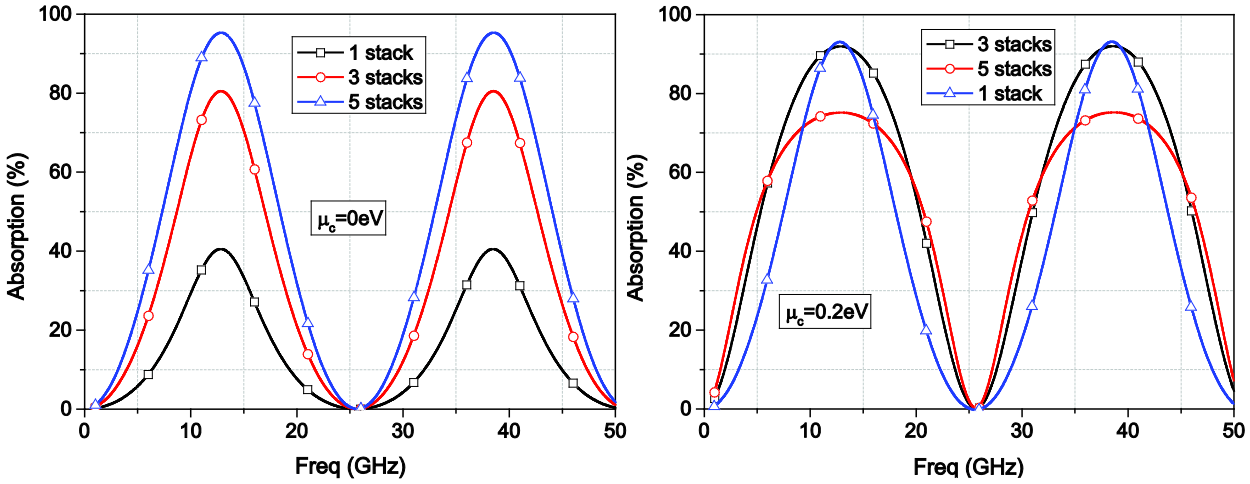

(a) (b)

Figure 6.11 Absorption spectra for of the graphene absorber with different number of graphene stacks. $\Gamma = 5\text{meV}$, $\varepsilon_r = 3.8$, and h=3mm. (a) $\mu_c = 0\text{eV}$ and (b) $\mu_c = 0.2\text{eV}$.

The absorption spectra for the graphene absorber with different number of stacking is shown in Figure 6.11. With no electric or magnetic bias, the single layer graphene's peak absorption is only 40%, but with multiple layers of graphene stacked together, the peak absorption is increased to 80% for 3 layers and 95% for 5 layers. The amount of increase from 3 layer to 5 layers is less than that from 1 layer to 3 layers, which suggests that to graphene's absorption through stacking several layers has a marginal effect, and the absorption will slowly cease to increase with the number of layers. When the electric bias is present and the chemical potential is increased to 0.1eV, the single layer of graphene has the maximum absorption of 93%, while with multiple layer, the maximum absorption decreases to 75%. This complies with the results shown in Figure 6.4, that increasing the chemical potential does not linearly increase the peak absorption, and once it reaches a turning point, the absorption will decrease with further increase of the chemical potential.

Then the magnetic bias is added to a 5 layer stacked graphene, with the corresponding $\mu_c = 0\text{eV}$ and $\mu_c = 0.1\text{eV}$, respectively. The magnetic bias is 0.02T, 0.2T and 2T, respectively.

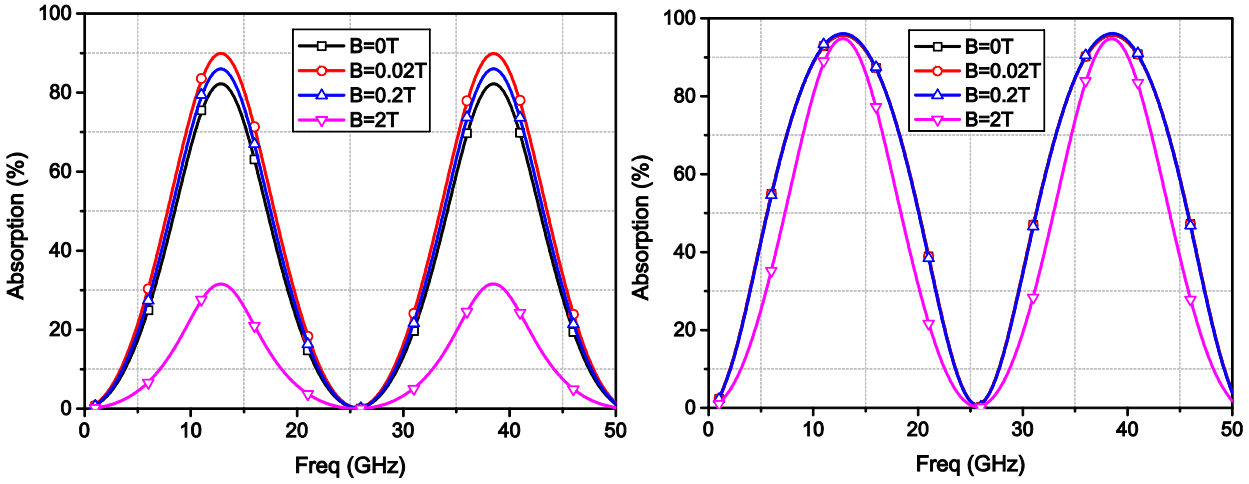

Figure 6.12 Absorption spectra of a 5 layer stacked graphene absorber with normal incidence, (a) $\mu_c = 0$ and (b) $\mu_c = 0.1\text{eV}$.

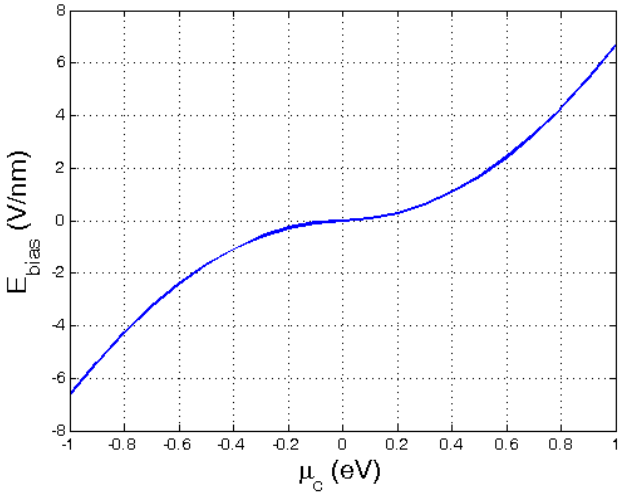

Figure 6.13 Relationship between applied field and chemical potential.

Similar to the single layer case, Figure 6.12 shows that the applied magnetic bias first increase the absorption and with the further increase of the bias field, reduces the absorption. It appears that in the absense of electric bias, the tuning range effect is much significant than the case when both electric and magnetic bias are applied.

From the analysis on the single and multi-stacked graphene absorber, the conclusion can be drawn that both electric and magnetic bias tunes the absorption of the graphene based microwave absorber. It appear that tuning through electric bias is more effective than the magnetic bias, because the magnetic bias of 2T is extremely large and difficult to realize in real-life applications. However, the change of chemical potental is realized by the change of electric field, which is described by (2.18). From Figure 6.13, it is clear that the unit for electric bias is V/nm, which is also extreme large in macroscopic sizes.

However, it has also been shown that the change of scattering rate also tunes the absorption of the graphene absorber. For example, Figure 6.8 shows that in the absence of all bias field, the low bias field results in higher absorption. This indicates that the increase of the graphene sheet's own quality can also significantly increase the absorption. Furthermore, graphene sheets with lower scattering rate are also much more effective in the tuning through the magnetic field than the graphene sheet with higher scattering rate. So it is more important to develop synthesizing techniques that produces higher quality graphene for the microwave absorbing applications.

6.4.3 Multilayers of graphene and substrate.

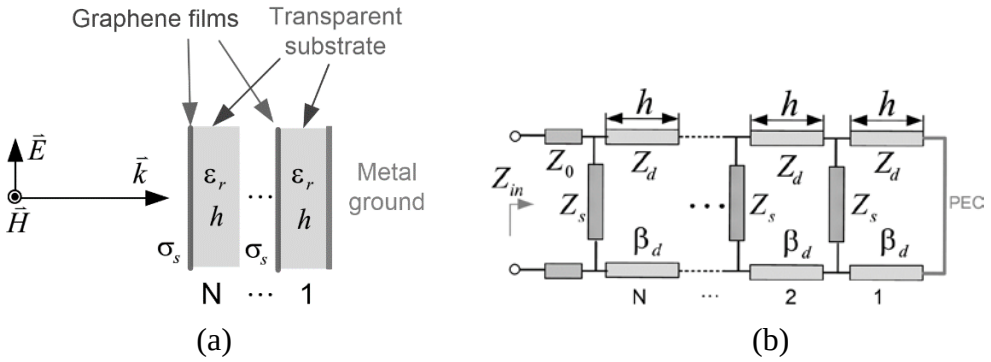

Figure 6.14 A multilayer graphene on top of a dielectric substrate (a) geometric configuration and (b) equivalent circuit model.

Similar to the Jaumann screen, which extends the Salisbury screen to multilayer, the single layer graphene resonant absorber can also be extended to multilayer, in order to improve the bandwidth. The schematic configuration and equivalent circuit model is shown in Figure 6.14.

The total input impedance of the multilayer graphene can be calculated by the following iterative equation:

$$Z_{in}^{i}=\begin{cases}\left(Y_s+Y_{d,TE}\cdot\dfrac{Y_{in,TE}^{i-1}+jY_{d,TE}\tan\left(\beta_d h\right)}{Y_{d,TE}+jY_{in,TE}^{i-1}\tan\left(\beta_d h\right)}\right)^{-1} & \text{(TE)}\\ \left(Y_s+Y_{d,TM}\cdot\dfrac{Y_{in,TM}^{i-1}+jY_{d,TM}\tan\left(\beta_d h\right)}{Y_{d,TM}+jY_{in,TM}^{i-1}\tan\left(\beta_d h\right)}\right)^{-1} & \text{(TM)}\end{cases} \tag{6.11}$$

where i=1,2,…,N is the i-th layer.

The S_{11} of the corresponding TE and TM wave incidence and can be calculated as

$$S_{11}=\begin{cases}\dfrac{Y_{0,TE}-Y_{in,TE}^{N}}{Y_{0,TE}-Y_{in,TE}^{N}} & \text{(TE)}\\ \dfrac{Y_{0,TM}-Y_{in,TM}^{N}}{Y_{0,TM}-Y_{in,TM}^{N}} & \text{(TM)}\end{cases} \tag{6.12}$$

The calculated absorption responses (N=1, 2, 3) achieved by circuit model calculation is shown in Figure 6.15. The graphene films are assumed to have a scattering rate of 5 meV and a chemical potential of 0.2 eV, which corresponds to a sheet resistance of 645 Ω/sq at room temperature. The substrate has a relative permittivity of 1.1 and a height of 1mm, which can be realized by transparent plastic films separated with a large air gap. If N=1, the absorber has an absorption peak of 90% around 70 GHz, while N=2, 3 the graphene absorbers have 2 or 3 absorption peaks and a wide absorption band from 20 GHz to 120 GHz. If the number of units keeps increase from N=3 to N=8, the increased number of absorption peaks not only improves the absorption level but also widens the bandwidth. The periodic absorption bands can be extended to low THz region, but each bandwidth is limited to $2f_0$ due to the periodic absorption zeroes at $f_{zi}=2if_0$ $(i=1,2\cdots)$. Moreover, the desired sheet resistance of graphene films increases from 645 to 1274 Ω/sq, which can be easily achieved by most CVD procedure.

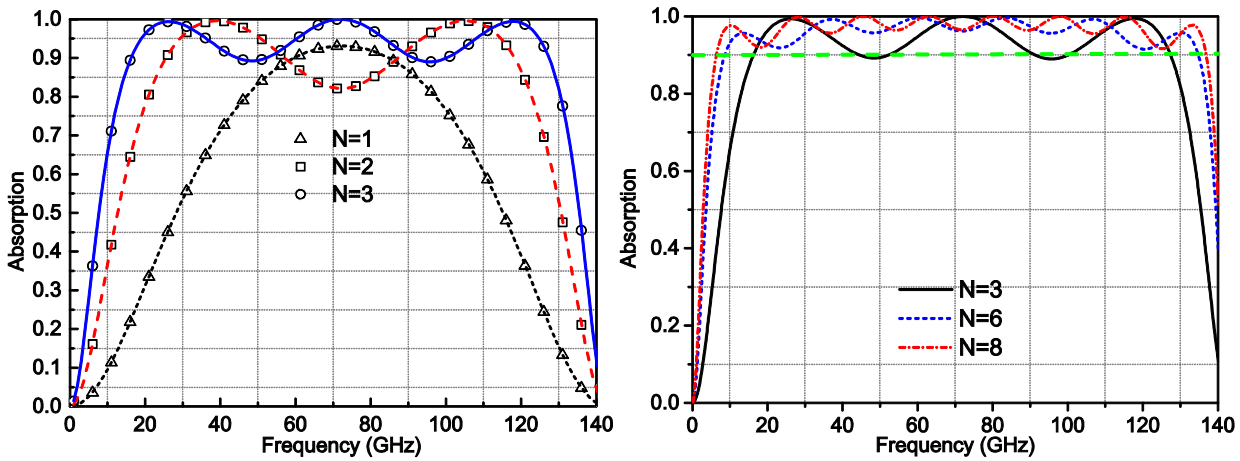

(a) (b)

Figure 6.15 Absorption spectra of N=1,2,3 graphene-based plane wave absorber (a) 1 to 3 layers and (b) further increasing N to 8 layers. Marks are results obtained from HFSS and lines are results obtained from MATLAB.

Next, the magnetic bias is applied to the multi-layer graphene absorber in the case of N=2 and 3. The results is shown in Figure 6.16.

Clearly, for multi-layer absorber, the applied magnetic bias makes the sheet transparent to microwaves with the increase of the bias field. It appears that the multi-layer absorber has a more significant tuning effect than that of single-layer. It can be found that in the case of single layer, the only same strong reduction in absorption can only be seen in Figure 6.8(b), where the chemical potential is only 0.11meV. This first confirm the previous conclusion that better quality grahpene can increase the tuning effect of the magnetic bias field, second, it suggests that to achieve the same tuning effect, the multi-layer graphene is more tolerant in graphene quality than single layer, as the result is Figrure 6.16 is simulated with Γ=5meV.

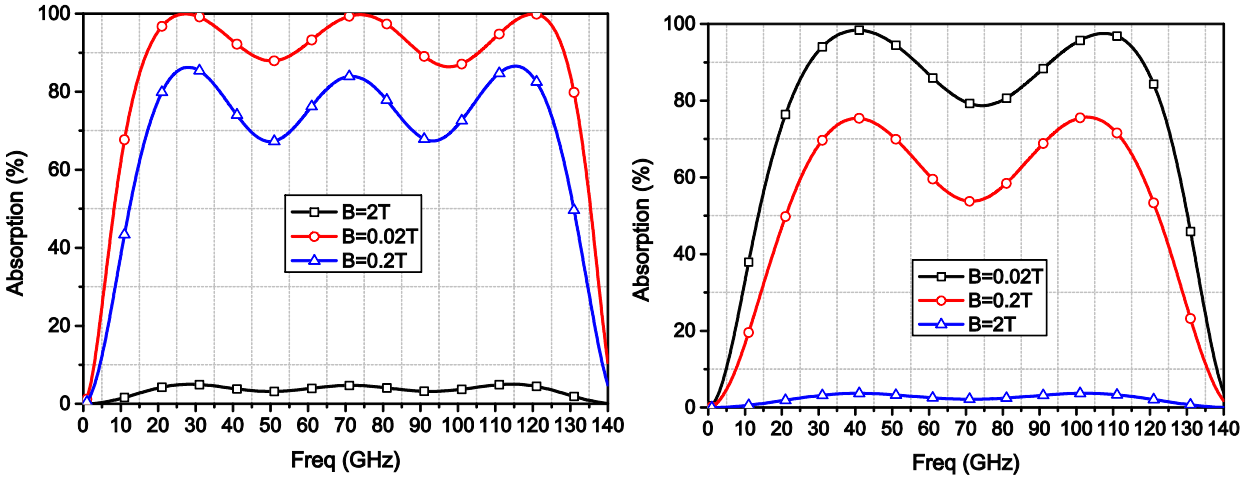

(a) (b)

Figure 6.16 Absorption spectra of N=2,3 graphene-based plane wave absorber with magnetic bias (a) 3 layers and (b) 2 layers.

6.5 Summary

In chis chapter, a graphene based microwave absorber is presented. Compared to normal Salisbury screen and Jaumann screen absorbers, it features optical transparency and flexibility. The cases of single layer of graphene, multiple layers of graphene and multiple layers of graphene plus substrate are discussed. It can be observed that the single or multi-layer graphene absorber is narrow band while the multilayer graphene with substrate demonstrates wide bandwidth. The bandwidth increases with the increase of the total number of layers. Also, the absorber keeps a good performance for large incident angles, especially for the TE polarized wave. In the worst case scenario, the absorption can still get 70% of the absorption in the normal incident case.

The tuning of the absorption is possible by applying electric or magnetic bias. For a graphene sheet without any bias, the absorption is weak and by applying an electric bias, the absorption can get close to 95%. If the magnetic bias is also added, the absorption will decrease gradually and the absorber eventually becomes transparent to microwaves. However, the required magnetic bias is very strong and hard to obtain in normal lab conditions. On the other hand, tuning the scattering

rate can reduce the magnetic bias required to achieve microwave transparency, which means better quality graphene is required.

The multi-layer graphene absorber has shown to have better absorption and wider bandwidth than the single –layer graphene absorber. In addition, the multi-layer absorber can achieve that same tuning effect with magnetic bias for poorer quality graphene. Therefore the multi-layer absorber is preferred, except for narrow band applications.

References

[1]. H. W. Kroto, J. R. Heath, S. C. Obrien, R. F. Curl, and R. E. Smalley, "C-60 - Buckminsterfullerene," *Nature*, vol. 318, pp. 162-163, 1985.

[2]. S. Iijima, "Helical Microtubules of Graphitic Carbon," *Nature*, vol. 354, pp. 56-58, Nov 7 1991.

[3]. Novoselov, K. S. et al. Electric field effect in atomically thin carbon films. *Science* 306, 666-669 (2004).

[4]. Y. Y. G. Huang, D. Y. Khang, J. L. Xiao, C. Kocabas, S. MacLaren, T. Banks, H. Q. Jiang, and J. A. Rogers, "Molecular scale buckling mechanics on individual aligned single-wall carbon nanotubes on elastomeric substrates," *Nano Letters*, vol. 8, pp. 124-130, Jan 2008.

[5]. T. Cagin, G. H. Gao, and W. A. Goddard, "Energetics, structure, mechanical and vibrational properties of single-walled carbon nanotubes," *Nanotechnology*, vol. 9, pp. 184-191, Sep 1998.

[6]. X. J. Zhou, J. Y. Park, S. M. Huang, J. Liu, and P. L. McEuen, "Band structure, phonon scattering, and the performance limit of single-walled carbon nanotube transistors," *Physical Review Letters*, vol. 95, Sep 30 2005.

[7]. Z. Yao, C. L. Kane, and C. Dekker, "High-field electrical transport in single-wall carbon nanotubes," *Physical Review Letters*, vol. 84, pp. 2941-2944, Mar 27 2000.

[8]. S. Berber, Y. K. Kwon, and D. Tomanek, "Unusually high thermal conductivity of carbon nanotubes," *Physical Review Letters*, vol. 84, pp. 4613-4616, May 15 2000.

[9]. Ding, Li and Liang, Shibo and Pei, Tian and Zhang, Zhiyong and Wang, Sheng and Zhou, Weiwei and Liu, Jie and Peng, Lian-Mao, “Carbon nanotube based ultra-low voltage integrated circuits: Scaling down to 0.4 V” *Applied Physics Letters*, 100, 263116 (2012).

[10]. Yun Wang and John T. W. Yeow, “A Review of Carbon Nanotubes-Based Gas Sensors,” *Journal of Sensors*, vol. 2009, Article ID 493904, 24 pages, 2009.

[11]. Seung Woo Lee , Naoaki Yabuuchi , Betar M. Gallant , Shuo Chen ,Byeong-Su Kim , Paula T. Hammond & Yang Shao-Horn, “High-power lithium batteries from functionalized carbon-nanotube electrodes”, *Nature nanotechnology* vol.5 , pp. 531-537, Jul 1 2010.

[12]. Dillon, A. C.; Jones, K. M.; Bekkedahl, T. A.; Kiang, C. H. Bethune, D. S.; Heben, M. J. " Storage of hydrogen in single-walled carbon nanotubes," *Nature* 386, 377 – 379, 27 March 1997;

[13]. Wei, Jinquan; Jia, Yi; Shu Qinke; Gu, Zhiyi; wang, Kunlin; Zhuang, Daming; Zhang, Gong; Wang, Zhicheng; Luo, Jianbin; Cao, Anyuan; Wu, Dehai; “Double-Walled Carbon Nanotube Solar Cells,” *Nano Letters*, vol. 7, no. 8, pp. 2317-2321, Aug 1 2007.

[14]. Hanson, G.W., "Fundamental transmitting properties of carbon nanotube antennas," *Antennas and Propagation, IEEE Transactions on* , vol.53, no.11, pp.3426,3435, Nov. 2005.

[15]. Nicholson, J. W., R. S. Windeler, and D. J. DiGiovanni. "Optically driven deposition of single-walled carbon-nanotube saturable absorbers on optical fiber end-faces." *Optics express* 15.15 (2007): 9176-9183.

[16]. Cho, Won Bae, et al. "Passive mode-locking of a Tm-doped bulk laser near 2 μm using a carbon nanotube saturable absorber." *Optics express* 17.13 (2009): 11007-11012.

[17]. Naeemi, A; Meindl, J.D., "Compact Physics-Based Circuit Models for Graphene Nanoribbon Interconnects," *Electron Devices, IEEE Transactions on* , vol.56, no.9, pp.1822,1833, Sept. 2009

[18]. Neto, AH Castro, et al. "The electronic properties of graphene." *Reviews of modern physics* 81.1 (2009): 109.

[19]. Zhang, R.; Zhang, Y.; Zhang, Q.; Xie, H.; Qian, W.; Wei, F. (2013). "Growth of Half-Meter Long Carbon Nanotubes Based on Schulz–Flory Distribution". *ACS Nano* **7** (7): 6156.

[20]. A. Thess, R. Lee, P. Nikolaev, H. Dai, P. Petit, J. Robert, C. Xu, Y. H. Lee, S. G. Kim, A. G. Rinzler, D. T. Colbert, G. E. Scuseria, D. Tománek, J. E. Fischer, and R. E. Smalley, "Crystalline Ropes of Metallic Carbon Nanotubes," *Science*, vol. 273, pp. 483-487, 1996

[21]. K. L. Jiang, Q. Q. Li, and S. S. Fan, "Nanotechnology: Spinning continuous carbon nanotube yarns - Carbon nanotubes weave their way into a range of imaginative macroscopic applications.," *Nature*, vol. 419, pp. 801-801, Oct 24 2002.

[22]. F. Wei, Q. Zhang, M. Q. Zhao, J. Q. Huang, Y. Liu, Y. Wang, and W. Z. Qian, "Vertically aligned carbon nanotube arrays grown on a lamellar catalyst by fluidized bed catalytic chemical vapor deposition," *Carbon*, vol. 47, pp. 2600-2610, Sep 2009.

[23]. F. Wei, Q. Zhang, W. P. Zhou, W. Z. Qian, R. Xiang, J. Q. Huang, and D. Z. Wang, "Synchronous growth of vertically aligned carbon nanotubes with pristine stress in the heterogeneous catalysis process," *Journal of Physical Chemistry C*, vol. 111, pp. 14638-14643, Oct 11 2007.

[24]. R. H. Hauge, C. L. Pint, S. T. Pheasant, M. Pasquali, K. E. Coulter, and H. K. Schmidt, "Synthesis of high aspect-ratio carbon nanotube "Flying Carpets" from nanostructured flake substrates," *Nano Letters*, vol. 8, pp. 1879-1883, Jul 2008.

[25]. Li, Shengdong, et al. "Electrical properties of 0.4 cm long single-walled carbon nanotubes." *Nano Letters* 4.10 (2004): 2003-2007.

[26]. Cassell, Alan M., et al. "Large scale CVD synthesis of single-walled carbon nanotubes." *The Journal of Physical Chemistry B* 103.31 (1999): 6484-6492.

[27]. P. G. He, L. Z. Yang, Y. Xu, X. H. Wang, J. Zhu, R. Y. Zhang, and Y. Z. Fang, "The application of beta-cyclodextrin derivative functionalized aligned carbon nanotubes for electrochemically DNA sensing via host-guest recognition," *Analytica Chimica Acta*, vol. 689, pp. 39-46, Mar 9 2011.

[28]. Y. Z. Fang, J. Yang, R. Y. Zhang, Y. Xu, and P. G. He, "Direct electrochemistry study of glucose oxidase on Pt nanoparticle-modified aligned carbon nanotubes electrode by the assistance of chitosan-CdS and its biosensoring for glucose," *Electrochemistry Communications*, vol. 10, pp. 1889-1892, Dec 2008.

[29]. W. D. Zhang and B. Xu, "A solid-state pH sensor based on WO(3)-modified vertically aligned multiwalled carbon nanotubes," *Electrochemistry Communications*, vol. 11, pp. 1038-1041, May 2009.

[30]. M. Penza, R. Rossi, M. Alvisi, M. A. Signore, G. Cassano, D. Dimaio, R. Pentassuglia, E. Piscopiello, E. Serra, and M. Falconieri, "Characterization of metal-modified and vertically-aligned carbon nanotube films for functionally enhanced gas sensor applications," *Thin Solid Films*, vol. 517, pp. 6211-6216, Sep 30 2009.

[31]. Bonaccorso, Francesco, et al. "Production and processing of graphene and 2d crystals." *Materials Today* 15.12 (2012): 564-589.

[32]. Hirsch, Andreas, Jan M. Englert, and Frank Hauke. "Wet chemical functionalization of graphene." *Accounts of chemical research* 46.1 (2012): 87-96.

[33]. Emtsev, Konstantin V., et al. "Towards wafer-size graphene layers by atmospheric pressure graphitization of silicon carbide." *Nature materials* 8.3 (2009): 203-207.

[34]. Ismach, Ariel, et al. "Direct chemical vapor deposition of graphene on dielectric surfaces." *Nano letters* 10.5 (2010): 1542-1548.

[35]. Ju, Long, et al. "Graphene plasmonics for tunable terahertz metamaterials."*Nature nanotechnology* 6.10 (2011): 630-634.

[36]. Koppens, Frank HL, Darrick E. Chang, and F. Javier Garcia de Abajo. "Graphene plasmonics: a platform for strong light–matter interactions." *Nano letters* 11.8 (2011): 3370-3377.

[37]. Grigorenko, A. N., Marco Polini, and K. S. Novoselov. "Graphene plasmonics."*Nature photonics* 6.11 (2012): 749-758.

[38]. Nikitin, A. Yu, et al. "Edge and waveguide terahertz surface plasmon modes in graphene microribbons." *Physical Review B* 84.16 (2011): 161407.

[39]. Pallecchi, Emiliano, et al. "Graphene microwave transistors on sapphire substrates." *Applied Physics Letters* 99.11 (2011): 113502.

[40]. Perruisseau-Carrier, J., "Graphene for antenna applications: Opportunities and challenges from microwaves to THz," *Antennas and Propagation Conference* (LAPC), 2012 Loughborough, vol., no., pp.1,4, 12-13 Nov. 2012.

[41]. Burke, Peter J. "An RF circuit model for carbon nanotubes." Nanotechnology, 2002. IEEE-NANO 2002. *Proceedings of the 2002 2nd IEEE Conference on*. IEEE, 2002.

[42]. Maffucci, A., Miano, G., Villone, F. "A transmission line model for metallic carbon nanotube interconnects," *Int. J. Circ. Theor. Appl.*, vol. 36, issue 1, pp. 31-51, 2008.

[43]. Xu, Y. and Srivastava, A. (2010), A model for carbon nanotube interconnects. *Int. J. Circ. Theor. Appl.*, 38: 559–575.

[44]. Sihvola, Ari H., ed. Electromagnetic mixing formulas and applications. No. 47. Iet, 1999.

[45]. Ando, Tsuneya. "Theory of transport in carbon nanotubes." *Semiconductor science and technology* 15.6 (2000): R13.

[46]. AlexanderAlUS. "Graphen." Own work. Licensed under Creative Commons Attribution-Share Alike 3.0 via Wikimedia Commons.

[47]. Sariciftci, N. S., et al. "Semiconducting polymer-buckminsterfullerene heterojunctions: Diodes, photodiodes, and photovoltaic cells." *Applied Physics Letters* 62.6 (1993): 585-587.

[48]. Odom, Teri Wang, et al. "Atomic structure and electronic properties of single-walled carbon nanotubes." *Nature* 391.6662 (1998): 62-64.

[49]. Neto, AH Castro, et al. "The electronic properties of graphene." *Reviews of modern physics* 81.1 (2009): 109.

[50]. Hanson, George W. "Fundamental transmitting properties of carbon nanotube antennas." *Antennas and Propagation, IEEE Transactions on* 53.11 (2005): 3426-3435.

[51]. Llatser, Ignacio, et al. "Graphene-based nano-patch antenna for terahertz radiation." *Photonics and Nanostructures-Fundamentals and Applications* 10.4 (2012): 353-358.

[52]. Chen, Xiangyu, et al. "Fully integrated graphene and carbon nanotube interconnects for gigahertz high-speed CMOS electronics." *Electron Devices, IEEE Transactions on* 57.11 (2010): 3137-3143.

[53]. Srivastava, Navin, and Kaustav Banerjee. "Performance analysis of carbon nanotube interconnects for VLSI applications." Computer-Aided Design, 2005. ICCAD-2005. *IEEE/ACM International Conference on*. IEEE, 2005.

[54]. Xu, Chuan, Hong Li, and Kaustav Banerjee. "Graphene nano-ribbon (GNR) interconnects: A genuine contender or a delusive dream?." Electron Devices Meeting, 2008. *IEDM 2008. IEEE International.* IEEE, 2008.

[55]. Awano, Yuji. "Graphene for VLSI: FET and interconnect applications." *IEDM Tech. Dig* (2009): 1-4.

[56]. Martel, Richard, et al. "Single-and multi-wall carbon nanotube field-effect transistors." *Applied Physics Letters* 73.17 (1998): 2447-2449.

[57]. Danaeifar, M., et al. "Graphene-based tunable terahertz and infrared band-pass filter." *Applied optics* 52.22 (2013): E68-E72.

[58]. Butt, Haider, et al. "Metamaterial high pass filter based on periodic wire arrays of multiwalled carbon nanotubes." *Applied physics letters* 97.16 (2010): 163102.

[59]. Li, Jing, et al. "Carbon nanotube sensors for gas and organic vapor detection."*Nano letters* 3.7 (2003): 929-933.

[60]. Wei, Jinquan, et al. "Double-walled carbon nanotube solar cells." *Nano letters* 7.8 (2007): 2317-2321.

[61]. Wang, Xuan, Linjie Zhi, and Klaus Müllen. "Transparent, conductive graphene electrodes for dye-sensitized solar cells." *Nano letters* 8.1 (2008): 323-327.

[62]. Blackman, L.C.F. and A.R. Ubbelhode, Stress Recrystallization of Graphite. *Proceedings of the Royal Society of London. Series A, Mathematical and Physical Sciences*, 1962. 266(1324): p. 20-32.

[63]. Levitt, A.P., Whisker Technology. 1970, New York: Wiley-Interscience.

[64]. Radushkevich LV, Lukyanovich VM. O strukture ugleroda, obrazujucegosja pri termiceskom razlozenii okisi ugleroda na zeleznom kontakte. *Zurn Fisic Chim* 1952;26:88-95.

[65]. M. Endo, Mecanisme de croissance en phase vapeur de fibres de carbone (The growth mechanism of vapor-grown carbon fibers), PhD thesis, University of Orleans, Orleans, France, (1975) .

[66]. M. Endo, PhD thesis, Nagoya University, Japan, (1978).

[67]. Smalley, R.E. in *Department of Defence Workshop*. 1990. Washington, DC.

[68]. Huffman, D.R. in *Department of Defence Workshop*. 1990. Washington, DC.

[69]. Dresselhaus, M.S. in *Department of Defence Workshop*. 1990. Washington, DC.

[70]. Dresselhaus, M.S., G. Dresselhaus, and P.C. Eklund. in *University of Pennsylvania Workshop*. 1991.

[71]. Iijima, S., Helical *microtubules of graphitic carbon*. Nature, 1991. 354(6348): *p. 56-58.*

[72]. *T. W. Ebbesen and P. M. Ajayan, "Large-Scale Synthesis of Carbon Nanotubes," Nature, vol. 358, pp. 220-222, Jul 16 1992.*

[73]. *C. Schafhaeutl, J. Prakt. Chem. 1840, 21, 129.*

[74]. *Marcano, Daniela C., et al. "Improved synthesis of graphene oxide." ACS nano4.8 (2010): 4806-4814.*

[75]. *H. P. Boehm, A. Clauss, G. O. Fischer, U. Hofmann, Z. Naturf.1962, 17, 150.*

[76]. *H. P. Boehm, A. Clauss, G. Fischer, U. Hofmann in Proceedings of the Fifth Conference on Carbon, Pergamon Press, Heidelberg, Germany, 1962, p. 73.*

[77]. Park, Sungjin, and Rodney S. Ruoff. "Chemical methods for the production of graphenes." *Nature nanotechnology* 4.4 (2009): 217-224..

[78]. Blakely, J. M., J. S. Kim, and H. C. Potter. "Segregation of Carbon to the (100) Surface of Nickel." *Journal of Applied Physics* 41.6 (1970): 2693-2697.

[79]. van Bommel, A.J., Crombeen, J. E., van Tooren, A. LEED and Auger electron observations of the SiC(0001) surface.*Surf. Sci.* 48, 463-472 (1975).

[80]. Eizenberg, M., and J. M. Blakely. "Carbon interaction with nickel surfaces: Monolayer formation and structural stability." *The Journal of Chemical Physics*71.8 (1979): 3467-3477.

[81]. Patil, H. R., and J. M. Blakely. "Electron energy losses in thin graphite layers on the (111) face of nickel." *Journal of Applied Physics* 45.9 (1974): 3806-3808.

[82]. Hamilton, J. C., and J. M. Blakely. "Carbon segregation to single crystal surfaces of Pt, Pd and Co." *Surface Science* 91.1 (1980): 199-217.

[83]. Hamilton, J. C., and J. M. Blakely. "Carbon layer formation on the Pt (111) surface as a function of temperature." *Journal of Vacuum Science and Technology* 15.2 (1978): 559-562.

[84]. Schedin, F., et al. "Detection of individual gas molecules adsorbed on graphene." *Nature materials* 6.9 (2007): 652-655.

[85]. Schakel, Adriaan MJ. "Relativistic quantum Hall effect." *Physical Review D* 43.4 (1991): 1428.

[86]. González, J., F. Guinea, and M. A. H. Vozmediano. "Unconventional quasiparticle lifetime in graphite." *Physical review letters* 77.17 (1996): 3589.

[87]. Peierls, R. E. Quelques proprietes typiques des corpses solides. *Ann. I. H. Poincare* 5, 177-222 (1935).

[88]. Landau, L. D. "Zur Theorie der phasenumwandlungen II." *Phys. Z. Sowjetunion*11 (1937): 26-35.

[89]. Venables, J. A., G. D. T. Spiller, and M. Hanbucken. "Nucleation and growth of thin films." *Reports on Progress in Physics* 47.4 (1984): 399.

[90]. Evans, J. W., P. A. Thiel, and Maria C. Bartelt. "Morphological evolution during epitaxial thin film growth: Formation of 2D islands and 3D mounds." *Surface Science Reports* 61.1 (2006): 1-128.

[91]. S. M. Huang, X. Y. Cai, and J. Liu, "Growth of millimeter-long and horizontally aligned single-walled carbon nanotubes on flat substrates," *Journal of the American Chemical Society*, vol. 125, pp. 5636-5637, May 14 2003.

[92]. J. Tersoff and R. S. Ruoff, "Structural-Properties of a Carbon-Nanotube Crystal," *Physical Review Letters*, vol. 73, pp. 676-679, Aug 1 1994.

[93]. Wang, Xueshen, et al. "Fabrication of ultralong and electrically uniform single-walled carbon nanotubes on clean substrates." *Nano letters* 9.9 (2009): 3137-3141.

[94]. Bor Z. Jang, Wen C. Huang, "Multilayer crystal structure graphite sheets; from petroleum, coar tar pitch; carbonization, exfoliation, attrition," US Patent: US7071258 B1,2006.

[95]. K. Sattler, "Scanning-Tunneling-Microscopy of Carbon Nanotubes and Nanocones," *Carbon*, vol. 33, pp. 915-920, 1995.

[96]. Jean-Marc Bonard, Hannes Kind, Thomas Stöckli, Lars-Ola Nilsson, Field emission from carbon nanotubes: the first five years. Solid-State Electronics, 2001, 45: p. 893-914

[97]. Pauling, Linus. "The nature of the chemical bond. Application of results obtained from the quantum mechanics and from a theory of paramagnetic susceptibility to the structure of molecules." *Journal of the American Chemical Society* 53.4 (1931): 1367-1400.

[98]. G. L. Sewell, *Quantum mechanics and its emergent macrophysics*. Princeton ; Oxford: Princeton University Press, 2002.

[99]. R. Saito, M. S. Dresselhaus, and G. Dresselhaus, *Physical Properties of Carbon* Nanotubes. London, UK: Imperial College Press, 2003.

[100]. R. Saito, M. Fujita, G. Dresselhaus, and M.S. Dresselhaus, Electronic structure of chiral graphene tubules. Applied Physics Letters, 1992, 60(18), p. 1804-1811

[101]. E. D. Graugnard, "The electronic properties of multi-walled carbon nanotubes," Ph.D. thesis, Purdue University, December 2000.

[102]. Kittel, Charles (1996). Introduction to Solid State Physics. New York: Wiley

[103]. Anantram, M. P., and F. Leonard. "Physics of carbon nanotube electronic devices." Reports on Progress in Physics 69.3 (2006): 507.

[104]. Carter T. White, and John W. Mintmire, Fundamental Properties of Single-Wall Carbon Nanotubes, J. Phys. Chem. B 2005, 109(1): p. 52-65.

[105]. Cabria, I., J.W. Mintmire, and C.T. White, Metallic and semiconducting narrow carbon nanotubes. Physical Review B, 2003. 67(12): p. -.

[106]. White, C.T. and J.W. Mintmire, Fundamental properties of single-wall carbon nanotubes. Journal of Physical Chemistry B, 2005. 109(1): p. 52-65.

[107]. White, C.T., D.H. Robertson, and J.W. Mintmire, Helical and Rotational Symmetries of Nanoscale Graphitic Tubules. Physical Review B, 1993. 47(9): p. 5485-5488.

[108]. Popov, Valentin N., and Philippe Lambin, eds. Carbon nanotubes: from basic research to nanotechnology. Vol. 222. Springer, 2006.

[109]. Hanson, George W. "Dyadic Green's functions and guided surface waves for a surface conductivity model of graphene." Journal of Applied Physics 103.6 (2008): 064302.

[110]. D. V. Khveshchenko, "Magnetic-field-induced insulating behavior in highly oriented pyrolitic graphite," Phys. Rev. Letts., vol. 87, p. 206401 (1-4), 2001.

[111]. E. V. Gorbar, V. P. Gusynin, V. A. Miransky, and I. A. Shovkovy, "Magnetic field driven metal-insulator phase transition in planar systems," Phys. Rev. B, vol. 66, p. 045108 (1-22), 2002.

[112]. Novoselov, K. S. A., et al. "Two-dimensional gas of massless Dirac fermions in graphene." nature 438.7065 (2005): 197-200.

[113]. Lovat, Giampiero. "Equivalent circuit for electromagnetic interaction and transmission through graphene sheets." Electromagnetic Compatibility, IEEE Transactions on 54.1 (2012): 101-109.

[114]. Naeemi, Azad, and James D. Meindl. "Compact physics-based circuit models for graphene nanoribbon interconnects." Electron Devices, IEEE Transactions on56.9 (2009): 1822-1833.

[115]. Naeemi, Azad, and James D. Meindl. "Compact physical models for multiwall carbon-nanotube interconnects." Electron Device Letters, IEEE 27.5 (2006): 338-340.

[116]. Datta, Supriyo. Quantum transport: atom to transistor. Cambridge University Press, 2005.

[117]. Forro, Laszlo, and Christian Schoenenberger. "Physical properties of multi-wall nanotubes." Carbon Nanotubes. Springer Berlin Heidelberg, 2001. 329-391.

[118]. Mann D, Javey A, Kong J, Wang Q, Dai H. 2003. Ballistic transport in metallic nanotubes with reliable Pd ohimc contacts. Nano Lett. 3:1541-44.

[119]. Baym, Gordon, and Christopher Pethick. *Landau Fermi-liquid theory: concepts and applications*. John Wiley & Sons, 2008.

[120]. M. P. A. Fisher and L. I. Glazman, Transport in a one-dimensional Luttinger liquid. Dordrecht, the Netherlands: Kluwer, 1997.

[121]. Ph. Avouris, M. S. Dresselhaus, and G. Dresselhaus, Eds., Carbon Nanotubes: Synthesis, Structure, Properties, and Applications. Berlin, Germany: Springer-Verlag, 2001, 80, Topics in Applied Physics.

[122]. S. Tomonaga, Remarks on Bloch's method of sound waves applied to many-Fermion problems, Prog. Theor. Phys., 1950, 5(4): p. 544-569.

[123]. J. M. Luttinger, An exactly solvable model of a many-Fermion system, J. Math. Phys., 1963, 4(9): p. 1154.

[124]. P. J. Burke, Lüttinger Liquid Theory as a Model of the Gigahertz Electrical Properties of Carbon Nanotubes, IEEE TRANS. on Nanotech., vol1, No. 3, pp. 129-144.

[125]. Maffucci, A., G. Miano, and F. Villone. "A transmission line model for metallic carbon nanotube interconnects." *International Journal of Circuit Theory and Applications* 36.1 (2008): 31-51.

[126]. Sarto, Maria Sabrina, and Alessio Tamburrano. "Single-conductor transmission-line model of multiwall carbon nanotubes." *Nanotechnology, IEEE Transactions on* 9.1 (2010): 82-92.

[127]. Sarto, Maria Sabrina, and Alessio Tamburrano. "Electromagnetic analysis of radio-frequency signal propagation along SWCN bundles." *Nanotechnology, 2006. IEEE-NANO 2006. Sixth IEEE Conference on*. Vol. 1. IEEE, 2006.

[128]. Maffucci, Antonio, Giovanni Miano, and Fabio Villone. "A new circuit model for carbon nanotube interconnects with diameter-dependent parameters."*Nanotechnology, IEEE Transactions on* 8.3 (2009): 345-354.

[129]. Nieuwoudt, A.; Massoud, Y., "Understanding the Impact of Inductance in Carbon Nanotube Bundles for VLSI Interconnect Using Scalable Modeling Techniques," *Nanotechnology, IEEE Transactions on* , vol.5, no.6, pp.758,765, Nov. 2006.

[130]. Pozar, David M. *Microwave engineering*. John Wiley & Sons, 2009.

[131]. Paul, Clayton R. *Analysis of multiconductor transmission lines*. John Wiley & Sons, 2008.

[132]. P. J. Burke, "An RF circuit model for carbon nanotubes," *IEEE Transactions on Nanotechnology*, vol. 2, pp. 55-58, Mar 2003.

[133]. Naeemi, Azad, and James D. Meindl. "Carbon nanotube interconnects."*Proceedings of the 2007 international symposium on Physical design*. ACM, 2007.

[134]. E. Pop, D. Mann, J. Reifenberg, K. Goodson and Honjie Dai, Electro-thermal transport in metallic single-wall carbon nanotubes for interconnect applications, Electron Devices Meeting, 2005. IEDM Technical Digest. IEEE International, pp. -252-256, 5-5 Dec. 2005.

[135]. Javey A, Guo J, Paulsson M, Wang Q, Mann D, et al. High-field quasiballictic transport in short carbon nanotubes. Phys. Rev. Lett. 92:106804, 2004.

[136]. Liang W, Bockrath M, Bozovic D, Hafner JH, Tinkham M, Park H. Fabry-Perot interference in a nanotube electron waveguide. Nature 411:665-69. 2001.

[137]. Hjortstam O, Isberg P, Soderholm S, Dai H., Can we achieve ultralow resistivity in carbon nanotube-based metal composites? Appl. Phys. A 78:1175-79, 2004.

[138]. A. Naeemi and J. D. Meindl, Performance Modeling for Single- and Multiwall Carbon Nanotubes as Signal and Power Interconnects in Gigascale Systems, IEEE TRANS. on ELECTRON DEVICES, vol. 55, No. 10, pp. 2574-2582.

[139]. Park, Ji-Yong, et al. "Electron-phonon scattering in metallic single-walled carbon nanotubes." *Nano Letters* 4.3 (2004): 517-520.

[140]. Jiang J, Saito R, Gruneis A, Chou SG, Samsonidze GG, at al., Photoexcited electron relaxation processes in single-wall carbon nanotubes. Phys. Rev. B 71:045417-19, 2004.

[141]. Huang S, Woodson M, Smalley R, Liu J. , Growth mechanism of oriented long single walled carbon nanotubes using “fast-heating” chemical vapor deposition process. Nano Lett. 4:1025-28, 2004.

[142]. Hong L, Wen-Yan Y, Kaustav B and Jun-Fa M., Circuit modeling and Performance Analysis of Multi-walled Carbon Nanotube Interconnects, IEEE TRANS on ELECTRON DEVICES, vol. 55, No. 6, pp. 1328-1337, 2008.

[143]. C. T. White and T. N. Todorov, Carbon nanotubes as long ballistic conductors, Nature, vol. 393, pp. 240-242, 1998.

[144]. J. Jiang, J. dong, H. T. Yang, and D. Y. Xing, Universal expression for localization length in metallic carbon nanotubes, Phys. Rev. B. Condens. Matter, vol. 64, No. 4, p. 045 409, Jul.2001.

[145]. N. Sriastava, H. Li, F. Kreupl, and K. Banerjee, On the applicability of single-walled carbon nanotubes: Quantum effects of electron-phonon coupling, J. Phys., Condens. Matter, vol. 19, No. 18, p. 183 203, Apr. 2007.

[146]. H. J. Li, W. G. Lu, J. J. Li, X. D. Bai and C. Z. Gu, Multichannel ballistic transport in multiwall carbon nanotubes, Phys. Rev. Lett., vol. 95, No. 8, p. 86 601, Aug. 2005.

[147]. M. S. Sarto and A. Tamburrano, Electromagnetic analysis of radio-frequency signal propagation along SWCNT bundles, Int. Symp. IEEE-NANO 2006, Cininati, OH, Jul.

[148]. M. S. Sarto and A. Tamburrano, Multiconductor transmission line modelling of SWCNT bundles in common-mode excitation, IEEE Int. Symp. Electromagn. Compat., Portland, OR, Aug. 2006.

[149]. M. D'Amore, M. S. Sarto, and A. Tamburrano, Signal integrity of carbon nanotube bundles, IEEE Int. Symp. Electromagn. Compact., Honolulu, HI, Jul. 6-9, 2007.

[150]. Maarouf AA, Kane CL, Mele EJ. 2000. Electronic structure of carbon nanotube ropes. Phys. Rev. B 61:11156.

[151]. Stahl H, Appenzeller J, Martel R, Avouris P, Lengeler B. 2000. Intertube coupling in ropes of single-wall carbon nanotubes. Phys. Rev. Lett. 85: 5186.

[152]. Robert Filter, Jing Qi, Carstern Rockstuhl, and Ralk Lederer, Circular optical nanoantennas: an analytical theory, Phys. Rev. B 85, 125429, 2012.

[153]. D'Amore, M., M. S. Sarto, and A. Tamburrano. "Modelling of multiwall carbon nanotube transmission lines." *Electromagnetics in Advanced Applications, 2007. ICEAA 2007. International Conference on*. IEEE, 2007.

[154]. Katsounaros, Anestis, Jiefu Zhang, and Yang Hao. "Microwave modeling of single multi-wall carbon nanotubes." *Antennas and Propagation (EUCAP), 2012 6th European Conference on*. IEEE, 2012.

[155]. Available: http://www2.rohde-schwarz.com/file_3463/RAC-0607-0019.pdf

[156]. Mao, Shau-Gang, Shiou-Li Chen, and Chen-Wei Huang. "Effective electromagnetic parameters of novel distributed left-handed microstrip lines."*Microwave Theory and Techniques, IEEE Transactions on* 53.4 (2005): 1515-1521.

[157]. Nicolson, A. M., and G. F. Ross. "Measurement of the intrinsic properties of materials by time-domain techniques." *Instrumentation and Measurement, IEEE Transactions on* 19.4 (1970): 377-382.

[158]. Weir, William B. "Automatic measurement of complex dielectric constant and permeability at microwave frequencies." *Proceedings of the IEEE* 62.1 (1974): 33-36.

[159]. Katsounaros, Anestis. *Characterization of multi-wall carbon nanotubes and their applications*. Diss. Queen Mary, University of London, 2011.

[160]. Katsounaros, A., J. Zhang, and Y. Hao. "Microwave characterization of a single multi-wall carbon nanotube." *Electromagnetics in Advanced Applications (ICEAA), 2012 International Conference on*. IEEE, 2012.

[161]. Chen, X., Akinwande, D., Lee, K. J., Close, G. F., Yasuda, S., Paul, B. C., ... & Wong, H. S. (2010). Fully integrated graphene and carbon nanotube interconnects for gigahertz high-speed CMOS electronics. Electron Devices, IEEE Transactions on, 57(11), 3137-3143.

[162]. Shan, G.C., et al. Nanolaser with a Single-Graphene-Nanoribbon in a Microcavity. Journal of Nanoelectronics and Optoelectronics. 2011, 6: 138-143.

[163]. Wang, Z. F., Shi, Q. W., Li, Q., Wang, X., Hou, J. G., Zheng, H., Yao, Y., Chen, J. (2007). "Z-shaped graphene nanoribbon quantum dot device". Applied Physics Letters 91 (5): 053109.

[164]. K. I. Bolotin, K. J. Sikes, J. Hone, H. L. Stormer, and P. Kim, “Temperature dependent transport in suspended graphene,” Phys. Rev. Lett., vol. 101, no. 9, p. 096 802, Aug. 2008.

[165]. D. A. Areshkin, D. Gunlycke, and C. T. White, “Ballistic transport in graphene nanostrips in the presence of disorder: Importance of edge effects,” Nano Lett., vol. 7, no. 1, pp. 204–210, Jan. 2007.

[166]. C. T. White and T. N. Todorov, “Carbon nanotubes as long ballistic conductors,” Nature, vol. 393, no. 6682, pp. 240–242, May 1998

[167]. Xu, Chuan, Hong Li, and Kaustav Banerjee. "Modeling, analysis, and design of graphene nano-ribbon interconnects." Electron Devices, IEEE Transactions on56.8 (2009): 1567-1578.

[168]. L. X. Benedict, V. H. Crespi, S. G. Louie, and M. L. Cohen, “Static conductivity and superconductivity of carbon nanotubes—Relations between tubes and sheets,” Phys. Rev. B, Condens. Matter, vol. 52, no. 20, pp. 14 935–14 940, Nov. 1995.

[169]. D. Gunlycke, H. M. Lawler, and C. T. White, “Room-temperature ballistic transport in narrow graphene strips,” Physical Review B, vol. 75, 2007.

[170]. D. A. Areshkin, D. Gunlycke, and C. T. White, “Ballistic transport in graphene nanostrips in the presence of disorder: Importance of edge effects,” Nano Letters, vol. 7, pp. 204–210, 2007.

[171]. Ragheb, Tamer, and Yehia Massoud. "On the modeling of resistance in graphene nanoribbon (GNR) for future interconnect applications." Proceedings of the 2008 IEEE/ACM International Conference on Computer-Aided Design. IEEE Press, 2008.

[172]. Palmer, Harlan B. "The capacitance of a parallel-plate capacitor by the Schwartz-Christoffel transformation." Electrical Engineering 56.3 (1937): 363-368.

[173]. Behnam, Ashkan, et al. "Transport in nanoribbon interconnects obtained from graphene grown by chemical vapor deposition." Nano letters 12.9 (2012): 4424-4430.

[174]. Cui, Jiang-Peng, et al. "Signal transmission analysis of multilayer graphene nano-ribbon (MLGNR) interconnects." Electromagnetic Compatibility, IEEE Transactions on 54.1 (2012): 126-132.

[175]. F. Stellari and A. L. Lacaita, “New formulas of interconnect capacitances based on results of conformal mapping method,” IEEE Trans. Electron. Devices, vol. 47, no. 1, pp. 222–231, Jan. 2000.

[176]. Kim, Hyungsuk, and Charlie Chung-Ping Chen. "Be careful of self and mutual inductance formulae." Online: http://ccf. ee. ntu. edu. tw/~ cchen/research/CompInduct9. pdf (2009).

[177]. Alexopoulos, Nicolaos G., and Shih-Chang Wu. "Frequency-independent equivalent circuit model for microstrip open-end and gap discontinuities."Microwave Theory and Techniques, IEEE Transactions on 42.7 (1994): 1268-1272.

[178]. Chen, Z., et al. "Thermal contact resistance between graphene and silicon dioxide." Applied Physics Letters 95.16 (2009): 161910.

[179]. Venugopal, A., L. Colombo, and E. M. Vogel. "Contact resistance in few and multilayer graphene devices." Applied Physics Letters 96.1 (2010): 013512.

[180]. Nikitin, A. Yu, et al. "Edge and waveguide terahertz surface plasmon modes in graphene microribbons." *Physical Review B* 84.16 (2011): 161407.

[181]. Shareef, Sultan, Yee Sin Ang, and Chao Zhang. "Room-temperature strong terahertz photon mixing in graphene." *JOSA B* 29.3 (2012): 274-279.

[182]. Gomez-Diaz, Juan Sebastian, Juan R. Mosig, and Julien Perruisseau-Carrier. "Effect of spatial dispersion on surface waves propagating along graphene sheets." *Antennas and Propagation, IEEE Transactions on* 61.7 (2013): 3589-3596.

[183]. Correas-Serrano, Diego, et al. "Spatially dispersive graphene single and parallel plate waveguides: Analysis and circuit model." (2013): 1-12.

[184]. Moon, J. S., et al. "Epitaxial-graphene RF field-effect transistors on Si-face 6H-SiC substrates." *Electron Device Letters, IEEE* 30.6 (2009): 650-652.

[185]. Habibpour, Omid, et al. "A subharmonic graphene FET mixer." *Electron Device Letters, IEEE* 33.1 (2012): 71-73.

[186]. Moon, J. S., et al. "Graphene FETs for zero-bias linear resistive FET mixers."*Electron Device Letters, IEEE* 34.3 (2013): 465-467.

[187]. Wang, Han, et al. "Graphene-based ambipolar RF mixers." *Electron Device Letters, IEEE* 31.9 (2010): 906-908.

[188]. Fallahi, Arya, and Julien Perruisseau-Carrier. "Design of tunable biperiodic graphene metasurfaces." *Physical Review B* 86.19 (2012): 195408.

[189]. Naishadham, Krishna, and Prasad K. Kadaba. "Measurement of the microwave conductivity of a polymeric material with potential applications in absorbers and shielding." *Microwave Theory and Techniques, IEEE Transactions on* 39.7 (1991): 1158-1164.sdfsdf

[190]. Dixon, Paul. "Cavity-resonance dampening." *IEEE Microw. Mag* 6.2 (2005): 74-84.Fante, Ronald L., and Michael T. Mccormack. "Reflection properties of the Salisbury screen." *Antennas and Propagation, IEEE Transactions on* 36.10 (1988): 1443-1454.

[191]. Chambers, B., and A. Tennant. "Optimised design of Jaumann radar absorbing materials using a genetic algorithm." *IEE Proceedings-Radar, Sonar and Navigation* 143.1 (1996): 23-30.

[192]. Fante, Ronald L., and Michael T. Mccormack. "Reflection properties of the Salisbury screen." *Antennas and Propagation, IEEE Transactions on* 36.10 (1988): 1443-1454.

[193]. Costa, Filippo, Agostino Monorchio, and Giuliano Manara. "Ultra-thin absorbers by using high impedance surfaces with resistive frequency selective surfaces."*Antennas and Propagation Society International Symposium, 2007 IEEE*. IEEE, 2007.

[194]. Padooru, Y. R. et al. Circuit modeling of multiband high-impedance surface absorbers in the microwave regime. *Physical Review B* 84, 035108 (2011).

[195]. John S. Seybold (2005) Introduction to RF propagation. 330 pp, eq.(2.6), p.22.

[196]. Lin, M. F., D. S. Chuu, and KW-K. Shung. "Low-frequency plasmons in metallic carbon nanotubes." *Physical review B* 56.3 (1997): 1430.

[197]. Haus, Hermann A., and James R. Melcher. Electromagnetic fields and energy. Englewood Cliffs: Prentice Hall, 1989.

[198]. Kalluri, Dikshitulu K. Electromagnetics of time varying complex media: frequency and polarization transformer. CRC Press, 2010. pp 38-40.

[199]. Kasap, S. O. (2006). Principles of Electronic Materials and Devices (Third ed.). Mc-Graw Hill. p. 126.

[200]. Rakheja, Shaloo, Vachan Kumar, and Azad Naeemi. "Evaluation of the potential performance of graphene nanoribbons as on-chip interconnects." *Proceedings of the IEEE* 101.7 (2013): 1740-1765.

[201]. Lin, Haiyan, et al. "Microwave-absorbing properties of Co-filled carbon nanotubes." *Materials Research Bulletin* 43.10 (2008): 2697-2702.

[202]. Lin, Haiyan, et al. "Investigation of the microwave-absorbing properties of Fe-filled carbon nanotubes." *Materials Letters* 61.16 (2007): 3547-3550.

[203]. Xiang, Changshu, et al. "Microwave attenuation of multiwalled carbon nanotube-fused silica composites." *Applied physics letters* 87.12 (2005): 123103.

[204]. Wen, Bo, et al. "Temperature dependent microwave attenuation behavior for carbon-nanotube/silica composites." *Carbon* 65 (2013): 124-139.

[205]. Zhu, Yanwu, et al. "Graphene and graphene oxide: synthesis, properties, and applications." *Advanced materials* 22.35 (2010): 3906-3924.

[206]. Zhang, Yuanbo, et al. "Direct observation of a widely tunable bandgap in bilayer graphene." *Nature* 459.7248 (2009): 820-823.

[207]. Katsounaros, Anestis, et al. "Near-field characterization of chemical vapor deposition graphene in the microwave regime." *Applied Physics Letters* 102.23 (2013): 233104.

[208]. Wu, Bian, et al. "Microwave absorption and radiation from large-area multilayer CVD graphene." *Carbon* 77 (2014): 814-822.

[209]. Khatami, Yasin, et al. "Metal-to-multilayer-graphene contact—Part II: Analysis of contact resistance." *Electron Devices, IEEE Transactions* on 59.9 (2012): 2453-2460.

[210]. Matsuda, Yuki, Wei-Qiao Deng, and William A. Goddard III. "Contact Resistance for “End-Contacted” Metal− Graphene and Metal− Nanotube Interfaces from Quantum Mechanics." *The Journal of Physical Chemistry C* 114.41 (2010): 17845-17850.

[211]. Cho, Kyeongjae, et al. "First-Principles and Quantum Transport Studies of Metal-Graphene End Contacts." *MRS Proceedings*. Vol. 1259. Cambridge University Press, 2010.

[212]. Lee, Eduardo JH, et al. "Contact and edge effects in graphene devices." *Nature nanotechnology* 3.8 (2008): 486-490.

[213]. Abergel, D. S. L., and Vladimir I. Fal'ko. "Optical and magneto-optical far-infrared properties of bilayer graphene." *Physical Review B* 75.15 (2007): 155430.

[214]. Liu, Yonghao, et al. "Approaching total absorption at near infrared in a large area monolayer graphene by critical coupling." *Applied Physics Letters* 105.18 (2014): 181105.

[215]. Yan, Hugen, et al. "Tunable infrared plasmonic devices using graphene/insulator stacks." *Nature Nanotechnology* 7.5 (2012): 330-334.

[216]. Phaedon Avouris, Alberto V. Garcia, Chun-Yung Sung, Fengnian Xia, Hugen Yan, "Graphene based structures and methods for shielding electromagnetic radiation.", US 20130333937.

[217]. Chen, Jian-Hao, et al. "Intrinsic and extrinsic performance limits of graphene devices on SiO2." Nature nanotechnology 3.4 (2008): 206-209.

[218]. Raymond A. Serway (1998). Principles of Physics (2nd ed.). Fort Worth, Texas; London: Saunders College Pub. p. 602.

[219]. Vollebregt, Sten, et al. "Size-Dependent Effects on the Temperature Coefficient of Resistance of Carbon Nanotube Vias." Electron Devices, IEEE Transactions on 60.12 (2013): 4085-4089.

[220]. Alison Reeves. Introduction to Electrodynamics (3rd ed.). Upper Saddle River, New Jersey: Prentice Hall, 1999. p. 286.

[221]. Jocelyn Phillips. Physics for Scientists and Engineers with Modern Physics (4th ed.). Upper Saddle River, New Jersey: Prentice Hall, 2009. p. 658.

[222]. De Volder, Michael FL, et al. "Carbon nanotubes: present and future commercial applications." *Science* 339.6119 (2013): 535-539.

[223]. Graphene-info.com, (2015). *Graphene applications: revolutionary graphene-based applications you should know | Graphene-Info*. [online] Available at: http://www.graphene-info.com/graphene-products